Prediction of Petro-physical Properties for Carbonates

Juan Ernesto Juri

Institute of Petroleum Engineering

Heriot Watt University

This dissertation is submitted for the degree of

Doctor of Philosophy

Abstract

This thesis is concerned with the inversion of lattice pore-network model parameters of carbonate rocks using only the capillary pressure, and then the use of the inverted parameters to predict the water-flooding relative permeabilities of the carbonate rocks. Background: There has been a tendency to claim that pore-network modelling using three-dimensional micro-computed tomography or 3D mathematically created images can predict imbibition relative permeabilities for wettabilities other than strongly water/oil-wetting. This is based on the flexibility for matching data, which is a weakness of pore-network modelling. The method proposed in this thesis is important because a large percentage of the porosity in carbonates is microporosity.

Conclusions: We applied stochastic inversion of lattice pore-network model parameters using Hamiltonian Dynamics (Hamiltonian Monte Carlo) to three carbonate rock samples and we predicted water-flooding relative permeabilities with good accuracy by using as constraint only routinely obtained data, such as mercury intrusion capillary pressure (MICP) and oil/water capillary pressure. We found that there is a strong correlation between the amount of microporosity and the volume exponent parameter. This suggests that when microporosity is ignored, the volume exponent will tend to be systematically strongly underestimated. HMC found large variability in wettability that causes mid-sized pores to be invaded at the same level of pressure as larger pores. The coexistence of these events reduces the tendency for preferential flow through large pores, resulting in more uniform flow at the pore scale compared with the case in which flow is restricted only to large pores. Mid-sized pores have an important effect on the connectivity because they could have higher contact angles than larger pores. Therefore, they do not spontaneously imbibe and shield larger pores, improving water-flooding displacement. The wettability of micropores could better explain the gentle curvature of the imbibition water relative permeability compared with the generally assumed mixed-wet large wettability model. The importance of the maximum and minimum observed capillary pressure is directly connected to accounting for the full pore-size distribution. Thus, the common assumption that microporosity can be ignored is unsatisfactory. The ranges of advancing contact angles obtained from the HMC inversion

were wider than the ranges of apparent advancing contact angles obtained with analytical determinations in previous studies, and in one case our results were contradictory to the analytical determination. It follows that variability in advancing and receding contact angles is not reflected in the apparent contact angle data outside porous media. Apparent contact angle data outside porous media cannot completely characterise the wettability in pore-network models because the data does not capture the contact angle variability in porous media. The existence of wetting films depends on the maximum capillary pressure during drainage, and thus wettability alteration during ageing. Our results suggest that matching both connate water at the maximum drainage capillary pressure before ageing and matching residual oil at the minimum imbibition capillary pressure leads to better estimation of the advancing and receding variability in the contact angles.

Acknowlegements

I am thankful to God for blessing me in many different ways. I am thankful to Jesus Christ my companion.

I would like to thank my wife Gisela. Thanks a lot for your love, patience, and for taking care of our twins Mia and Guada during the daytime.

I am extremely grateful to my supervisors, Professor Ken Sorbie and Dr. Rink van Dijke who showed understanding, patience and supported me in various ways during this difficult effort. Thank you very much for giving me the opportunity to do this Ph.D. I had the fortune to work not only with two great academics but also with two wonderful people who gave me guidance and sympathy to overcome difficult situations.

I would like to especially thank Dr. Shehadeh Masalmeh of Shell Technology for funding part of the work and for supplying the carbonate data. Also this research benefited from a Dorothy Hodgkin Research grant.

I would also like to thank Dr. Igor Bondino, who introduced me to the exciting world of pore-network modelling.

I would like to thank Professor Peter Mathews and Professor Vasily Damianov for their helpful comments which have greatly improved the quality of final version of the thesis.

Contents

List of Figures

List of Tables

Nomenclature

Greek Symbols

$\vartheta_{ow_n}^{adv}$ Oil/water advancing contact angle in the pore n [deg]

α Absolute temperature in Gibbs Equation (Variance in statistical context)

Σ Covariance matrix

$\boldsymbol{\theta}^t$ Current model (current state in the Markov chain)

$\Delta\tau$ Pseudo time step

Λ Brooks-Corey pore-size distribution index

λ Conductance exponent

ν Volume exponent

ϕ Porosity [fraction]

$\boldsymbol{\theta}$ Vector of model parameters

$\pi(\boldsymbol{\theta}_j)$ Model probability

π Posterior probability distribution function

$\boldsymbol{\theta}^{'}$ Proposed model (proposed move in the Markov chain)

$\vartheta_{ow_n}^{rec}$ Oil/water receding contact angle in the pore n [deg]

σ_{Hga} Mercury/air interfacial tension [N/m]

σ_{ow} Oil/water interfacial tension [N/m]

σ_{wa} Water/air interfacial tension [N/m]

τ Pseudo time in Hamiltonian formulation

τ_0 : Initial time

$\boldsymbol{\theta}$ Model parameters vector

θ Parameter

φ_{ow}^{adv} Oil/water advancing operative contact angle [deg]

φ_{ow}^{rec} Oil/water receding operative contact angle [deg]

ϑ_{ow}^{T} Oil/water equilibrium contact angle [deg]

ϑ_{ow}^{adv} Oil/water advancing apparent contact angle [deg]

$\vartheta_{ow_{MAX}}^{A-rec}$ Oil/water receding contact angle upper bound for population A [deg]

$\vartheta_{ow_{MAX}}^{A-adv}$ Oil/water advancing contact angle upper bound for population A [deg]

$\vartheta_{ow_{MIN}}^{A-rec}$ Oil/water receding contact angle lower bound for population A [deg]

$\vartheta_{ow_{MIN}}^{A-adv}$ Oil/water advancing contact angle lower bound for population A [deg]

$\vartheta_{ow_{MAX}}^{B-rec}$ Oil/water receding contact angle upper bound for population B [deg]

$\vartheta_{ow_{MAX}}^{B-adv}$ Oil/water advancing contact angle upper bound for population B [deg]

$\vartheta_{ow_{MIN}}^{B-rec}$ Oil/water receding contact angle lower bound for population B [deg]

$\vartheta_{ow_{MIN}}^{B-adv}$ Oil/water advancing contact angle lower bound for Population B[deg]

ϑ_{Hga} Mercury/air contact angle [deg]

ϑ_{ow}^{rec} Oil/water receding apparent contact angle [deg]

ϑ_{ow}^{T} Oil/water intrinsic contact angle [deg]

$\vartheta_{ow_{Th}}^{ow}$ Oil/water contact angle threshold for the existence of oil-wetting [deg]

$\vartheta_{ow_{Th}}^{ww}$ Oil/water contact angle threshold for the existence of water-wetting [deg]

Superscripts

A Population A of pores

adv Advancing

B Population B of pores

rec Receding

t Current time along the chain

Subscripts

a Air

α: Fluid phase

Hg Mercury

o Oil

w Water

Other Symbols

$\mathscr{A}^*$ Transformed set of events

$\mathscr{A}$ Set of events

I_o Amott oil wettability index

I_w Amott water wettability index

$A2$ Area under the secondary drainage capillary pressure curve

$A2$ Area under the imbibition capillary pressure curve

D Dimensions

ΔS_o Total change in oil saturation

ΔS_{ws} Change in water saturation

ΔS_{wt} Total change in water saturation

$E(\boldsymbol{\theta})$ Energy (misfit)

E_m Microscopic displacement efficiency

A_i	Event
F	Inverse probability function
$\widehat{f^*}$	Transformed pore-size distribution estimator
F^{-1}	Inverse probability
f_w	Fractional-wet
f_w	Fraction of pores in population A [fraction]
G	Forward operator (pore-network model simulator)
H	Entropy of the set
h	Entropy of an event
$\mathscr{H}$	Hamiltonian
$\mathscr{I}$	Identity matrix
K	Absolute permeability [md]
K	Kinetic energy
l	Lag distance
L	Lattice pore-network model size
$\mathscr{L}$	Lagrangian
r_-	Bin left bound [m]
$P^*_{c,Hga}$	Logarithmic transformation of mercury air capillary pressure
$P_{c,Hga}$	Mercury/air capillary pressure [Pa]
$\boldsymbol{p}$	Momentum vector
n	Number of time steps
N	Total number of bins in the pore-size distribution estimator
n	Total number of bins in the transformed pore-size distribution estimator

$\boldsymbol{X}$ Observation vector

$\boldsymbol{p}$ Conjugate momentum

$\mathscr{P}$: Set of frequencies

P Probability

P_{Acc} Transition probability

p_i^* Bin probability in the transformed parameterisation

$P_{c,ow}$ Oil/Water capillary pressure [Pa]

$P_{c,ow}^{obs}$ Observed oil/water capillary pressure [Pa]

$P_{c,ow_{MAX}}^{obs}$ Observed maximum drainage capillary pressure [Pa]

$P_{c,ow_{MIN}}^{obs}$ Observed minimum imbibition capillary pressure [Pa]

P_{ref} Reference pressure [Pa]

p_i Probability of a bin i

P_{nw} Nonwetting pressure [Pa]

P_w Wetting pressure [Pa]

r Radius [m]

r_+ Bin right bound [m]

r_{max} Maximum radius in the pore-size distribution [m]

r_{min} Minimum radius in the pore-size distribution [m]

r_{pt} Radius at percolation threshold [m]

RT-I Rock type I

RT-II Rock type II

RT-III Rock type III

R_{Wet} Threshold radius in the pore-size distribution that separates population A from population B [m]

S 2 20 Sample 2 20 - RT-III

S 2 4 Sample 2 4 - RT-II

S 28 Sample 28 - RT-I

S_{Hg} Mercury saturation

S_{oi} Initial oil saturation

S_{or} Residual oil saturation

S_{or}^{obs} Observed residual oil saturation

S_w Water saturation

S_{wc} Connate water saturation

S_{wc}^{obs} Observed connate water saturation

T Total integration time

T_2 Relaxation time [ms]

$\mathscr{U}$ Uniform distributed random variable

$\widehat{f}$ Pore-size distribution estimator

x Random number from $\mathscr{U}$

Y Random variable

y Random number from $\mathscr{U}$

Acronyms / Abbreviations

2D Two-dimensional

3D Three-dimensional

ACF Autocorrelation function

AH Amott: wettability index

BSEM Backscattering scanning electron microscope

CDF Cumulative distribution function

ECDF Empirical cumulative distribution function

E_m Microscopic displacement efficiency

EnKF Ensemble Kalman filter

EOR Enhanced oil recovery

HMC Hamiltonian Monte Carlo

IFT Interfacial tension [N/m]

KLD Kullback–Leibler distance

KL Kalman Filter

MCMC Markov Chain Monte Carlo

MICP Mercury intrusion capillary pressure

μ-CT Micro-computed tomography

NMR Nuclear magnetic resonance

PDF Probabilistic distribution function

PTFE Polytetrafluoroethylnes material

REV Representative elementary volume

SANS Small angle neutron scattering

SEM Scanning electron microscope

SSIP Statistical solution to the inverse problem

USBM United States Bureau of Mines wettability index

Var Variance

Chapter 1

Introduction

1.1 Background

A large percentage of the world's remaining oil is located in carbonate rocks (estimated to be 50% [304]). The pore sizes in carbonates may vary by several orders of magnitude, and describing in detail all of the features of the pores at different length scales may not be possible [321]. Because of the steady growth in oil demand and the decline in discovery, enhanced oil recovery (EOR) processes have become important to produce reserves from already developed oil reservoirs.

From a global viewpoint, the development of EOR technologies should align with worldwide initiatives to reduce carbon dioxide emissions. With regard to global warming, projects such as gas injection might be important. In the petroleum industry, macroscale full-field flow simulations to provide an economic basis to sustain the technical developments are well established. A reservoir model of this scale integrates information from pore-scale displacements to the scale of facies and formations to produce the output in terms of the fluids produced in the wells. Therefore, it is important to develop a model of functions that reflects the reality of the underlying recovery process. These functions are the relative permeabilities and capillary pressures. It is clear that EOR processes will dominate the future of oil recovery, and therefore understanding the physics at the pore scale is important to identify the key factors for a successful strategy.

pore-network models have attracted much interest in the last decade, although they date back to the work of Fatt [106]. Lattice networks have been known in physics for more than 50 years, while unstructured network models have only recently attracted attention. They allow the underlying physical principles to be included and the macroscopic behaviour to be simulated.

1.2 Using Pore-Scale Models to Model Carbonate Rocks

Pore-scale modelling seeks to implement the physics describing the fluid flow at the pore scale to predict macroscopic properties from first principles. These macroscopic properties are the inputs for continuous models of the porous media. In some situations, laboratory measurements are difficult and expensive to carry out. Using pore-scale modelling, one can understand how to improve oil recovery and predict flow functions that give better estimates of a given process at a large scale to support significant capital investments.

1.2.1 Limited Resolution of Micro-Computed Tomography

There has been considerable interest in obtaining X-ray micro-computed tomography (μ-CT) three-dimensional (3D) digital images of porous media as a source for pore-network models. The maximum resolution of μ-CT is approximately 1 μm [199], which leaves a large percentage of the total porosity in carbonates unresolved. For carbonate rocks, the pore-size distribution and connectivity may vary considerably with image size.

Moreover, the connectivity below μ-CT resolution is important [14, 40], and there is a trade-off between resolution and the length scale. At the highest resolution, the length scale of the reconstructed rock sample is a few millimetres [402], but carbonate rock samples may be heterogeneous in the centimetre range [284, 310]. Thus, a 3D image cannot simultaneously represent the large and small pores present in carbonates. We refer the reader to the review papers of Blunt et al. [48], Fusseis et al. [124], and Sheppard et al. [353], and the references therein, for more details.

1.2.2 Multiscale Problem

The limited resolution of μ-CT has motivated the development of algorithms that derive statistics from high-resolution scattering electron microscopy images of the microstructure. These algorithms [19, 20, 42–44, 55, 205, 227, 229, 293, 331, 407] produce 3D images of the porous media, similar to those produced by μ-CT. Overall, the results agree well with the bulk properties, such as the absolute permeability[283], formation factor, and porosity. However, the pore-size distributions of porous media are rarely reported. The combined effect of the resolution and volume of the reconstructed porous media (known as the multi-scale problem [104, 180, 379, 384]) makes it difficult to capture the wide range of pores present in carbonate rock samples. When the material is highly heterogeneous because of a large variation in pore sizes, (i) the resolution must be sufficient to resolve the smallest

features and (ii) there must be sufficient volume to accommodate all scales. These two requirements are only met in isotropic macroscopically homogeneous materials [400].

1.2.3 Characterisation of Wettability

Wettability is essential in various EOR processes, such as gas injection [79, 108, 112, 143, 157, 158, 167, 192, 193, 208, 209, 219, 233, 234, 285, 297–299, 301, 308, 313, 337, 389, 390, 392, 395, 397–399] and surfactant injection [137, 359, 361–363, 408, 412]. The wettability plays an important role in determining the water-flooding performance [236, 238, 240, 247, 248, 295], residual oil saturation [74, 145, 306, 307, 385, 387], and improving the productivity of gas wells in gas fields [1, 220, 410].

There is a threshold in pressure beyond which the thickness of water wetting films reaches a lower limit and they collapse. This lower limit is related to the displacement pressure from pores of a given size. When the films collapse, the surface is available to developed mixed-wet wettability [265].

Any EOR method attempting to change the wettability needs to first assess the current wettability and determine whether the changes from the initial conditions significantly change the macroscopic properties. The complex pore structure and mineralogy of reservoir rocks along with the interaction with crude oil result in there being a complicated relationship between the wettability and the capillary pressure.

1.3 What Makes Prediction of Relative Permeabilities Using Pore-Network Models Nontrivial?

In general, the main problem when using pore-network models is the uniqueness of the estimated pore-network model parameters [51, 160, 360]. capillary pressure measurement predictions are not sufficient to predict the relative permeabilities, because the data being predicted are used to characterise the network model. Additionally, little attention has given to characterising wettability in pore-network models.

The multiplicity of models that equally estimate the capillary pressure indicates that pore-network model parameter estimation is a difficult problem. capillary pressure, porosity, and absolute permeability were the only data available in this study. Reliable predictions are difficult with limited information, which suggests that using only capillary pressure as a calibration measurement is a strong limitation when predicting flow functions.

Wettability is an important parameter for any pore-network model that aims to predict water-flooding or gas-flooding rock functions. In the last decade, considerable effort has been made to rigorously model the coexistence of multiple phases within a single pore using pore-network models [46, 92, 111, 146, 249, 311, 312, 337, 388, 393, 394].

Pores with angular cross-sections have been proposed as a more realistic conceptualization of the real pore space [201, 300]. While these models have progressively captured more of the physics of the pore-scale displacement mechanisms, they have not focused on characterising the wettability parameters in the models.

1.4 Using Lattice Pore-Network Model to Characterise Carbonates

This work uses lattice pore-networks to investigate carbonate rock samples shown in Fig. 1.1a, as opposed to irregular pore-networks, shown in Fig 1.1b, more closely resembling realistic pore structures.

Diagenetic processes in carbonates rocks have modified the initial porous media leading to complex multiscale system with complex wettability. A large part of the pore-size distribution is located in the sub-micrometer range of pore sizes (25–50% of the total porosity [71]). Therefore, these systems require high resolution below 1 micron. However, μ-CT cannot provide (We will discuss this further in Section 2.3.2).

Using different scanning electron microscope (SEM) images at different resolutions can incorporate different scales [181]. However, this type of approaches may result in practical difficulties and uncertainties in how to merge the scales. Images at different scales are different in size and are very tiny. The pore-size distributions obtained at each scale may be not representative. In addition, the variability from the multiple scales is frequently neglected. There are difficulties in these approaches which include (1) unknown relationship between SEM image, the resulting training template or training image and the final product which is the 3D reconstructed 3D image (2) ad hoc assumption in the segmentation of the raw SEM image. Therefore, the question of whether reconstructed porous media are faithful representations of the real microstructures has not been fully answered.

Simplifying real porous media with any pore-network model causes a problem of uniqueness of the estimated pore-network model parameters [51, 160, 360]. A weakness of pore-network models is the multiplicity of models that equally match capillary pressure, porosity and absolute permeability. This indicates that pore-network model parameter estimation is

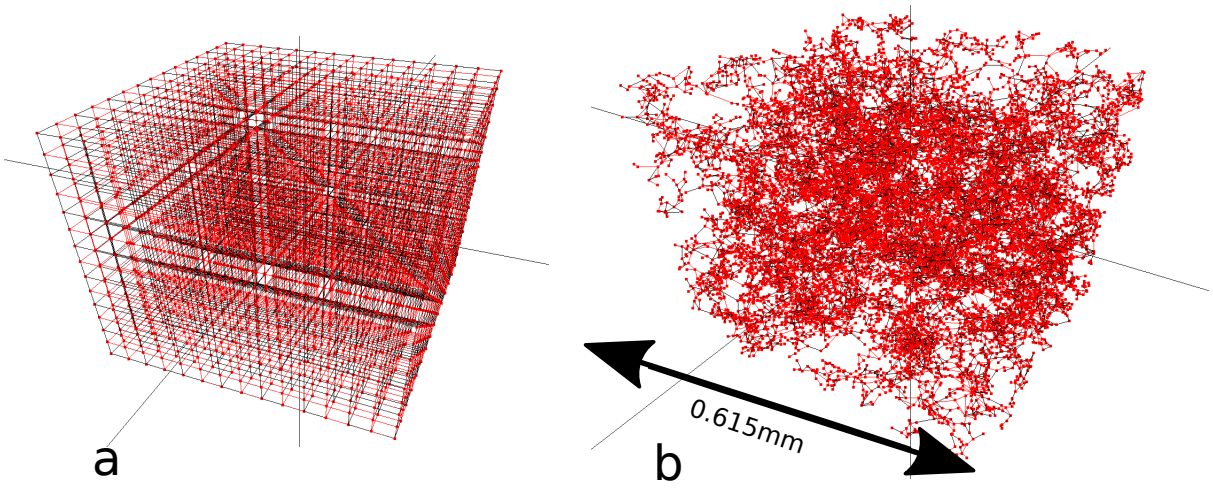

Fig. 1.1 (a) Lattice pore-network model; (b) Irregular pore-network model.

a difficult problem.

The work done in predicting relative permeabilities for carbonates using irregular networks have only considered a limited part of the pore-size distribution attentive only to feature of resembling realistic pore structures and neglecting. However, it is well-known that the universality in relation to percolation properties applies equally to lattice and to other type of pore-network models, such as irregular pore-network models extracted from the digital reconstruction of the porous media. Basically, at low fluid velocities the capillary forces dominates and the system is capillary dominated [217]. Fluid distribution at low capillary number is independent of the orientation of pores. Jerauld et al. [176, 179] showed that if the average coordination number of a lattice network equals the average coordination number of an irregular network, transport and percolation properties of both networks are in agreement.

In this work, we use lattice pore-network models tha have parameters that can be investigated sythematically using probability theory. In that sense a probabilistic approach can give better insight into of the relation between the porous media represented by the data set and the numerical model of reality represented by the network of interconnected capillary elements. The principal disadvantage of lattice network (Fig. 1.1a) compared with an irregular pore-network that inputs the skeleton extracted from the digital reconstruction (Fig. 1.1b) of porous media is that the maximum coordination number is 6. However, as mention above average coordination number is usually below six. Variable volume and conductance exponents in lattice pore-networks can capture a realistically wide range of the complexity of porous media. In inverse problems the probability of nouniqueness increases if more complex representations are used. And therefore, more complex pore-network models may

produce better matching of the capillary pressure data but they will not necessarily produce better predictions. However, the implications of this nonuniqueness are not that obvious and may depend on the interplay between the different parameters. In Sections 2.3, 2.4, 2.5, and 2.6 we discuss a number of approaches to characterise pore-network models that readily show the problem of nonuniqueness of pore-network model parameters.

Adopting a probabilistic approach without forcing the model to fit data allows the underlying phenomena to produce patterns of variability and flexibility that may offer the possibility to make better predictions. We feel that this method will become increasingly important in the future as the oil industry is moving towards more difficult rocks such us unconventional resources in which pore sizes are smaller and maybe mercury intrusion capillary pressure is the only data available [70, 105, 114, 374, 413, 414]. Moreover, our method can provide more complex approaches with a baseline for understanding more complex pore-network models.

It has become increasily apparent the role of microporosity [49, 59, 70, 77, 123, 188, 318, 414]. There are two hypothesis; one that neglects microporosity and another that allocates microporosity everywhere as a virtual network [25] with weakly oil wet.

The idea is to use lattice networks (Figs 1.1a and 1.2) combined with indirect measurements of real samples to characterise the pore-network structures [33, 163, 221, 252, 269, 314, 319, 378, 379, 381, 383, 384]containing any possible range of pore sizes and any possible pore-size distribution that allows interaction of the different length scales with wettability. Chapter 7 will show that accounting for microporosity turned to be a key component in determining the wettability.

We first focused on deriving prior information from MICP data that is independent of the several orders of magnitude of pore sizes in carbonate rock samples. We then incorporated this information into the inversion algorithm by parameterising the pore-size distribution using information theory. The main concern in information theory is to define the parameters or the probabilistic distribution functions (PDFs) using the least possible number of assumptions based on the information at hand. This approach is different from other methods, which rely on strong assumptions regarding the parametric form of the PDF.

There has been little discussion about the distribution of contact angles. Characterisation of porous media involves the interplay of parameters that are involved in the capillary pressure behaviour. The same patterns of contact angle hysteresis have been observed in two systems with different complexity but with the same fluids and solid substrate [274]. The dependence between the pore structure and the wettability results in a number of solutions. Despite the efforts made in identifying wettability models and quantifying the wettability

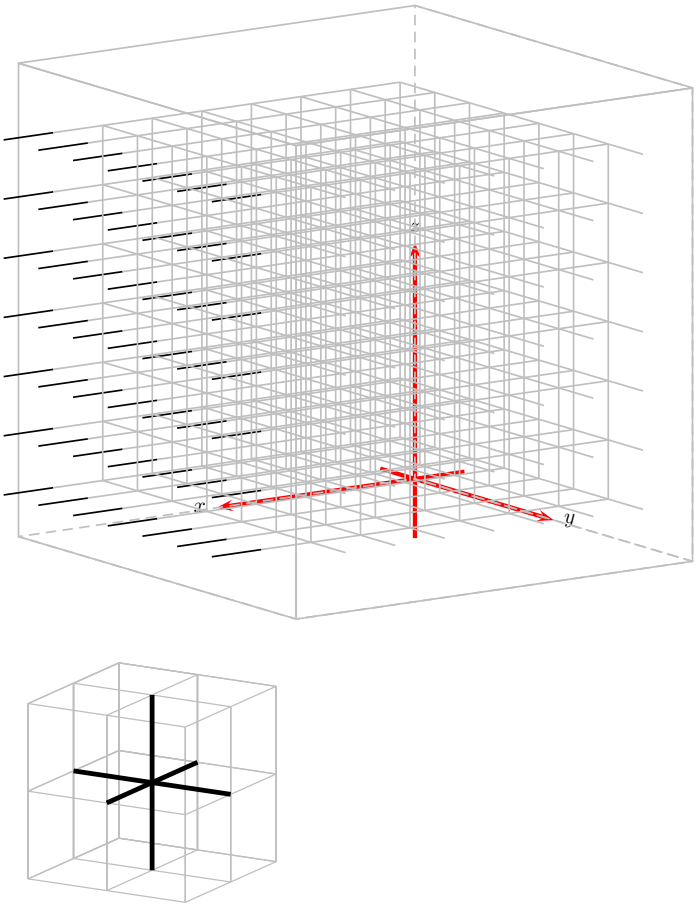

Fig. 1.2 The top figure shows the lattice network. The black pores offseting the cube represent the inlet pores. The bottom figure shows a typical junction in which the branch are cut to vary the coordination number.

behaviour wettability indexes, they are still not reliable. The distribution of contact angles influences spontaneous imbibition and has effects that are difficult to directly interpret from two-phase capillary pressure data ([86, 237, 257]). A carbonate rock sample with a pore-size distribution of 4 to 5 orders of magnitude might contain both expressions of heterogeneous wettability.

Using probability theory, the solution to the inverse problem of parameter estimation is a distribution of possible model parameters. A probabilistic approach involves sampling the solution space using a search algorithm, which must be able to escape from local minima. We proposed stochastic inversion as a solution to the nonuniqueness of lattice-type pore-network model parameters. We used a hybrid algorithm that combines molecular dynamics steps with stochastic steps using Hamiltonian equations. The proposed Hamiltonian Monte Carlo (HMC) method has a unique combination of desirable properties: it can move large distances in a complex misfit landscape and escape from local minima to find the global minimum. The method solves the general statistical equation for the parameter estimation problem using sampling. We validated the proposed method using synthetic capillary pressure data, and applied it to three carbonate rock samples.

1.5 Objectives

The main objective of this work is to model multiphase flow in carbonate sedimentary rocks. Within this sedimentary rock group, this work is specific to a data set from a reservoir in the Middle East . This work focuses on using routinely acquired measurements, such as mercury intrusion and oil/water capillary pressure, to predict relative permeabilities.

The core idea behind our study based on HMC is that interaction of parameters leads to complex collective behaviour. Stochastic Inversion allowed us to generate large amount of simulation data. And certain properties/characteristics of pore-network models conditioned to data only emerge and thus become visible when dealing with lots of simulations .

1.6 Contributions

This is the first application of HMC to pore-network model parameter estimation, in particular to the complicated case of carbonates and using only capillary pressure as the only data to constrain the inversion algorithm. The findings are unique in the sense that HMC has allowed correlations to emerge that contribute to an ongoing debate about wettability in carbonates. These correlations challenge the usual assumption that microporosity is water-wet and only large pores maybe oil-wet.

1.6.1 Contributions

- We developed a methodology to **fully characterise lattice network parameters** only with routinely acquired **capillary pressure** data.
- We developed a new implementation of **Hamiltonian Monte Carlo** stochastic inversion.
- We developed a **Nonparametric** representation of the pore-size distribution based on information entropy, with **equal information per bin**.
- We developed a new pore-size distribution **estimator**.
- We **validated** the methodology using a synthetic case with a difficult pore-size distribution.
- We successfully **applied** the methodology to three very different carbonate samples.

1.7 Organisation of the Thesis

This thesis is divided into eight chapters. Chapter 2 reviews the previous research of estimation of pore-network models to predict the relative permeability of sandstones and carbonates. Chapter 3 introduces the available carbonate data set. Chapter 4 presents a method for scale-independent parameterisation of the pore-size distribution. The key concept is the Shannon information. The technical aspects of implementing Hamiltonian dynamics coupled with stochastic steps, which forms the core of the Hamiltonian Monte Carlo (HMC) inversion method, along with the pore-network model are presented.

In Chapter 5, the HMC algorithm is benchmarked to an analytical problem. Application of the proposed theory and methods to a synthetic case is demonstrated in Chapter 6. The first part of this chapter investigates the effect of recovering the true pore-network model parameters generated in a large network using a small network for the inversion. The second part of Chapter 6 focuses on the advantages of the proposed parameterisation. The proposed pore-size distribution parameterisation approach is compared with a log-uniform parameterisation, and suggests that care is required when there are several orders of magnitude difference in pore sizes. The effects of pore-network model lattice size and statistical temperature are also investigated in a statistical context.

Chapter 7 applies the methods to a real carbonate data set. This chapter is divided into three parts. The first part focuses on inversion of the pore-network model structural

parameters, and the second part applies the HMC to the inversion of pore-network model wettability parameters. The last part of the chapter uses a full set of estimated parameters to predict the imbibition relative permeabilities, and the importance of microporosity is discussed in detail together with its implications.

Finally, Chapter 8 summarises the findings and presents recommendations for possible new research directions.

Chapter 2

Literature Review

2.1 Introduction

The purpose of this literature review is to provide the context of this work and give an overview of the key research in this area (Sections 2.3, 2.5 and 2.6). The method is developed in detail in Chapter (4), and additional specific references will be given.

Characterising porous media involves two interrelated aspects. First, the pore sizes and the connection between them, i.e., the structure of the porous media (Section 2.3). The second aspect is the wettability, which describes the multiple immiscible phases that are in contact (Section 2.5) and can be correlated with the pore size. Section 2.3 reviews how the structure of porous media is characterised at the pore scale. This can be essentially performed in two ways.

First, indirect observed data is used to construct a single model to describe the porous media. This model simulates the behaviour of real porous media. The important role of micropores (microporosity), and their connection with wettability mainly distinguishes carbonate rocks from clastic sedimentary rocks. The micropores result in an extremely large variation in the pore sizes in the internal structure of the rock, and influence the distribution of oil, water, and gas within the porous media. The deterministic nature of the approaches reviewed in this section raises questions about the uniqueness of the solution to the inverse problem.

The second approach involves methods that seek an exact representation of the porous media as if it was a direct measure. These methods have limitations in terms of resolution and the representative elementary volume (REV). The methods that use this approach are micro computerised tomography (μ-CT) and algorithms that statistically reconstruct an exact representation of the porous media. There is an intermediate step that extracts the

network from the void space of these reconstructed porous media involving assumptions without a single solution.

Section 2.5 discusses wettability, i.e., the affinity of fluids for the solid surface, which is an additional characteristic of the complete porous-media/fluid system. The first part of this section explains the concept of wettability, the methods to quantify wettability, and the effect of wettability on capillary pressure. Even though there are indices that quantify wettability, they might not completely convey the underlying wettability at the pore level. The second part of this section explains the relationship between wettability and pore structure, and determination of contact angles from capillary pressure measurements.

Section 2.5 describes how wettability is accounted for at the pore scale. The multiple wettability scenarios at the pore scale can produce similar behaviour at the scale of capillary pressure measurements. The capillary pressure depends on both the wettability and the pore structure.

2.2 Pore-Scale Modelling Aspects of Reservoir Engineering

Proper understanding of the physics at the pore scale can incorporate knowledge about various aspects from large-scale production strategies to detailed description of laboratory experiments. Ultimately, at the field scale, the quality of production forecasts will be determined by whether the measurements made in the laboratory are representative of the in situ conditions in the reservoir.

Different layer sweep efficiencies can essentially give the same oil recovery at water breakthrough (Fig. 2.1). Capillary, viscous, and gravitational forces affect the vertical distribution of saturation (Fig. 2.1). Thus, it is necessary to consider all of these forces and ensure that the dynamics in the reservoir is satisfactorily represented.

Generally, reservoir engineers have to continuously adjust field-scale models. One of the reasons is that some of the pore-scale behaviour of the capillary pressure is ignored in field-scale reservoir simulators. Positive capillary pressure is effective in promoting cross-flow towards low permeability layers (Fig. 2.1, $P_{c,ow} > 0$), increasing the vertical sweep performance in which the fluids are swept. The opposite effect is caused by negative capillary pressure, which delays cross-flow until highly permeable layers are depleted. Taking wettability into account in field-scale reservoir simulations can have a large effect on the recovery factor [245] (Fig. 2.2b), not only the sign of the capillary pressure, but also its

functional form (Fig. 2.2a).

Microscopic efficiency is a crucial reservoir engineering aspect of any oil recovery process. The previous example discussed the vertical efficiency of water-flooding. The expression of microscopic displacement efficiency $E_m = S_{oi} - S_{or}/S_{oi}$ quantifies the maximum potential of oil recovery and involves the initial (S_{oi}) and residual oil saturation (S_{or}) [266].

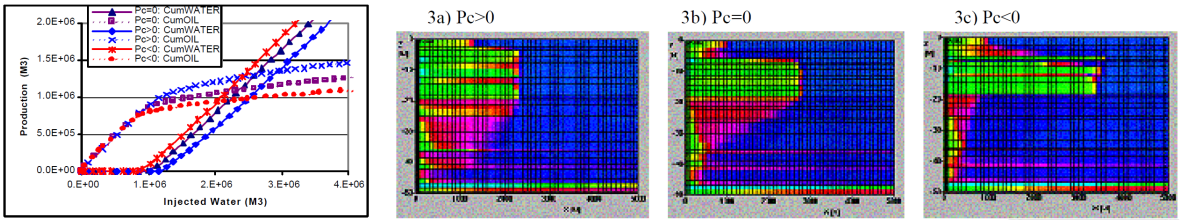

Fig. 2.1 Assessment of the effect of considering capillary pressure by simulation of three water-flooding scenarios: positive, zero, and negative capillary pressure. Different layer sweep efficiency can give essentially the same oil recovery at water breakthrough (cases 3a, 3b, and 3c) but the fluid distribution is different because of the wettability [245].

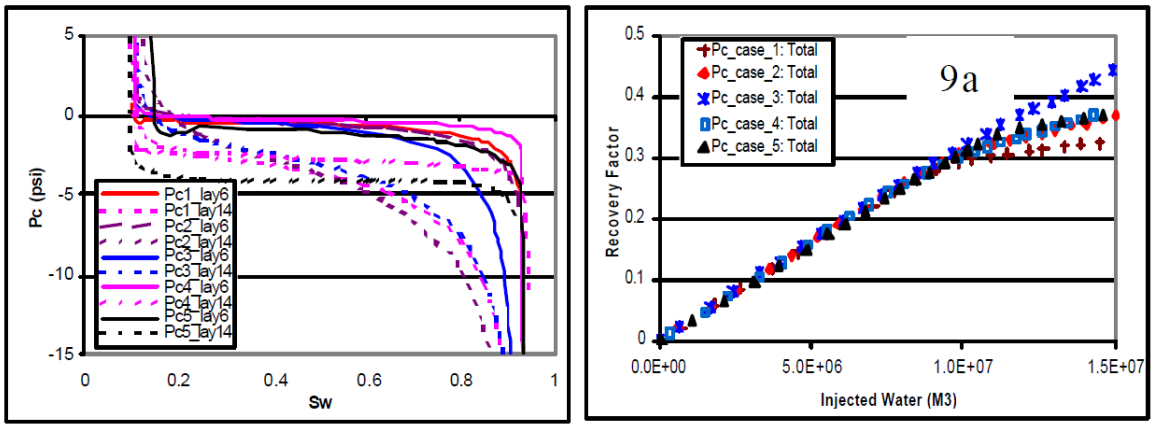

a b

Fig. 2.2 (a) Different negative capillary pressure curves; (b) Recovery factor versus cummulative water injected from field-scale reservoir simulations using capillary pressure curves in (a) [245]

There are essentially two types of mechanisms observed in laboratory experiments. (1) In fluid/rock systems in which the rock exhibits a strong preference for being in contact with the water phase (i.e., strongly water-wet systems), the oil phase is left behind as the water front sweeps the medium. This oil phase is located in disconnected oil-saturated clusters. Thus, E_m reaches a maximum value after one pore volume of injected water. Further

injection of water is incapable of pushing out the disconnected oil clusters and there is no significant additional oil production. Similar behaviour but with even higher oil recovery has been observed for weakly water-wet conditions [278]. (2) In fluid/rock systems in which the rock exhibits mixed-wet, intermediate-wet/neutral-wet (mixed-wet will be used to refer to these systems: mixed-wet and intermediate-wet/neutral-wet systems), and oil-wet behaviour (Section 2.5 gives a more detailed definitions of these systems), the oil phase shows continuity even at very low oil saturations. Thus, oil recovery is a function of the number of pore volumes injected. These two conditions are important to design the recovery process.

The microscopic efficiency in mixed-wet systems shows counterintuitive behaviour in terms of the absolute permeability. Absolute permeability is an intrinsic property of porous media. The microscopic efficiency correlates well with the absolute permeability in the majority of rock/fluid systems, except for mixed-wet systems. The microscopic efficiency in mixed-wet systems seems to be independent of the absolute permeability even at very low absolute permeability [238].

Wettability depends not only on lithology, but also on the crude oil composition. Studying the effect of wettability on water-flooding performance has a long history in the oil industry. There is a common laboratory practice of studying the alteration of the initial wettability of porous media by putting the rock surface in contact with crude oil and brine for a long period of time in an attempt to simulate geological time. Bobek et al. [50] found that combining different sets of core materials (carbonates and sandstones) with different types of crude oil from the Texas basin resulted in uncorrelated behaviour between the crude oil and the lithology. Crude oil can affect different types of rock lithology in different ways and the same lithology is affected differently by different crude oils.

Wettability is important to identify the optimum conditions for oil recovery. The enhanced oil recovery (EOR) process needs to know the potential of the reservoir in terms of remaining oil. Bobek et al. [50] found that water-wet cores led to more initial recovery than oil-wet cores. This highlights the importance of evaluating the wettability to identify the potential of a reservoir for EOR and to determine whether there is a mechanism to shift the wettability to recover more oil. The wettability of the rock controls the optimum conditions for oil recovery (Fig. 2.3) and incorrectly characterising the wettability can directly affect the design of production facilities. This may seem to be a strong justification for investing resources in determining the wettability. In addition, not only are laboratory experiments necessary, but care and effort also needs to be taken in interpreting laboratory measurements [245].

The laboratory protocol is based on the assumption that all reservoirs are water-wet be-

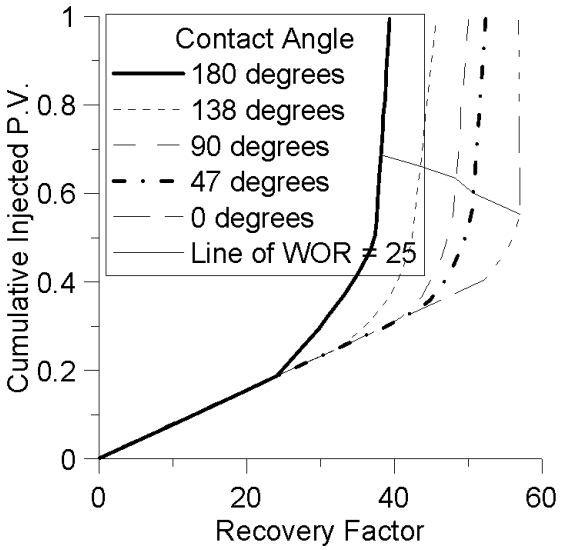

Fig. 2.3 Recovery factor as a function of contact angle. The line across the curves indicates WOR= 25. Figure taken from [50]

cause oil migrates into the rock body that was initially filled with water. Therefore, core cleaning is a laboratory protocol that seeks to render the rock water-wet to calculate the initial saturation distribution in the reservoir regardless of the actual conditions of the reservoir. The assumption of strongly water-wet conditions may influence interpretation of capillary pressure measurements, especially in cases where the reservoir is actually intermediate- or oil-wet [12]. The shape of the capillary pressure curve changes, causing underestimation of the vertical distribution of saturation (Fig. 2.4).

Introducing imbibition capillary pressure in field-scale numerical simulation models ensures that the vertical saturation distribution match the wire-line log [162]. Many reservoir engineering studies underestimate the effect of capillary pressure and it is often ignored (scenario $P_{c,ow} = 0$ in Fig. 2.1). Including imbibition capillary pressure in the field-scale numerical model significantly reduces the predicted water-cut in producers located towards the low part of the flanks of the reservoir structure compared with simulations assuming $P_{c,ow} = 0$. This helps to define a strategy to place the producers closer to oil–water contact to increase oil recovery [162]. The distribution of wettability across the oil zone can be complex and directly affects the water-flooding performance [294].

Figure 2.5 shows the variation of wettability with depth in terms of the wettability indices (Amott and United States Bureau of Mines (USBM) wettability indices will be explained in detail in Section 2.5.1). There is a clear indication that the wettability of the reservoir changes from water-wet at the bottom near the water–oil contact to intermediate

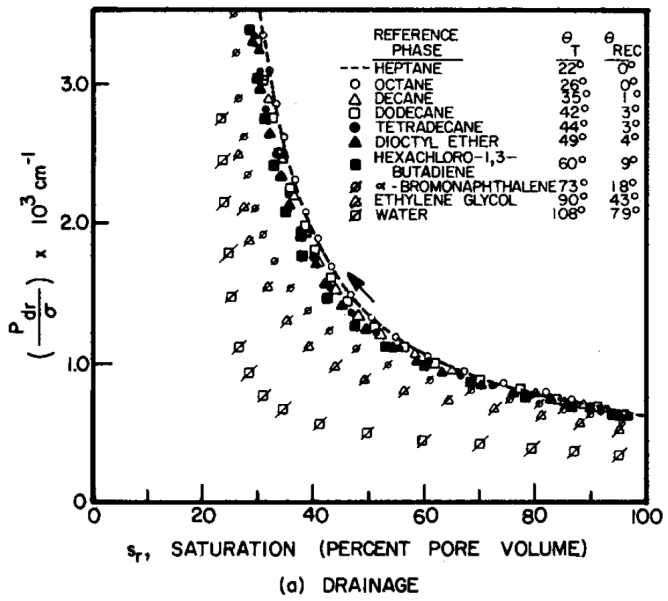

Fig. 2.4 Effect of contact angle (the upper right corner shows the association of symbols and contact angles ϑ_T) on drainage capillary pressure [275]. The figure shows that the relative shapes of the curves change as the contact angle increases. Figure taken from [275]

and/or oil-wet behaviour at the top. The oil wetting character increases towards the top of the oil column and is correlated with the decrease in water saturation.The large variation in the wettability indices may influence the water-flooding performance. The laboratory measurements of residual oil saturation with depth varied by five times.

The variation of wettability with height affects the oil recovery in carbonate reservoirs differently than in sandstone reservoirs. The Prudhoe Bay reservoir, a giant oil reservoir in North America, shows mixed-wet behaviour towards the top of the geological structure while more water-wet behaviour is observed near the water-oil contact [177]. In sandstone reservoirs, the vertical position has a significant effect on the relative permeabilities, and oil recovery is highly correlated with the absolute permeability [139]. However, in mixed-wet carbonate reservoirs, the residual oil saturation seems to be independent of the initial oil saturation and absolute permeability even for extremely low residual oil saturation values [238]. Mixed-wet systems do not show the usual correlations found in sandstone reservoirs. Many attempts have been made to correlate the static geological description of the reservoir (i.e., depositional facies) with flow properties [238, 292, 375].

Generally, the mineralogy in sandstone rocks creates mixed-wet systems with fractional-wet behaviour. (Section 2.5.3 will discuss the concept of heterogeneous wettability, such as fractional-wet behaviour). Hamon [138] found that none of 26 wettability measurements at

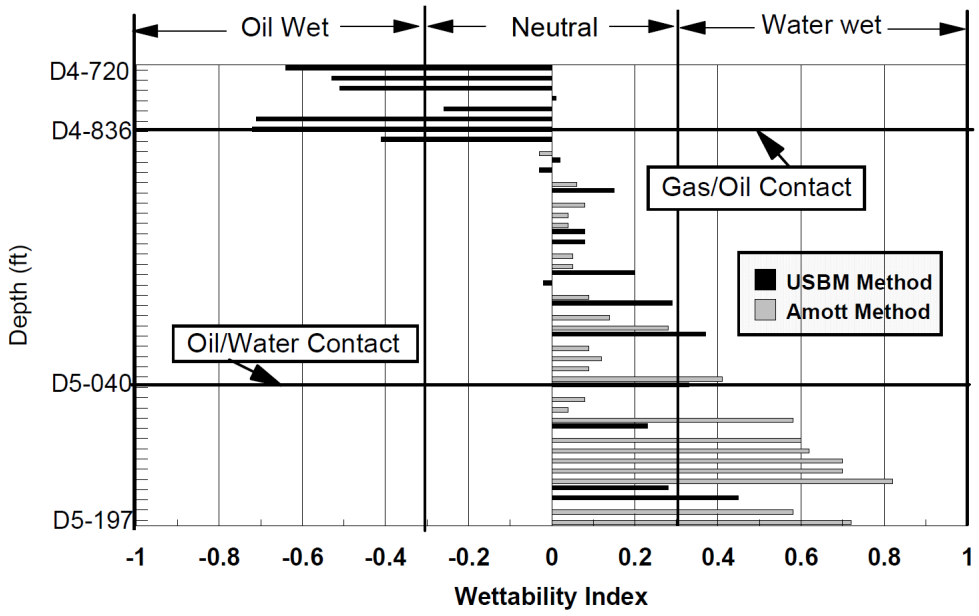

Fig. 2.5 Variation of wettability (measured by wettability indexes) with depth in a carbonate reservoir. Figure taken from [294].

different heights above the water oil contact in a sandstone reservoir showed fractional-wet behaviour despite the increasing amount of kaolinite, which is believed to be responsible for producing more oil wetness. The authors posed the question of whether the presence of kaolinite clay modifies the pore shape. Therefore, the pore shape might have more effect on the wettability than the presence of kaolinite in producing fractional-wet behaviour [138].

Mixed-wet carbonate reservoirs also show counterintuitive behaviour of other properties, such as water-flooding entry pressure and connate water saturation. It might be intuitive to think that a medium with higher hydraulic conductance will allow better displacement of the fluids saturating the porous media. The oil displacing water from the porous media in quasistatic conditions (i.e., drainage capillary pressure) shows a correlation with the absolute permeability. In contrast, in mixed-wet carbonates, very low connate water saturation has been observed even for absolute permeabilities of 1 mD [375]. Furthermore, water-flooding entry pressure seems to be independent of the absolute permeability of porous media [238, 375]. The above considerations suggest that the wettability at the pore level are important during water-flooding [257].

To obtain a correct result it is necessary to incorporate capillary pressure for convergence of the macroscopic equations that model flow in porous media at the reservoir scale [166]. capillary pressure and relative permeabilities are petrophysical properties and depend on the direction of saturation changes (i.e., hysteresis). Field-scale reservoir simulators are fitted

with empirical hysteresis models that incorrectly predict hysteresis patterns compared with authentic hysteresis predicted from pore-scale modelling, leading to underestimation of the predicted oil recovery. Pore-scale modelling is a useful tool to calculate correct scanning curves. These curves depend on the initial water saturation, which depends on the vertical height from the water oil contact [166].

Network modelling is a process-based method that can incorporate any of the various pore-scale phenomena, track the processes as they happen, examine the consequences, and generate capillary pressure and relative permeabilities to supply field-scale reservoir simulators that integrate the pore scale with macroscopic geological features. Moreover, Buckley-Leverett analyses using pore scale simulated relative permeabilities curves showed that the most efficient displacement actually takes place in a system containing approximately 50 percent of oil-wet pores [257]. This is in line with core floods results indicating that the most efficient immiscible displacement is obtained with both, oil and water, capable of spontaneously imbibing into the porous media [254]. Pore-scale modelling can determine the combined conditions to understand laboratory experiments.

The ability to model a physical process at the pore scale can provide a way of calibrating field-scale reservoir models, screening and planning EOR strategies, and designing meaningful laboratory experiments.

2.3 Characterisation of Pore-Network Model the Structure

In this section we review the use of lattice network models combined with indirect measurements of real samples as an approach to characterise pore-network model structures [33, 163, 221, 252, 269, 314, 319, 378, 379, 381, 383, 384]. Hereafter, we will refer to these approaches as indirect methods. However, few studies using this approach have made predictions of data that are not used as matching data. All of these indirect approaches incorporate the wide range of pore sizes in the pore-size distribution, and the results agree well with mercury intrusion capillary pressure (MICP) measurements. Most of these indirect methods have combined additional data with the MICP, and do not confirm that the obtained pore-network model parameters are unique. However, in general, the main problem with using lattice pore-network models and pore-network models is the uniqueness of the estimated pore-network model parameters [51, 160, 360]. Capillary pressure measurement predictions are not sufficient to predict the relative permeabilities, because the data being predicted are used to characterise the network model. Additionally, few studies have reported relative permeabilities predictions from experimental data.

2.3.1 Indirect Methods

MICP

Fitting the MICP, porosity, and absolute permeability using a network-model simulator does not guarantee uniqueness of the solution to predict the transport properties [207, 255]. Even manually fitting simulated data generated by the network model can produce multiple outcomes [255]. Fitting is an important part of direct methods and usually involves fitting the MICP. Forced intrusion of mercury into a porous material is usually used to characterise the pore-space microstructure. Washburn [403] suggested a method to obtain a pore-size distribution from measurements of the volume injected versus the pressure applied, and this methodology became routine after the work of Drake and Ritter [93] [329]. Purcell [316] introduced the procedure to the petroleum industry. Since then, reservoir engineering calculations routinely use MICP curves measured for reservoir rock samples.

However, pore-size distributions derived from MICP will always overestimate small pores. On its way to the interior of the rock, mercury is likely to come across smaller pores than some of the pores in the interior. Larger pores are therefore only invaded at high capillary pressure, and are hence incorrectly assigned to the small pores in the pore-size distribution. Thus, the number of pores entered through small pores will be overestimated. Quantitative evidence of this effect is provided by comparing pore-size distributions obtained by photomicrographic (two-dimensional (2D) photomicrographs also do not provide the true pore-size distribution) techniques with pore-size distributions determined from mercury injection pressures [97].

The usual method to determine a pore-size distribution from MICP data assumes that the pore volume invaded after a particular pressure increment is contained in pores of radius equal to that of a cylindrical capillary that would be invaded at the given pressure (Chapter 4 will introduce a variation of this method). Geologists commonly use Thomeer hyperbola curves to match the MICP and describe different porous systems in carbonates [71]. The classic experiment is very rapid and simple. The amount of mercury injected into a sample increases as the pressure of mercury is increased step-wise. At each step, mercury is pushed against the capillary forces into progressively smaller pore cavities. This is known as pressure-controlled measurement of MICP.

Volume-controlled experiments seem to provide more information to characterise porous media than pressure-controlled experiments [417]. Another interesting mercury intrusion experiment consists of keeping the pressure constant and observing the fluctuation in pressure owing to Haines jumps [125, 133, 273]. When the volume is kept constant, the shape

of each mercury meniscus adjusts to accommodate the pore shape and pressure difference. The capillary pressure follows the Laplace equation, which is inversely proportional to the mean radius of curvature of the mercury meniscus. Fluctuations in the curvature cause fluctuations in the capillary pressure, and modelling these fluctuations provides a good description of the porous media structure [376]. Unfortunately, this experiment has received little attention in industry and it is not routinely performed as a counterpart to conventional pressure-controlled mercury porosimetry.

There is extensive literature on mercury intrusion simulators and retraction experiments [15, 66, 163, 183, 191, 253, 314, 323, 380, 382]. However, these simulators have been used to study the effect of network parameters without considering the uniqueness of the solution. Few of these studies have made forward prediction of data that are not used as matching data. Analytical calculations using parameterised pore-size distributions and power-law-type volume relationships along with fully accessible porous media readily show that the volume and pore-size distribution can compensate each other to produce similar capillary pressure behaviour [258].

Application of Indirect Methods to Real Rock Samples

Adding additional constraints may reduce the number of possible outcomes. Some investigators have assumed that the pore-size distribution follows a Weibull probabilistic distribution function (PDF) [33, 163]. This choice may be related to the fact that the Weibull distribution offers some flexibility despite it being a parametric PDF. These studies only looked at a few simulations (five simulations). The network model had similar parameters to the ones that are going to be introduced in Chapter (4). Although this approach is interesting, it does not account for the distribution of coordination numbers and the variation of the volume exponent (which will be introduced in Chapter 4). They focus on investigating the effect of the relationship between the formation factor and the selection of the pore-size distribution for a given wettability.

Microporosity plays an important role in the capillary pressure [416], although it is often ignored. There are various definitions of microporosity. Here, we define microporosity as the porosity associated with pores less than 10 μm in diameter. This is related to the maximum resolution to reliably determine pores in 3D μ-CT images. Scanning electron microscope (SEM) images can reach sub-micrometer resolution. Youssef et al. [416] determined the microporosity from high-resolution SEM images and incorporated it as an embedded analytical virtual network connected to the nodes of the macroporosity lattice network constructed based on the pore-size distribution from 3D μ-CT images.

Increasing the number of parameters increases the solution space, requiring robust methods to obtain reliable parameters. While MICP relates pressures and volumes, the accessibility function is a parallel concept in terms of the fraction of pores available for invasion at each mercury pressure level. Thus, the accessibility function and MICP are linked and convey information about the connectivity [163, 221, 252, 314, 381, 383]. Tsakiroglou et al. [378] proposed multistep iterative workflow for matching of the MICP and nitrogen sorption (Fig. 2.6 shows the workflow). They stressed that the critical point is the initial guesses, which are the bottle neck for the performance and the quality of the results. A parameterised analytical accessibility function incorporates a polygonal description of the pores in which the pore wall angularity is one of the parameters to optimise. The pore volume follows a power law (which will be introduced in Chapter 4). The optimisation step is deterministic (a commercial package for nonlinear parameter estimation is ATHENA [364]) and it is performed via the parameterised accessibility function. The parameters are the percolation threshold and the accessibility function slope after the percolation threshold.

Deterministic methods are not able to guarantee that the global minimum is found, which is why they are highly dependent on the initial guesses. In addition, they lack a mechanism to escape from local minima [21, 343]. Despite their shortcomings, deriving pore-size distributions from MICP and nitrogen adsorption has been widely applied to obtain initial guesses for analytical models based on parameterised accessibility functions.

Previous work on carbonates has been limited to assessing the quality of the proposed approach on the basis of matching the MICP [31, 164]. Dual-porosity structures are characterised by the primary (matrix) porosity and secondary porosity consisting of vugs or fractures. Lattice network models take into account the matrix by average values of its properties and a virtual network linking the macropore network. The volume exponent is assumed to be equal to zero (Chapter 4 will introduce this parameter). Therefore, the pore volume is constant regardless of the size. The vug lattice network is constructed by randomly placing vugs using the pore-size distribution obtained from the procedure described above. The vug network is attached throughout the virtual network, representing the matrix with homogeneous capillary pressure and conductance calculated from the mean radius [31].

There is often a tendency to classify as unimodal pore-size distribution to bell shape MICP based pore-size distribution. The variety of mercury intrusion derived pore-size distributions indicate that there is a diversity of possible shapes in which the predominance of microporosity or macroporosity or both along with the range of pore size and diagenetic processes will produce a typical character. However, the common pattern of bell shapes in-

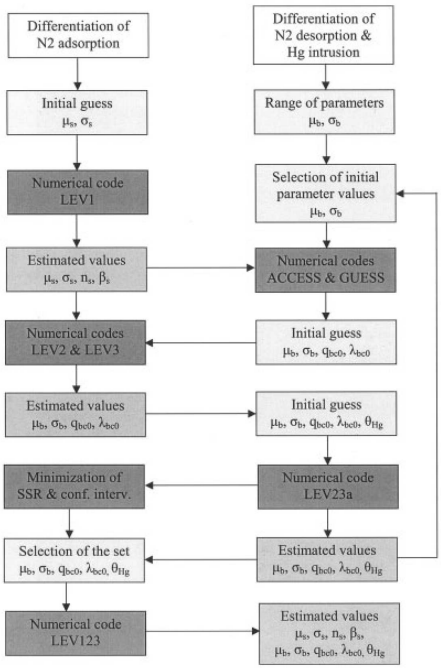

Fig. 2.6 Workflow for the multistep optimisation process to obtain network model parameters from MICP data and nitrogen sorption. Figure taken from [378].

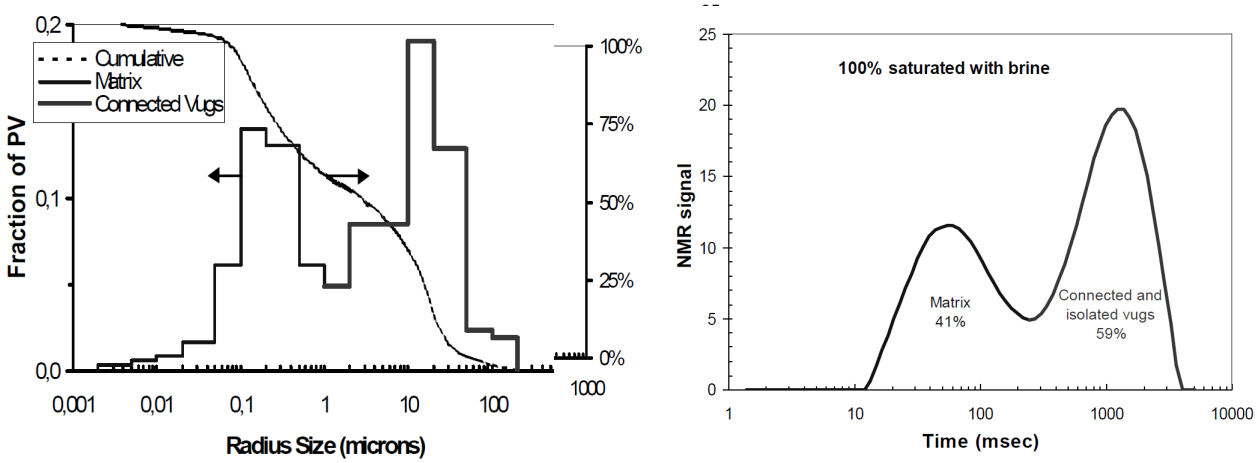

a b

Fig. 2.7 (a) Pore-size distribution derived by combining simultaneous measurements of the capillary pressure; (b) nuclear magnetic resonance (NMR). Figures taken from [31].

dicates shielding effect of small pores as mercury percolates in the media before reaching the percolation threshold (Section 4.2 expands on this subject). Therefore, whether the underlying pore-size distribution is uniform or unimodal, the MICP based pore-size distribution will always be unimodal between some bounds in the porous media. If the underlying distribution is bimodal and the modes are separated enough, the bimodal pattern in the MICP based pore-size distribution is preserved however one of the modes may be shifted due to the shielding effect. In Chapter 6 we will test our method for a wide uniform distribution.

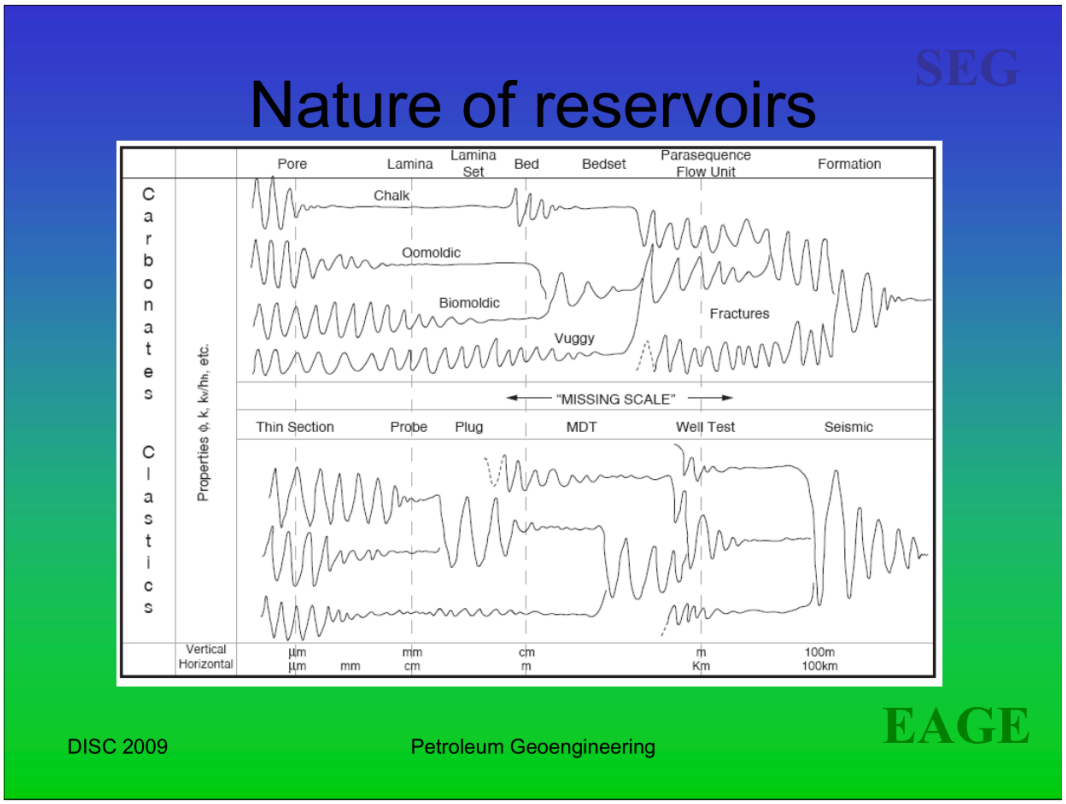

Fig. 2.8 Diagram showing the variability in petrophysical properties for carbonates and sandstones as function of the measurement scale [75].

Carbonates are mainly characterised by a strong diagenetic footprint introducing large variability in all length scales compared with sandstones (Fig 2.8). This variability challenges the deterministic characterisation of carbonates. The missing scale in carbonates (patterns of variability similar in all scales Fig. 2.8) compared with sandstones points towards a scale invariance which appears often in nature. Scale invariance indicates that the patterns or amplitude of variability repeat itself with similar features at all length scales. This makes appropriate the transformation of the estimator in the pore-size distribution and shape factors distribution, one of which will be introduce in Section 4.2.1. On the contrary,

in sandstones there seems to be different patterns of variabilities for different scales (Fig 2.8).

The major advantage of NMR and also μ-CT (Section 2.3.2 discusses this method) is that both are nondestructive techniques. Moreover, different fluids and particles can be added to the fluids to study some interactions with the porous media and monitor the changes in the porous media.

NMR interpretation of pore-size distribution could turn out to be very difficult. While mercury intrusion capillary pressure depends strongly on throat size, the distribution of the relaxation time of the fluid in the porous media so-called T_2 distribution depends on volume to surface ratio and surface roughness. T_2 distribution is often scaled to match the MICP based pore-size distribution estimator (Section 4.1 will introduce these estimators).

Carbonates are very complicated pore structures originated from living organisms and very often with a strong diagenetic footprint that can strongly influence the T_2 distribution due to phenomena called pore coupling [118]. The important thing about these combined phenomena is that information from MICP, petrography and expertise on the subject is required to identify and possibly correct the T_2 distribution.

The advantage could be to use NMR as additional information to capillary pressure. Simultaneously measuring the NMR response and capillary pressure data at different saturations makes it possible to relate both measurements (Fig. 2.7) [269]. The pore-size parametric distribution is taken as the fitting parameter to match the MICP.

There has been little discussion about the treatment of wettability (Fig. 2.10) Note the large jumps in the capillary pressure (Fig. 2.10) and relative permeabilities (Fig. 2.10). There is a tendency to assume that macropores are more oil-wet (larger advancing contact angles) than micropores. Both micropores and macropores control the shape of the capillary pressure (Fig. 2.9a , 2.10) and relative permeabilities (Fig. 2.11) curves. The oil-wet character and the dual-porosity structure (early water breakthrough through the interconnected vuggy structure) causes the intersection of relative permeabilities at rather low water saturation (Fig. 2.11) (less than 17%).

Tsakiroglou et al. [379] reported one of the first studies to draw attention to the multi-scale problem and combined two techniques used in petrology to qualitatively analyse the microstructure of rocks. The combination of backscattering SEM (BSEM) and small-angle neutron scattering (SANS) images was used to combine the large scale (BSEM) and the small scale SANS [319, 379]. However, the method involves making a number of assumptions. They adopted a spherical pore shape. The small pores adopt a fractal model (power law) with exponent equal to the slope of the MICP versus mercury saturation in the high

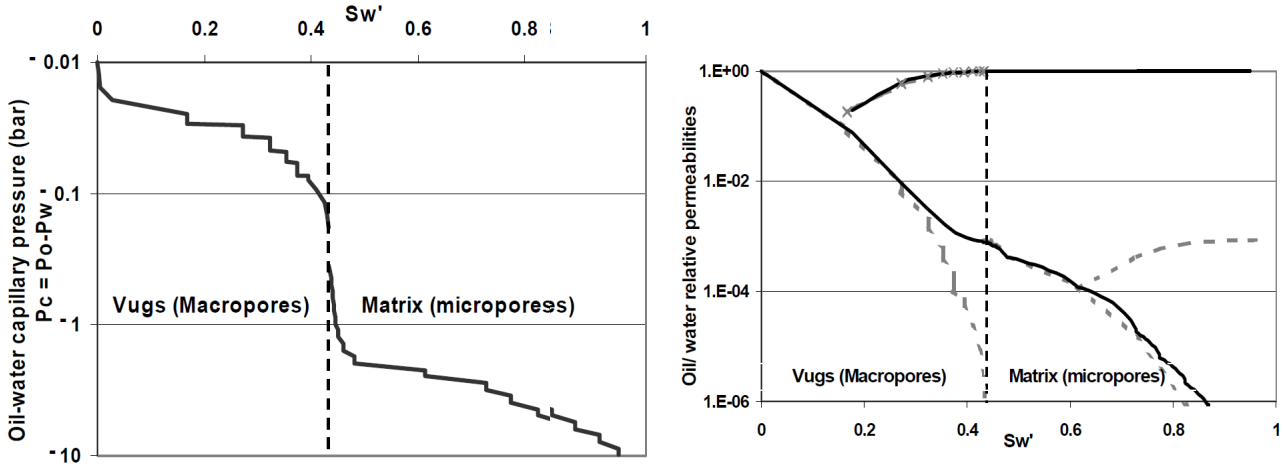

a b

Fig. 2.9 (a) Imbibition capillary pressure in negative logarithmic vertical coordinates and (b) imbibition relative permeabilities for the matrix and vugs networks of a carbonate rock. Only one contact angle is assumed for both micropores and macropores, inducing a large jump in the capillary pressure. Figures taken from [31].

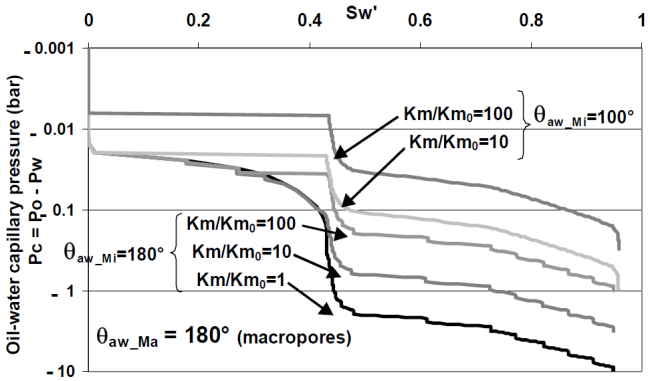

Fig. 2.10 Oil/water capillary pressure of a dual-network for different contrast of permeability and different wettability of the matrix. Modelling assumes that there is a superposition of effects. The microspores act as a separate system. Macropores are more oil-wet than micropores. Figures taken from [31].

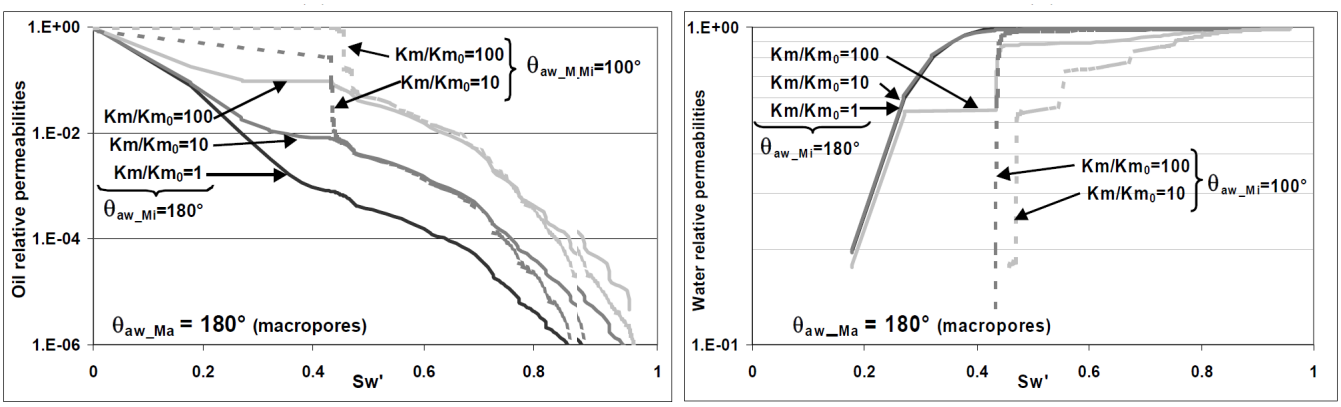

a b

Fig. 2.11 (a) Oil relative permeability and (b) water relative permeability of a dual-network for different contrast of permeability and different wettability of the matrix. Figures taken from [31].

pressure range. The pore-size distribution follows a linear combination of two log-normal functional forms, one that characterises the fractal behaviour and one for the BSEM scale behaviour. A second set of a linear combination of log-normal distributions was used to model the macropores. The parameters that characterise these distributions, along with the mathematical expression for the accessibility function, were tuned to match the MICP. They used mathematical models of the accessibility function to simulate the MICP and the commercial package ATHENA [364] for nonlinear parameter estimation [378]. They found a significant overlap of the pore- and throat-size distributions (Fig. 2.12) and there seemed to be a gap between the micropore and macropore distributions, which may be a consequence of the initial assumption that the macropores are filled first and small pores are only accessible through macropores.

The Euler number describes the spatial connectivity in image analysis. Vogel et al. [400] proposed a size-dependent Euler number. This function relates the 3D Euler number to the smallest pore radius derived from a 3D μ-CT image. The Euler number as a function of the smallest pore radius describes the connectivity of the pore space on a size basis. The process starts with the largest pores and locates them in the lattice network such that the Euler number in the network agrees with the Euler number calculated in the 3D μ-CT 3D image, and then continues following decreasing pore sizes. This method has been recently implemented in the generation of a multiscale stochastic pore-network model [180]. The contribution of the different scales is a tuning parameter.

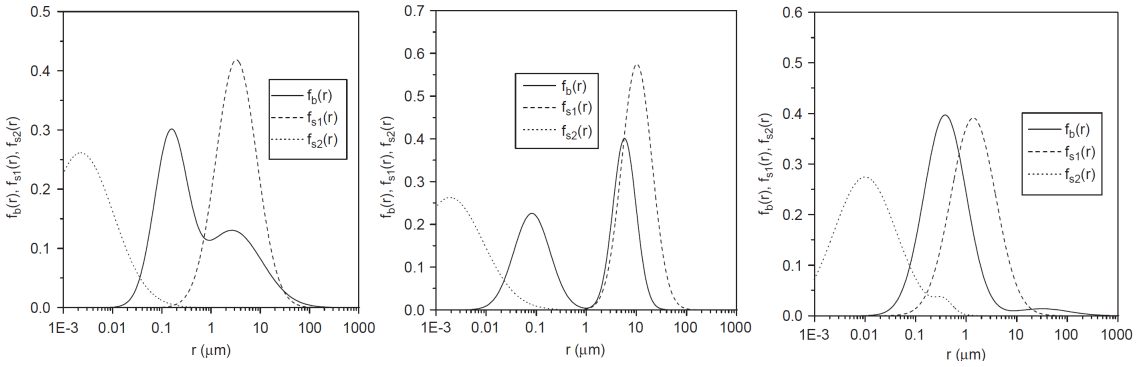

Fig. 2.12 Pore- and throat-size distributions obtained by the procedure proposed by Tsakiroglou et al. [379]. There is considerable overlap between the pore and throat size distributions. Figure taken from [379].

2.3.2 Direct Methods

Computed Tomography

The success of CT in medical tomography, has led to a higher resolution technique known as X-ray μ-CT for small pieces of materials [99]. μ-CT produces cross-sectional slices of the porous media that are combined using mathematical algorithms to generate a 3D image of the porous media [72]. The maximum resolution of the 3D images is about 1 μm. The maximum sizes of porous media data sets are around 2000^3 voxels [199].

In addition to being a nondestructive technique, a major advantage of μ-CT is that it provides 3D visualization and characterization of the rock. It also allows time lapses to see the changes in the porous media as given treatment takes place and allows correlation of the changes with the rock textures [123]. However, the main disadvantage lies in the REV versus resolution problem. The REV of carbonates is usually larger than sandstones, because of heterogeneities at all length scales. In addition there is a large fraction of microporosity, which requires submicron resolution. For the sake of argument, one can consider capturing small features with a single voxel, thus the voxel resolution should be around 0.05 microns. On the other hand if the large pores have a diameter of between 100-400 microns, the data set should be larger than 8000^3 voxels. It is challenging in all the different steps along the workflow to acquire, process and manipulate a 3D image of this size.

The porosity, permeability, formation factor, NMR, and drainage capillary pressure in strongly water-wet conditions can be directly calculated on the 3D image domain [141]. Moreover, the 3D image is a realistic computational domain for solving Navier–Stokes equations [2, 36] and for Lattice-Boltzmann simulations [110, 339]. The method is non-invasive, so the sample can be used for further tests [341]. μ-CT allows visualisation of the

saturation changes as displacement occurs [73].

Pharmaceutics has also looked at the multiscale problem because the body accesses drugs in tablets through percolation. μ-CT suggests that the majority of porosity is located in large pores. In contrast, the pore-size distribution derived from the MICP (using the variation of the usual formula proposed by Ritter and Drake, Chapter 4 will explain variations of the Ritter and Drake method) method seems to indicate that the majority of porosity is located in small pores (Fig. 2.13). The majority of porosity in the pore-size distribution derived from MICP is below μ-CT resolution. This appears to suggest that mercury has to penetrate into pores smaller than 7μm to reach an internal cluster of large pores [104]. A major drawback of these comparative calculations is that there is always a bias in the Ritter and Drake method because of the many orders of magnitude variation in the pore sizes (this issue will be discussed in Chapter 4).

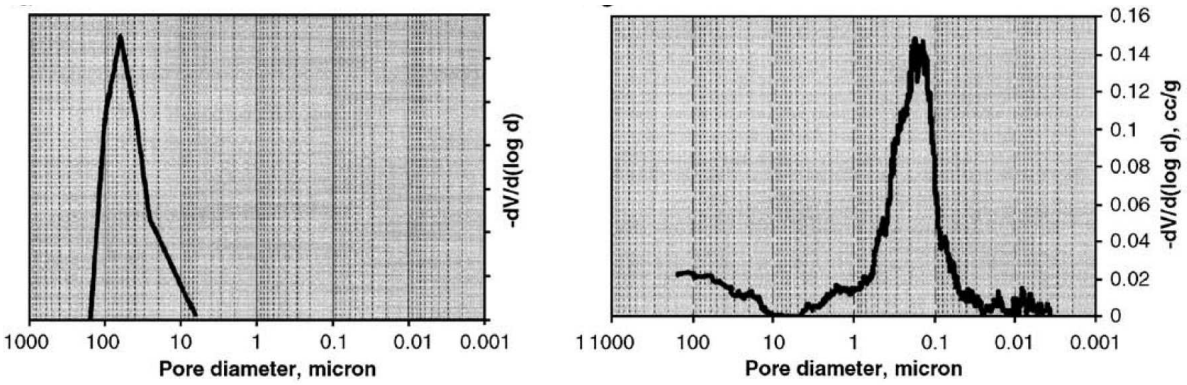

a b

Fig. 2.13 (a) Pore-size distribution showing equivalent volume logarithmic differentiation (variation of the usual Ritter and Drake method) using the μ-CT signal. (b) Actual volume logarithmic differentiation using the MICP data for the same sample. The MICP has a peak at around 0.2μm, which is below the resolution of μ-CT. The pore-size distribution from μ-CT shows only the large pores. Figure taken from [104].

Numerical Reconstruction

Statistical parameters derived from thin-sections and photomicrographs combined with mathematical algorithms can produce 3D images of porous media, such as the ones measured with μ-CT. The geological processes that produce sandstones are easier to describe than those that produce carbonates rocks. Bryant et al. [55], and Bakke and Øren [19] developed algorithms to simulate sedimentological and diagenetic processes, namely, process-based

modelling (PBM), that generate 3D images of the pore space without the need for μ-CT. Microporosity in carbonate rocks is the result of many complex geological processes. Carbonate rocks are different in genesis to clastics. Carbonate rocks are the final product of many different processes that can involve living organisms. Moreover, there are lots of diagenetic processes that change the original porosity in carbonates. These two phenomena are responsible for the microporosity in carbonate rocks that μ-CT cannot resolve. This has motivated efforts to develop algorithms that derive statistics from the microstructure imaged by high-resolution SEM beams [20, 205, 227, 229, 293, 331, 407].

One of the main issues in the application of numerical reconstruction to carbonate rocks is the reconstruction of a 3D image with a REV capable of integrating the various orders of magnitude to include macroporosity and microporosity. In the field of geostatistics, multipoint statistics are used to describe spatial features. Okabe [293] applied multipoint statistics to reconstruct 3D images of carbonate rocks, the multipoint statistic model is derived from a subset (512×512 pixels) of a BSEM image. The template (9×9 pixels) propagates the statistics to generate the 3D image. The size of the final image is a cube of 128^3 voxels. This represents total dimensions of 45 μm in each direction. However, the work does not report any pore-size distributions. This readily shows that the volume reconstructed is small. The merit of the method was assessed by comparing the simulated and measured absolute permeabilities.

SEM images of carbonate rocks readily show the presence of paleo-organisms that create the porous space. Object-based reconstruction is able to reconstruct these features with great detail [42–44, 210]. However, it focuses on comparing two-point correlation functions of the reconstructed images with those calculated from μ-CT or SEM images, and pore-size distributions and capillary pressure are not reported.

Network Extraction

In general, the methods described in the previous section show good agreement with bulk properties such as porosity (some methods use porosity as an initial parameter). However, pore-size distributions are rarely reported. Performing two- and three-phase calculations of 3D images is computationally demanding (for a recent review of the methods applied to 3D images see Meakin and Tartakovsky [263]). This computational complexity has motivated the use of simplified networks models extracted from the void space in 3D images.

Before obtaining a network model from the void space of a 3D image (μ-CT or mathematical reconstruction), the raw images need to go through a set of image processing routines that clean the images and make them suitable for further calculations. μ-CT and

process-based reconstruction require the grey scale to be divided into a binary domain composed of solids and voids. This is not a trivial step, ad hoc assumptions have to be made, and often much information is lost [341]. Some techniques apply histogram equalisation to increase the grey scale distance or contrast between the phases. Interpolation with indicator kriging and two threshold values in the grey scale distinguishes between voids and solids more clearly [291]. When the 3D image is in a binary domain, there are then morphological operations that smooth the image to make it ready for network extraction from the void space.

Even in homogeneous rock such as Berea sandstone, μ-CT and numerical reconstruction show discrepancies (Fig. 2.14). Network extraction techniques produce a single voxel skeleton from the porous media. The discrepancies between extraction methods are greater for carbonate rocks (Fig. 2.15) than for sandstones (Fig. 2.14) [91].

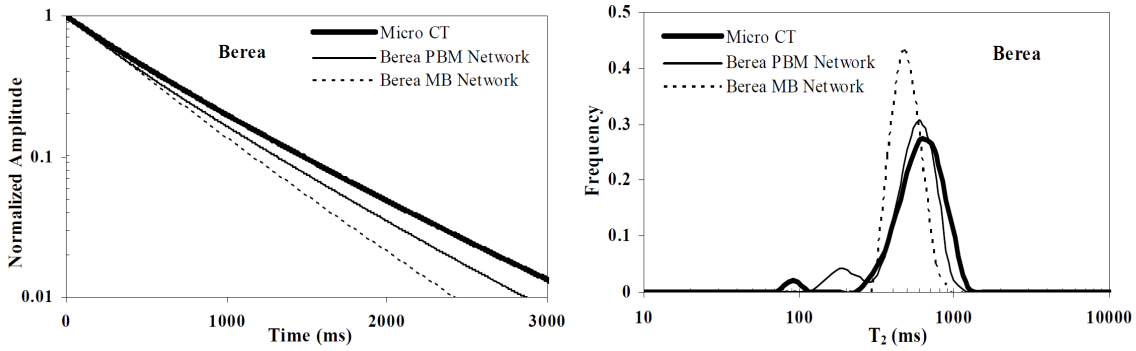

Fig. 2.14 For a simple porous media such Berea, μ-CT and the network model differ when used to calculate the NMR response. The abbreviations are as follows: Process-based reconstruction method (PBM) and maximal ball (MB).Figure taken from [369].

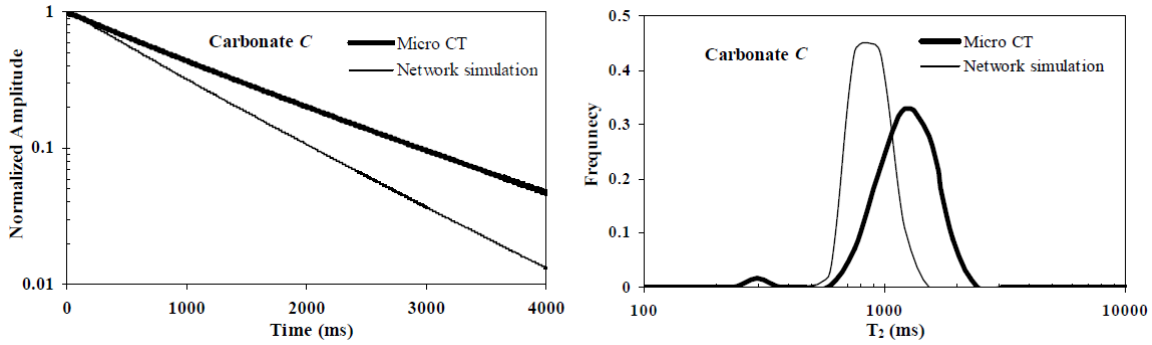

Fig. 2.15 In carbonates, the differences between μ-CT and the network model are greater than those of sandstones. Figure taken from [369].

The samples tested were sandstones and carbonate rocks with narrow pore- and throat-size distributions (Figs. 2.16 and 2.17).

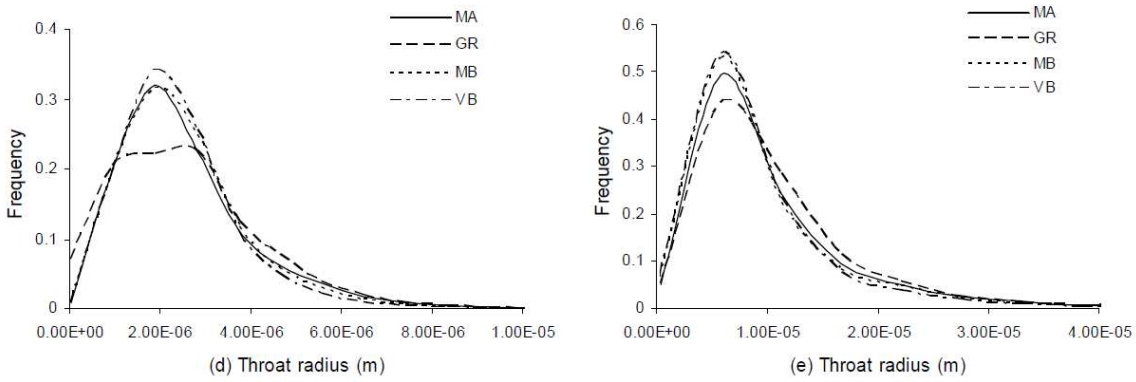

Fig. 2.16 Throat-size distributions for various network extraction methods (medial axis (MA), maximal ball (MB), grain-recognition-based algorithms (GR) and velocity-field-based algorithm (VF)) . Nearly all of the sizes are concentrated within less than one order of magnitude. Figure taken from [91].

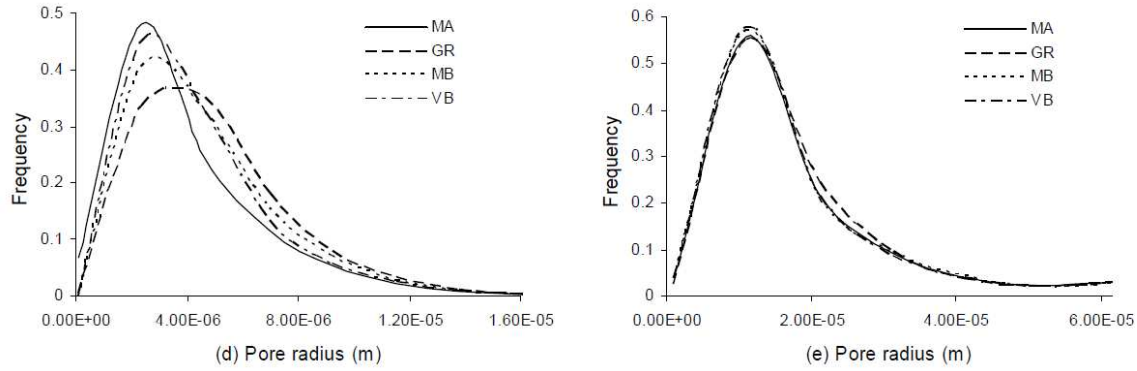

Fig. 2.17 Associated pore-size distribution (medial axis (MA), maximal ball (MB),grain-recognition-based algorithms (GR) and velocity-field-based algorithm (VF)). The pore-size distribution is very similar to the throat-size distribution shown in Fig. 2.17. Figure taken from [91].

In high-porosity carbonate rocks, the greatest discrepancy in the network extraction methods is in describing low coordination values (Fig. 2.18).

Absolute permeability is the property used to assess the quality of reconstructions. Further studies of carbonates using multipoint statistics [293] highlighted that the REV does not capture the complete range of pores sizes [7]. Usually, there is no indication of how the image is divided into black and white. The image is small (54.1 μm) in the order of the size

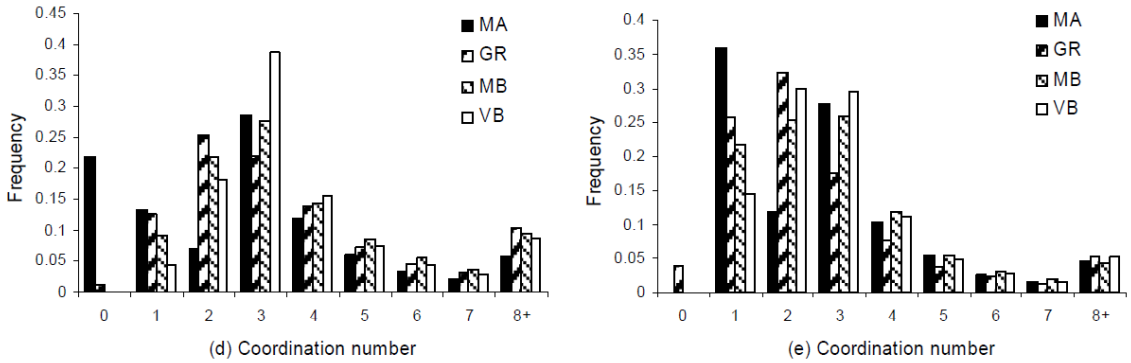

Fig. 2.18 Distribution of coordination numbers calculated from the extracted networks showing that coordination numbers above 6 account only for less than 15% of all connections. Medial axis (MA), maximal ball (MB), grain¬recognition-based algorithm (GR), and velocity-field-based algorithm (VF). Figure taken from [91].

of one single macropore. There is a difference in magnitude of seven between the largest and the smallest pore (Fig. 2.19). The coordination number distribution is usually skewed to the right (Fig. 2.20) with few large values that are usually associated with artefacts [7].

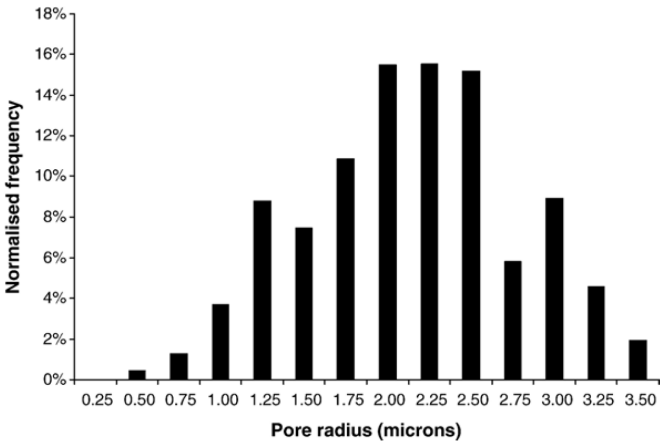

Fig. 2.19 Pore-size distribution obtained from reconstruction followed by network extraction. More than 80% of the capillary elements have sizes in a narrow range (1.25–3 μm). Figure taken from [7].

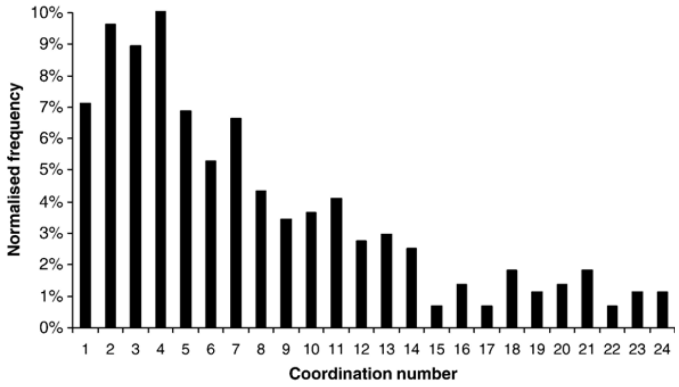

Fig. 2.20 Coordination number distribution for the reconstruction of porous media followed by network extraction shown in Fig. 2.19. 50% of the values are above 6. However, the distribution is skewed to the right and concentrated between 3 and 5 [7]. Figure taken from [7].

2.3.3 Comparative Studies

Methods for characterising and simulating flow in porous media have tended to focus on how to translate measurements into model parameters. They have not investigated whether adding additional parameters to the characterisation of flow affects the results. Scaling theory states that the behaviour of certain properties is independent of how the systems are characterised. For example, at a phase transition (percolation process), physical quantities diverge (infinitive) and it is not possible to simulate a large enough system to characterise the quantity with a given characteristic length of the system.

The product of the critical probability (or percolation threshold) times the coordination number shows dimensional invariance. It depends only on the dimensionality and is independent of the type of structure being considered [89, 419]. Even for high values of the coordination number (e.g., 42) the relation still holds [351]. Furthermore, this not only holds for lattices, but also for amorphous structures that are not regular lattices [345].

In the literature, there are examples in which simplified 3D networks have given good predictions for steady state relative permeabilities (Section 2.5.5 will explain the difference between steady and unsteady state relative permeabilities) in sandstones (Talash and Berea sandstones) [115, 144]. However, 2D networks will give incorrect results for real porous media irrespective of the complexity added into them [115].

The influence of the average coordination number on the percolation process seems to be entirely captured by the average value for the porous medium [176, 178, 179]. Both lattice and Voronoi random networks give nearly identical relative permeabilities. The Voronoi

network has a distribution of coordination numbers varying from 3 to 12 [178]. Similar observations have been made in studies of networks with different geometric structures, for example, hexagonal and ditetragonal [66, 178].

Two networks with different complexity can give predictions with similar accuracy. For a similar lattice network to the one used in the present thesis [367], fitting the lattice network to two-phase data capillary pressure and relative permeabilities gave reasonable quantitative predictions of three-phase relative permeabilities with the same accuracy as predictions made using more complex network models [311]. There are other studies in which capillary pressure and relative permeabilities were first both matched to predict other data that was either more difficult to obtain [256, 396] or because the mechanical conditions of the rock meant that some laboratory measurements were unreliable (carbonates and friable rocks) [411].

Three pore-scale methods with large differences in complexity gave similar results, although the work was applied to a rather homogeneous and small volume sample [400]. It is worth comparing calculations using the lattice-Boltzmann model, a full-morphology model (defining the mean curvature in the 3D image and calculating the capillary pressure at each step, see references in [400]), and a pore-network model for determining the capillary pressure. The predictions using these three methods are very similar (Fig. 2.21).

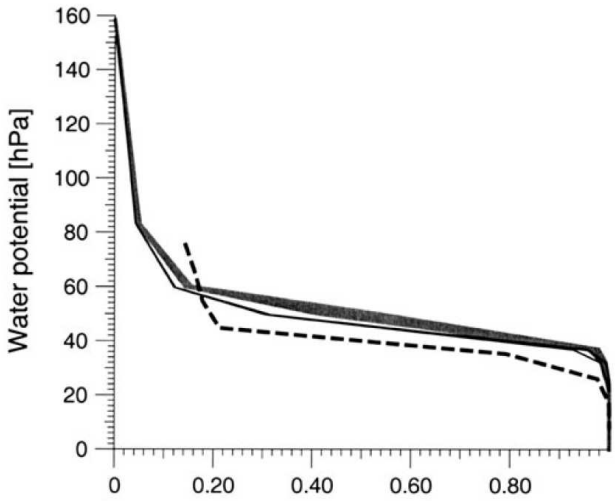

Fig. 2.21 Predictions using three pore-scale techniques of very different complexity to simulate drainage capillary pressure: lattice-Boltzmann (thick dashed line), full-morphology model (solid line), and pore-network model (20 realisations shown as grey lines). Figure taken from [400].

2.4 Pore-Network Model Structure Parameter Estimation Methods

Alternatively, a probabilistic formulation can be used to solve the issue of uniqueness in the parameter estimation problem. The probabilistic model (explained in detail in Section 4.3) gives a general statistical equation for the parameter estimation problem, which is typically referred to as the posterior distribution of the model parameters. The general statistical equation can be deterministically solved if it is assumed that there is a Gaussian distribution that describes the problem and there is a linear relationship between the parameters and the system dynamic response [371]. The solution is a multivariate gaussian posterior distribution of model parameters subject to some observations.Methods to determine the model parameters that correspond to the maximum in the multivariate gaussian posterior distribution include maximum likelihood point estimation and the steepest descent method (see [116, 117, 343, 372] for reviews of the methods).

The Kalman filter (KF) is a parameter estimation method that works as a noise filter for the multivariate gaussian posterior distribution. This method can automatically control dynamical systems for problems in which new observables become available over time, for example, weather, hydrology, and oil field development applications. The ensemble KF (EnKF) is an improvement of the KF that attempts to treat the nonlinearities of these types of problems [102, 103]. The algorithm updates each of the multiple models in a linear fashion using the KF algorithm. The EnKF assumes that the prior distribution of the model parameters and the distribution that relates the model parameters to the observed data (likelihood) are Gaussian (strong assumption). However, these assumptions break down in most cases [349]. Violation of the Gaussian assumption leads to various inconsistencies between the vector ($\boldsymbol{X}$) of observed data and the updated model parameters ($\boldsymbol{\theta}$) [4, 418]. A number of methods have been proposed to improve the EnKF in nonlinear conditions [34, 35, 153, 211, 232, 365].

The EnKF has been applied to pore-network model parameter estimation [151]. However, the pore-size distributions were narrow, and the variation was limited to one order of magnitude. Additionally, the shape of the pore-size distribution was restricted. In pore-network model simulations, all of the data are available simultaneously. Therefore, we cannot reduce the computation time using the EnKF. Thus, any update in the model parameters requires that the entire model be restarted from scratch to update the multivariate gaussian posterior distribution.

The above methods have problems when attempting to solve a model-parameter-solution

space for nonlinear problems that have multiple local minima. Arguments in favour of these methods state that if the nonlinearities are not too severe then the methods can still be applied under the assumption that the problem is approximately linear in the vicinity of the solution. However, the vicinity of the solution is typically unknown. Therefore, these methods are not considered to be robust because they may not be able to solve difficult problems [282].

Most optimisation methods for parameter estimation are based on a misfit function that compares the observed (MICP data) and simulated values. This means that the methods are dependent on good initial guesses. Moreover, local minima can result in ineffective exploration of the solution space.

The Bayesian approach has been used extensively for inverse problems in subsurface studies such as reservoir history matching and seismic inversion [17, 22, 26, 27, 38, 39, 63, 69, 78, 101, 131, 222, 223, 228, 270, 344, 366, 409]. Solving these problems involve a great deal of uncertainties and integration of information. The forward problem used in the inversion problem already has lots of assumptions about finer scale models used to interpret raw data making it a very intricate and very complex problem to be solved.

It is beyond the scope of this work to discuss in detail the different methods that use Bayesian approach. However, the information entropy method as considered by Jaynes [173] emphases making weak assumptions with respect to the data. In that sense, little research to date has focused on formulating the inverse problems from well logs that lead to well correlations. It is frequently seen in integrated subsurface projects that two geologists using the same raw well log data arrive at very different well log correlations leading to completely different maps of properties regardless of the sophistication of the algorithm used for mapping.

2.5 Wettability Evaluation

As well as water-flooding relative permeabilities, wettability alteration is related to the surfactant concentration and the initial contact angle [187]. Indeed, the change in the contact angle during surfactant injection has a strong influence on the recovery factor [147]. To identify the mechanism, it is important to design effective EOR surfactant formulations. The surfactant formulation required to reduce the recovery factor to the optimum value for maximising oil recovery will differ depending on the initial contact angle [67].

Reservoir wettability is one of the most important pieces of information for the efficient design of any oil recovery process [190]. Many methods have been proposed to measure wettability on a qualitative or quantitative basis (see [11, 76] and the references therein).

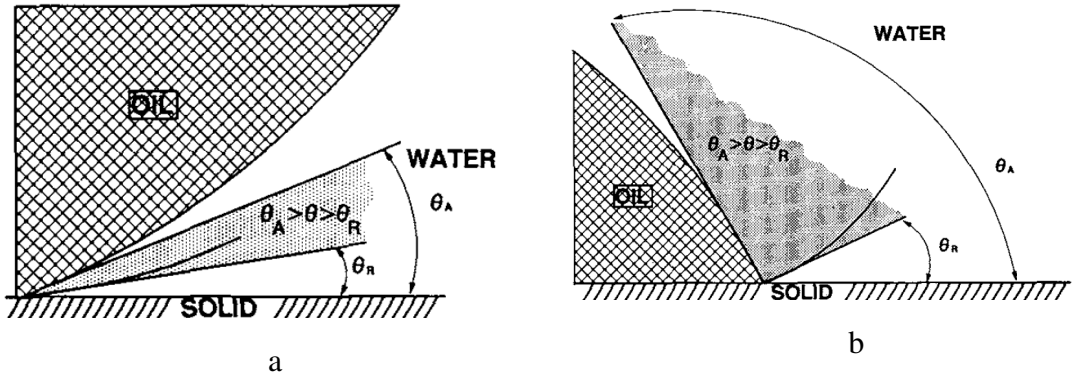

Fig. 2.22 Contact angle hysteresis is the variation of the contact angle between water-advancing and water-receding contact angles. (a) Small hysteresis. (b) Large hysteresis. Figure taken from [276].

Wettability is defined by the contact angle between the liquid and the solid when a drop of liquid is placed in contact with a solid surface immersed in a second immiscible liquid (Fig. 2.22). The contact angle is the most quantitative indication of wettability. For pure liquids on smooth surfaces, there is a unique equilibrium value of the contact angle (intrinsic contact angle) bounded by relatively reproducible maximum and minimum values.

The maximum angle is obtained by pushing a liquid over the surface, while the minimum angle is obtained by pulling the liquid back from its equilibrium state. These two angles are referred to as the advancing and receding contact angle, respectively. Contact angle hysteresis is almost always observed for crude-oil/brine/rock systems, and can be greater than 60° [182].

Receding contact angles are generally low ($< 30°$) and seldom exceed 60°, whereas advancing contact angles show a wide range of variation (Fig. 2.22). The conditions prevailing in reservoirs are very difficult to reproduce in the laboratory. Therefore, it is difficult to determine the contact angle under reservoir conditions with the same complexity, heterogeneity, roughness of the rock surface, and chemical composition found in the reservoir. Generally, when the angle is small, the surface is water-wet; when the angle is about 90°, the surface is neutral-wet; and when the angle is large, the surface is oil-wet.

The majority of reservoirs are not water-wet under water-advancing conditions (imbibition) (Fig. 2.23), which is relevant for water-flooding purposes. Treiber et al. [377] used an extensive data set to measure contact angles of crude-oil and simulated reservoir brine at reservoir temperature and ambient pressure with polished quartz and calcite, which dominate the mineral composition of reservoir rocks. There are obvious limitations representing

the rock surface by a single mineral. However, this is an important finding, especially for carbonate rocks because calcite is present in high quantities.

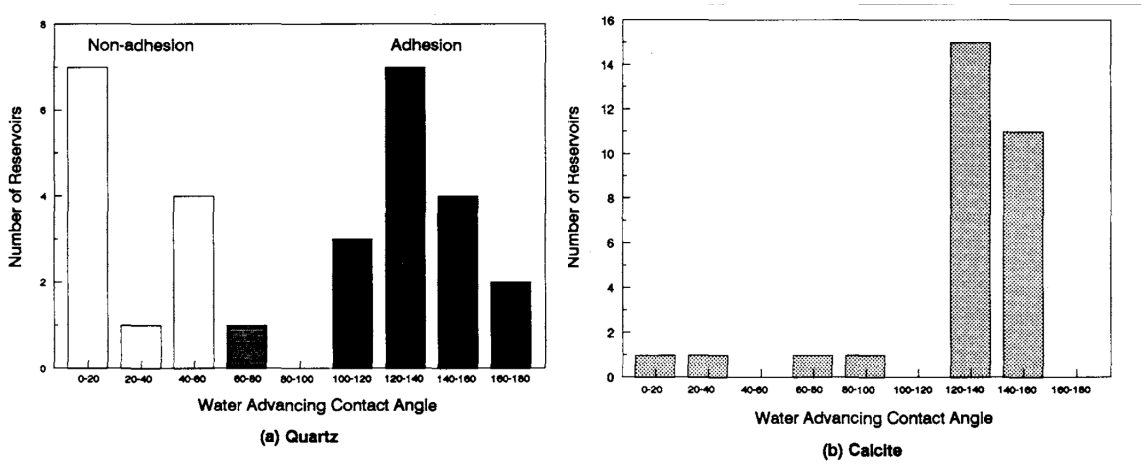

a b

Fig. 2.23 Advancing contact angles for (a) crude-oil/brine/quartz and (b) crude-oil/brine/calcite systems. The figure shows that strongly water-wet and water-wet systems are very rare especially for systems with a calcite substrate. The majority of systems are neutral and oil-wet. Figure taken from [276].

2.5.1 Wettability Indices

Wettability indices characterise wettability. These indices use the imbibition and secondary drainage capillary pressure cycle. The oil industry widely uses two indices: the Amott index ([10]) and USBM wettability indices determined using the method proposed by Donaldson et al. [90].

The Amott index (I_{AH}) is the subtraction of so-called oil and water indices (Fig 2.24) and it is calculated with the formulae here below. In the Amott test, water is first displaced by oil by centrifuging. The aim is to reach the initial water saturation (S_{wi} in the reservoir before oil migration (S_{wi} is difficult to estimate [277]). The crude oil is then left for a period of 2 to 4 weeks at reservoir temperature to mimic the change of the initial wettability through ageing during geological time.

The core at S_{wi} is then immersed in water to allow spontaneous imbibition. Spontaneous imbibition of water ceases at some change in water saturation (ΔS_{ws}). Then, water is forced until a given minimum capillary pressure producing a change in water saturation of ΔS_{wt}. The wettability index to water (I_w) is given by $I_w = \Delta S_w / \Delta S_{wt}$. Similarly, the wettability

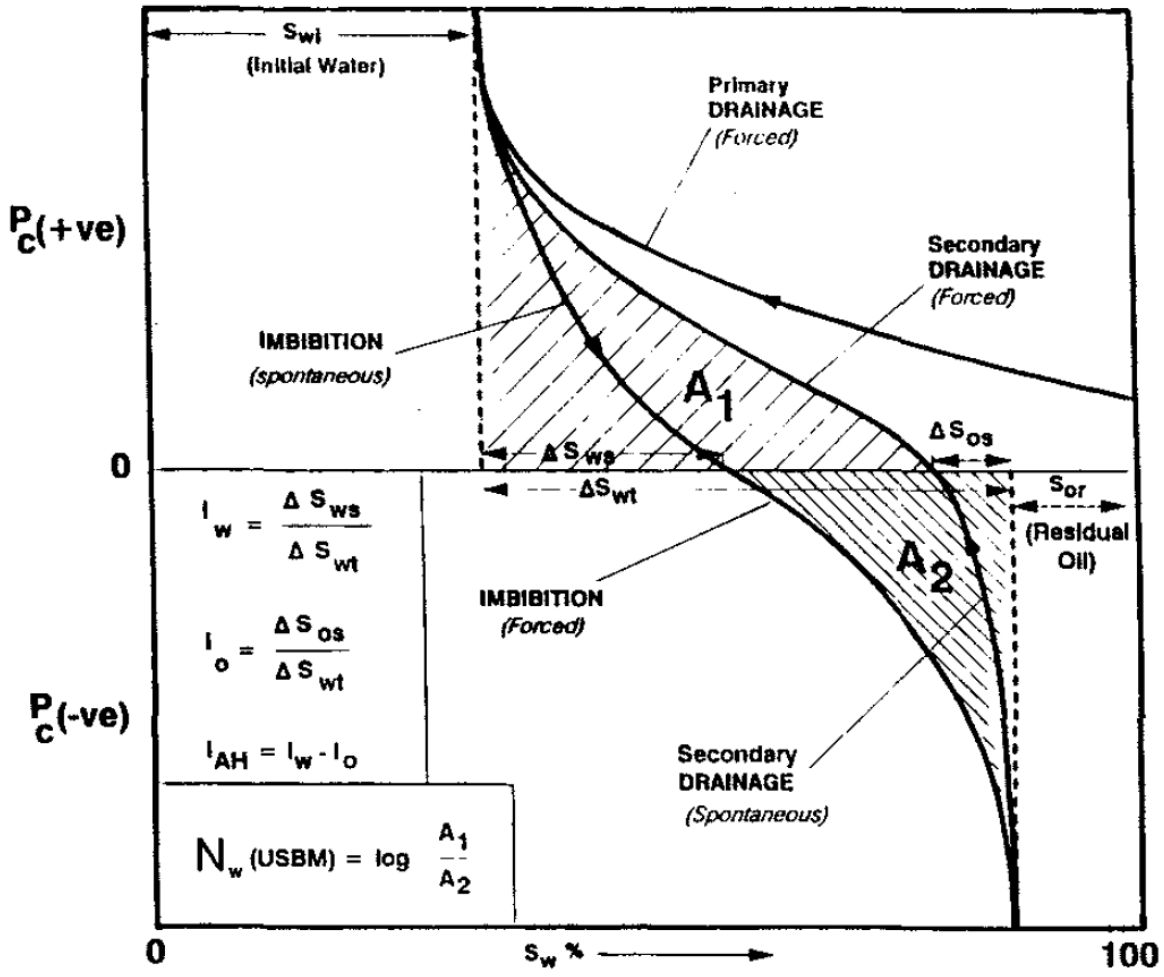

Fig. 2.24 Graphical explanation of how to calculate wettability indices. Figure taken from [352].

index to oil is $I_o = \Delta S_o / \Delta S_{wt}$. The difference $I_w - I_o$ is used to characterise the wettability by a single number (known as the Amott index, I_{AH}). The exact conditions when the capillary pressure is zero are difficult to assess, especially in mixed-wet systems [404]. The index varies from -1 (strongly oil-wet) to 1 (strongly water-wet).

The USBM index takes into account the area under the capillary pressure curve as a measure of the change in energy because of wettability alteration. The wettability number is defined as $N_w = \log(A_1/A_2)$, where A_1 is the area under the secondary water-drainage curve (drainage from residual oil) and A_2 is the area under the imbibition curve falling below the zero capillary pressure axis. The areas are shown in Fig. 2.24.

2.5.2 Wettability and Roughness

Research on contact angle hysteresis has demonstrated that there are various types of contact angles depending on whether the water is advancing or receding and the relative surface energies of the phases [279]. The intrinsic contact angle (ϑ_{ow}^{T}) is the angle measured on smooth low energy surfaces under static conditions. The advancing and receding operative contact angles (φ_{ow}^{adv} and φ_{ow}^{rec}) are calculated from capillary pressure measurements at the core scale and depend on the displacement direction. The advancing and receding apparent contact angles (ϑ_{ow}^{adv} and ϑ_{ow}^{rec}) are the angles measured on rough surfaces at the pore scale.

The apparent contact angle seems to be dominated by the effect of roughness. Morrow [274] examined the effect of roughness on the hysteresis behaviour of the contact angle using polytetrafluoroethylene (PTFE) tubes and a wide range of fluid systems to cover the complete range of possible intrinsic contact angles. PTFE was used because it allows reproducible results to be obtained and thus the effect of surface roughness can be investigated. Real rock surface are high energy surface that introduce variability in the results and might complicate the analysis. It was found that for a given intrinsic contact angles below 45°, the apparent advancing contact angle was lower than the intrinsic contact angle. Conversely, for a given intrinsic contact angle above 45°, the apparent contact angle was greater than the intrinsic contact angle [274]. These observations are in agreement with [120].

Moreover, a study of synthetic cores has suggested that the contact angle hysteresis is the same as that of roughened cylindrical tubes [279]. This suggestion contradicts calculations of the entry pressure for different pore shapes [65, 264, 309, 317, 415]. Morrow [275] observed remarkably close agreement between operative contact angles at the core scale (φ_{ow}^{adv} and φ_{ow}^{rec}) and apparent contact angles on rough surfaces (ϑ_{ow}^{adv} and ϑ_{ow}^{rec}). It is unclear whether roughness or pore shape is dominant determining the intrapore contact

angle. Chapter 3 will present similar observations made for the carbonate samples in this study. However, average apparent contact angles may be associated to significantly different distribution at the intrapore level.

The impact of pore shapes on wettability has three aspect linked together, pore shape geometry, pore wall curvature, pore size, contact angle and wetting-films. There is complex interplay between that makes our approach especially suitable to address the interaction between these pore-network model parameters. This interplay leads to a multiplicity of configuration. We will show later that grain shapes may be responsible for microporosity wettability.

2.5.3 Heterogeneous Wettability: Experimental Observations

There are counterintuitive behaviours in wettability, such as a core initially saturated with water will imbibe oil, whereas the same core initially saturated with oil will imbibe water. This is not expected in porous media in which the wettability is the same throughout its surfaces [13, 56, 138, 177]. When water-flooding for long periods of time, some native preserved cores spontaneously imbibe water and reach very low residual oil saturation, while the same core rendered strongly water-wet shows much higher residual oil saturation [325].

The concept of heterogeneous wettability seeks to explain such counterintuitive behaviour. The experimental work of various investigators seems to indicate that components of crude oil interact differently with the different minerals present in reservoir rocks [129, 177, 184, 332]. This produces another type of wettability in which different parts of the rock surface have different affinities for water and oil, suggesting that intrapore variation of wettability can also occur [54]. There are two possible underlying distributions of surface wettability: fractional wettability when the wettability is uncorrelated with pore size and mixed wettability when there is a correlation between wettability and pore size.

In initially strongly water-wet reservoir rocks, oil first invades large pores during oil migration. This scenario makes it likely that large pores will change their wettability towards oil, while small pores that remain water-filled will persist as water-wet pores [338]. This scenario is known as mixed wettability and explains the spontaneous displacement of both oil and water [60]. There are other studies that confirm the higher recovery in weakly water-wet media compared with strongly water-wet media, but they do not confirm the spontaneous imbibition of both fluids [278, 305, 322, 401].

For an increasing fraction of oil-wet grains, the capillary pressure in fractionally wet sand packs are parallel and the S_{wc} values are almost the same (Fig. 2.25) [107]. The connate

water saturation seems to be independent of the fraction of oil-wet pores. When the oil-wet pores are correlated with the grain sizes, the capillary pressure curves are no longer parallel and crossover the water-wet capillary pressure curve (Fig. 2.25b) [370]. Similar behaviour has been observed for water-wet cleaned versus native state plugs [225, 335, 347, 406].

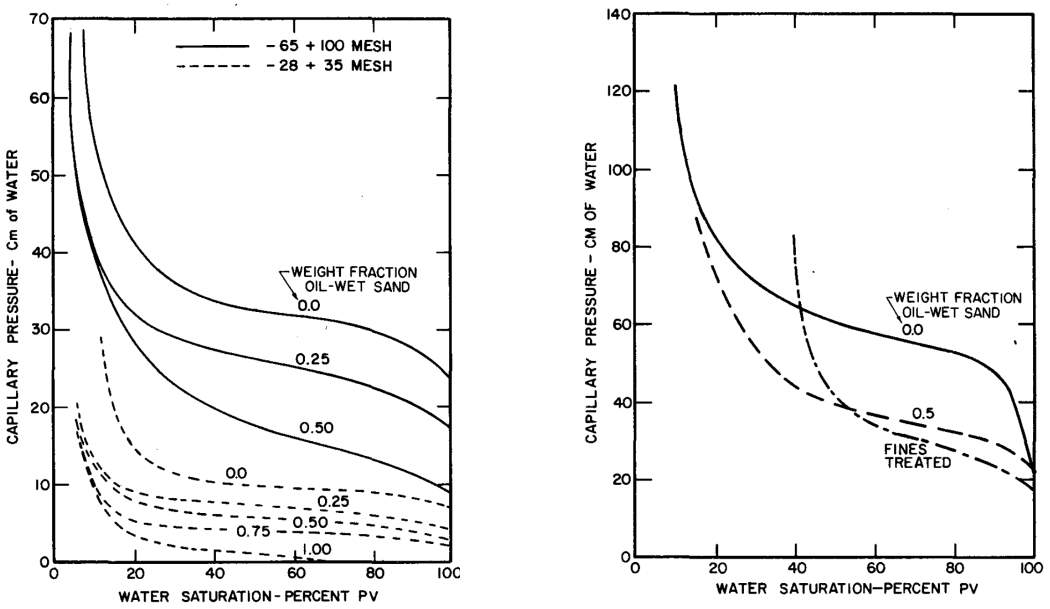

a b

Fig. 2.25 (a) Effect of fractional wettability on capillary pressure. For increasing fraction of oil-wet grains, the capillary pressure curves are parallel. (b) Behaviour of a mixed-wet system. A small fraction of the pores are oil-wet. Figures taken from [12].

In Fig. 2.26, the native state capillary pressure curve is lower than the cleaned water-wet curve at low capillary pressure. The native-state capillary pressure curve then crosses over with a higher S_{wc}, which is in better agreement with the S_{wc} measured by oil flooding a native-state core [325, 338]. In contrast, S_{wc} for a neutral or fractionally-wet core is the same or slightly lower than S_{wc} when the core is water-wet (Fig. 2.24). The proposed interpretation is that oil first enters large oil-wet pores, explaining the lower entry pressure compared with cleaned water-wet cores. The oil bypasses water in small water-wet pores. Large pores filled with water may be surrounded by small water-wet pores, explaining the crossover that leads to higher S_{wc} (Fig. 2.26) [347].

There is a threshold in pressure beyond which the thickness of water-wetting films reaches a lower limit and they collapse. This lower limit is related to the displacement pressure for pores of a given size. When the films collapse, the surface is available to develop mixed wettability [265]. A large number of studies on mixed-wet carbonates have

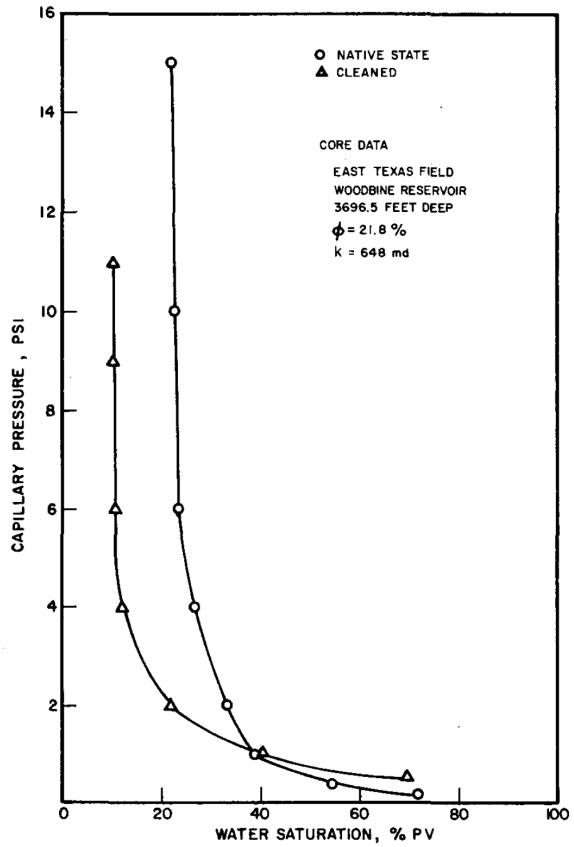

Fig. 2.26 Two drainage capillary pressure curves measured in native and cleaned states. Because of the scale of geological time, it may be an incorrect assumption to consider that the fluids are still vertically distributed, as an strongly water-wet condition predicts. Figure taken from Anderson [12].

shown similar behaviour [237]. This similarity suggests that secondary oil flooding in aged rock may correspond to the capillary behaviour in native plugs.

2.5.4 Characterising Heterogeneous Wettability

McDougall and Sorbie [257] systematically studied heterogeneous wettability using a pore-network model and varying the percentage of oil-wet pores in an initially fully oil-saturated network (direct water-flooding at 100% oil saturation) for both fractional- and mixed-wet models. They found that both the percentage of oil-wet pores and the type of heterogeneous wettability model (fractional-wet or mixed-wet) affected the capillary pressure and relative permeabilities differently. The next two sections describe the differences.

Fractionally-Wet Systems

In the fractionally-wet model, the fraction of oil-wet pores is not correlated with the pore size. Fractionally-wet systems have shown to spontaneously imbibe more oil than strongly water-wet systems when the fraction of oil-wet pores exceeds the fraction of pores needed for the system to percolate (Fig. 2.27) [257].

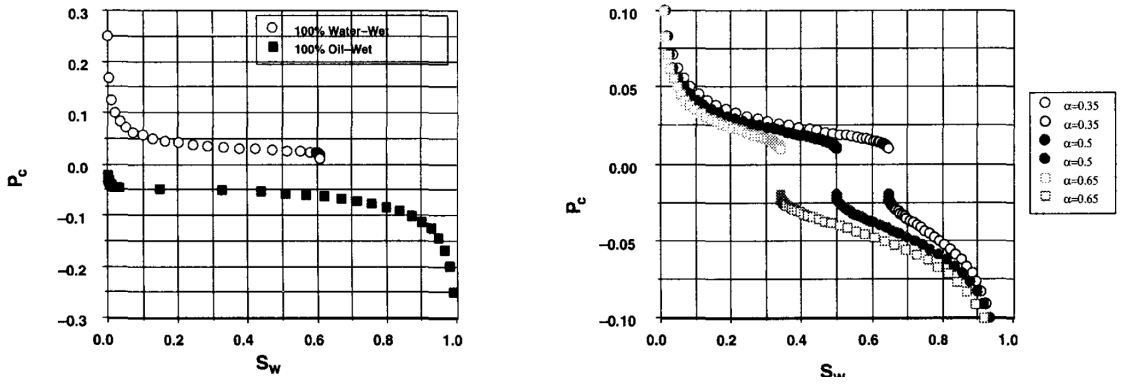

a b

Fig. 2.27 (a) Imbibition oil–water capillary pressure for both strongly water-wet and strongly oil-wet conditions. (b) Fractionally-wet systems with various fractions of oil-wet pores. Fractionally-wet systems can spontaneously imbibe more oil than strongly water-wet systems. There is a jump when the process switches from invading water-wet pores to invading oil-wet pores. Figure taken from [257].

Mixed-Wet Systems

In mixed-wet systems, less spontaneous imbibition is observed with increasing percentage of oil-wet pores. Opposite to fractionally wet systems, the imbibition capillary pressure in mixed-wet systems always comes to an abrupt end (Fig. 2.28). The Amott index is an unreliable indicator of the water wetness because it includes spontaneous imbibition, which can be greater in fractionally wet systems than in strongly water-wet systems [257].

Despite its shortcomings, the Amott index has been widely used to tune the distribution of contact angles in network model studies [28]. Other approaches to predict relative permeabilities in fractionally wet and mixed-wet systems depend on tuning the contact angles to match the residual oil saturation [6, 19, 47, 296, 311, 312, 386]. Distributions of advancing and receding contact angles allow distinction between strongly and weakly wetted pores in the network model [86] to account for the large differences between advancing and receding contact angles seen in laboratory experiments [275]. There are more complex approaches

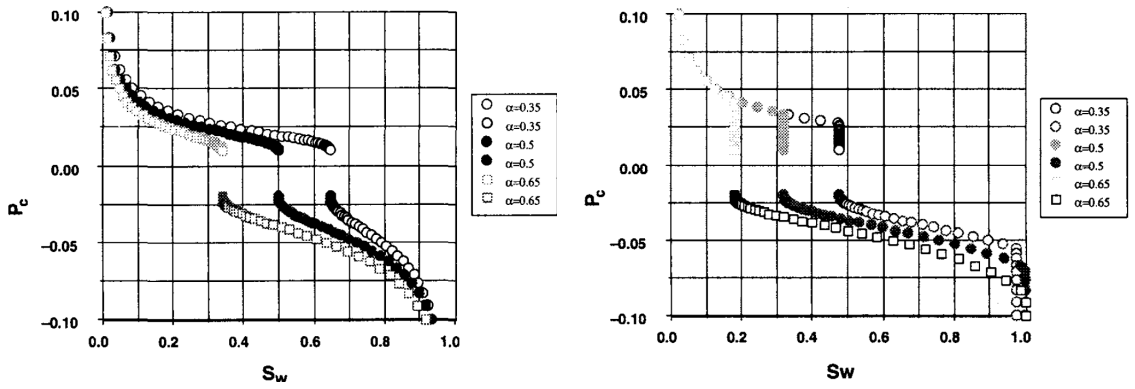

Fig. 2.28 (a) Imbibition capillary pressure for three fractionally wet system. (b) Imbibition capillary pressure for three mixed-wet system. The jump shifts to the left in the mixed-wet system compared with the fractionally wet system because water-wet pores have less volume. The jump is more abrupt followed by a displacement at lower relative pressures because the pores remaining to be invaded are larger and have greater volume. Figures taken from [257].

that make use of the individual Amott indices, namely, water and oil indices [86]

2.5.5 Methods to Measure Relative Permeabilities

The Laplace equation describes the different displacement mechanisms fairly well [218]. Understanding the effect of wettability on the relative permeabilities is more difficult because it involves an additional parameter (pore conductance). Relative permeabilities experiments are one of the more complex experiments to carry out. There are a number of initial conditions, such as core plug homogeneity, initial reservoir water saturation, and capillary end effects, that can make it difficult to derive relative permeabilities before considering the wettability [142]. There are three main core analysis methods to obtain relative permeabilities, which are described below.

Steady State Method

This experiment is very time consuming. The pressure drop across the plug establishes a constant flow of the two phases that determines the fractional flow. Stabilising the flow and pressure at each fractional flow saturation is very time consuming (1–2 days or more). In general, high flow rates (25–100 ft/day) are used to reduce experimental times and ensure the accuracy of the measured pressure gradients.

Regardless of the high flow rates used in the experiments (more than ten times greater than the rates in the reservoir), the method seems to reproduce the dynamics of capillary dominated flow. [126, 266, 302]. This might indicate that there is a capillary equilibrium at the microscopic level [53, 100].

Measuring reliable relative permeabilities requires controlled conditions (Fig. 2.29). The effect of the flow rate on the relative permeabilities is different under different wettability conditions. However, steady-state relative permeabilities are independent of the flow rate and fluid viscosity [90, 324].

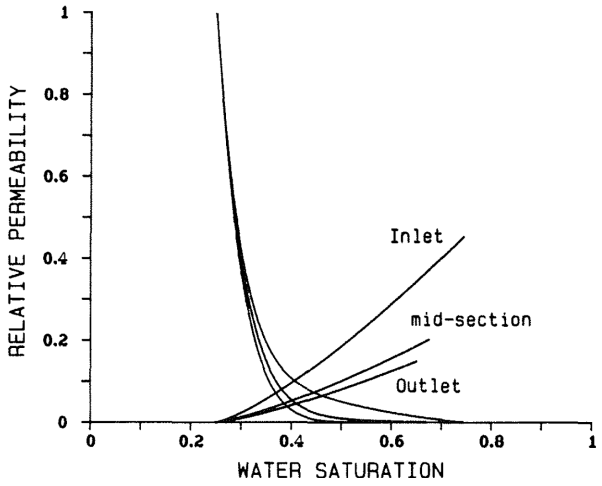

Fig. 2.29 Measuring steady state relative permeabilities is difficult and sometimes measurements are hindered by laboratory noise. Figure taken from Heaviside [142].

Unsteady State Method

This method is faster that the steady state method and involves injecting one phase and measuring the production of both phases and the pressure drop. The Buckley–Leverett model is used to interpret the raw data. There is a discontinuity in the saturation at the shock front. Therefore, saturation values below the shock front cannot be measured.

Centrifuge Method

The centrifuge method can measure very low wetting-phase relative permeabilities. The centrifugal force produces the flow. This method is usually conducted on small core plugs. A greater number of assumptions are needed to interpret the data. The rate of desaturation at each rotation speed is measured and interpretation of this data can provide wetting-phase relative permeabilities.

2.6 Pore-Network Model Wettability Parameter Estimation Methods

The wide range of pore sizes is the main problem in modelling carbonate rocks, and this is linked to wettability. Because the effect of not characterising the entire pore size distribution remains unclear, changes in the wettability depend on water film rupture. Water film rupture also depends on the maximum pressure during the first oil flooding [24, 37, 74, 121, 152, 165, 202, 206, 356, 357].

Wettability is a crucial parameter for predicting relative permeabilities using pore-network models. This involves assigning a contact angle to every pore for each process (i.e., drainage, imbibition, and secondary drainage). In the last decade, research on pore-network models has included considerable effort into rigorously modelling the coexistence of multiple phases in a single pore [46, 92, 111, 146, 249, 311, 312, 337, 388, 393, 394]. Regularly shaped pores with angular cross-sections (e.g., square and triangles) have been proposed as more realistic conceptualisations of actual pore space [201, 300].

These models have progressively captured more of the physics of the pore-scale displacement mechanisms. However, no study has addressed the issue of characterising the wettability parameters. The probability of nonuniqueness may increase if more complex representations of the displacement conditions are used.

Contact angles (i.e., water advancing and water receding) are often measured outside the porous medium [272]. pore-network model studies typically use measurements outside the porous medium to populate the pore-network model. These simplified assumptions for characterising the contact angles may be acceptable as initial attempts to modelling new situations.

However, the prediction capability of pore-network models is the subject of debate in the pore-network model community [51, 160, 360]. Some pore-network model studies have claimed to predict relative permeabilities. These predictions are mainly for Berea and Bernheimer sandstone , which are rather homogeneous rocks. These rock samples are used because they are common rocks for benchmarking.

The usual approach is to tune the bounds of a uniform distribution of contact angles to match the residual oil saturation and wettability indices [168, 387]. From the viewpoint of the inverse problem, the prediction is incomplete because residual oil is used, which is part of the information being predicted. It can be argued that estimation of the relative permeabilities is more complicated than just matching the residual oil saturation and wettability indices for lattice pore-network models [29, 33, 113, 256, 258, 320, 367, 396, 399], which

contain additional parameters to define the pore-network structure along with the wettability parameters. No studies have predicted imbibition relative permeabilities without using drainage relative permeabilities to tune some of the lattice network parameters. Combining the capillary pressure and relative permeabilities can provide a reasonably narrow estimation of the network structure and pore conductance [259]. However, this method requires the use of both the capillary pressure and relative permeabilities.

Other studies have used parameters that correlate with relative permeabilities, such as the resistivity index, to constrain the lattice network parameters [29, 33]. However, although the effect of a single contact angle for each population within the pore size distribution has been investigated using sensitivities , the resulting capillary pressure behaviour does not seem comparable with real data [32]. There have been attempts to characterise the wettability at the pore scale using the USBM and Amott indices for wettability [80, 84, 85, 150]. However, it is challenging to determine a one-to-one relationship with the contact angles because the wettability indices exhibit considerable scatter, which indicates that there are additional parameters that are not controlled.

Stochastic inversion with gaussian assumptions and a genetic algorithm have been used to solve the inverse problem of pore-network model parameter estimation [151, 169]. However, either no relative permeabilities for imbibition were reported [151], or the relative permeabilities for drainage were used in the optimisation algorithm [169]. In highly non-Gaussian (nonlinear) inverse problems, the approach used by Holm et al. [151] can cause the posterior probability density to be poorly represented by a mean model and covariance matrix. For practical reasons, allowing departures from the assumed Gaussianity may be relevant, so we should look for alternative estimators that are less sensitive to such departures.

Studies on contact angle hysteresis [275, 279] (Section 2.5.2) have led to analytical models of the hysteresis between advancing and receding contact angles [280]. These analytical models have been implemented in pore-network models [387].

Using contact angles measured outside porous media does not include the nonlinear effect of roughness on the contact angle [24, 57, 58, 148, 157, 216, 280, 333, 342] or the change of roughness because of the change in wettability cause by asphaltenes [342].

There has been little investigation into predicting relative permeabilities for carbonate imbibition. A small-size pore-network model (a reconstructed pore-network model that was a few tens of microns long) was used to predict relative permeabilities for imbibition [8]. The imbibition relative permeability for oil was fairly well predicted. However, the imbibition relative permeability for water was underpredicted. This may be because the

maximum drainage capillary pressure was less than the experimental value before the start of imbibition. Water-wetting films rupture, and the minimum capillary pressure during imbibition depends on the maximum capillary pressure during primary drainage.

In models with more complex treatment of the wetting films but simplified geometries (triangular, square, circular, and star cross-sections), the question of uniqueness is more problematic, and fits of similar quality can be obtained even with a single contact angle. This leads to underestimation of the range of receding and advancing contact angles. Therefore, further in-depth analyses of the concept of uniqueness of the inverse problem are needed.

The ability to implement additional physics at the pore scale has not kept pace with the ability to characterise the wettability parameters. Estimation of pore-network wettability parameters is considerably less developed. Attempts to establish a link among the wettability indices and define the distribution of contact angles and pore-space fraction with a given distribution are currently inconclusive. No study has predicted relative permeabilities for imbibition without using relative permeabilities for drainage to tune some lattice network parameters.

There has been little discussion on the distribution of contact angles. Characterisation of porous media involves the interplay of parameters that are convoluted in the capillary pressure behaviour. There has been observed the same patterns of contact angle hysteresis in two systems with different geometrical complexity but with the same systems of fluids and solid substrate [274]. The interaction of pore structure and wettability opens a number of multiple solutions. Despite efforts made in identifying wettability models and quantifying the wettability behaviour wettability indexes are not reliable. The distribution of contact angles influence the spontaneous imbibition and have effects that are difficult to interpret directly from two-phase capillary pressure ([86, 237, 257]). A carbonate piece of rock with a pore-size distribution of 4 to 5 orders of magnitude might well contain both expression of heterogeneous wettability.

Chapter 3

Description of the Data

This chapter describes the experiments on carbonate rock samples from the Middle East that were made available for this study. It consists of a subset of the extensive data set that was comprehensively studied by Masalmeh and Jing [242].

Mercury intrusion data can be used to determine the model parameters that describe the structure of porous media, namely the pore-size distribution, coordination number, and pore-size versus pore-volume relationship. Chapter 4 will address the specific analysis of the pore-size distribution. The oil–water centrifuge capillary pressure curves show the effect of wettability for the different directions of saturation changes, and they will be used to infer the pore-network model wettability. Centrifuge capillary pressure is often used to calculate the wettability indices, which were discussed in Chapter 2 in relation to the estimation of the fraction of oil-wet pores in pore-network models [86].

To facilitate the exposition, the process in which oil displaces water independently of the underlying wettability starting from 100% water saturation will be referred to as drainage, the process in which water displaces oil from the porous media starting from connate water saturation will be referred to as imbibition or water-flooding. The aim of this chapter is to familiarise reader with the data used in this study.

3.1 Special Core Analysis Data

Special core analysis groups reservoir rock types based on their mercury intrusion capillary pressure (MICP) behaviour [244]. The rock types follow a petrophysical classification that describes the pore space in terms of its fabric, namely, organisation of the pore space (Lucia classification [224]) and the Dunham classification [98], which takes into account the paleoenvironment where the sediments that made the rocks were deposited.

Table 3.1 Thermodynamic properties of the set of fluids used in the experiments. σ_{ow} , and σ_{Hga} are oil/water and mercury/air IFT respectively.

System	IFT [mN/m]
σ_{ow}	27
σ_{Hga}	470

Table 3.2 Summary of all of the properties of the three samples. ϕ is porosity, K is absolute permeability, Amott and USBM are the wettability indices, S_{wc}^{obs} is the observed connate water saturation, and $S_{or}^{obs}$is the observed residual oil saturation.

Rock Type (Sample)	ϕ [%]	K [mD]	Amott	USBM	S_{wc} [frac]	S_{or} [frac]
RT–I (S 28)	29.1	78.09	0.038	0.297	0.03	0.0548
RT–II (S 2 4)	28.7	13.5	0.015	-0.263	0.05	0.07
RT–III (S 2 20)	21.6	1.9	-0.01	-0.408	0.08	0.055

The interfacial tension (IFT) values of the oil/water (σ_{ow}) and mercury/air (σ_{Hga}) systems used in all of the experiments are given in Table 3.1

Table 3.2 summarises the petrophysical properties and wettability indices that are going to be presented in this chapter.

3.2 Rock Type I - Sample 28

Rock type I (RT-I) is a fine to coarse grainstone associated with a high energy shoal and beach paleoenvironment. The porosity is mainly of the intergrain type with grain texture [224]. The range of absolute permeabilities is 40–800 mD with very low capillary entry pressure. RT-I has the best reservoir quality in terms of absolute permeability. Table 3.3 gives the bulk properties of sample 28 (S 28), which is a member of RT-I. The MICP curve for S 28 has low entry pressure that can be related to the presence of macropores, although the absolute permeability is not particularly high.

3.2.1 MICP of S 28

The MICP will be used to characterise the pore-network model structure. The MICP is routinely measured for small plugs or chips. It is a destructive experiment, so oil/water capillary pressure and relative permeabilities are performed in adjacent plugs.

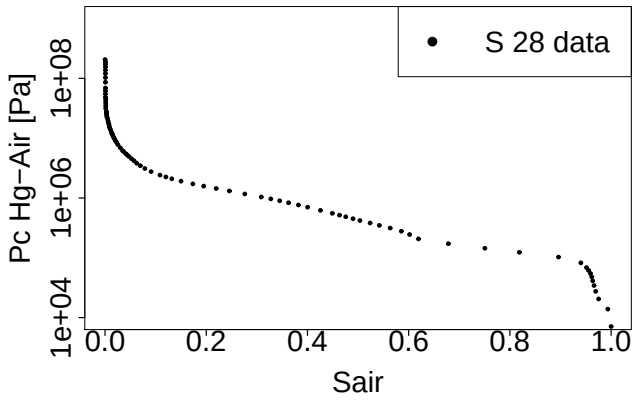

Fig. 3.1 MICP of S 28.

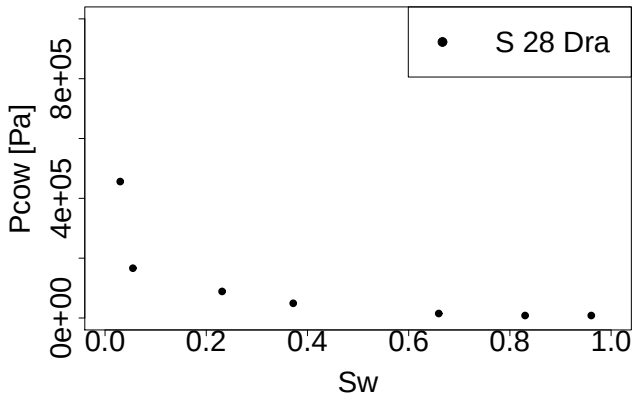

Fig. 3.2 Oil/water drainage capillary pressure of S 28.

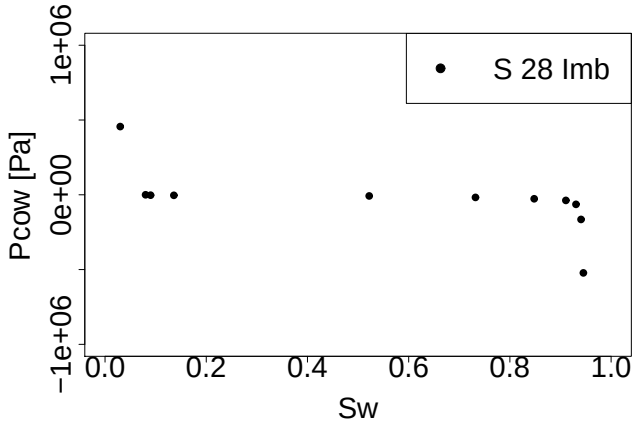

Fig. 3.3 Oil/water imbibition capillary pressure of S 28.

Figure 3.1 shows the MICP for S 28. Because the capillary pressure spans around, five orders of magnitude, a wide range of pore sizes is anticipated. Notice that multiple slopes (see Fig. 3.1), suggesting a bimodal pore-size distribution.

3.2.2 Oil/Water Drainage Capillary Pressure of S 28

The plugs were cleaned to render them strongly water-wet. Figure 3.2 shows the primary drainage oil-water capillary pressure.

3.2.3 Oil/Water Imbibition Capillary Pressure of S 28

After primary drainage, the core was aged with crude oil at reservoir temperature to restore the wettability to the conditions that presumably occur in the reservoir. Water was then injected in the aged core and the capillary pressure was measured. Figure 3.3 shows the capillary pressure curve. A more detailed description of the laboratory procedure is given in [247].

The first imbibition capillary pressure value was ($S_{wc}^{obs} = 8.01\%$, $P_{c,ow}^{obs} = 0.0$) given that the last saturation value in drainage at positive capillary pressure was $S_{wc}^{obs} = 3\%$ (see Fig. 3.2). Small spontaneous imbibition was evident. Stochastic inversion of this data will determine the distribution of the advancing contact angles at the pore level.

In Fig. 3.3, the medium seems to have become entirely oil-wet as shown by all the displacement for a negative capillary pressure during water-flooding. Unlike the studies in bimodal samples discussed in Chapter 2, where the data followed distinctive trends, because of the contrast between macroporosity and microporosity, there are no such trends evident among the data for the imbibition capillary pressure. The residual oil saturation was very low ($S_{or}^{obs} = 5.6\%$).

3.2.4 Oil/Water Secondary Drainage Capillary Pressure of S 28

After the first water flooding, a second drainage curve was determined. Oil enters the core plug at residual oil saturation with the same wettability as water flooding. Hardly any spontaneous oil invasion was observed (Fig. 3.4).

Figure 3.5 compares the capillary pressure curve for primary drainage (water-wet conditions) and secondary drainage (altered wettability), where oil invades an aged medium at residual oil saturation. Section 2.5.3 discussed heterogeneous wettability, and examples of capillary pressure curves for heterogeneous wettability from the literature were shown.

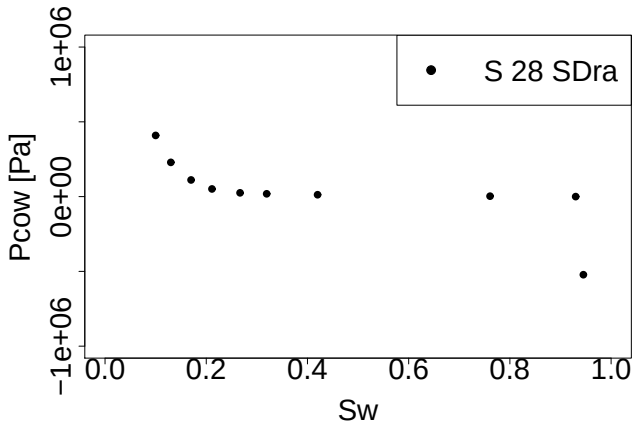

Fig. 3.4 Oil/water secondary drainage capillary pressure of S 28.

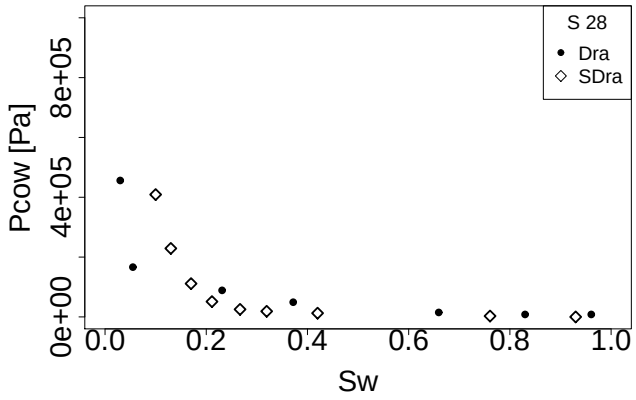

Fig. 3.5 Comparison between oil/water drainage and secondary drainage capillary pressure of S 28

As can be seen in Fig. 3.5 additional trapping of water occurs during secondary drainage, possibly indicating that the displacement mechanism is different from the one occurring during primary drainage. Similar to the capillary pressure data in native cores (Chapter 2), the secondary drainage capillary pressure in Fig. 3.5 crosses over the water-wet primary drainage capillary pressure curve.

In Section 2, we discussed how the choice of a drainage curve in an mixed-wet system will affect the assessment of the transition zone in the reservoir. Figure 3.5 shows that if the primary drainage curve is used in reservoir engineering calculations, which is usually the case, the height of the transition zone will be overestimated compared with the vertical distribution of the fluids at the actual wettability conditions in the reservoir. It could be argued that oil migration into the reservoir rock took place at strongly water-wet conditions

and the reservoir remained in a metastable state until it was discovered. However, the timing factor is an important variable given that a a number of geological events could have taken place during geological time that produce the disturbance needed to move the metastable saturation distribution to the stable configuration.

3.2.5 Oil/Water Imbibition Relative Permeabilities of S 28

Figure 3.6 shows the steady-state imbibition relative permeabilities for S 28. The end-point relative permeabilities of oil and water are similar. The water saturation at the intersection of relative permeabilities is slightly lower than 50%. From the plotted data, the relative permeability at the intersection is low, indicating a high multiphase interference effect.

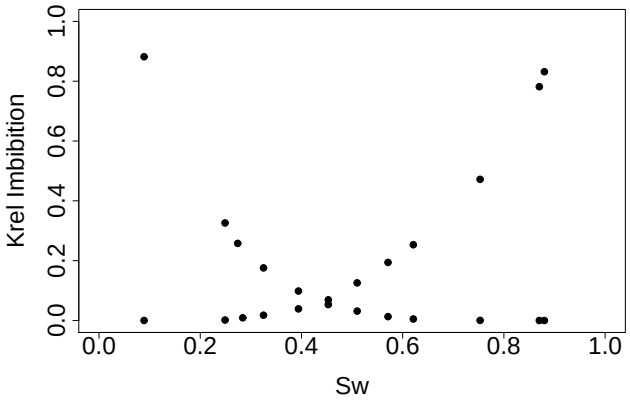

Fig. 3.6 Oil/water imbibition relative permeabilities of S 28.

3.2.6 Wettability Indices of S 28

Table 3.3 gives the USBM (United States Bureau of Mines wettability index) and Amott indices calculated using drainage and imbibition capillary pressure curves

3.2.7 Estimation of Contact Angles from SCAL Data

This work focuses on three samples. The complete data, including more than 100 samples, has been studied in detail and published in a vast number of articles [236–246]. However, most of the samples do not have a complete data set (mercury intrusion capillary pressure, full flooding cycle oil/water capillary pressure and steady state relative permeabilities). It has been noted that imbibition seems to be a mirror image of primary drainage shifted by

a saturation value given by the difference between the connate water and the residual oil saturation, and it is also affected by the ratio of the cosine of the average apparent contact angles. Based on that observation, Masalmeh and Jing [242] proposed an analytical method (similar to the method discussed in Chapter 2) to calculate the average apparent advancing contact angle by fitting both curves with an analytical equation. The method assumes that after ageing, the change of the wettability is such that the pore filling sequence is the same as primary drainage.

Observations in micromodel experiments show that the distribution of residual water after primary drainage makes additional routes available for water to invade the porous media compared with oil invading the porous media at 100% water saturation. This will affect the filling sequence of pores [213, 215, 218].The method also assumes that the intrinsic contact angle during primary drainage is less than 60°. Therefore, the average apparent contact angle is 0°[250, 279].

Wettability data was obtained by fitting an analytical model to drainage and imbibition capillary pressure [242]. The model has the receding and advancing contact angles as free parameters and assumes an invasion sequence of pore sizes. The method produces contact angle distributions.

Figure 3.7 shows two empirical cumulative distribution functions (ECDFs) of the contact angles, summarizing the values reported by Masalmeh and Jing [242]. When they applied the method to bimodal samples, such as the one grouped in RT-I, two contact angles were needed to fit different portions of the imbibition capillary pressure (Fig. 3.7), suggesting different behaviour in the bimodal pore-size distribution samples compared with unimodal samples.

3.2.8 Visual Features in Scanning Electron Microscope Multiscale Images of S 28

All carbonate reservoirs have undergone one or more different diagenetic processes that produce complex visual patterns. Therefore, in this section we summarise some of most general patterns in scanning electron microscope images at three magnifications scales (Fig. 3.10). However, this presentation is not intended as a deep petrographical analysis.

Carbonate rocks have diverse components, the most general classification (Foks's classification) considers two groups of components: transported calcium carbonate grains such as ooids (clast nucleus wrapped with concentric layer of calcium carbonate) and bioclast. These grains are analogous to grains in sandstone. They are usually transported large dis-

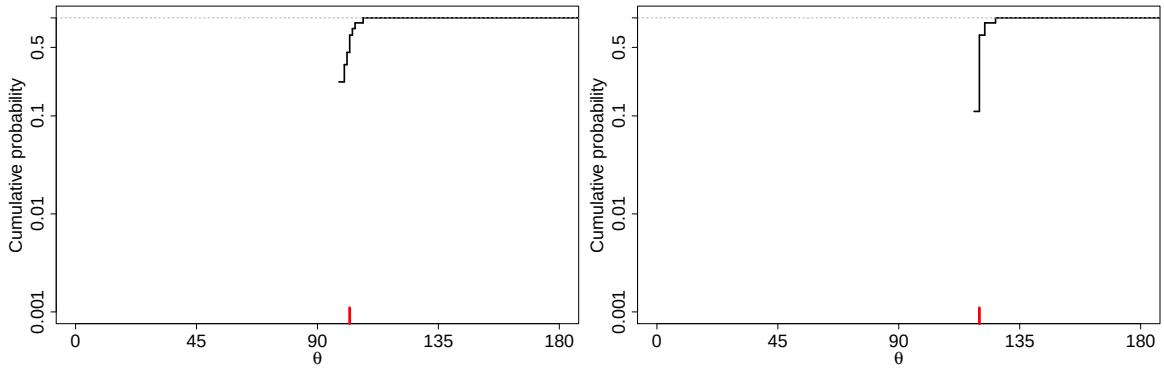

Fig. 3.7 Cumulative distribution function of the average apparent advancing contact angles. Bimodal pore-size distribution samples [242]. (a) Small pores. (b) Large pores. The red line indicates the median.

tances before being deposited [315]. The description of the images will be based on the different porosity types which are shown in Figure 3.8.

On the other hand, the second group of calcium carbonate crystals are created in situ: (1) microcrystalline calcite matrix, or micrite, which is fine-grained (finer than 4 microns in diameter) carbonate mud; (2) microcrystalline sparry cement, or spar, is relatively clear interlocking crystals of calcium carbonate, analogous to cement in sandstone [315]. Note that spar can be primary cement or secondary recrystallisation of micrite into spar [315]. Figure 3.9 shows schematic representation of the second group. Calcium carbonate cement is very important since recent cryogenic electron microscope images have shown that wettability alternation depends on the type of calcium carbonate crystal shape [235] which further influence pore shapes [188].

In rock type I, grains form the framework of the rock, though grains are not always obvious because of dissolution and further micritic cement around grains [88].

Figure 3.10a shows that sample S 28 is very well connected, very heterogeneous with some cement patches, micritic cement around grains.There is very good intergranular porosity and secondary mouldic porosity created by remotion of preferential elements from sediments [88].

Cementation is very important because it could strongly influence pore shapes and therefore intrapore wettability. Basically, if crystals forming cement can grow freely they develop well defined crystal faces. This is know as euhedral calcite or micrite grain. However, often it is more common to find interlocked crystal faces forming an irregular mosaic type of

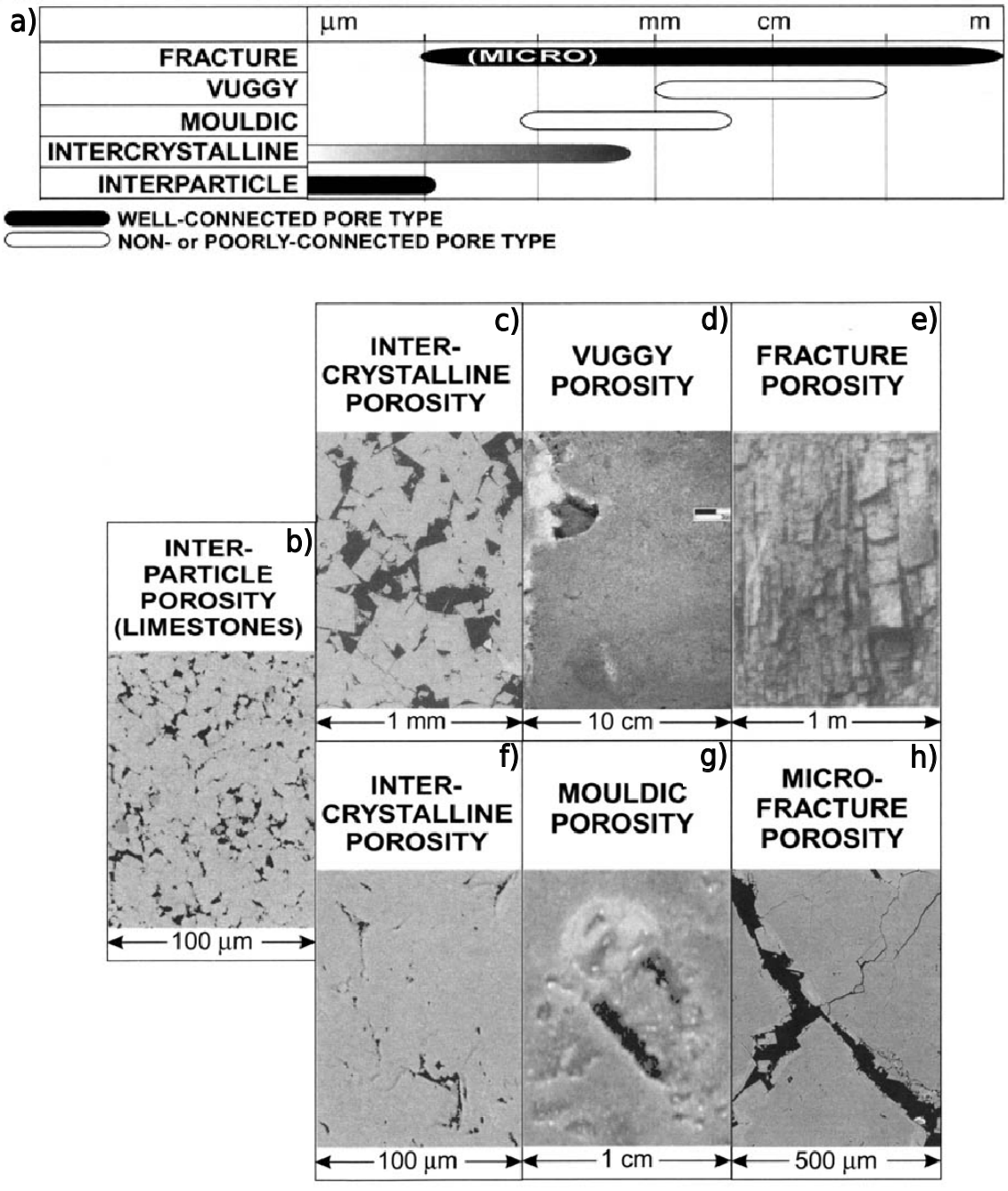

Fig. 3.8 Classification of the different porosity types in carbonates. Figure taken from [52].

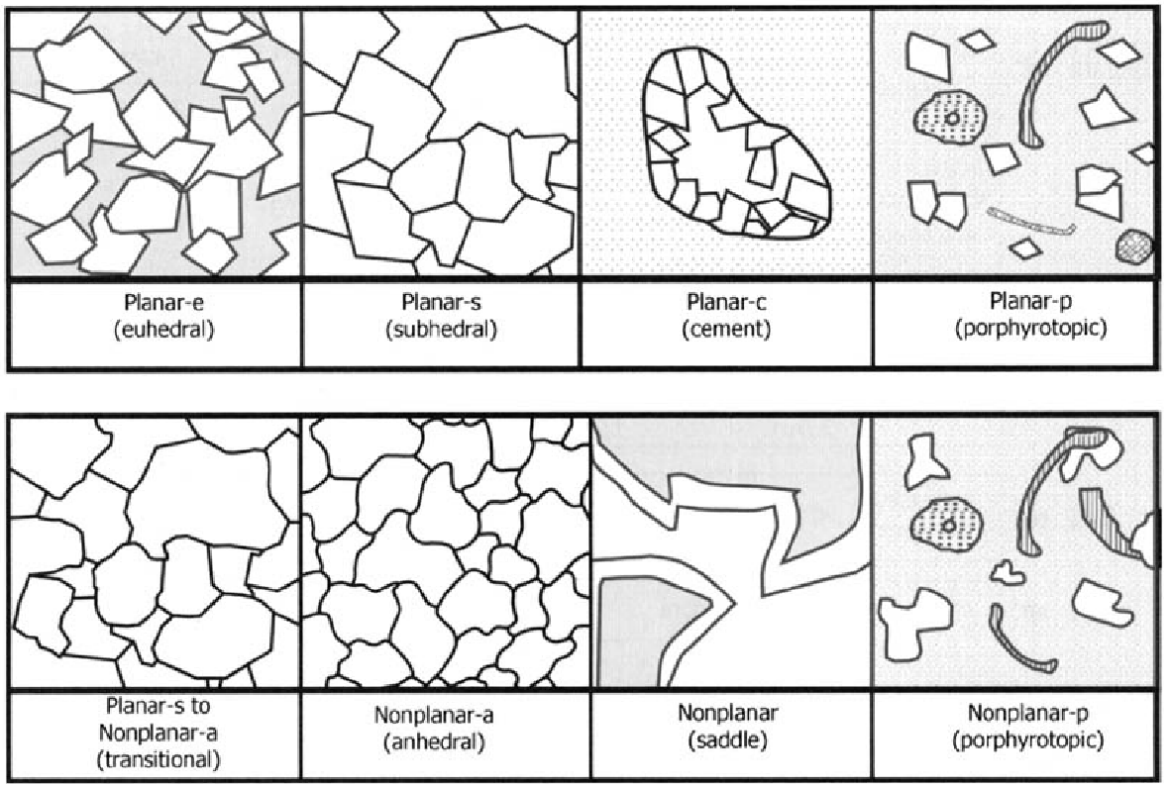

Fig. 3.9 Classification of dolomite crystal shapes. Figure take from [230].

cementation [61, 119], such as seen in Fig. 3.10c.

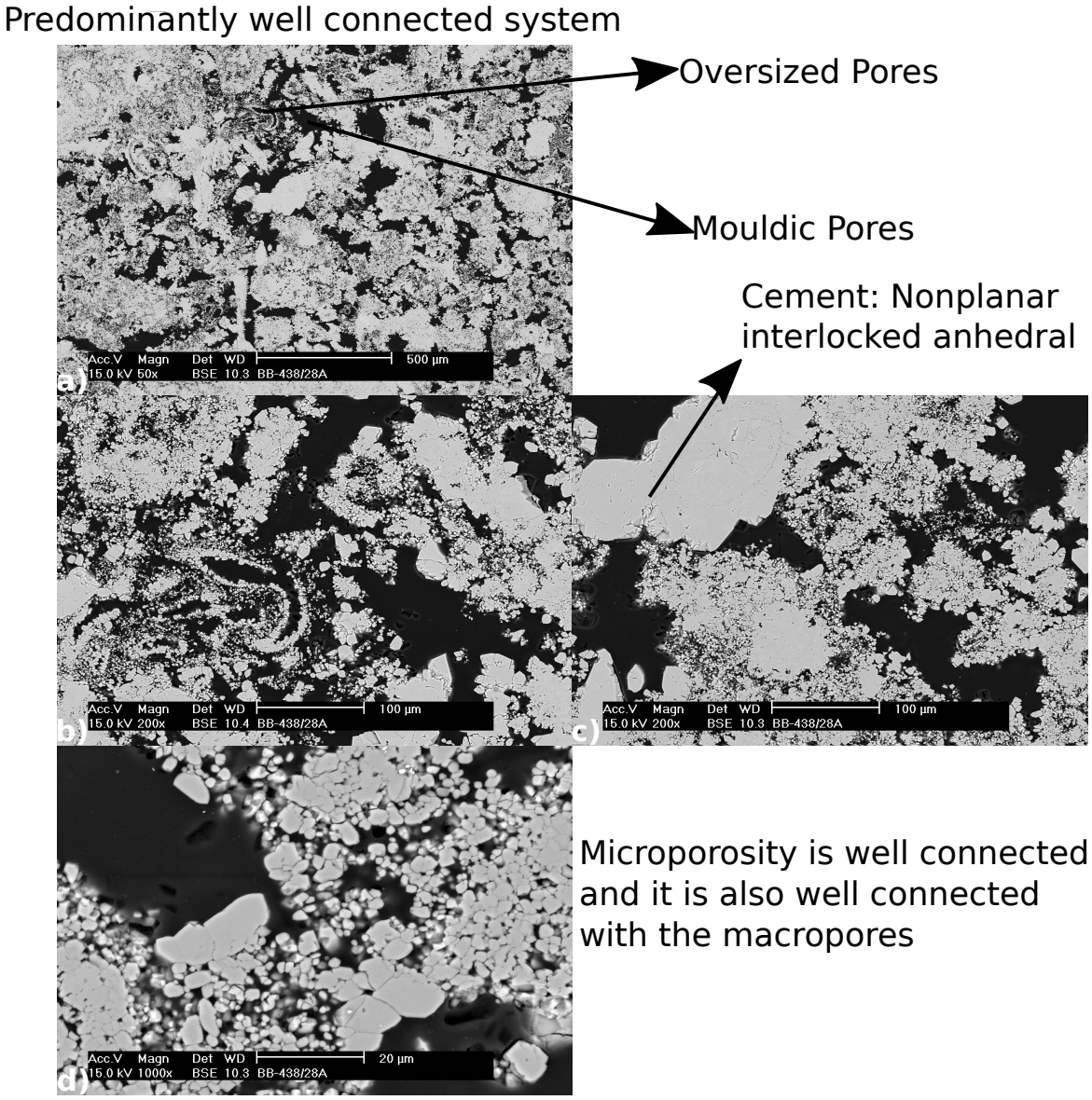

Fig. 3.10 Multiscale scanning electron microscope images of S 28. (a) 50x. (b) 200x. (c) 200x. (c) 1000x.

3.3 Rock Type II - Sample 2 4

The second sample is S 2 4 and is classified as rock type II (RT-II). Table 3.3 gives the bulk properties of this sample. The mercury entry pressure is higher than S 28 and the absolute permeability is lower. Figures 3.11, 3.12, 3.13, and 3.14 show the MICP, drainage, imbibition and secondary drainage capillary pressure.

3.3.1 MICP of S 2 4

Unlike S 28, the MICP of S 2 4 does not develop multiple slopes (see Fig. 3.11), suggesting a unimodal range of pore sizes.

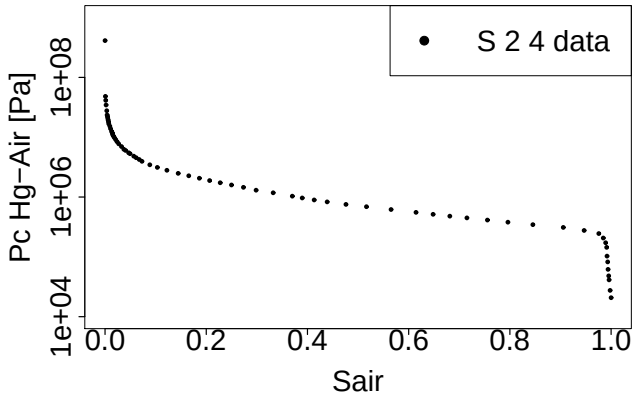

Fig. 3.11 MICP of S 2 4.

3.3.2 Oil/Water Drainage Capillary Pressure of S 2 4

The connate water saturation is slightly higher than that of S 28 but is still a low value, despite S 2 4 appearing to be a tight rock given the capillary entry pressure in Fig. 3.12.

3.3.3 Oil/Water Imbibition Capillary Pressure of S 2 4

Spontaneous water imbibition is rather small. The curve is flat (see Fig. 3.13) and it is similar to the imbibition capillary pressure curve for S 28. The residual oil saturation is slightly higher than S 28 (see Fig. 3.13)

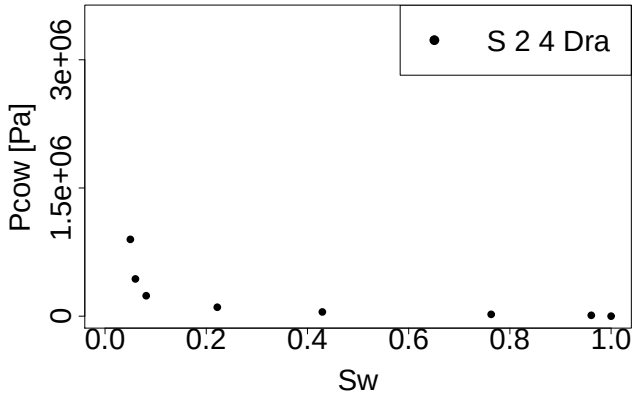

Fig. 3.12 Oil/water drainage capillary pressure of S 2 4.

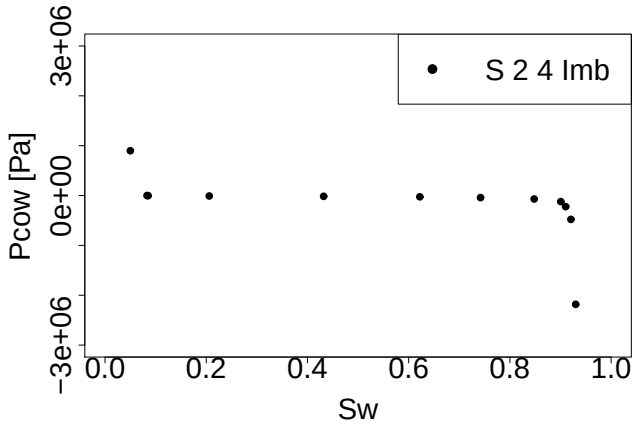

Fig. 3.13 Oil/water imbibition capillary pressure of S 2 4.

3.3.4 Oil/Water Secondary Drainage Capillary Pressure of S 2 4

Like previous sample, S 28, no spontaneous oil invasion of the core at residual oil saturation was observed. Comparison of Fig. 3.14 and primary drainage Fig. 3.12 interestingly shows that secondary drainage lies below primary drainage crossing over the primary drainage capillary pressure close to the initial connate water saturation. In addition, the residual water saturation after the second oil flooding is lower than for S 28.

3.3.5 Oil/Water Imbibition Relative Permeabilities of S 2 4

Figure 3.16 shows the steady-state imbibition relative permeabilities for S 2 4. The end-points oil and water relative permeabilities are similar to those of S 28. However, the water saturation at the intersection of the relative permeabilities is slightly lower than 40% (more

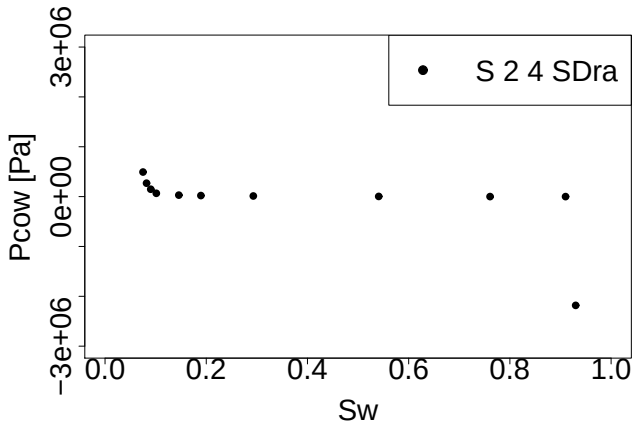

Fig. 3.14 Oil/water secondary drainage capillary pressure of S 2 4.

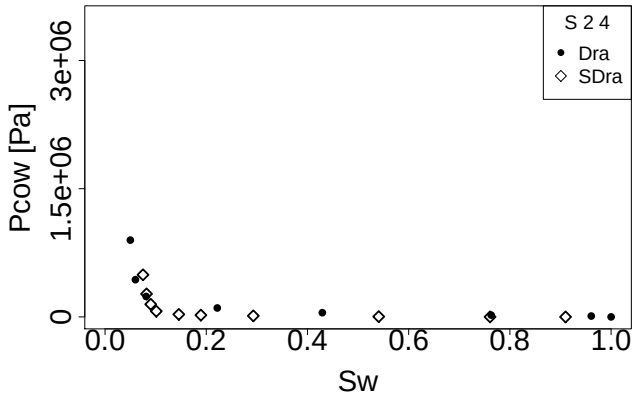

Fig. 3.15 Comparison between Oil-Water drainage and secondary drainage capillary pressure of S 2 4

oil-wet than S 28).

Similar to S 28, the relative permeability at the intersection is low indicating a high multiphase interference effect. It is worth noting that the water relative permeability curve is less concave and steeper than that of S 28 (Fig. 3.16).

3.3.6 Wettability Indices of S 2 4

The Amott index, Section 2.5.1, of S 2 4 (0.015) is less than half that of S 28 (0.038), and the USBM index is similar in magnitude but negative (–0.263 for S 2 4 and 0.297 for S28).

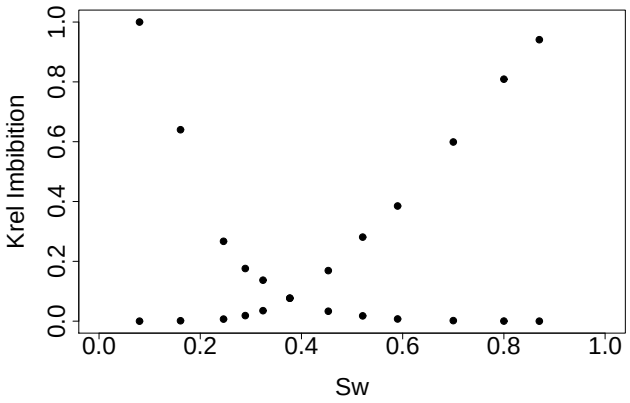

Fig. 3.16 Oil/water imbibition relative permeabilities of S 2 4.

3.3.7 Estimation of Contact Angles from SCAL Data

Figure 3.17 shows the ECDF of the average apparent advancing contact angles derived from capillary pressure data [242] for unimodal pore-size distribution samples (RT-II and RT-III).

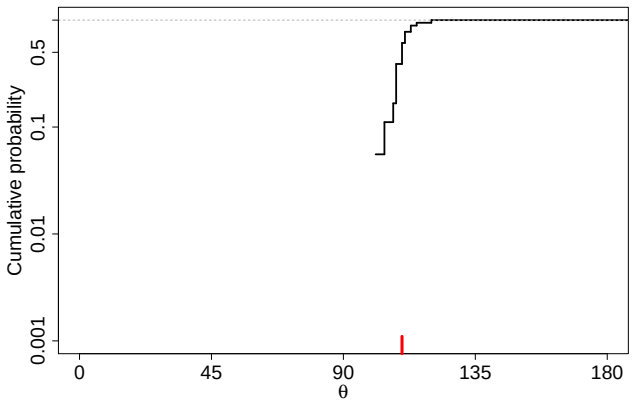

Fig. 3.17 Distribution of average apparent advancing contact angles for unimodal pore-size distribution derived from capillary pressure data [242].

3.3.8 Visual Features in Scanning Electron Microscope Multiscale Images of S 2 4

Figure 3.18 shows the scanning electron microscope image of S 2 4. S 2 4 is packstone to grainstone. At the largest image magnification scale (50x) Fig 3.18a S 2 4 looks heterogeneous. Cementation is weak to moderate with grain coating of irregular micrite cement.

Dolomite crystals are visible filling some pores [88]. Moderate intergranular porosity, with sparse oversized pores, up to 200 microns across probably indicate dissolved peloids [88]. There are sparse distributed vuggs (300 microns in size) with a significant contribution of microporosity in between the precipitated spar and dolomite calcite [88].

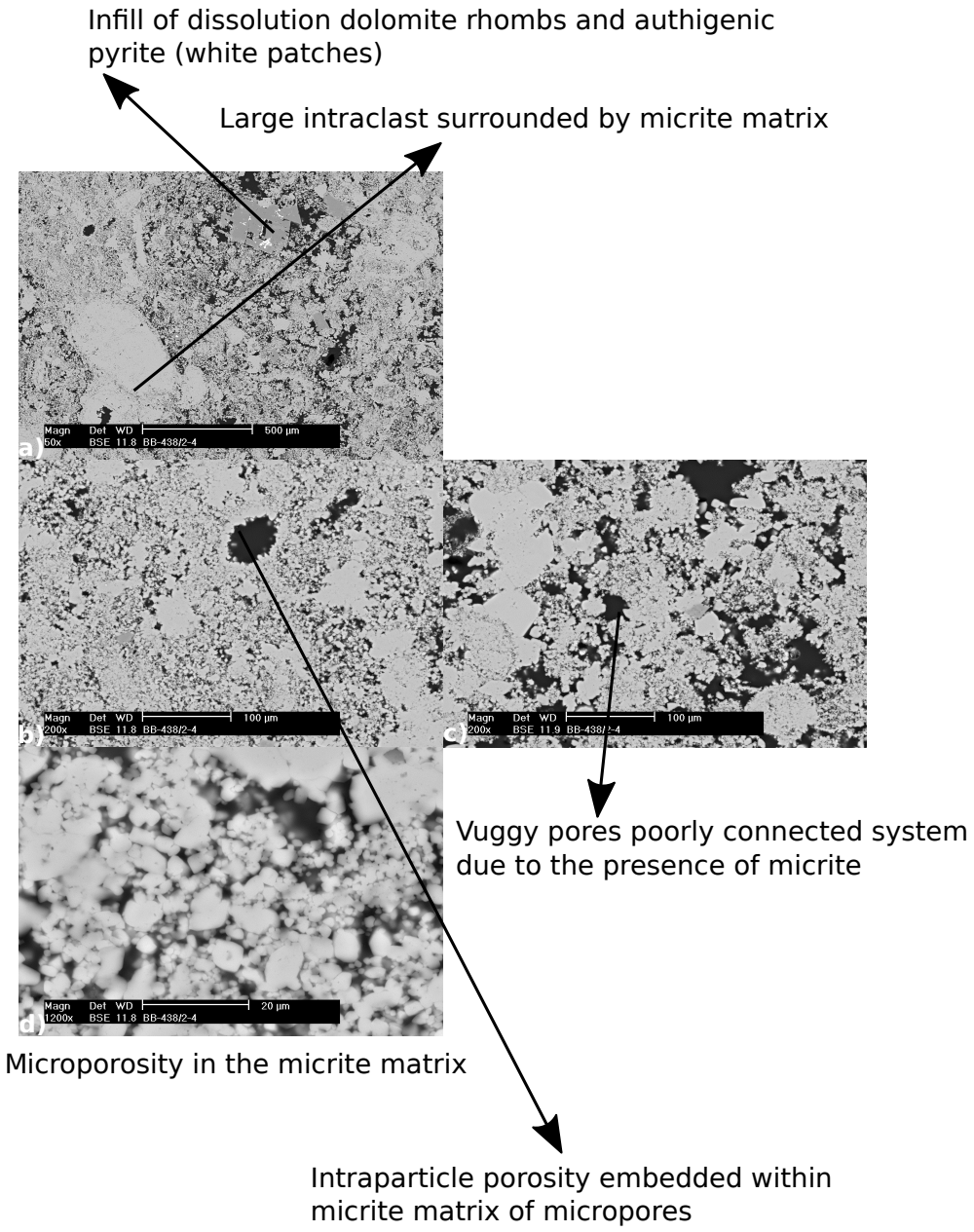

Fig. 3.18 Multiscale scanning electron microscope images of S 2 4. (a) 50x. (b) 200x. (c) 200x. (c) 1200x.

3.4 Rock Type III - Sample 2 20

Table 3.3 shows the bulk properties of Sample S 2 20. S 2 20 belongs to rock type III (RT-III) and has the lowest absolute permeability of the three samples. Figures 3.19, 3.20, 3.21 and 3.22 show the MICP, drainage, imbibition, and secondary drainage capillary pressure of S 2 20, respectively.

3.4.1 MICP of S 2 20

S 2 20 shows a high entry pressure for mercury and the MICP curve (Fig. 3.19) is similar to that of S 2 4, but different from that of S 28.

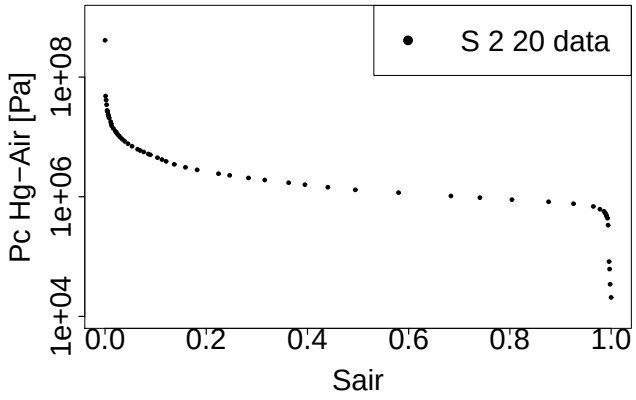

Fig. 3.19 MICP of S 2 20.

3.4.2 Oil/Water Drainage Capillary Pressure of S 2 20

The connate water is greater for S 2 20 than S 2 4 (Fig. 3.20). It seems that connate water is correlated with the decrease in absolute permeability.

3.4.3 Oil/Water Imbibition Capillary Pressure of S 2 20

Similar to the previous two samples, little spontaneous water imbibition was observed. The residual oil was lower than in the previous samples which have higher absolute permeabilities. It seems that there is no link between absolute permeability and residual oil saturation.

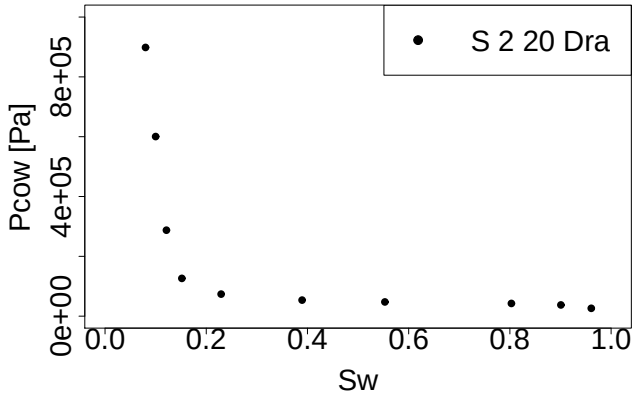

Fig. 3.20 Oil/water drainage capillary pressure of S 2 20.

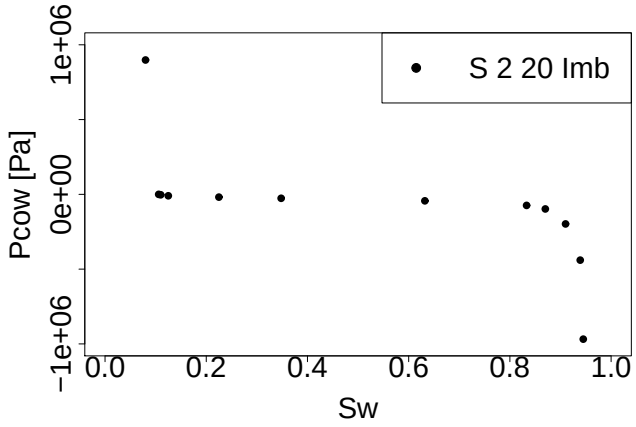

Fig. 3.21 Oil/water imbibition capillary pressure of S 2 20.

3.4.4 Oil/Water Secondary Drainage Capillary Pressure of S 2 20

In a similar way to the previous two samples, there is spontaneous invasion of oil in the core at residual oil saturation (Fig. 3.22) However, the residual water saturation is greater than in the previous rock types.

Similar to RT-I, the secondary drainage capillary pressure crosses-over the primary drainage capillary pressure curve (Fig. 3.23). However, the maximum secondary drainage capillary pressure is about two times smaller than the primary drainage capillary pressure, while the maximum capillary pressure values are comparable to those of RT-I (Fig. 3.5).

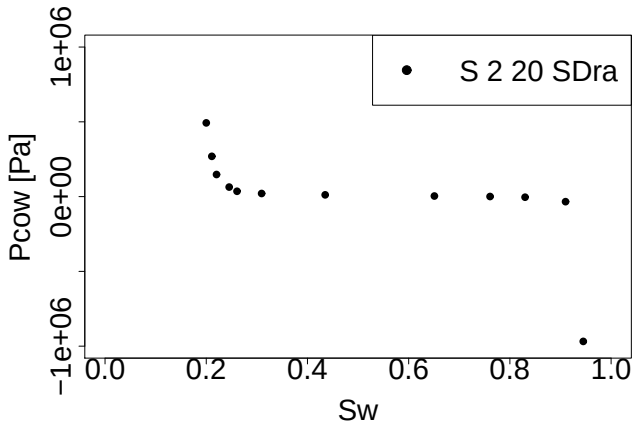

Fig. 3.22 Oil/water secondary drainage capillary pressure of S 2 20

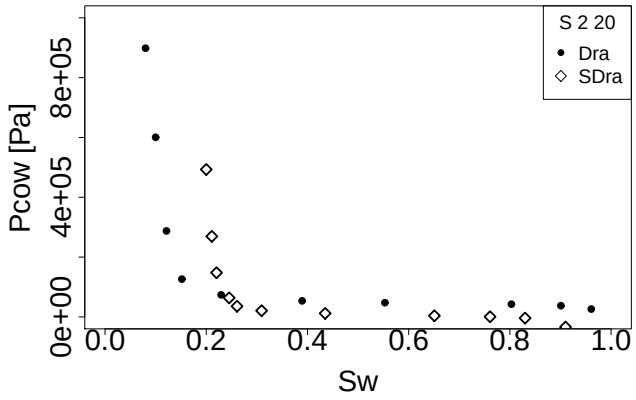

Fig. 3.23 Comparison between Oil-Water drainage and secondary drainage capillary pressure of S 2 20

3.4.5 Oil/Water Imbibition Relative Permeabilities of S 2 20

Figure 3.24 shows the steady-state imbibition relative permeabilities for S 2 20. The endpoint relative permeabilities of oil and water are similar to those for RT-I and RT-II. The intersection of relative permeabilities is close to the middle at 50%. The relative permeability at the intersection is low and the relative permeability curve is more concave than the curves for RT-I and RT-II indicating a higher multiphase interference effect.

3.4.6 Wettability Indices of S 2 20

Table 3.3 gives the wettability indices of S 2 20. The USBM and Amott indices suggest that S 2 20 is more oil-wet than the other two samples. This contradicts the average apparent

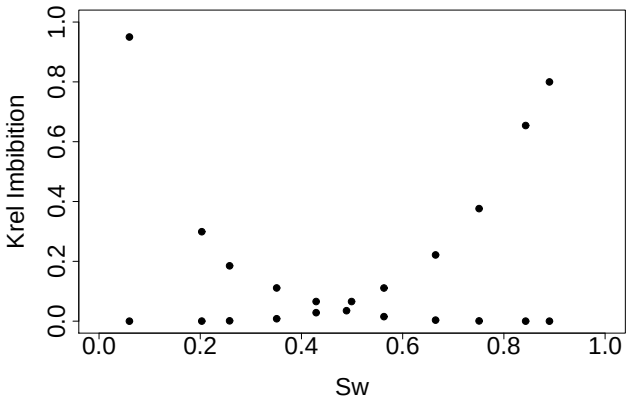

Fig. 3.24 Oil/water imbibition relative permeabilities of S 2 20.

advancing contact angles derived in [242] for RT-II and RT-III and the water saturation value at the intersection, and shows that it is difficult to estimate pore-network model wettability using wettability indices.

3.4.7 Estimation of Contact Angles from SCAL Data

RT-III and RT-II share the same ECDF of average apparent advancing contact angles derived from capillary pressure data [242] (Fig. 3.25).

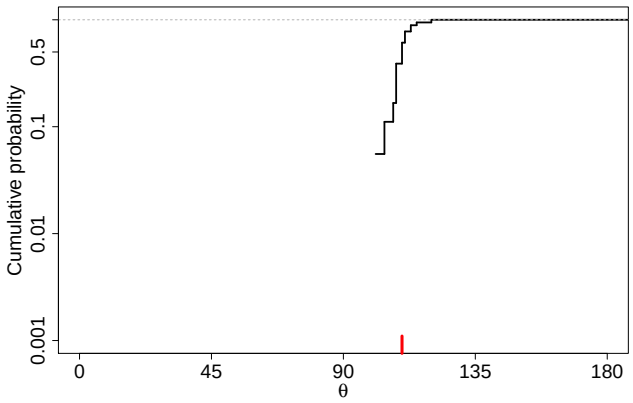

Fig. 3.25 Distribution of average apparent advancing contact angles for unimodal pore-size distribution derived from capillary pressure data [242].

3.4.8 Visual Features in Scanning Electron Microscope Multiscale Images of S 2 20

Figure 3.26 shows scanning electron microscope images of S 2 20. Rock type III is tighter than the two previous rock types. It has structure similar to rock type II. However, the strong micritization makes it more wackestone type. Macropores are present in the packstone structure. There are dolomite crystals Figs. 3.26c,e and mouldic pores Fig. 3.26b. Microporosity is the dominant porosity [88].

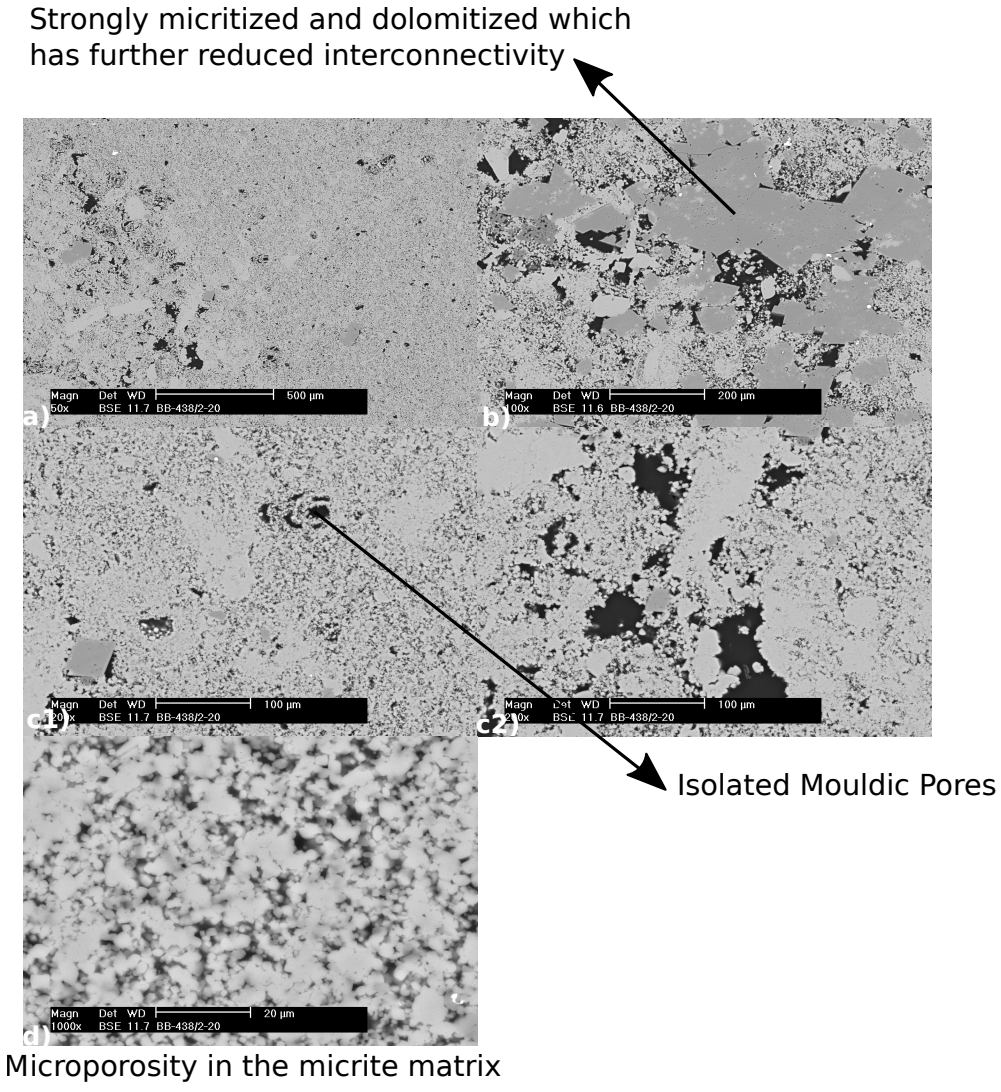

Fig. 3.26 Multiscale scanning electron microscope images of S 2 20. (a) 50x. (b) 200x. (c) 200x. (c) 1200x.

3.5 Summary of Observations

A comparison of the results mentioned above is given in Table 3.3. There is an inverse correlation between the mercury entry pressure and the absolute permeability. The connate water is inversely correlated with the absolute permeability. The residual oil does not seem to be correlated with any of the other properties.

The inverse correlation suggests that little vuggy porosity is present in these carbonates [224]. There is a type of grainstone described by Lucia [224] (ooid grainstone type) that presents bimodal behaviour similar to S 28, in which the low entry capillary pressure is because of the intergrain pore space and the higher capillary pressure relate to the intragrain microporosity, which accounts for the majority of the porosity.

There have been attempts in the literature to derive the wettability type and the fraction of oil and water-wet pores using a combination of both indices in a cross-plot [81, 150]. However, the scatter in the cross-plots suggests that additional variables are not controlled, and that they strongly affect the indices. One could estimate that RT-I may fit a mixed-wet large model, RT-II may fit a fractionally-wet model, and RT-III may fit a mixed-wet small model by the positions of the indices in the cross-plots in [81, 150] and Fig. 3.27 . The cross-plots also suggest that the three samples are weakly oil wet.

Table 3.3 Summary of all of the properties of the three samples. ϕ is porosity, K is absolute permeability, Amott and USBM are the wettability indices, S_{wc}^{obs} is the observed connate water saturation, and S_{or}^{obs} is the observed residual oil saturation.

Rock Type (Sample)	ϕ [%]	K [mD]	Amott	USBM	S_{wc}^{obs} [frac]	S_{or}^{obs} [frac]
RT–I (S 28)	29.1	78.09	0.038	0.297	0.03	0.0548
RT–II (S 2 4)	28.7	13.5	0.015	-0.263	0.05	0.07
RT–III (S 2 20)	21.6	1.9	-0.01	-0.408	0.08	0.055

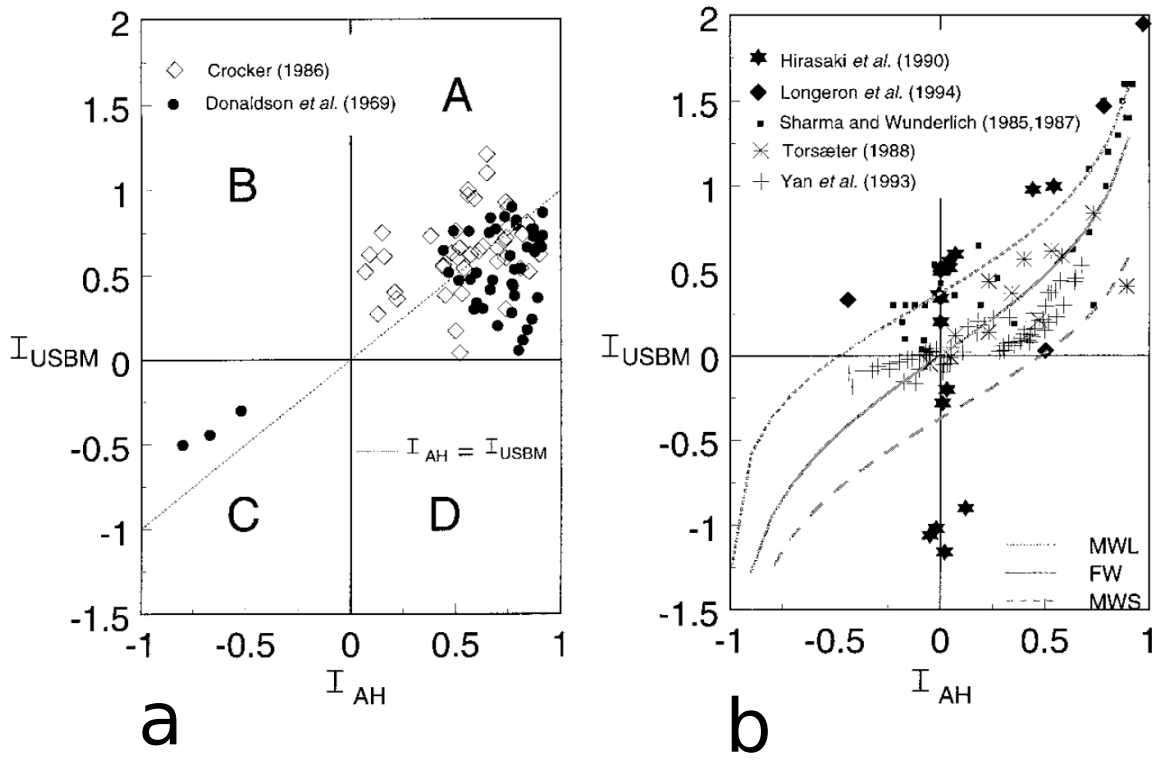

Fig. 3.27 Cross plots of USBM wettability index versus Amott-Harvey index from literature data (a) Experiments performed on twin core plugs of the same rock type. (b) Experiments performed on the same plug. The correlations in (b) are derived from pore-network model simulations. MWL refers to mixed-wet large wettability model where large pores are oil-wet; MWS refers to mixed-wet small wettability model where small pores are oil-wet and FW refers to fractional wettability model where the wettability is uncorrelated with pore size. Figure taken from [83].

Chapter 4

Methods

4.1 Introduction

In the first part of this chapter, we derive a parameterisation of the pore-size distribution using information theory. This method uses the entropy of the pore-size distribution as guidance for determining the bin partitions of the sizes in the pore-size distribution. The second part starts with a detailed description of the inversion method proposed to estimate pore-network model parameters, and involves molecular dynamics with stochastic steps. Finally, we present the pore-network model. While describing the features, the specifications of the structural and wettability parameters, which were used for the inversion, are also presented.

4.2 Methods: Pore-Size Distribution Parameterisation

Previous work on the prediction of petrophysical properties using lattice networks has not investigated in depth how to incorporate prior information derived from data. Predictions using stochastic methods or Bayesian analysis usually resort to simple assumptions for convenience. Prior information, if available, can be used to constrain the solution to the inverse problem.

A first estimate of the pore-size distribution is typically derived using the Ritter and Drake method [93, 328, 329]. This method is highly dependent of the range of pore sizes. In the following section, we propose a transformation of the Ritter and Drake method that produces an initial estimate of the pore-size distribution that is independent of the scale of the problem (range of pore sizes).

The Ritter and Drake method assumes that the cumulative volume of mercury intruded (mercury saturation S_{Hg}) is a probabilistic cumulative distribution function of the pore radius (r). There is an implicit one-to-one relationship between the cumulative volume of mercury intruded and the number of pores invaded.

The Ritter and Drake method is defined as

$$\widehat{f}(r) = -\frac{dS_{Hg}}{dr}, \tag{4.1}$$

where $\widehat{f}(r)$ is an estimator of $f(r)$, which is the pore-size distribution function, and

$$r = \frac{2\sigma\cos\vartheta_{Hga}}{P_{c,Hga}}, \tag{4.2}$$

where σ_{Hga}, ϑ_{Hga}, and $P_{c,Hga}$ are the mercury–air interfacial tension, contact angle, and capillary pressure, respectively.

The Young–Laplace equation (Eq. (4.2)) includes the MICP, giving the estimator of the pore-size distribution

$$\widehat{f}(r) = \frac{P_{c,Hga}^2}{2\sigma_{Hga}\cos\vartheta_{Hga}}\frac{dS_{Hg}}{dP_{c,Hga}}. \tag{4.3}$$

The classical Ritter and Drake method is still used as the main source of prior information to characterise the porous media in indirect methods of pore-network model parameter estimation. This is one of the simplest models for porous media. However, the relationships between the Ritter and Drake method and other measurements of the pore-size distribution are not clear. These other measurements include the relaxation time in nuclear magnetic resonance, measurements from petrographic image analysis, gas adsorption and the volumetric form of the pore-size distribution [23, 195–198].

The problem with models like Eq. (4.3) is that they are scale dependent. For the sake of argument, consider using Eq. (4.3) with the MICP measured in two porous media with exactly the same characteristics (same average coordination number, same pore-volume to pore-size relationship) but two logarithmic uniform distributions of different pore-size ranges. This will result in completely different pore-size distribution estimators ($\widehat{f}(r)$). As the maximum MICP increases, the pressure square factor heavily skews the distribution towards the right, even though the intrusion sequences in both porous media are the same.

Estimating the pore-size distribution from mercury percolation underestimates the number of large pores, because accessible pores are invaded first and mercury continues invading small pores that shield some of the large pores. There are at least two possible underlying

microstructures that produce very similar mercury intrusion-based pore-size distributions.

(1) The first possibility is that the underlying pore-size distribution is nonuniform with a peak at the pore size r_{pt}. As mercury invades the porous media, some pores larger than r_{pt} are invaded. When the process starts invading pores of size r_{pt}, there are some larger pores that are shielded by pores of size r_{pt}. These pores are spontaneously invaded. Therefore, the volume of the shielded large pores will be assigned to r_{pt}, increasing the frequency of this peak relative to the true underlying frequency of the pores of size r_{pt}.

(2) The second possibility is that the pore-size distribution is uniform. In this case, the pore-size distribution frequency will also peak at the pore size of the percolation threshold. Similarly, the volume of the shielded large pores will be assigned to the percolation threshold pore size, which coincides with the peak in the pore-size distribution function.

4.2.1 Transformation of the MICP

No complete agreement on Eq. (4.3) remains. Some studies have put forward arguments in favour of choosing the logarithmic derivative $dS_{Hg}/d(\log dP_{c,Hga}) = P_{c,Hga}dS_{Hg}/dP$ to give [214]

$$\widehat{f}(r) \propto P_{c,Hga}\frac{dS_{Hg}}{dP_{c,Hga}}. \tag{4.4}$$

Note that we can integrate Eq. (4.3) to give dimensionless units in agreement with probability units, which is not true for Eq. (4.4).

To make the estimator independent of the absolute pressure level, we propose the logarithmic transformation

$$P^*_{c,Hga} = \log\frac{P_{cHga}}{P_{ref}} \qquad (P_{ref} = 1[Pa]), \tag{4.5}$$

which gives the scale-independent probability density function (PDF) estimator [354]

$$\widehat{f}(r) = \frac{P_{ref}(P^*)^2_{c,Hga}}{2\sigma\cos\vartheta_{Hga}}\frac{dS_{Hg}}{dP^*{}_{c,Hga}}. \tag{4.6}$$

A general conceptualisation of the scale invariant prior information has been explained in detail in [173], and it has been fully applied to seismic inversion [371]. There are also heuristic arguments about the benefits of the log transformation [149].

4.2.2 Approximation of the Pore-Size Distribution

For numerical applications, the typical approach is to choose a parametric PDF to approximate the pore-size distribution estimator and tune the parameters to fit the MICP assuming an unknown functional form of the pore-size distribution. In this work, we propose a weak constraint on the functional form and a parameterisation that can produce different functional forms to avoid hindering the stochastic inversion algorithm. A robust statistical approach is to use nonparametric methods [16, 135, 155, 226, 355].

We use the histogram as the nonparametric estimator of the PDF. The optimisation algorithm samples the posterior distribution of the bin probabilities given the MICP data to give a distribution of bin probabilities. This type of distribution is known in the statistical domain as a Dirichlet process [109]. A Dirichlet process has no restriction on the width of the bins, meaning that the class boundaries can be freely defined [16]. Any Dirichlet process, regardless of the number of bins, follows a discrete treatment of the bin probabilities [45, 109] (i.e., $\sum_{i=1}^{n} \widehat{f_i} = 1$).

We apply Eq. (4.6) to real MICP data using a finite difference approximation for the derivative $(S_{Hg_{i+1}} - S_{Hg_{i-1}})/({P^*}_{c,Hga_{i+1}} - {P^*}_{c,Hga_{i-1}})$. This generates an ensemble of frequencies, namely, the histogram $\mathscr{F}_{\mathscr{A}} = \left\{\widehat{f_1}, \widehat{f_2}, \ldots, \widehat{f_k}, \ldots, \widehat{f_N}\right\}$ with a set of events $\mathscr{A} = \{A_1, A_2, \ldots, A_N\}$, where $A_i = \{r : r_i < r \leq r_{i+1}\}$. The next section presents the parameterisation of this histogram.

4.2.3 Pore-Size Distribution Parameterisation by Information Theory

Normal MICP data has 70 to 100 values. Therefore, Eq. (4.6) usually gives a set ($\mathscr{A}$) of a large number of bins (A_i). We aim to reduce the number of bins while maximising the information. We propose to parameterise the pore-size distribution with the bin probabilities so that each bin width accounts for the same amount of information.

The entropy of an event A_i with some probability of occurrence $\mathrm{P}(A_i) = p_i$ is given by

$$h(p_i) = \log \frac{1}{p_i}. \tag{4.7}$$

The entropy of a set of events in $\mathscr{A} = \{A_1, A_2, \ldots, A_N\}$ with frequencies in $\mathscr{P} = \{p_1, p_2, \ldots, p_N\}$ is given by

$$H(\mathscr{P}) = \sum_{i=1}^{N} p_i \log \frac{1}{p_i}, \tag{4.8}$$

Equation (4.8) is known as Shannon's theorem [350]. The entropy is usually interpreted

as a measure of information. For example, if event A_i has a very small probability of occurring ($P(A_i)$), then occurrence of event A_i is unusual, and it is difficult to detect and quantify its impact. However, if $P(A_i)$ is large, that is, A_i is a probable event, then it is anticipated that event A_i will occur.

The new parameterisation $\mathscr{A}^*$ has a set of events $\mathscr{A}^* = \{A_1^*, A_2^*, \ldots, A_n^*\}$, where $n << N$ and $\widehat{f}_i^* = \left\{r : r_i^* < r \leq r_{i+1}^*\right\}$ with $\mathscr{F}_{\mathscr{A}^*}^* = \left\{\widehat{f}_1^*, \widehat{f}_2^*, \ldots, \widehat{f}_k^*, \ldots, \widehat{f}_n^*\right\}$. This parameterisation adds entropy to the initial estimator ($\widehat{f}(r_j)$). The difference can be calculated by the Kullback–Leibler distance (KLD):

$$\text{KLD} = \sum_{i=1}^{N} \widehat{f}(r_j) \log \frac{\widehat{f}(r_j)}{\widehat{f}^*(r_j)}, \tag{4.9}$$

which is also known as the relative entropy or the distance between two probabilistic distribution functions. This new parameterisation $T(\mathscr{A}) \longrightarrow \mathscr{A}^*$ groups the bins (bin widths) in the original set ($\mathscr{A}$) so that the bin probabilities in $\mathscr{A}^*$ are equal, with each bin having the same entropy or the same information. This maximises the entropy of the set $H(\mathscr{A}^*)$ (Eq. (4.8)). Replacing the original set $\mathscr{A}$ by $\mathscr{A}^*$ results in an increase of entropy (i.e., $H(\mathscr{P}^*) > H(\mathscr{P})$).

Sampling the transformed pore-size distribution estimator ($\widehat{f}^*$) generates a sequence of values represented by the random sample of size $Y_j (j = 1, 2, \ldots, m)$. This random sample is sorted in the initial binning ($\mathscr{A}$), giving $\mathscr{F}_{h\mathscr{A}} = \left\{\widehat{f}_{h1}, \widehat{f}_{h2}, \ldots, \widehat{f}_{hk}, \ldots, \widehat{f}_{hN}\right\}$. We can use Jensen's inequality [18, 200] to prove that KLD≥ 0, where the equality holds only when $\widehat{f} = \widehat{f}^*$. This demonstrates that the proposed parameterisation increases the entropy.

Because mercury capillary pressure is normally used to derive pore size rather than pore shape pore, shapes in carbonates do not affect the parameterisation.

4.2.4 Sampling the Histogram - Stratified Sampling

Sampling from the nonparametric pore-size distribution, $\mathscr{F}_{\mathscr{A}^*}^*$, is carried out on two strata [189]. Stratification ensures that a number of observations from each stratum end up in the sample, rather than allowing distribution of samples across strata to be random. The sample is less variable, and so gives more stability. This is important because we used small networks (9x9x9) for the inversion to speed up the calculations. Simple random sampling has greater variability in small network therefore the inversion algorithm will be more affected by random noise from taking different seeds. The synthetic data was generated in large network (20x20x20) and we recovered the true pore-network model parameters performing

the HMC inversion in a small network.

On the top level it samples $\mathscr{F}^*_{\mathscr{A}^*}$ by the inverse sampling method as follows:

$$\widehat{f}(r) = \sum_{i=1}^{n} \widehat{f}_i^* \; y(r), \tag{4.10}$$

$$\mathscr{P}^*(r) = \sum_{i=1}^{n} \widehat{f}_i^* = 1, \tag{4.11}$$

$$\mathscr{P}^{*-1}(y) = \{(r_-, r_+) \; : \; r_-, r_+ \in \quad \mathscr{A}^*\}, \tag{4.12}$$

which uses a realisation of a uniform distributed random variable y in the interval $\mathscr{U}(0,1)$ to move to the sampling at the next level:

$$\mathscr{P}^*(r_-) < y \leq \mathscr{P}^*(r_+). \tag{4.13}$$

The second stratum of sampling focuses on the interval (r_-, r_+). It is important to choose a function in the second stratum that correctly represents the state of knowledge of the variable that is going to be sampled. The stratified sampling in the second stratum continues by generating another random number x from $\mathscr{U}(0,1)$. We then use the inverse sampling method to obtain a realisation of the random variable radius (r):

$$y = F(x) = \frac{1}{\ln(r_{max}/r_{min})} \int_{\ln r_{min}}^{\ln r} \frac{1}{x} dx, \tag{4.14}$$

$$\ln(r) = F^{-1}(y) = \ln(r_{min}) + x \ln\left(\frac{r_{max}}{r_{min}}\right), \tag{4.15}$$

$$r = \exp\left(\ln(r_{min}) + x \ln\left(\frac{r_{max}}{r_{min}}\right)\right). \tag{4.16}$$

4.3 Methods: Parameter Estimation Problem with Limited Information

The solution space contains all of the possible combinations of the parameters and their associated misfit with the observations (hereafter referred to as the energy). As the dimension of the problem increases, the region of the solution space that contributes the most to statistical solution to the inverse problem concentrates in a small hypervolume [127, 330, 334]. This problem is called the curse of dimensionality, and makes it difficult to sample the so-

lution space.

When the gaussian assumptions do not hold, the posterior distribution of model parameters given the observables has multiple local minima and therefore the methods discussed in Chapter 2 cannot find the global minimum. The initial conditions strongly affect the estimates of the pore-network model parameters [378].

4.3.1 Hamiltonian Monte Carlo

When the information is incomplete, multiple sets of parameters are possible for a given set of data. In this context, probability theory can be applied to pore-network model parameter estimation to quantify the several local minima. Fundamentally, this means that there are degrees of incomplete information that lead to different numbers of solutions that agree with the information at hand. The problem of determining the network model parameters can be formulated as

$$G(\boldsymbol{\theta}) = \boldsymbol{X}, \tag{4.17}$$

where $\boldsymbol{\theta}$ is the vector of model parameters (pore-network model parameters) and $\boldsymbol{X}$ is the vector of observables (capillary pressure at a given saturation). G represents the forward problem, and contains a numerical description of the mathematical model that describes the real physical system. G is the implicit function that represents the pore-network model simulator (nonlinear operator), which does not have a mathematical closed form.

The statistical solution to the inverse problem (SSIP) is the posterior distribution $\pi(\boldsymbol{\theta}|\boldsymbol{X})$ over the space of all possible solutions constrained to observables $\boldsymbol{X}$, in which each point in the solution space is a model $\boldsymbol{\theta}_j$ with model parameters as entries in $\boldsymbol{\theta}$. Each model has probability $\pi(\boldsymbol{\theta}_j|\boldsymbol{X})$, which indicates how likely it is that it will predict the observables $\boldsymbol{X}$ in Eq. (4.17). The SSIP is the posterior distribution of the model parameters. An explicit formulation of $\pi(\boldsymbol{\theta}|\boldsymbol{X})$ is rarely achievable, although alternative sampling methods can solve these problems.

In the approach proposed in this work, the SSIP follows Gibbs's methodology, in which the network model parameters are analogous to the molecule positions in Gibbs's inference problem. In particle physics, it is convenient to transform the Lagrangian formulation of the equations of motion to the Hamiltonian formulation, because it simplifies the system of equations to a first-order system [128]. The Hamiltonian formulation introduces the conjugate momentum ($\boldsymbol{p}$), leading to two desirable properties: the Hamiltonian is invariant under motion or the first integral [134] and the isolines of the constant Hamiltonian have a

periodic topology, which reduces the number of samples required to derive reliable posterior distributions.

Markov Chain Monte Carlo methods based on the Metropolis random walk algorithm are sensitive to large changes in the model parameters. The chain slowly explores the solution space making it difficult to capture the variability.

In the approach proposed in this work, the trajectory exploring the space defined by the momentum and positions (augmented space known as the phase space) follows Hamiltonian dynamics, which theoretically means that the acceptance probability of the proposed state is one because of Hamiltonian conservation. Thus, the algorithm can travel long deterministic distances and better capture the variability and generate a final state that is theoretically certain to be accepted. In real applications, there are numerical integration errors that reduce the acceptance probability.

Since the pioneering work of Duane and Kogut [95],who applied Hamiltonian Monte Carlo to quantum chromodynamics the use of HMC was limited to a few cases [5, 64, 94, 132, 136, 140, 154, 170, 194, 287, 373]. Lately, HMC has gained much attention [9, 62, 175, 204, 268, 271, 288, 303] in parameter estimation problems.

The SSIP in statistical physics relates molecular microstates to thermodynamic macroscopic quantities [171, 172, 174]. The distribution of molecule locations (molecular configuration) in light of some macroscopic observables $\pi(\boldsymbol{\theta}|\boldsymbol{X})$ follows an exponential distribution of the energy (misfit between the forward problem and the observations) $E(\boldsymbol{\theta})$ associated with the configuration $\boldsymbol{\theta}$.

The pore-network model simulator is an implicit operator, G Eq. 4.19, that takes parameters $\boldsymbol{\theta}$ and outputs capillary pressure as function of saturation $\boldsymbol{X}$ Eq. 4.18.

$$\mathbf{X} = P^{sim}_{c,\alpha\beta} = \left\{P^{sim}_{c,Hga}, P^{sim}_{c,ow_{Dra}}, P^{sim}_{c,ow_{Imb}}\right\} \tag{4.18}$$

where $\alpha = Hg, oil$ and $\beta = air, water$ respectively for each experiment eg mercury intrusion, oil-flooding and water-flooding.

$$G(\boldsymbol{\theta}) = \boldsymbol{X}, \tag{4.19}$$

There are many measures of discrepancy of the forward model to the observed data. It is important to define the misfit function in relation to the problem at hand. In this study, from the data (Chapter 3) we can expect that pore-size distributions of our carbonate samples vary over many orders of magnitude then the capillary pressure will also vary many orders of magnitude. Therefore, we define the misfit of the pore-network model output (capillary

pressure for a given flooding cycle, eg mercury intrusion, oil-flooding, water-flooding) to the observed capillary pressure data as defined in Eq. 4.20.

The likelihood model is defined in terms of the misfit. There are more complex non-gaussian likelihood models [68, 161]. However, the choice of one particular model becomes based on some empirical tests [161]. We have found that Eq. 4.20 works very well in our problem as shown by the validation using the synthetic case in Chapter 6. Also, a similar definition of the misfit has been used in other pore network studies [251].

$$E(\boldsymbol{\theta}) = \text{Misfit} = \sum_{i}^{N_{obs}} \left(sgn(P^{obs}_{c,\alpha\beta}) log(\left| P^{obs}_{c,\alpha\beta} \right|) - sgn(P^{sim}_{c,\alpha\beta}) log(\left| P^{sim}_{c,\alpha\beta} \right| \right)^2 \tag{4.20}$$

We sample the Gibbs canonical distribution (Eq. (4.21)) using the Markov Chain method [267] with transition probability (Eq. (4.22)).

$$\pi(\boldsymbol{\theta}|\boldsymbol{X}) = \frac{\exp\left(\frac{-E(\boldsymbol{\theta})}{\beta}\right)}{\int \exp\left(\frac{-E(\boldsymbol{\theta})}{\beta}\right) d\boldsymbol{\theta}} \tag{4.21}$$

$$P_{Acc}(\boldsymbol{\theta}^{'}|\boldsymbol{\theta}^{t}) = T(\boldsymbol{\theta}^{'} \leftarrow \boldsymbol{\theta}^{t}) = min\left(1, \frac{\pi(\boldsymbol{\theta}^{t}|\boldsymbol{X})}{\pi(\boldsymbol{\theta}^{'}|\boldsymbol{X})}\right) \tag{4.22}$$

where t indicates the current time (current state along the Markov Chain) and P_{Acc} is the probability of accepting the proposed sample ($\boldsymbol{\theta}^{'}$). Equation (4.22) is used in the Metropolis algorithm, and it is the ratio of two unknown probabilities. Thus, the denominator in Eq. (4.21) (called the partition factor) cancels out in Eq. (4.22), which means that the Markov Chain method explores the Gibbs distribution without knowing the full target probability density (Eq. (4.21)). Assuming that the solution to the inverse problem uses the Gibbs equation, which is a mild assumption, Eq. (4.22) then becomes

$$P_{Acc}(\boldsymbol{\theta}^{'}) = \min\left(1,\ \exp\left(-(E(\boldsymbol{\theta}^{'}) - E(\boldsymbol{\theta}^{t}))/\beta\right)\right). \tag{4.23}$$

Equation (4.23) is called the acceptance rule. It is a key step in the algorithm because it ensures the detailed balance, which means that the Markov Chain will converge to the posterior distribution.

Equation (4.23) contains the energy difference as an explicit term. If the Markov Chain is initialized at $\boldsymbol{\theta}^{t_0}$ or is $\boldsymbol{\theta}^{t}$ at a given time, large changes in the model parameters ($\boldsymbol{\theta}^{'}$) result in large changes in the energy ($E(\boldsymbol{\theta}^{'})$). It follows that the acceptance probability is sensitive

to large energy changes. Thus, the chain slowly explores the solution space.

The Hamiltonian formulation is given by

$$\frac{d\boldsymbol{p}}{d\tau} = -\frac{\partial \mathscr{H}}{\partial \boldsymbol{\theta}}, \tag{4.24a}$$

$$\frac{d\boldsymbol{\theta}}{d\tau} = \frac{\partial \mathscr{H}}{\partial \boldsymbol{p}}, \tag{4.24b}$$

$$-\frac{\partial \mathscr{L}}{\partial \tau} = -\frac{\partial \mathscr{H}}{\partial \tau}. \tag{4.24c}$$

where $\mathscr{H}$ is the Hamiltonian and $\mathscr{L}$ is the Lagrangian. In the Hamiltonian formulation, the kinetic energy ($K(\boldsymbol{p})$) only depends on $\boldsymbol{p}$, and $E(\boldsymbol{\theta})$ only depends on $\boldsymbol{\theta}$ [128], that is,

$$\mathscr{H} = K(\boldsymbol{p}) + E(\boldsymbol{\theta}). \tag{4.25}$$

The system evolves along trajectories of constant $\mathscr{H}$, which are invariant under the movement. For a system of many-body particles, these equations are integrated with respect to time, moving the particles from an initial to a final spatial position. This is known as the molecular dynamics step. Duane [96] introduced the pseudo-time τ discretised in time steps $\Delta\tau$:

$$\tau_{n+1} = \tau_n + \Delta\tau, \tag{4.26}$$

which makes deterministic movements of the parameters in the solution space. At the end of a molecular dynamics step, the system has travelled to a new phase space coordinate $(\boldsymbol{\theta}', \boldsymbol{p}')$ that conserves $\mathscr{H}$. Therefore, the new sample comes from a joint distribution of the energy and the momentum.

The molecular dynamics step is unable to visit all possible energy states. K exchanges energy with E, because $\mathscr{H}$ is constant along the trajectory. However, this energy exchange does not ensure that all possible energy states $E(\boldsymbol{\theta})$ are visited by the molecular dynamics steps. To satisfy the ergodicity condition, we must perturbate $\mathscr{H}$. The distribution should be independent of the particles' spatial positions. A multivariate normal distribution (white noise) with a mean of zero and an identity covariance matrix satisfies these requirements.

This means that, in the long run, the Markov Chain will converge to the joint distribution. Therefore, the SSIP takes on the joint posterior distribution.

$$\pi(\boldsymbol{\theta}|\boldsymbol{X})\mathscr{N}(0,\mathscr{I}) \propto \exp\left(\frac{-E(\boldsymbol{\theta})}{\beta}\right)\exp\left(\frac{-\boldsymbol{p}\boldsymbol{p}^T}{\beta}\right). \tag{4.27}$$

The full process for generating a new candidate $\boldsymbol{\theta}^{'}$ is to draw an initial momentum vector from the multivariate normal distribution

$$\boldsymbol{p} \leftarrow \mathcal{N}(0, \mathcal{I}), \tag{4.28}$$

and then

$$\mathcal{H} = \boldsymbol{p}^T \boldsymbol{p} + E(\boldsymbol{\theta}^t). \tag{4.29}$$

The second-order leapfrog or Stormer–Verlet method [212, 281, 340] is a symplectic integration scheme for calculating the numerical approximation of the ordinary system of differential equations. This integration scheme moves the system forward in time and solves Eq. (4.24) for the period of time $T = n_{steps}\Delta\tau$. The following equations are developed for one parameter, but they can be generalized for multiple parameters. The algorithm consists of an initial half-step for the momentum variable

$$p\left(\frac{\delta\tau}{2}\right) = p(\tau_0) - \frac{\delta\tau}{2}\left(\frac{dE}{d\theta}\right)_{\tau_0}. \tag{4.30}$$

Followed by full steps (n_{steps})

$$\theta(\tau + \delta\tau) = \theta(\tau) + \delta\tau \cdot p\left(\tau + \frac{\delta\tau}{2}\right), \tag{4.31}$$

$$p(\tau + \delta\tau) = p\left(\tau + \frac{\delta\tau}{2}\right) - \frac{\delta\tau}{2}\left(\frac{dE}{d\theta}\right)_{\tau_\tau}. \tag{4.32}$$

Finally, to ensure that both variables finish at the same total time ($T = n_{steps}\Delta\tau$), there is a half-step for the momentum variable

$$p\left(\frac{\delta\tau}{2}\right) = p(\tau_0) - \frac{\delta\tau}{2}\left(\frac{dE}{d\theta}\right)_{T}. \tag{4.33}$$

Integrating Hamilton's equations into each molecular dynamics step defines a trajectory in the phase space $(\boldsymbol{\theta}(\tau), \boldsymbol{p(\tau)})$, which conserves $\mathcal{H}$. Therefore, the trajectory starts at $(\boldsymbol{\theta}(\tau_0), \boldsymbol{p(\tau_0)})$ and finishes at $(\boldsymbol{\theta}(T), \boldsymbol{p(T)})$. The probability of accepting the new state,

$$P_{acc}((\boldsymbol{\theta}(\tau_0), \boldsymbol{p(\tau_0)}) \rightarrow (\boldsymbol{\theta}(T), \boldsymbol{p(T)})) = \min(1, \exp -\Delta\mathcal{H}), \tag{4.34}$$

is based on

$$\Delta\mathscr{H} = \mathscr{H}(\boldsymbol{\theta}^{'}, \boldsymbol{p}^{'}) - \mathscr{H}(\boldsymbol{\theta}^{t}, \boldsymbol{p}^{t}). \tag{4.35}$$

The Hamiltonian is invariant under the movement, which makes Eq. (4.34) theoretically equal to one. In this way, the algorithm is able to travel long deterministic distances, generating a final state that is theoretically certain to be accepted. The chain is reversible because the pseudo-time can take negative values.

There are a number of methods to obtain the gradient in Eq. (4.30). In this study the gradient is calculated using the Richardson extrapolation method [326]. We extrapolate the finite difference $\Delta E(\theta)/\Delta\theta$ to $\Delta\theta = 0$ where $\Delta\theta$ is an increment in a given parameter. The method calculates two approximations of the gradient using backward finite differences at two progressively smaller increments of a given parameter (eg. $\Delta\theta_i = \Delta\theta_1$ and $\Delta\theta_i = \Delta\theta_1/5$) . It is widely used in many applications, it is easy to implement and there are several modification to achieve higher accuracy [156]. However, the calculations can be affected by the local irregularities of the energy landscape. We mitigate this source of error by controlling the conservation of the Hamiltonian at the end of each leapfrog step. If the Hamiltonian is not conserved the gradient is recalculated with a higher accuracy. And in the case that gradient recalculations do not achieve Hamiltonian conservation, the chain is stopped and rejected. If the Hamiltonian is not conserved at each leapfrog step there is the risk that there is some compensations of errors between the steps that lead to final conservation of Hamiltonian, while trajectories may be incorrect.

There are other approaches which create an analytical proxy model or surface of response by using experimental design. These approaches accelerate the calculation. However, there is no guarantee of a one to one relationship between phase space mappings of the HMC trajectories and the true mappings. There is a more flexible approach that uses proxy model with kernels to control the degree of smoothing over the energy landscape [231].

There is another method, the so-called adjoint method, in which gradient equations and the forward problem are formulated together. The adjoint method is often used for macroscopic finite difference models of flow in porous media. A linear system can be formulated adjoining the gradients to the differential equations which define the forward problem. This system can be solved at a computational cost of the same order as performing a single forward simulation [290]. However, the method is difficult to formulate and implement [140].

We introduced above the solution space in which $E(\boldsymbol{\theta})$ is a function of $\boldsymbol{\theta}$. The probability distribution defined over this space is the SSIP. In the Hamiltonian formulation, $\mathscr{H}$ is a function of both $\boldsymbol{\theta}$ and $\boldsymbol{p}$. Therefore, $\mathscr{H}$ is a $2N$-dimensional (N is the number of param-

eters) set consisting of all possible combinations of $\boldsymbol{\theta}$ and $\boldsymbol{p}$ of the particles (parameters in the statistical context). The sampling in the phase space is more efficient than in the solution space. The majority of algorithms, such as the Metropolis algorithm, sample over the position space by "walking" on the energy landscape.

The Hamiltonian formulation samples in the phase space along Hamiltonian trajectories or contour lines, in which the jumps between "orbits" are independent of the energy. Chapter 6 discussed this aspect in more detail when considering the synthetic case. At the beginning of each sample generation, the momentum vector $\boldsymbol{p}$ is refreshed from the multivariate normal distribution (Eq. (4.28)). Therefore, the new trajectory generating the proposed sample, $\boldsymbol{\theta}^{'}$ has a new value of $\mathscr{H}$ given by Eq. (4.29). This is shown in Chapter 5 6 in two numerical example validating the method with analytic and synthetic data. Hamiltonian systems show phase space periodic cycles (orbits) that assist sampling because the periodicity repeats itself at different Hamiltonian levels and is independent of the energy (misfit).

As an example, consider an energy landscape with two valleys separated by a high energy barrier. The Metropolis algorithm has a very low probability (Eq. (4.23)) of overcoming the barrier. However, Hamilton dynamics occur in the augmented phase space, in which contour lines of a high Hamiltonian can readily connect the two energy valleys and effectively remove the energy barrier. In contrast to the Metropolis random walk algorithm, a high Hamiltonian is much more likely to occur, because the Hamiltonian is set at the beginning of each sample generation step (Eqs. (4.28) and (4.29)) and is independent of any probability.

4.4 Methods: Pore-Network Model

The pore-network model simulator is the operator G. A more in-depth discussion of the implementation of the pore-level displacement inside the network model simulator can be found in [391]. We modelled the porous medium using a three-dimensional cubic lattice network of interconnected capillary elements that represent the pores (bonds in the lattice). The lattice had dimensions N_x, N_y, and N_z. The capillary number was $< 1 \times 10^{-5}$, and under this condition it is reasonable to assume that fluid flow is quasistatic and takes place through small pressure changes, which controls the distribution of phases by the local entry conditions at the pore level (Jerauld and Salter [178] and the references therein). This was modelled by an invasion percolation process [405]. The capillary elements were cylinders of constant length and cross-section, with radius defined by the pore-size distribution. A

cylinder does not allow the explicit treatment of wetting films. However, thresholds in the contact angle within the pores determine the existence of wetting films. The physical features related to modelling the MICP are discussed in the following sections.

4.4.1 Volume–Size Relationship

The model parameter ν defines the relationship between the volume of a capillary element V and the inscribed radius r_j according to

$$V(r_m) \propto r_j^{\nu} \quad j = \{1,\ldots,M\}\, M = \text{ number of capillary elements}, \tag{4.36}$$

where M is the number of capillary elements. The power law is a convenient parameterisation because both fractal and Euclidean geometries can occur.

4.4.2 Connectivity

Lattice bonds (Fig 4.1) can be removed to produce an average coordination number ($\overline{Z}$). The local coordination number Z is defined as the number of bonds leaving each site.

4.4.3 Pore-Size Distribution

When a number of bonds are removed for a given average coordination number, radii are assigned to the bonds that remain open to flow according to Section 4.2.3.

4.4.4 Conductance

The modified Poiseuille Law that defines the conductance of each capillary element filled with phase α [3, 289] is given by

$$g_\alpha(r_j) = \frac{\hat{r}^{3-\lambda}\ \pi\ r_j^{\lambda}}{8\mu_\alpha} \quad j = \{1,\ldots,M\}\ M = \text{ number of capillary elements}. \tag{4.37}$$

where $\hat{r}$ is the average radius in the pore-size distribution, r_j is a given pore, λ is the conductance exponent and μ_α is the viscosity of phase α.

The phases are assumed to be incompressible, so at each node

$$\sum_{j}^{Z_k} = q_{ij}^{\alpha}. \tag{4.38}$$

There is a balance of the volumetric flow rate of phase α between the nodes ij for a given local coordination number (Z_j) at node j. The modified Poiseuille Law has been used in other studies [80, 82, 84, 85, 113, 261, 289, 320].

Determination of λ

One drawback of the previous works that used lattice pore-network models is that λ is determined from drainage relative permeabilities [87, 259, 260, 262, 368]. Therefore, the approaches of those studies are not entirely predictive. We propose to determine the conductance exponent from the Brooks–Corey (BC) pore-size distribution index

$$P_{c,Hga} = Pc_{c,Hga_{th}}(S^*)^{-1/\Lambda} \tag{4.39}$$

In Eq. (4.39), where $P_{c,Hga_{th}}$ is the entry pressure, S^* is the normalised saturation (Eq. (4.40)) and Λ is the pore-size distribution index

$$S^* = \frac{S_{air} - S_r}{1 - S_r} \tag{4.40}$$

in Eq. (4.40), S_{air} is the air saturation, S_r is the residual air saturation. This choice of conductance determination makes the proposed approach useful for prediction. Based on the relationship between the pore-size distribution index, the saturation and the conductance exponent en the BC model we proposed the the following relationship between the pore-size distribution index and pore conductance exponent as follows:

$$\lambda = \nu\,(3 + 2/\Lambda) \tag{4.41}$$

where ν is the volume exponent, which is determined by inverting the pore network structure Chapter 7 [185] ; Λ is determined by fitting the BC model to the MICP; and λ is the conductance exponent applied to each pore according to Eq. (4.37). In the Chapter 7, we show that the proposed method turned out to predict relative permeabilities fairly well [186].

Equation 4.41 is proposed in this work to estimate the conductance exponent in Eq. 4.37. Brooks and Corey established a power law relationship between saturation (volume)

and conductance using the pore-size distribution index derived from the mercury intrusion capillary pressure. In an analogous manner, we propose multiplying the volume exponent (because our pore network model assumes that the volume of a pore follows a power law relationship with the pore radius Eq. 4.36) by the pore-size distribution index from Brooks and Corey's model. This is based on the argument that pore conductance follows a power law or has an exponential relationship with the volume of the pore, as demonstrated in [159]. Similar arguments have been used in Schlueter et al. [346], Friedman and Seaton [122] and Moulu et al. [286].

4.4.5 Wettability Models

The term drainage refers to the first oil-flooding, and imbibition refers to the first water flooding.

Drainage (Oil Displacing Water)

Initially, the network is fully saturated with water, and oil is the displacing phase. Drainage is modelled using a fractional wet model that allows the fraction of two populations of pores (Population A and Population B) f_w to vary between a lower and an upper bound:

$$\boldsymbol{\theta} = \left\{ \vartheta_{ow_{MIN}}^{A-rec}, \vartheta_{ow_{MAX}}^{A-rec}, f_w, \vartheta_{ow_{MIN}}^{B-rec}, \vartheta_{ow_{MAX}}^{B-rec} \right\}, \tag{4.42}$$

$$\vartheta_{ow_n}^{rec} = \begin{cases} \left[\vartheta_{ow_{MIN}}^{A-rec}, \vartheta_{ow_{MAX}}^{A-rec}\right] & \text{if } n \text{ is in Population A} \\ \left[\vartheta_{ow_{MIN}}^{B-rec}, \vartheta_{ow_{MAX}}^{B-rec}\right] & \text{if } n \text{ is in Population B} \end{cases}$$

Imbibition (Water Displacing Oil After the First Oil Flooding)

After the first oil flooding, the rock is aged to attempt to restore the wettability present in the reservoir. This process is modelled using a mixed-wet (MW). For the MW, the additional parameter r_{wet} is introduced, which is the threshold radius in the pore-size distribution that separates two populations of pores with different wettabilities (Population A and Population B). This parameter can take values in the full range of pore sizes between the minimum and the maximum radii in the pore-size distribution. The wettability parameters are

$$\boldsymbol{\theta} = \left\{ \vartheta_{ow_{MIN}}^{A-adv}, \vartheta_{ow_{MAX}}^{A-adv}, r_{wet1}, \vartheta_{ow_{MIN}}^{B-adv}, \vartheta_{ow_{MAX}}^{B-adv} \right\} \tag{4.43}$$

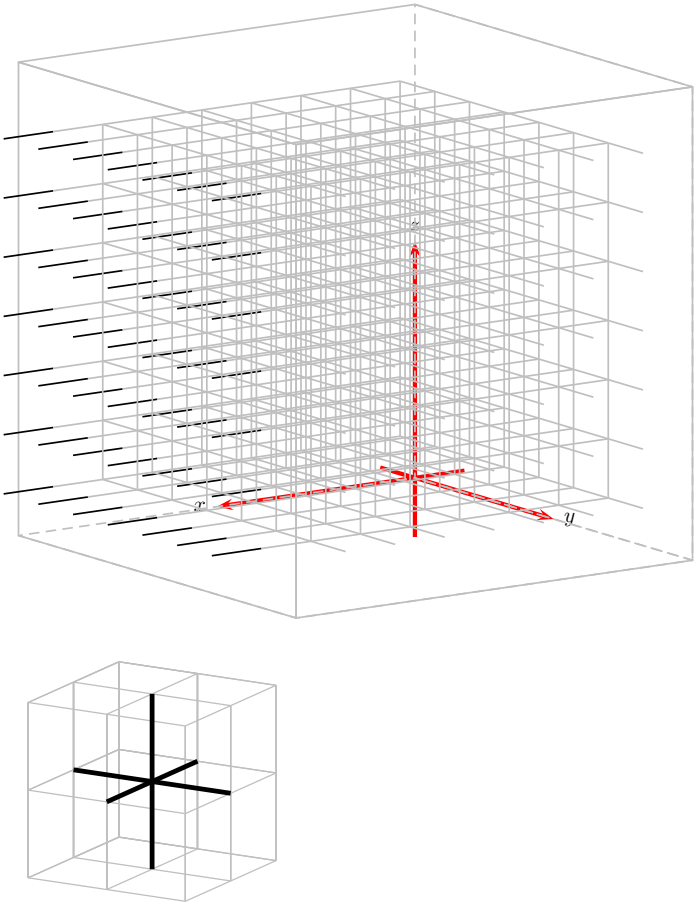

Fig. 4.1 The top figure shows the lattice network. The black pores offseting the cube represent the inlet pores. The bottom figure shows a typical junction in which the branch are cutted to vary the coordination number.

$$\vartheta_{ow_n}^{adv} = \begin{cases} \left[\vartheta_{ow_{MIN}}^{A-adv}, \vartheta_{ow_{MAX}}^{A-adv}\right] & \text{if } n \text{ is in Population A} \\ \left[\vartheta_{ow_{MIN}}^{B-adv}, \vartheta_{ow_{MAX}}^{B-adv}\right] & \text{if } n \text{ is in Population B} \end{cases}$$

Wetting Films

We define two contact angles ($\vartheta_{ow_{Th}}^{ww}$ and $\vartheta_{ow_{Th}}^{ow}$) that are threshold values for the existence of water-wetting and oil-wetting films, respectively. Thus, wetting films will exist in pores with contact angles satisfying one of the inequalities $\leq \vartheta_{ow_{Th}}^{ww}$ or $\geq \vartheta_{ow_{Th}}^{ow}$.

Chapter 5

HMC Benchmark

5.1 Introduction

This chapter is a numerical illustration showing the solution of a problem using the method proposed in Chapter 4 for a case in which the analytical multivariate posterior distribution is known. It also benchmarks the Hamiltonian Monte Carlo (HMC) against the classical Markov chain Monte Carlo (MCMC) method .

5.2 Hamiltonian Sampling Strategy

This section uses a simple numerical example to explain the HMC strategy to produce samples. The energy function is defined as

$$E(\theta) = \frac{\theta^2}{2\sigma^2}, \tag{5.1}$$

This is a single parameter (θ) problem and it is possible to visualise the two-dimensional (2D) phase space (θ, p). The conjugate momentum has a gaussian distribution with $\mu = 0$ and $\sigma^2 = 1$ (Eq. (5.2)).

$$p_i \leftarrow \mathcal{N}(0,1). \tag{5.2}$$

The momentum lacks physical meaning, although it has the important role of ensuring that all possible configurations of the system are attainable; i.e., ergodicity. This enables the system to jump from one orbit to another orbit with different values of the Hamiltonian.

The associated Hamiltonian has the form

$$\mathscr{H}(\theta, p) = E(\theta) + \frac{p_i^2}{2}. \tag{5.3}$$

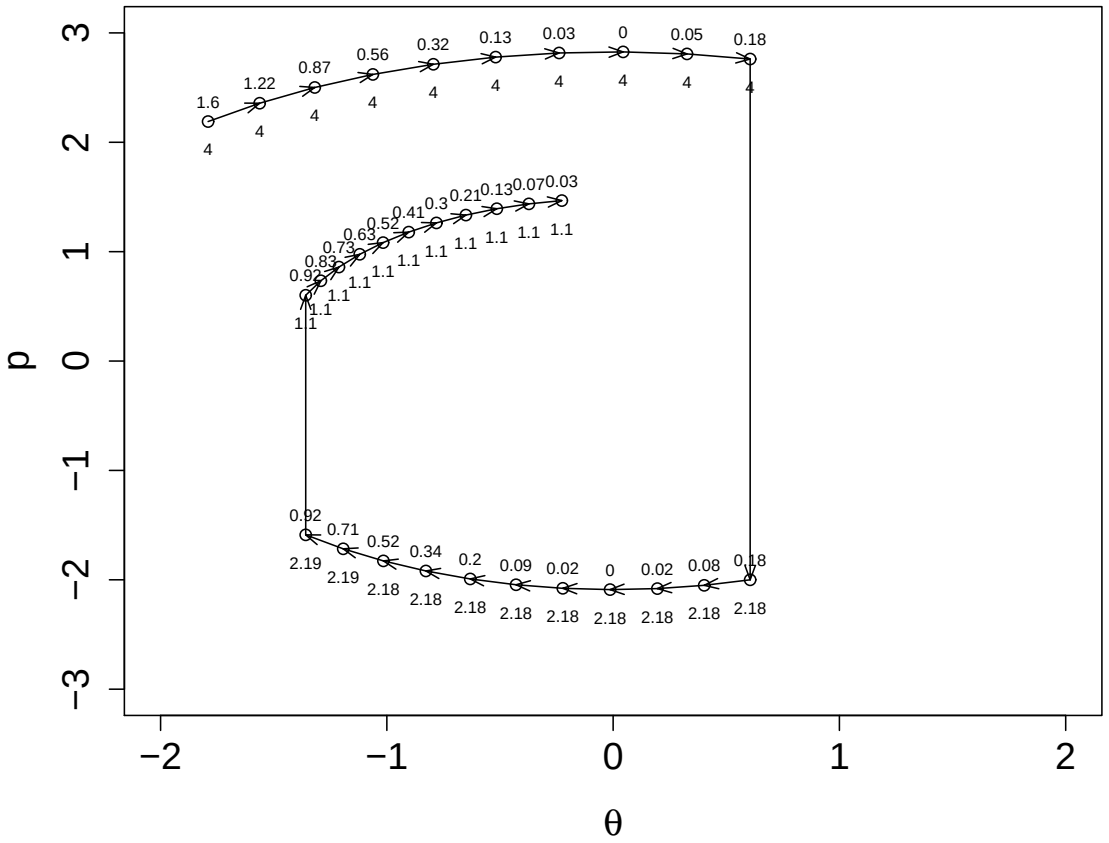

Fig. 5.1 Description of the dynamics in the phase space. The vertical axis is the momentum p and the horizontal axis is the parameter coordinate θ. The momentum coordinate augments the parameters/solution space constituting the phase space. The arrows on the curve indicate the trajectory followed by the particle, namely, parameter θ. Each trajectory tracks an orbit of constant total energy, namely, the Hamiltonian (labels below the arrows). The jumps are the momentum refreshment steps that allow different orbits to be visited. The labels on top of the arrows show the energy (misfit), which is related to the total energy by Eq. (5.3).

To advance the parameter in phase space, the algorithm solves the differential equations (Eq. 4.24). Figure 5.1 shows a single trajectory. The parameter starts at an initial position in the phase space (θ_j, p_j) and integration of Hamilton's equations define the trajectory of

the fixed Hamiltonian. The numbers on the graph indicate the value of the Hamiltonian (Eq. (5.3)) and the energy (Eq. (5.1)).

The momentum refreshment step (update) takes place at the beginning of a new trajectory and gives a new value for $p_i \leftarrow \mathcal{N}(0,1)$. This step changes the value of the Hamiltonian (Eq. (5.3)), which takes the integration of Hamilton's equations to a different orbit. Figure 5.2 shows how the sampling proceeds in different orbits.

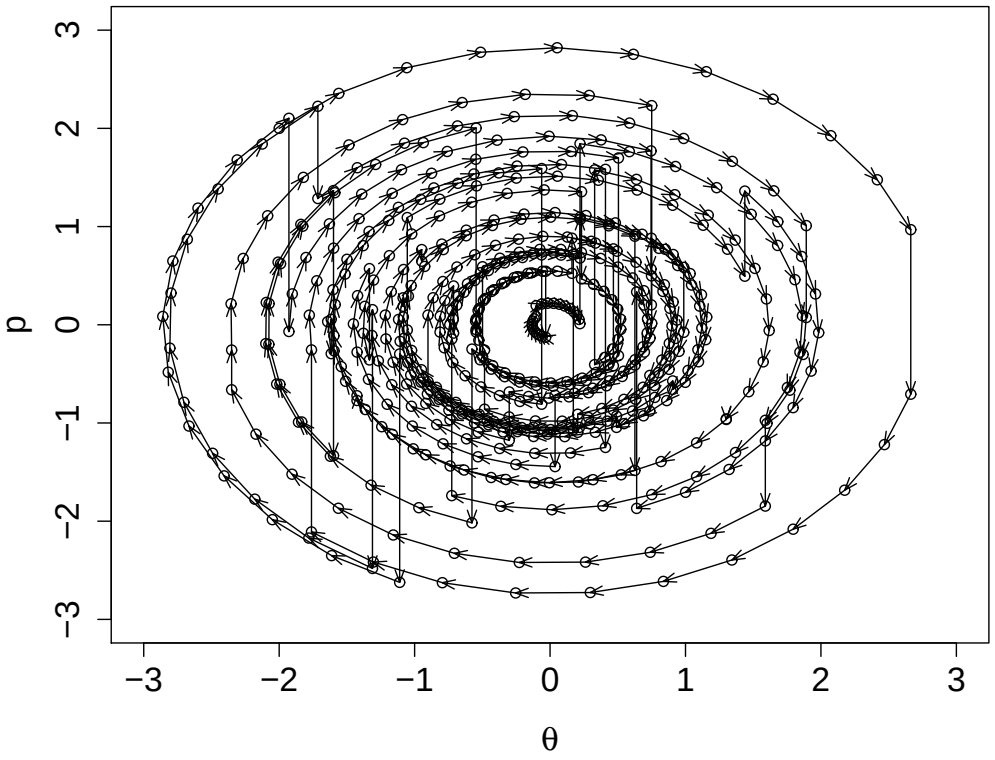

Fig. 5.2 Dynamics of the exploration of the phase space. Superposition of various orbits that sample the phase space gives the solution to the inverse problem. The forward model produces the energy. The ensemble of all of the trajectories is the solution to the inverse problem. The individual trajectories are not particularly meaningful.

5.3 Analytical Case A

The energy function is defined as

$$E(\theta_1,\theta_2) = 12.6265\ \theta_1^2 - 24.747\ \theta_1\theta_2 + 12.6265\ \theta_2^2. \tag{5.4}$$

with two parameters θ_1,θ_2. The associated Hamiltonian takes the following form

$$\mathscr{H}(\boldsymbol{\theta},\boldsymbol{p}) = E(\boldsymbol{\theta}) + \frac{\boldsymbol{p}^2}{2}. \tag{5.5}$$

The momentum vector at the beginning of each trajectory is drawn from the normal gaussian distribution for each element:

$$p_1 \leftarrow \mathscr{N}(0,1), \tag{5.6a}$$
$$p_2 \leftarrow \mathscr{N}(0,1). \tag{5.6b}$$

The HMC algorithm has two parameters: the time-step size (Eq. (4.26))

$$\tau_{n+1} = \tau_n + \Delta\tau \tag{5.7}$$

and the number of time steps in Eq. (4.31). Both quantities determine how much of the phase space is explored by the trajectory.

The step size depends on the system under consideration, and will be limited by the reasonable numerical stability of the Hamiltonian along the trajectory, which will affect the acceptance rate defined by the Metropolis rule (Eq. (4.34)).

The time discretisation of Hamilton's equations using the leapfrog algorithm moves the system forward a number of time steps along the trajectory in the phase space ($T = n_{steps}\Delta\tau$). When the step size is significant for the conditions of the system under investigation, the Hamiltonian will not be conserved within a tolerance, and it will increase and the trajectory will be rejected. However, it is desirable to take the largest possible time step.

An exploration run can give insight into the time-step size and the number of time steps. For example, we can take different values for the time step from $\mathscr{U}(0,2)$ and different number of time steps for each molecular dynamics step from $\mathscr{U}(1,14)$ and monitor the numerical stability of the Hamiltonian, which ultimately affects the acceptance rate.

Figure 5.3 shows the relationship between the time step (ts) and the number of time steps (# of ts). For the samples generated, the blue circles are the rejected samples based

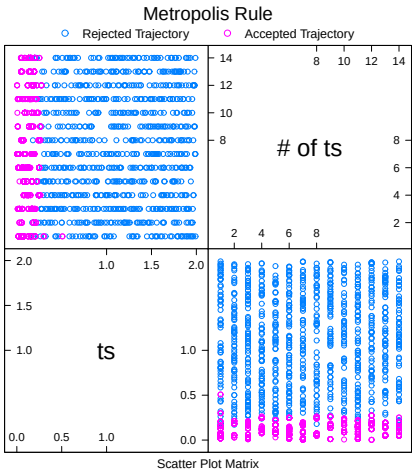

Fig. 5.3 Two scatterplots of the time-step size against the number of time steps for the exploratory run. The pink dots indicate the accepted trajectories based on the Metropolis rule (Eq. (4.34)). The blue dots are the rejected trajectories. The picture shows that there is a maximum time step above which the time integration of the equation does not conserve the Hamiltonian.

on the Metropolis rule evaluated at the end of the trajectory (Eq. (4.34)). Figure 5.3 shows that there is a limiting maximum time step ($\sim$0.3) that is independent of the number of time steps.

Figure 5.4 shows the percentage of accepted samples for different time steps and number of time steps. The number of time steps is given above each histogram. Taking the largest number of time steps will allow better exploration of the phase space and less correlation between successive samples in the Markov chain because two consecutive samples are further apart. For the case of 14 time steps (top right histogram), the maximum feasible time-step size seems to be in the range 0.15–0.2.

5.3.1 Autocorrelation

It is reasonable to compare the HMC method with the classical MCMC method based on the same computing time rather than the same number of samples. Figure 5.5 shows histograms for both parameters (θ_1 and θ_2) for HMC and classical MCMC. HMC and classical MCMC are both close to the true probability density function (black line). For the same computing time, the two methods generate a different total number of samples. This is reflected in the number of bins in the histograms, which follows Scott's rule [348] or the averaged shifted histogram rule.

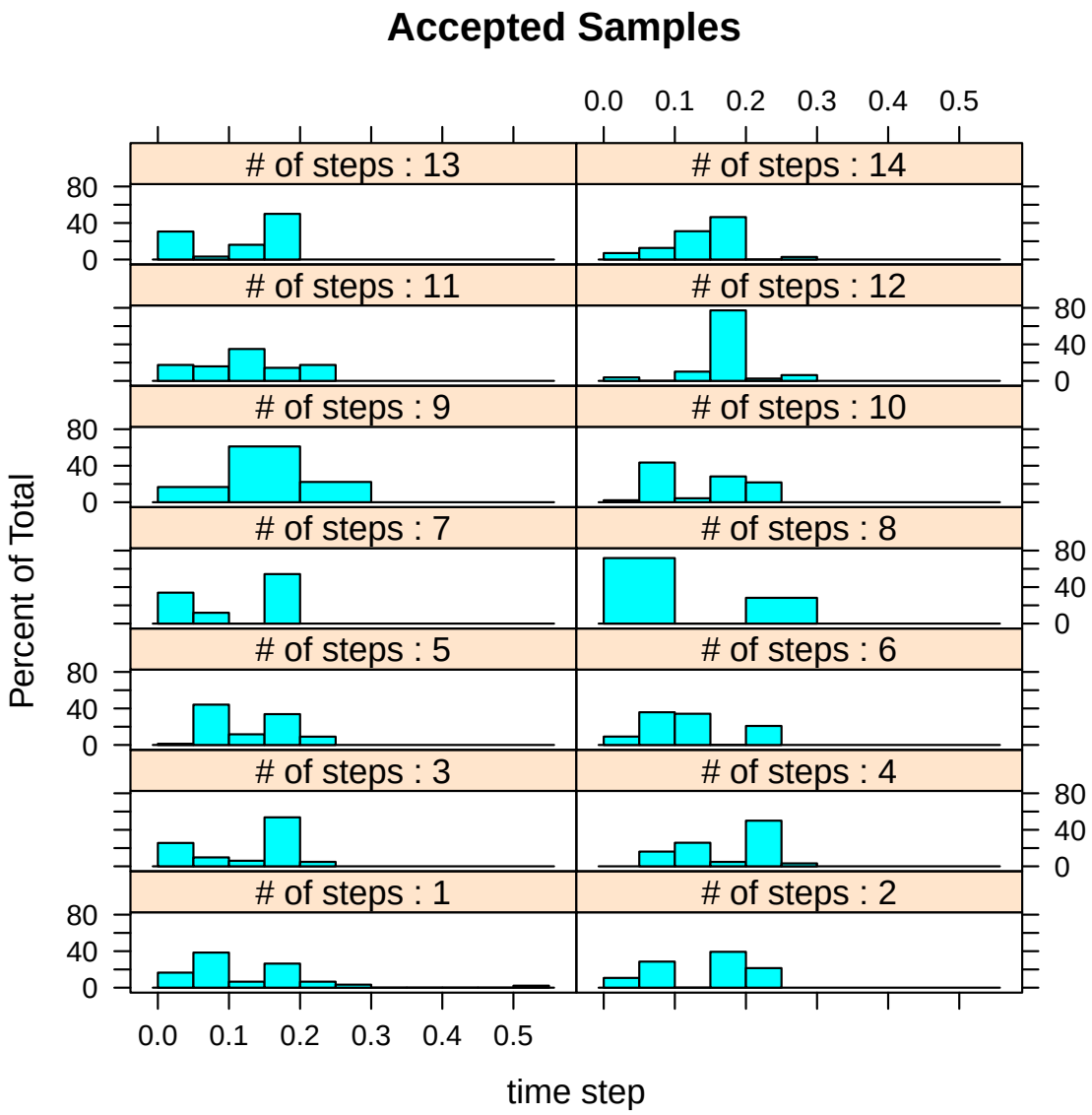

Fig. 5.4 Histograms of the accepted trajectories in the exploratory run (Fig. 5.3) for different time steps and different number of time steps. The Hamiltonian integration depends only on the time-step size and not on the number of time steps.

The optimal sampling performance for the classical MCMC acceptance rate should be around 0.23 to 0.27, which means that $\sim$75% of the samples are rejected. The chain progresses through small steps, and thus shows highly correlated behaviour.

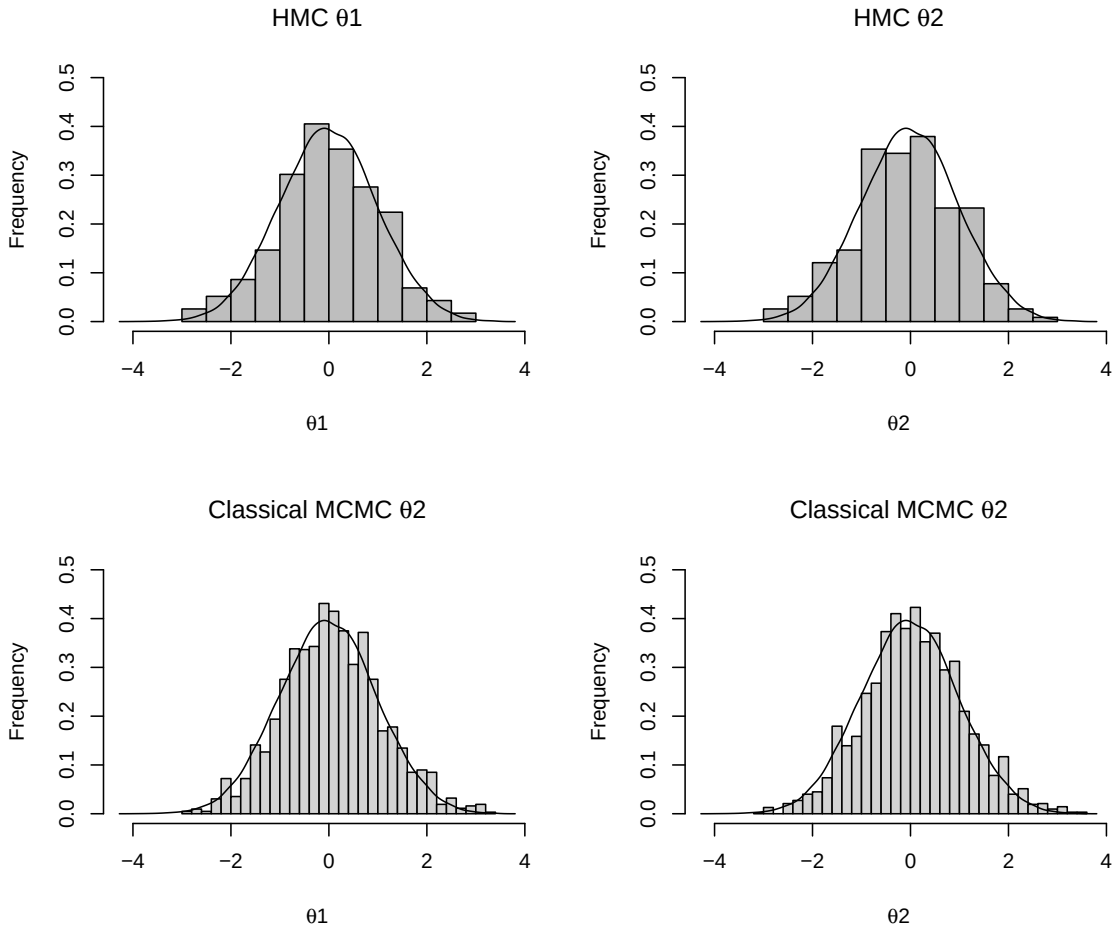

Fig. 5.5 Set of model parameter posterior distributions as a solution to the inverse problem. The top row of histograms shows the HMC solution. The bottom row shows the classical MCMC solution. The superimposed solid lines are the analytical solutions. The coarseness of the histograms is related to the number of samples generated by HMC and MCMC. HMC produces statistically equivalent results to MCMC with a smaller number of samples.

Successive states along the Markov chain are correlated. Therefore, a much larger numbers of samples are required compared with an uncorrelated sampler that draws independent identically distributed samples from a distribution.

The dependency between successive values of $\theta_i^{(t)}$ for different lags l of the chain is

measured by the autocorrelation function:

$$\rho(l) = \frac{\mathrm{Cov}(\theta_i^{(t)}, \theta_i^{(t+l)})}{\mathrm{Var}(\theta_i)}. \tag{5.8}$$

The lower the autocorrelation, the better the variability is captured. Figure 5.6 shows the autocorrelation function for both samplers. In the case of HMC, autocorrelation becomes negligible below 5 l, while classical MCMC is still highly correlated for 30 l. The very low correlation between the samples generated by HMC is remarkable. The algorithm is able to thoroughly explore the phase space with far fewer samples than classical MCMC.

Figure 5.7 summarizes the aforementioned concepts. The graph shows the sampling behaviour of both algorithms. For the example in Fig. 5.7, point 1 on the left graph has three red segments. This means that before making the next move to nearby point 2, three moves were rejected. In contrast, HMC on the right graph travels long distances with few rejections and captures better the variability. Figure 5.8 shows the complete sampling for both methods.

HMC is able to travel long distances with high efficiency, which is an important capability to create models that are more likely to be far apart. As the dimensions and difficulty of the problem increase, the correlated behaviour in classical MCMC is more acute, and there may be numerous rejections before one nearby state is accepted.

The solution to the inverse problem shown in Fig. (5.9) is

$$\pi_E(\theta) = \frac{1}{(2\,\pi)^{D/2} det(\mathbf{\Sigma})^{0.5}}\, \exp\left(-\frac{1}{2}\,\theta^{\mathbf{T}}\mathbf{\Sigma}^{-1}\theta\right) \tag{5.9}$$

with the covariance matrix

$$\mathbf{\Sigma} = \begin{pmatrix} 1 & 0.98 \\ 0.98 & 1 \end{pmatrix} \tag{5.10}$$

The correlated multivariate gaussian distribution (Eq. (5.9)) shows the analytical function that both methods successfully sampled in two dimensions $D = 2$. As discussed in Chapter 4, the normalization constant (partition function $(2\,\pi)^{D/2} det(\mathbf{\Sigma})^{0.5}$) does not have to be known to perform HMC and MCMC.

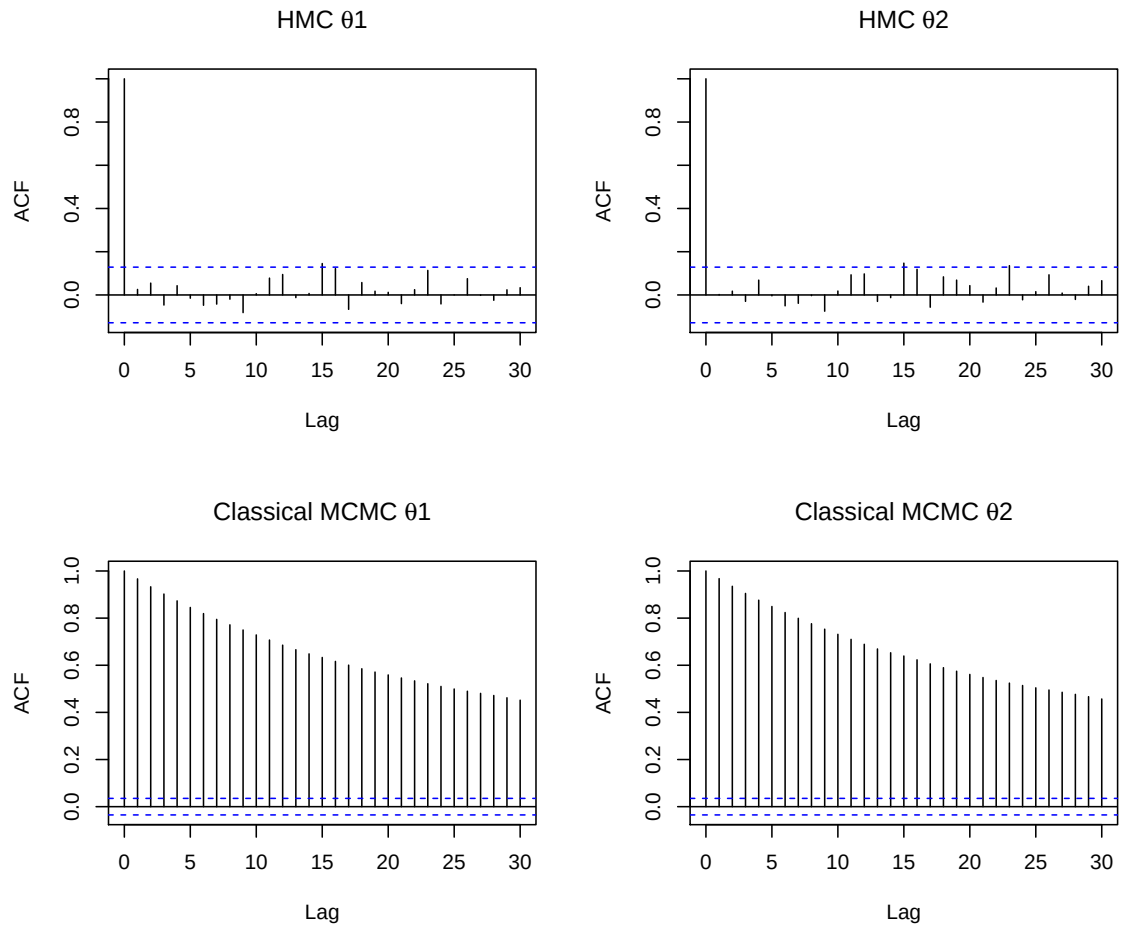

Fig. 5.6 Autocorrelation function (ACF) plotted against lag distance (l) . The top row of histograms corresponds to the HMC solution and the bottom row corresponds to the classical MCMC solution. The top ACFs decay immediately, indicating uncorrelated samples. In contrast, the bottom ACFs are correlated even at distances greater than 30 l, indicating highly correlated samples, that is, sample $i+30$ still remembers sample i. Correlation between the samples increases the total number of samples required to obtain a reliable posterior distribution of the parameters.

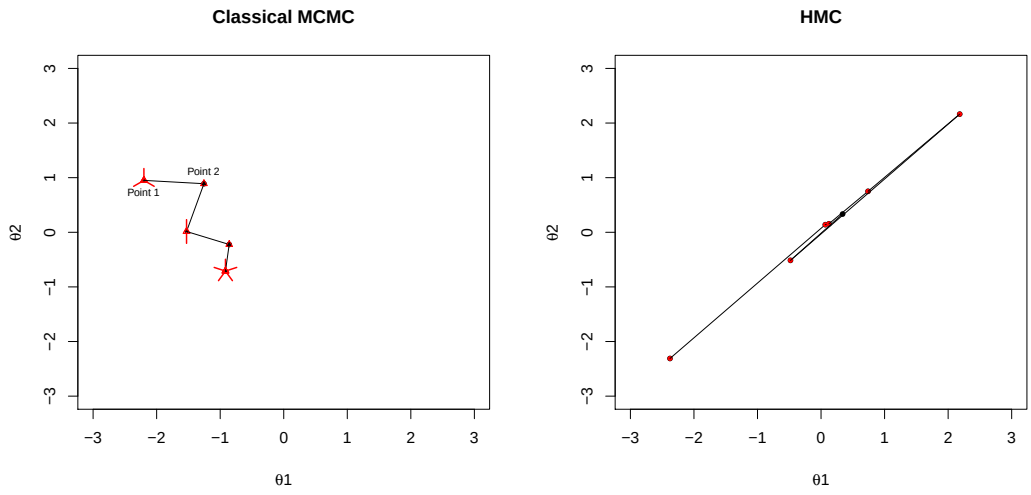

Fig. 5.7 HMC and MCMC algorithms sampling the solution space. The left graph shows 12 steps of the classical MCMC algorithm sampling the solution space. To avoid overplotting, each time a sample is rejected the iteration stays where it is and an additional segment is added at an angle. The right plot shows 6 steps of the HMC algorithm. The samples are far apart, showing why the autocorrelation function in Fig. 5.6 suddenly decays for HMC, unlike MCMC. The trajectories on the left show that exploration takes place along the region of maximum probability density.

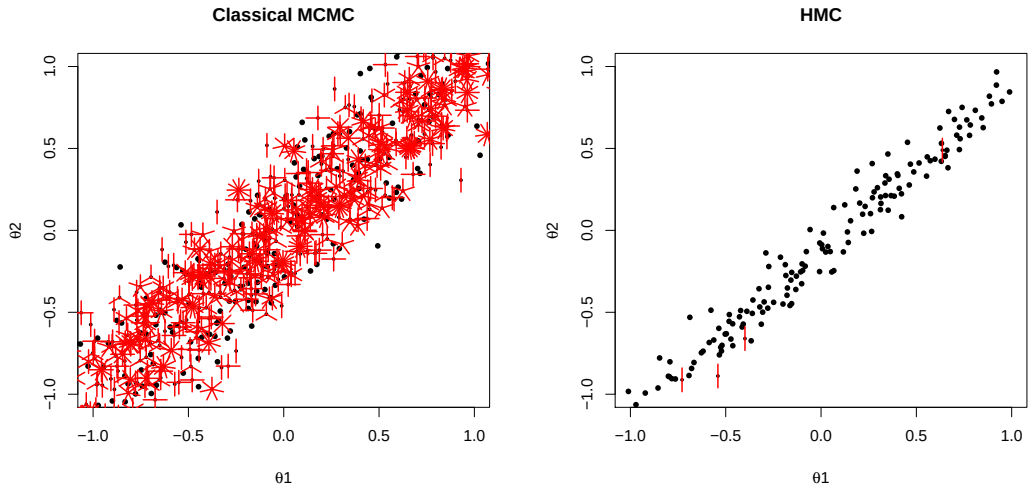

Fig. 5.8 Scatterplots of the two parameters θ_1 and θ_2 of the inverse problem plotted on the solution space. The graph on the left shows classical MCMC sampling the solution space, while the graph on the right shows HMC. The MCMC slowly explores the solution space because many samples are rejected. Hence, many samples are repeatedly obtained (crosses). The scales on the graphs are different from those in Fig. 5.7 to better show the overplotting.

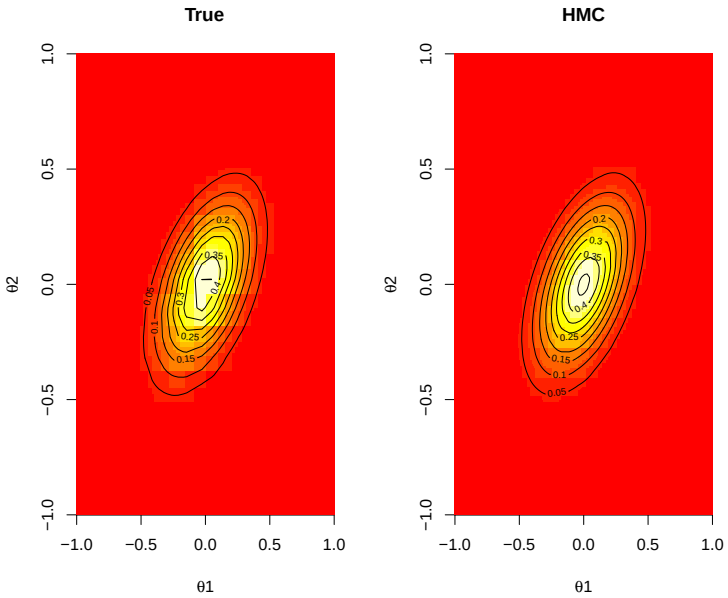

Fig. 5.9 Contours representing the statistical solution to the inverse problem: a) True solution drawn from Eq. (5.9). b) Solution obtained using the samples generated by HMC.

5.4 Analytical Case B

An energy function is defined as

$$E(\theta_1,\theta_2) = \left(\theta_1^2 + \theta_2 - 11\right) + \left(\theta_1 + \theta_2^2 + -7\right) \tag{5.11}$$

with two parameters θ_1,θ_2. Eq. 5.4 has four local minima at $(3,2)$, $(-2.81,3.13)$, $(-3.78,-3.28)$ and $(3.58,-1.85)$ where $E(\theta_1,\theta_2) = 0$.

We compare the performance of HMC to the Classical MCMC Metropolis on the basis of same number of function evaluation as HMC is more computational expensive. Therefore , to generate $N_{HMC} = 10.000$ we used 9 leapfrog steps and 3 function evaluation per leapfrog step to compute the gradient. This equates to $N_{MCMC} = N_{HMC} \times 9 \times 3 = 270.000$ samples for the Classical MCMC. We started the chains at the point $(0,0)$ and we generated 10.000 samples for HMC and $N_{MCMC} = 270,000$ of $\Delta\tau = 1.2$.

Figure 5.11a shows the fundamental problem described in Section 4.3.1 of the Metropolis based MCMC. The proposed moves are local and determined by the energy la function landscape. The chain slowly explores the solution space making it difficult to capture the variability. As we can see in Fig. 5.11a, the chain finds one of the minima at $(3,2)$ and suffers local trapping due to the high energy barrier between local minima not being able to

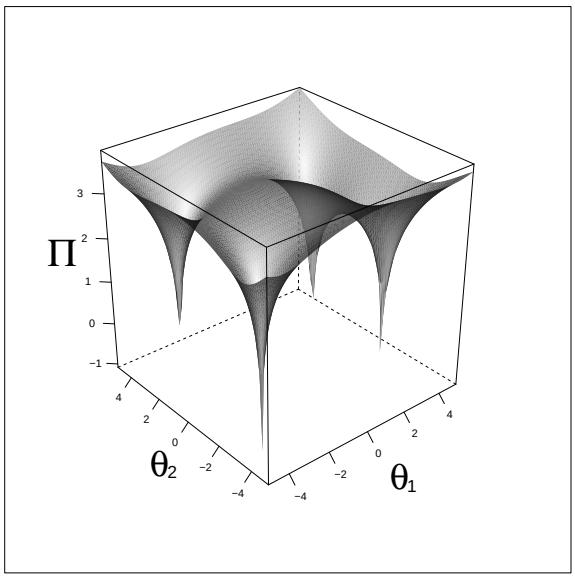

a

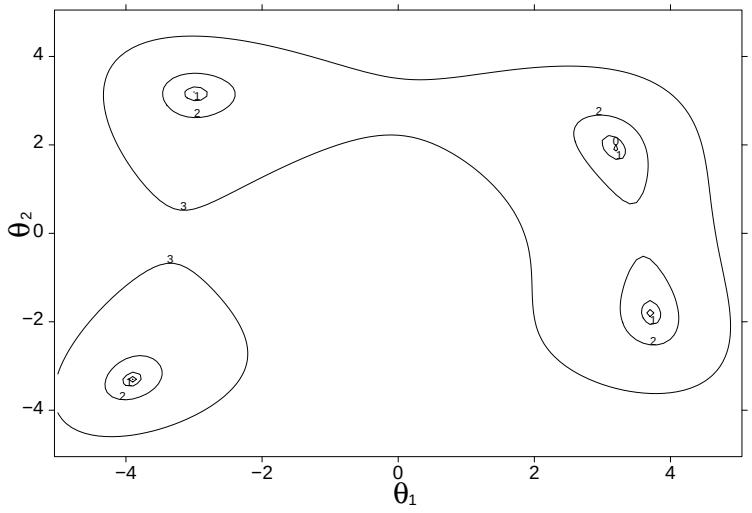

b

Fig. 5.10 (a) 3D surface of Eq. 5.4. (b) Contours representing the true statistical solution .

find the other three in 200.000 samples generated because random walk Metropolis based MCMC is sensitive to large changes in the model parameters. On the other hand HMC was able to find the four minima Fig. 5.12.

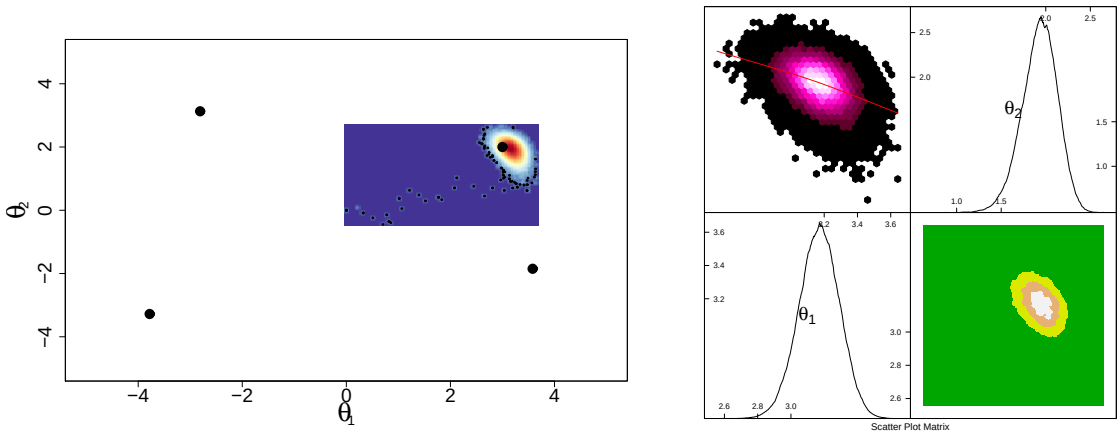

a b

Fig. 5.11 a) Heat map for classical MCMC of the two parameters θ_1 and θ_2. The black dots shows the four local minima of the inverse problem plotted on the solution space; b) Bivariate scatter plots of θ_1 and θ_2 parameters.Colour grading is used to contrast the regions of high density (white) with those of low density (green). Below the diagonal, the same pair of parameters is represented by a contour plot. This represents the density of points, which is an estimator of the probability density. The diagonal shows the marginal histogram (Fig. 6.3) with a kernel smoother on each parameter.

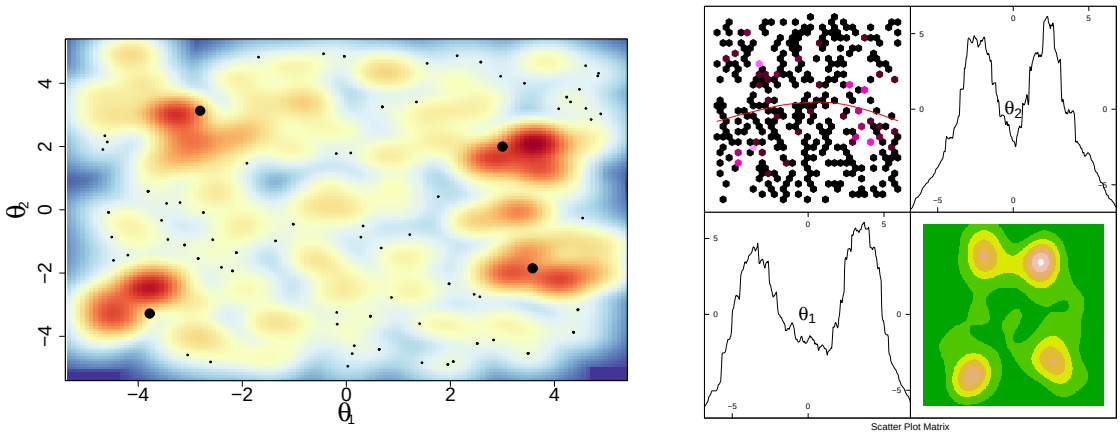

a b

Fig. 5.12 a) Heat map for classical HMC of the two parameters θ_1 and θ_2. The black dots shows the four local minima of the inverse problem plotted on the solution space; b) Bivariate scatter plots of θ_1 and θ_2 parameters.Colour grading is used to contrast the regions of high density (white) with those of low density (green). Below the diagonal, the same pair of parameters is represented by a contour plot. This represents the density of points, which is an estimator of the probability density. The diagonal shows the marginal histogram (Fig. 6.3) with a kernel smoother on each parameter.

Chapter 6

Synthetic Data

6.1 Introduction

This chapter applies the Hamiltonian Monte Carlo (HMC) algorithm described in Chapter 4 to estimate the network model parameters of synthetic data. The output of the HMC algorithm was two vectors: a vector of parameters and a momentum vector with the number of components equal to the number of parameters. Each vector of parameters represents a point (a sample) in the solution space.

The parameters vector $\boldsymbol{\theta}$ can be marginalised along each of its parameters. It can analyse the distributions and median statistics, and determine whether the output from the HMC reflects the true values used to generate the synthetic data.

In this study, the carbonate samples had pores varying in size by three to five orders of magnitude. The capillary pressure was the only available data. We first applied the method to a synthetic mercury intrusion capillary pressure (MICP) case where the pore sizes varied by up to five orders of magnitude. The uniform shape of the pore-size distribution ensured that at least two pore-size distributions were plausible, exacerbating the problem of multiple minima. The next section discusses the synthetic case.

6.2 Validation Using Synthetic Data

The pore-network model parameters used to simulate the synthetic MICP were average coordination number $\overline{Z} = 4.1$ and volume exponent $v = 0.5$ (Eq. (4.36)). Figure 6.1a shows the histogram of the pore sizes in the network model (log-uniform pore-size distribution ranging from 1×10^{-9} to 1×10^{-4} m) that was used to generate the synthetic MICP data

(Fig. 6.1b). The network model had a lattice defined by $N_x = 20$, $N_y = 20$, and $N_z = 20$ (short form lattice constant $L = 20$), which contained $24,400$ pores ($3 \times N_x \times N_y \times N_z + N_y \times N_z$). It is reasonable to assume that air can completely escape from the medium because its wetting characteristics are stronger than those of mercury.

Table 6.1 Range of variation of the pore-network model parameters.

Parameter	Minimum value	Maximum value
ν	0	2
$\bar{Z}$	3	6
p_1^*	0.001	0.6
p_2^*	0.001	0.6
p_3^*	0.001	0.6
p_4^*	0.001	0.6

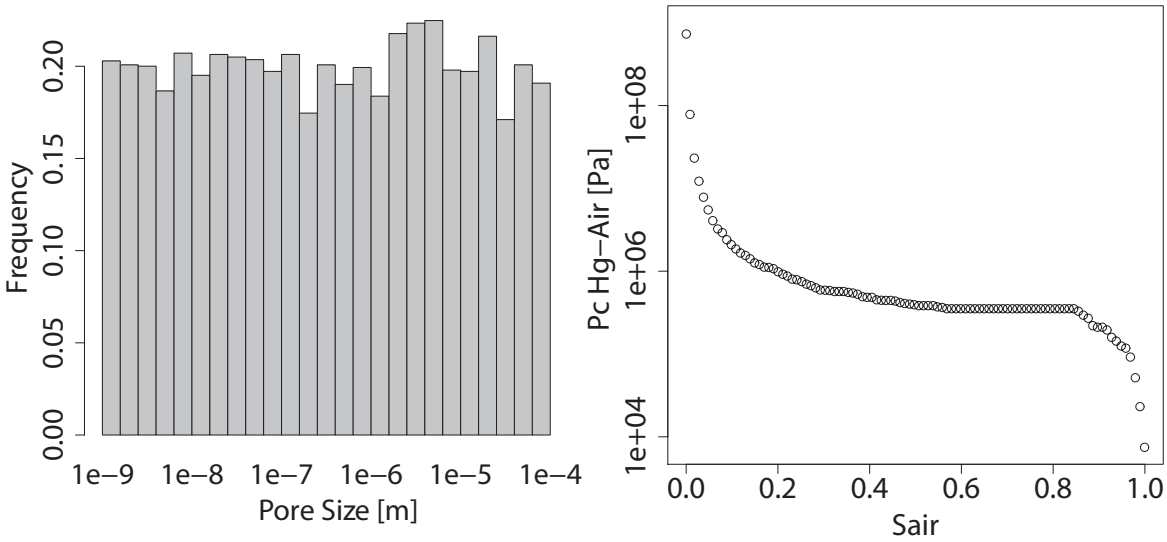

a b

Fig. 6.1 (a) Histogram showing the input pore-size distribution to generate the synthetic MICP. The histogram is normalised so that the sum of the bins is one. (b) Synthetic MICP data generated using the true values of the pore-network model parameters.

Unless stated otherwise, for the remainder of the text all of the histograms are normalised so that the sum of the discrete bins is equal to one. We compared the different pore-size histogram realisations by including a line at the centre of each class to give a continuum expression for easy comparison (e.g., Fig. 6.4). The gradient in the leapfrog algorithm (see

Section 4.3.1 in Chapter 4) was calculated by extrapolating to $\Delta\theta = 0$ using the Richardson method [326]. The tolerance of the relative error of Hamiltonian conservation during the time integration was 2%. Applying Eqs. (4.6) and (4.5) to the MICP data (Fig. 6.1b) produced the pore-size distribution estimator shown in Fig. 6.2a. The kernel technique smoothed out the noise (Fig. 6.2b). Each of the discrete points in Fig. 6.2b has a Shannon information content given by Eq. (4.7). Each bin in Fig. 6.2c is a parameter in the pore-size distribution parameterisation. The bins have different widths so that they contain the same amount of information (Fig. 6.2c).

The HMC algorithm performed the stochastic inversion of p_i^*, ν, and $\overline{Z}$. The inversion took approximately 16 h (on an Intel Xeon W5590 3.33 GHz processor) to accumulate a sufficient number of posterior samples to stabilize the acceptance rate and produce the correct posterior distributions. The misfit between the simulated MICP and the synthetic MICP is the energy in the Hamiltonian formulation (Eq. (4.25)). The aim was to use small networks ($L = 8$) in the calculation of the SSIP, and then perform forward predictions of the relative permeability in large networks. The effect of the network size on the stochastic inversion of the network parameters was negligible (Section 6.3f will show the effect of network size on the inversion results).

Small network models ($L = 8$) estimated the network parameters well. We stopped sampling when the medians of all of the parameters were unchanged after twice as many samples were generated. For the synthetic case, 2500 samples were sufficient. The reported carbonate sample results are from 10,000 samples generated by the HMC method. In statistical physics, the temperature (β) in Eq. (4.27) is specified. However, within the statistical context of this thesis the temperature behaves as a variance or a scaling parameter. If the temperature is high, there is more uncertainty in the observed measurements. Random numbers were used to sample the pore-size distribution and remove bonds to attain a given average coordination number. This introduces a certain level of noise or fluctuations into the simulated MICP. Thus, if the temperature is below the noise level, the noise dominates the solution. We used several realisations of the MICP generated with the true parameter values to estimate the noise level.

The HMC medians obtained from the SSIP reflected the true parameters (Figs. 6.3 and 6.4). The marginal histograms were the output from HMC sampling. HMC sampling produced an ensemble of vectors with network parameters entries in $\boldsymbol{\theta}$. Figure 6.3a shows the volume exponent posterior histogram. The bin with the highest frequency almost coincides with the true value. The histogram is skewed to the left, because the majority of the samples are around the true value. However, the spread indicates that other values are possible.

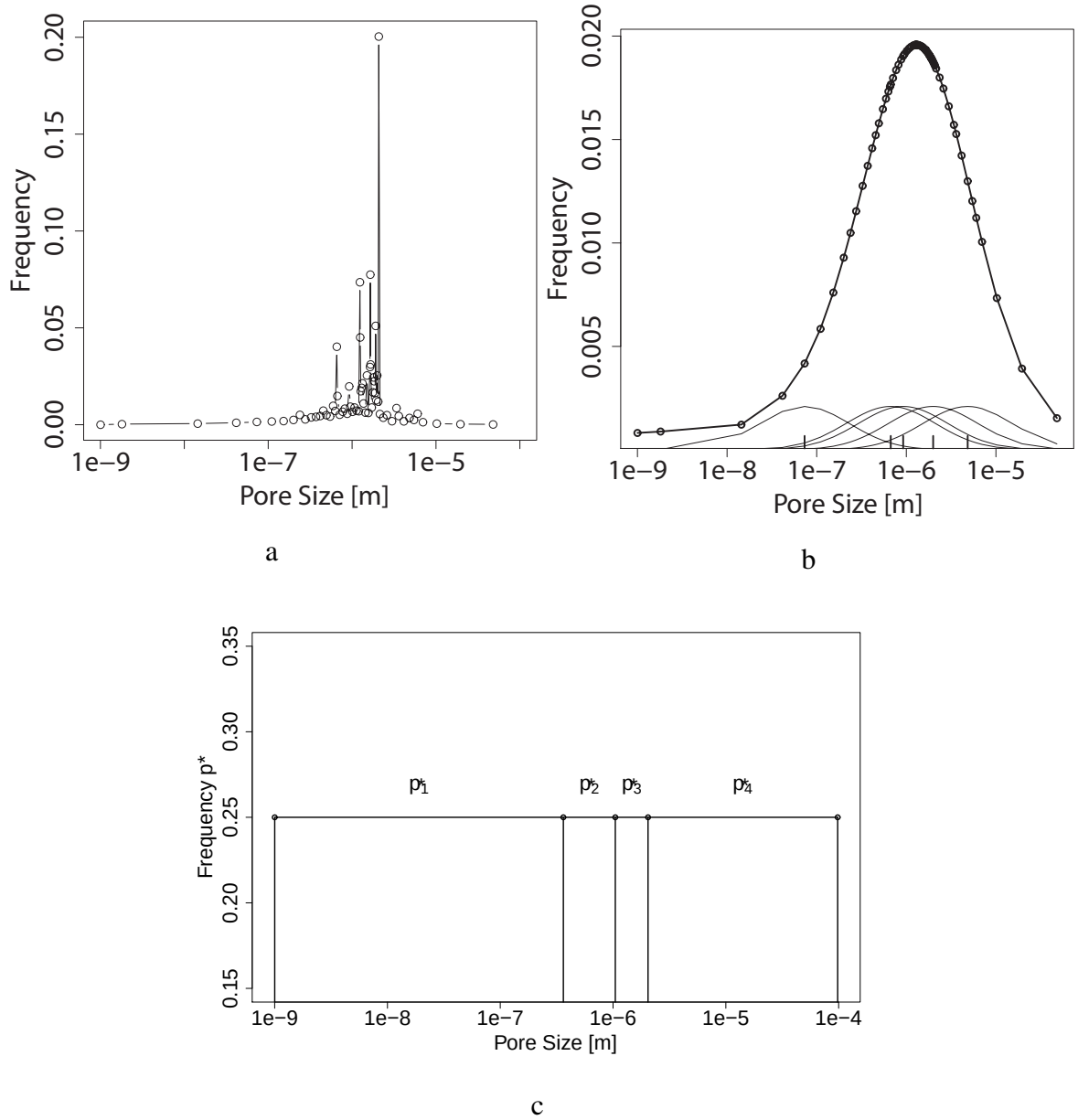

Fig. 6.2 (a) Raw frequency polygon obtained by applying Eq. (4.6) to the MICP data in Fig. 6.1b. (b) Further application of kernel smoothing to the graph shown in (a). We placed a gaussian function over each of the points in the frequency polygon (small bell-shaped curves shown on the graph). Then, the contribution of each of the Gaussian functions was added to produce the smooth curve (dot and line curve). (c) Parameterisation of the pore-size distribution, in which the entropy is maximised with respect to the pore-size distribution obtained by the transformation introduced earlier and shown in (b). The widths of the bins were chosen so that each bin contained the same amount of information (Chapter 4).

The median of the average coordination number in Fig. 6.3b is also around the true value. The histogram is skewed to the right with more spread than the histogram for the volume exponent. The volume exponent histogram is less uniform than the coordination number histogram, which could indicate that the volume exponent has more influence on the misfit than the average coordination number. As discussed above, the bin probabilities (Fig. 6.2c) are entries in the vector of model parameters $\boldsymbol{\theta}$ that produced the associated pore-size distribution for each realisation (Fig. 6.4a). The median pore-size distribution agrees with the known true pore-size distribution (Fig. 6.4a).

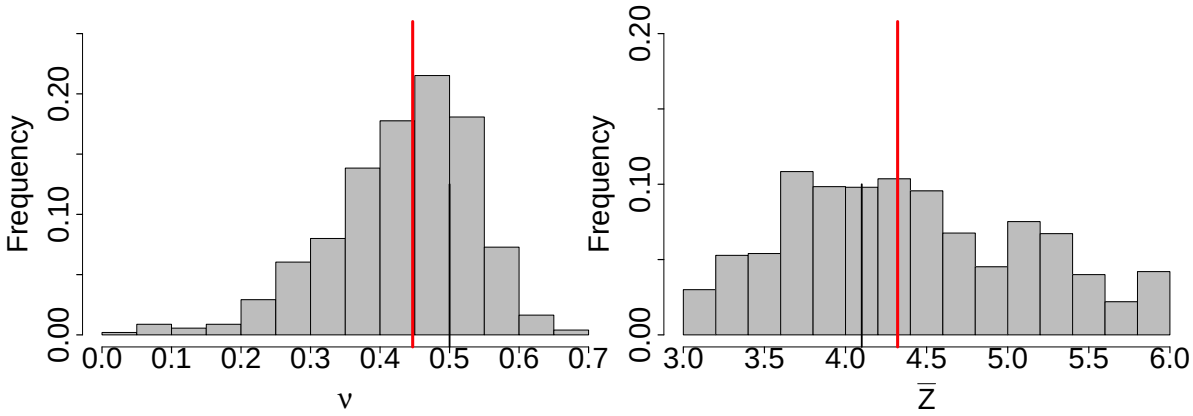

a b

Fig. 6.3 (a) Marginal histogram of the volume exponent (ν). (b) Marginal histogram of the average coordination number ($\overline{Z}$). The vertical red line indicates the median of the samples and the black line indicates the true value of the parameter.

In a number of samples, the pore-size distributions were concentrated in a relatively narrow range of pore sizes (Fig. 6.5a). These distributions are different from the true distribution shown in Fig. 6.1. A reasonable explanation why nonuniform pore-size distributions were identified as local minima is related to the percolation phenomena. Figure 6.5a shows a nonuniform pore-size distribution with a peak around 1 μm, and Fig. 6.5b shows the corresponding MICP simulations and true MICP. The MICP data produced by nonuniform (e.g., unimodal) and log-uniform pore-size distributions are similar. This is because at the percolation threshold there are pores that are spontaneously invaded that are larger than the pores currently being invaded. The additional volume contribution from the spontaneously invaded pores results in similar MICP behaviour to a rock sample with a high proportion of pore sizes around the size at which the percolation threshold occurs (unimodal pore-size distribution). The nonuniform pore-size distribution described above is evidence of multiple

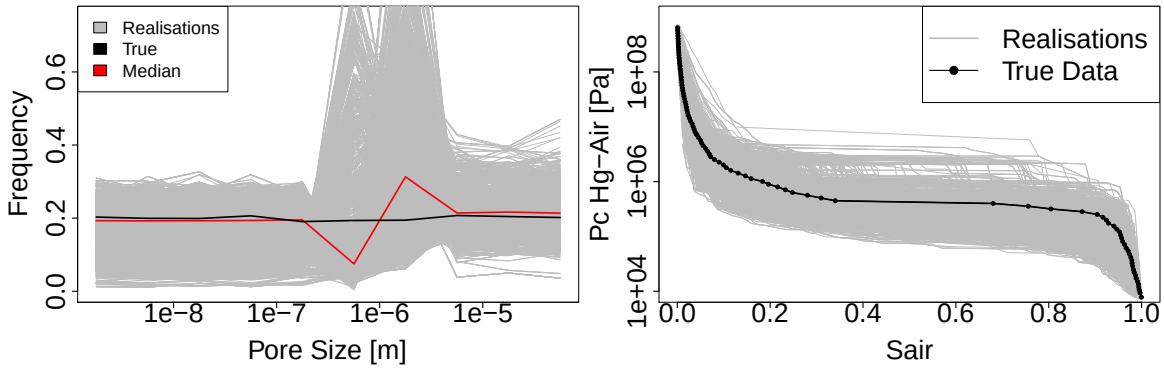

a b

Fig. 6.4 (a) Pore-size distributions corresponding to the two histograms of the parameters shown in Fig. 6.3. The red line indicates the median of the samples and the black line indicates the true pore-size distribution. (b) MICPs associated with the combination of pore-size distribution, volume exponent, and coordination number.

minima. It could be argued that the parameterisation causes the emergence of the unimodal function as a possible solution. However, the nonuniform distribution is a possible solution. Therefore, the parameterisation should allow the nonuniform distribution to emerge.

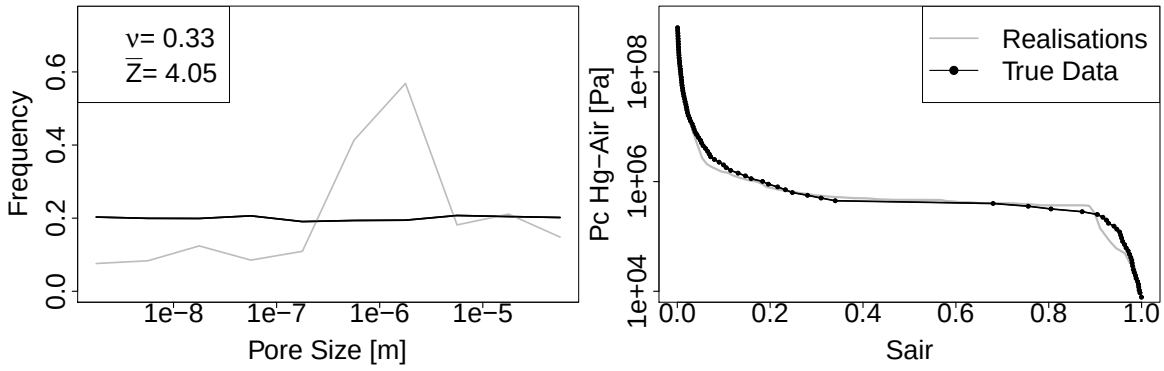

a b

Fig. 6.5 (a) Pore-size distribution that had a peak around 1 μm. (b) MICP simulation of the pore-size distribution in (a) (evidence of multiple minima).

For each case, we have included a matrix of all pairs of parameters (Fig. 6.6). We included both the upper and lower triangles to compare all of the variables by rows and columns. There is a nonlinear correlation between pairs of parameters (Fig. 6.6). The trend lines in the upper triangle cross-plots indicate that the marginal histograms are non-

Gaussian. If there were Gaussian relationships between the parameters, the HMC sample distribution would have a Gaussian elliptical shape in each cross-plot and an even spread around a linear trend Chapter 5). The regions of low energy (high posterior probability/low misfit) are located in narrow regions (Fig. 6.6, white regions). Figure 6.6 shows a graphical representation of the variance–covariance matrix. The variance–covariance matrix is an input for some of the methods discussed in Chapter 2 that assume a linear relationship between the energy and the parameters, and between the parameters themselves.

The volume exponent shows a nonlinear correlation with the bin probability of the small pores (p_1^*) in the pore-size distribution (Fig. 6.6). Apart from the nonlinear correlation, there are no consistent linear trends among the data that can justify linear Gaussian models. There are multiple local minimum energy regions. The cross-plots are projections of the solution space, and the topography of these projections suggests that the solution space landscape is complex. Projections like the ones shown in Fig. 6.6 demonstrate many of the difficulties that the methods discussed in Chapter 2 face when trying to thoroughly sample the solution space. The work discussed in Chapter 2 did not verify if the assumptions of linearity and homogeneity of variance were justified. Therefore, these methods are very much dependent on the initial estimates of the parameters.

Figure 6.7 shows the concepts of Chapter 4, Section 4.3.1, where the HMC sampling takes place on the phase space along trajectories of the constant Hamiltonian. These trajectories show periodicity in the phase space, making the sampling independent of the energy (misfit). Figure 6.7 shows that the trajectory can generate a new sample at the other end of the bounds of the parameter in a single step. Although the misfit is a term in the Hamiltonian (Eq. (4.25)), the value of the Hamiltonian for the trajectory being sampled depends on the initial sampling of the momentum in Eq. (4.28) (note the jump from $\mathscr{H} = 4.9$ to $\mathscr{H} = 1.2$ at $v = 0.5$). The graph shows two trajectories along the $v - p$ plane that produced two samples. The orbits preserve the periodic pattern, regardless of the Hamiltonian value (Fig. 6.7).

The reduction of the misfit with steps along the Markov chain is shown in Fig. 6.8. Looking closely at some tipical parts of the Markov chain it can be seen that the HMC is capable to generate samples from high to low misfit.

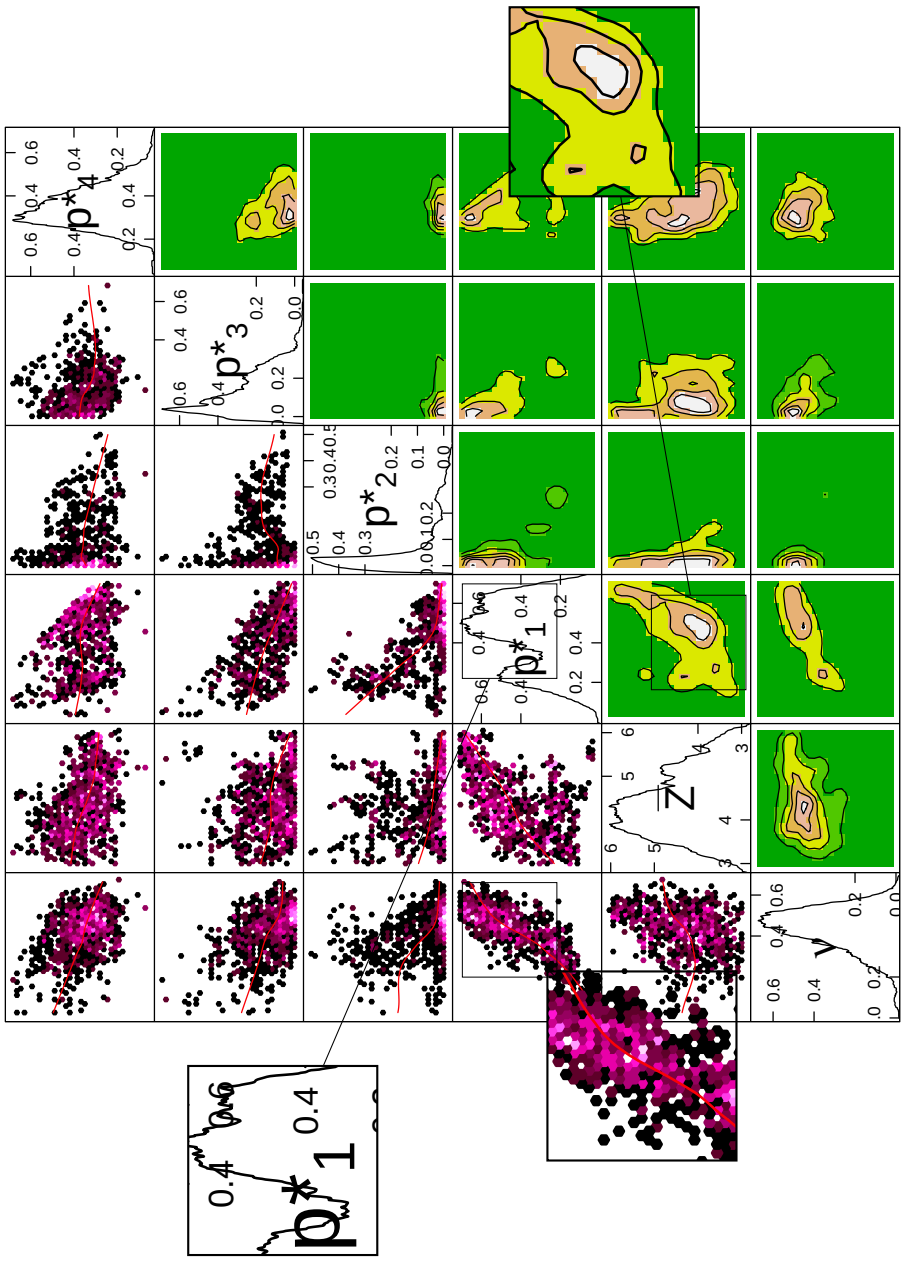

Fig. 6.6 Matrix of all pairs of parameters. Each grid cell shows a cross-plot of two parameters, with an overlaid locally weighted regression fit to visualise a possible trend. Colour grading is used to contrast the regions of high density (white) with those of low density (green). Below the diagonal, the same pair of parameters is represented by a contour plot. This represents the density of points, which is an estimator of the probability density. The diagonal shows the marginal histogram (Fig. 6.3) with a kernel smoother on each parameter. The magnified cells show examples of multiple minima and the correlations between low values of v and a small contribution from small pores in the pore-size distribution, corresponding to parameter p_1^*.

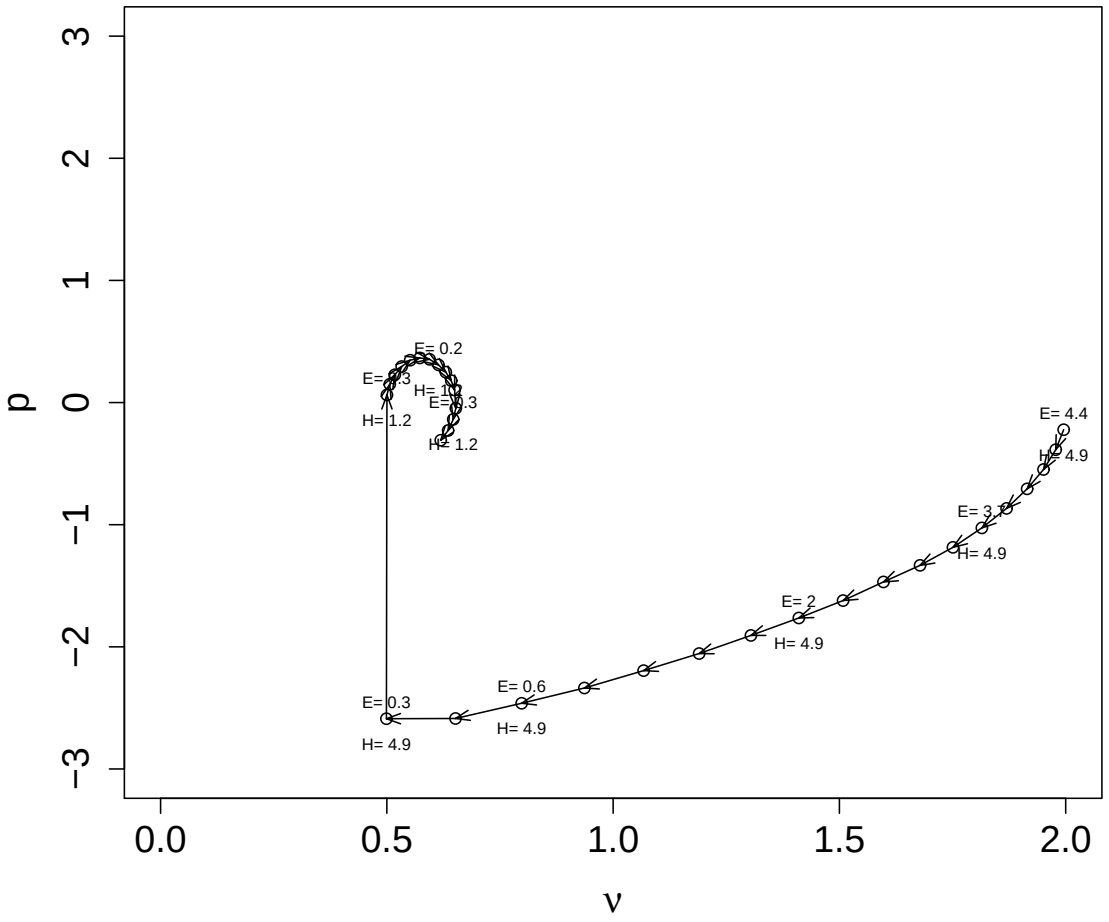

Fig. 6.7 Phase plane showing momentum (p) versus position of the volume exponent (ν). The numerical values of the Hamiltonian ($\mathscr{H}$) and the energy (E) have been rounded to the first decimal place to avoid overplotting. As the trajectory moves forward along the deterministic molecular dynamics steps, $\mathscr{H}$ is invariant whereas E changes. Along a single step, the molecular dynamics step could propose a sample that is located at the other end of the parameter variation range.

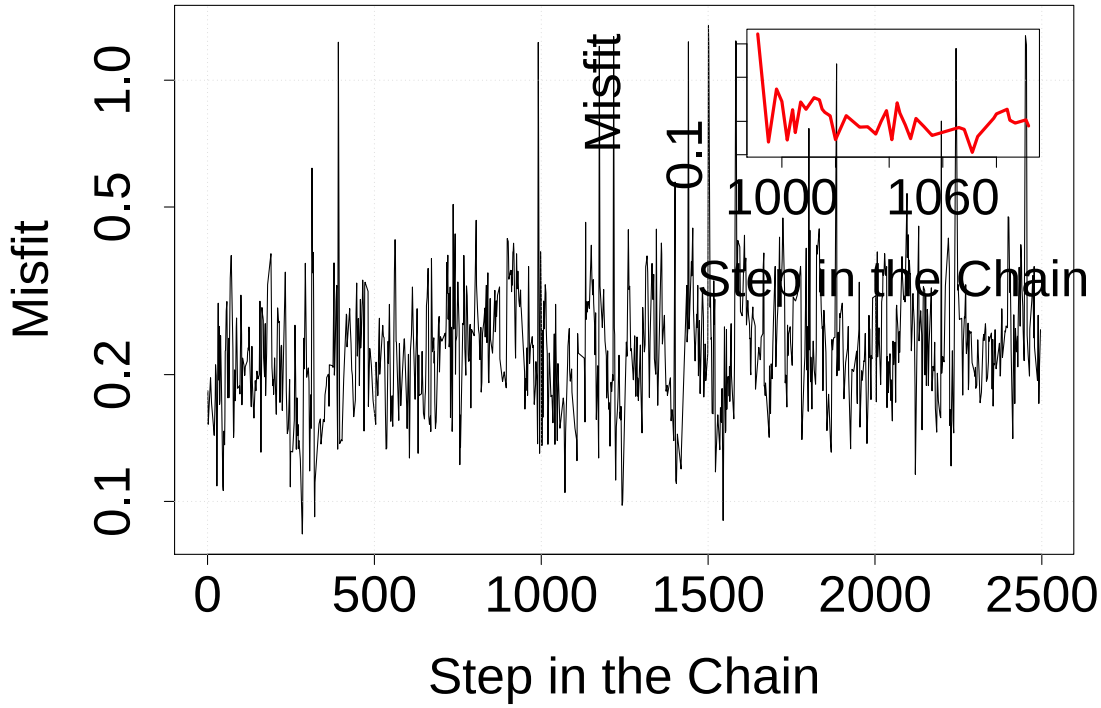

Fig. 6.8 Misfit along the Markov Chain. The subplot in the top right shows that HMC is capable of generating samples of very different misfit from high to low misfits even in one step of the chain.

6.2.1 Comparison with Another Type of Pore-Size Distribution Parameterisation

This section compares the parameterisation proposed in Chapter 4 with a regular parameterisation of the pore-size distribution with logarithmically equidistant bins (Fig. 6.9b).

First, Fig. 6.10a shows the marginal posterior histogram of the volume exponent for the entropy based parameterisation and Fig. 6.10b for the logarithmically equidistant bin parameterisation. From these figures it is clear that there is Fig. 6.10b is biased towards low volume exponent values and the median does not reflect the true value. The logarithmically equidistant parameterisation has two bins in the range of small pores, whereas the parameterisation proposed in this work has only one (Fig. 6.9a). Low values of the volume exponent are correlated with small contributions of small pores to the pore-size distribution. Therefore, the volume exponent in the logarithmically equidistant parameterisation is more strongly influenced by the correlation with the contribution of small pores in the pore-size

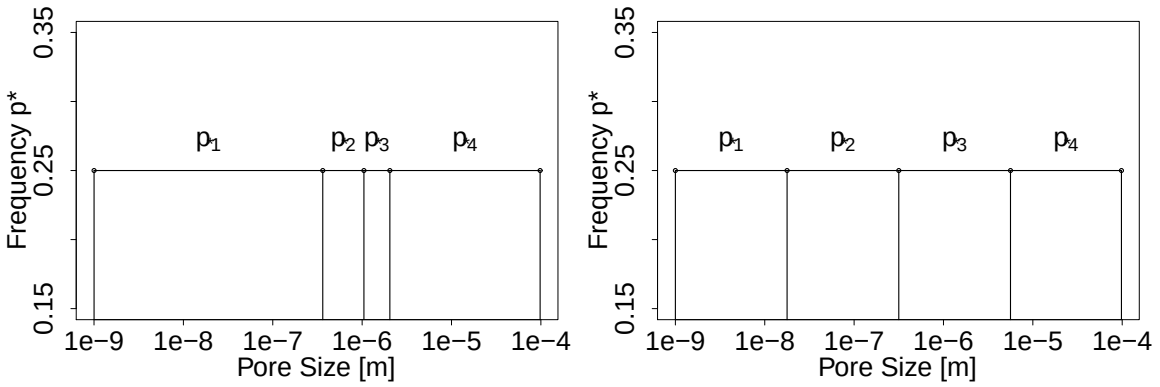

Fig. 6.9 (a) Parameterisation proposed in this work, where the widths of the bins are determined so that each contains the same information, as measured by information entropy. (b) Logarithmically equidistant bin parameterisation.

distribution (parameters p_1^* and p_2^*, Fig. 6.13).

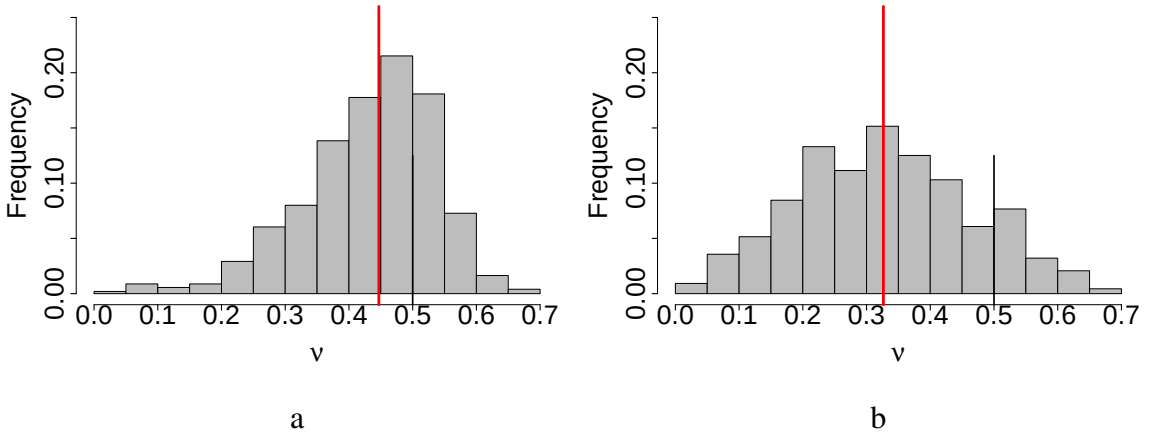

Fig. 6.10 (a) Marginal histogram of the volume exponent (ν) using the parameterisation proposed in this work. (b) Marginal histogram of ν using the logarithmically equidistant bin parameterisation. The vertical red line indicates the median of the samples and the black line indicates the true value of the parameter.

In Fig. 6.11 the marginal posterior histograms of the average coordination numbers are presented. It can be seen that the median for the average coordination number in both the entropy based and the logarithm equidistant binning are close to the true value. However, the marginal posterior histogram of our proposed entropy based parameterisation shows a greater concentration of values around the true value (Fig. 6.11a).

Figure 6.6 and Fig. 6.13 shows in the diagonal marginal posterior PDFs of the volume exponent, coordination number and the bins probabilities for our proposed entropy based parameterisation and for the logarithmic equidistant parameterisation respectively.

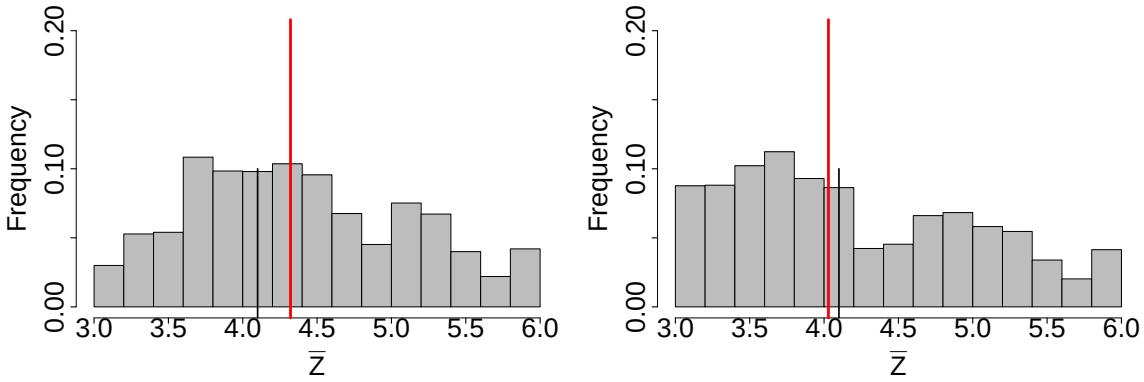

a b

Fig. 6.11 (a) Marginal histogram of the average coordination number $\bar{Z}$ using the proposed parameterisation. (b) Marginal histogram of $\bar{Z}$ using the logarithmically equidistant bin parameterisation. The vertical red line indicates the median of the samples and the black line indicates the true value of the parameter.

A clear trend can be observed in the pore-size distribution: small pores are underestimated because the equidistant bin parameterisation is more affected by strong correlation with the volume exponent (Fig. 6.12b).

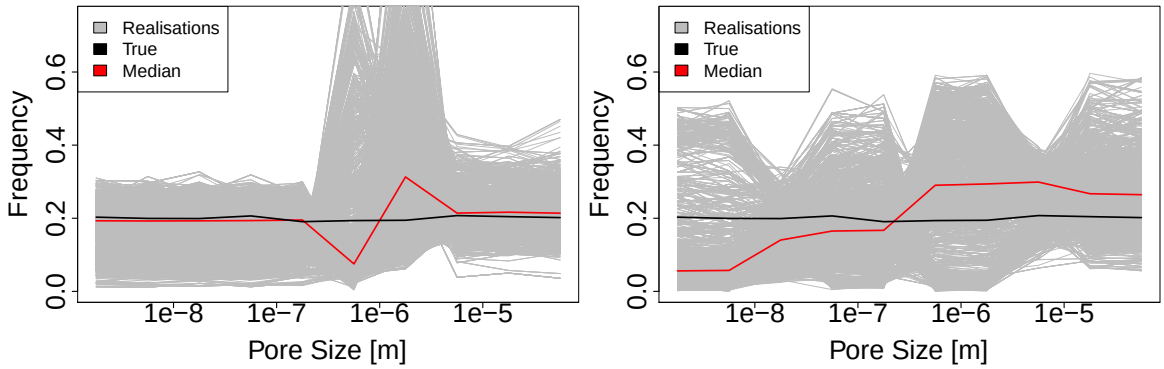

a b

Fig. 6.12 (a) Marginal pore-size distributions using the proposed parameterisation. (b) Marginal pore-size distributions using the logarithmically equidistant bin parameterisation.

Contrary to the case of our proposed parameterisation (Fig. 6.6, the marginal PDF for

the volume exponent for the case of logarithmically equidistant bin parameterisation does not reflect the true value(Fig. 6.11b and Fig. 6.13).

Table 6.2 summarises the mean squared errors (MSEs) of ν and $\bar{Z}$ with respect to the true values as a measure of the quality of the estimates:

$$\mathrm{MSE} = (\mathrm{median}(\theta) - \theta_{true})^2 \tag{6.1}$$

For the pore-size distribution, Table 6.2 also gives the Kullback–Leibler distance

$$\mathrm{KLD}(\boldsymbol{p}) = \sum_{i=1}^{N} \widehat{p}(r_j)_{true} \log \frac{\widehat{p}(r_j)_{true}}{\widehat{p}^*(r_j)}, \tag{6.2}$$

which measures the quality of an estimator of a probability density function. Visual inspection of Figs. 6.10–6.12 and the measures of quality reported in Table 6.2 indicate that the proposed parameterisation performed better than the logarithmically equidistant bin parameterisation. This is reflected in the topography of the solution space (Fig 6.13). Comparing the contours between Figs 6.6 and 6.13, the proposed parameterisation is more effective: the sampling reaches the posterior solution more quickly. In contrast Fig. 6.13 is more patchy: the sampling wanders more and discovers more local minima, and therefore the posterior histograms show bias for the same number of samples generated.

Table 6.2 Comparison of the quality of the two parameterisations in terms of the error.

Parameter	Irregular binning	Logarithmically equidistant binning
ν	0.018	0.05
$\bar{Z}$	0.723	0.846
$\mathrm{KLD}(\boldsymbol{p})$	0.107	0.307

In the oil industry, cumulative percentile/quantile is a probabilistic concept brought from evaluation of hydrocarbon reserves. In reservoir modelling probability it is linked to the nonuniqueness of subsurface scenarios with percentiles of cumulative probabilistic distribution - P10, P50 and P90 [327]. Thus, the cumulative distribution of misfit between data and simulation during the calibration phase can be used to select model parameters corresponding to P10, P50 and P90. These sets of model parameters are used as a basis for forward prediction. However, there is no guarantee that one of these models will be the true model or that the three models will envelope the true predictions [130]. Note that P50 model parameters might be different than the median from each individual parameter as it is in this

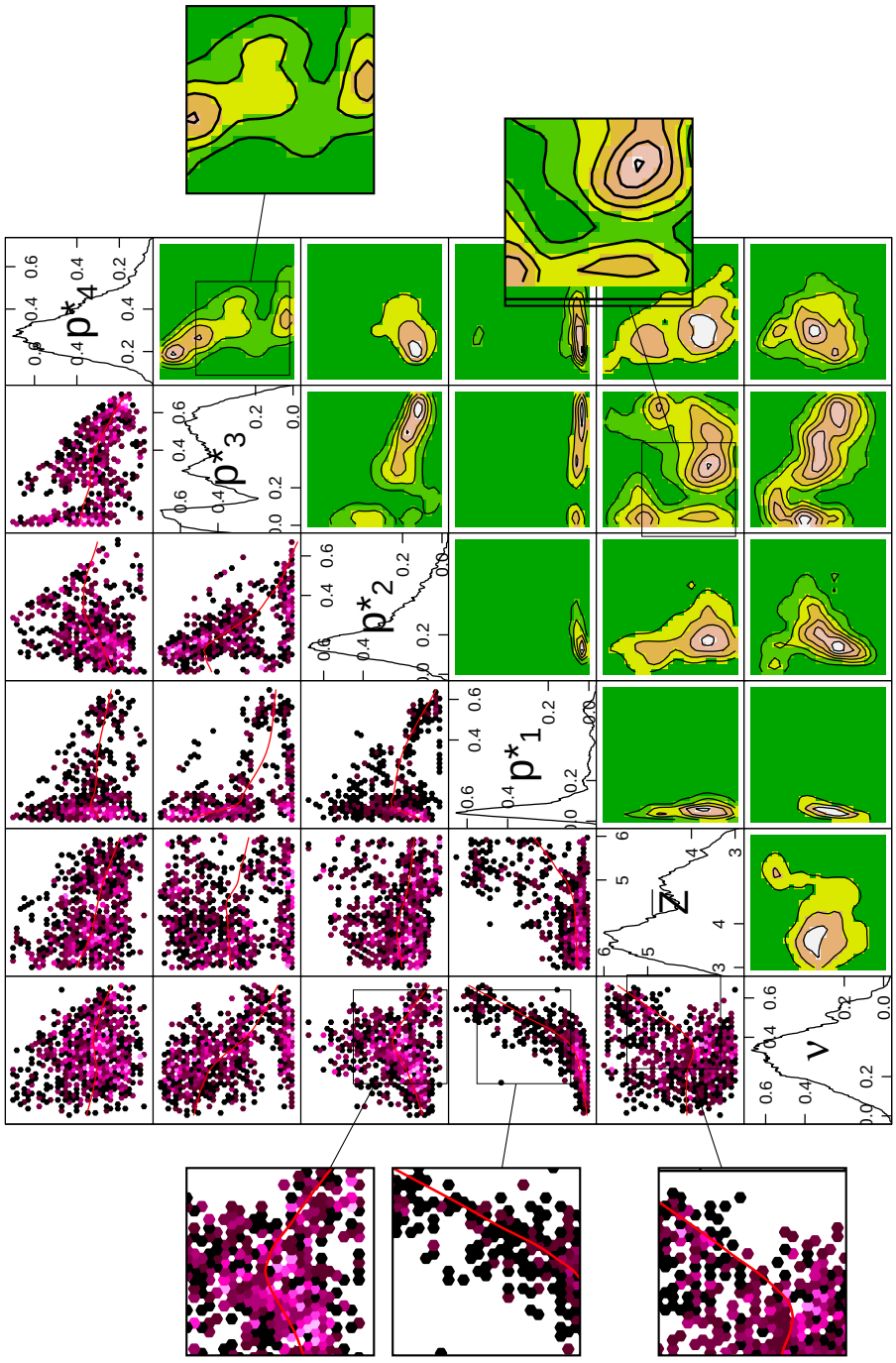

Fig. 6.13 Matrix of all pairs of parameters using the logarithmically equidistant bin parameterisation. The magnified cells show the strong correlations between small contributions from the small pores and the pore-size distribution (bins probabilities p_1^*, p_2^*). The magnified cells on the edge of the matrix show that ν is strongly correlated with p_1^* and p_2^*. The logarithmically equidistant parameterisation creates a more complex topography of the solution space than the parameterisation proposed in this work.

synthetic case. Tables 6.3 and 6.4 and Fig. 6.14 show the model parameters for P10, P50 and P90 for the two type of parameterisations.

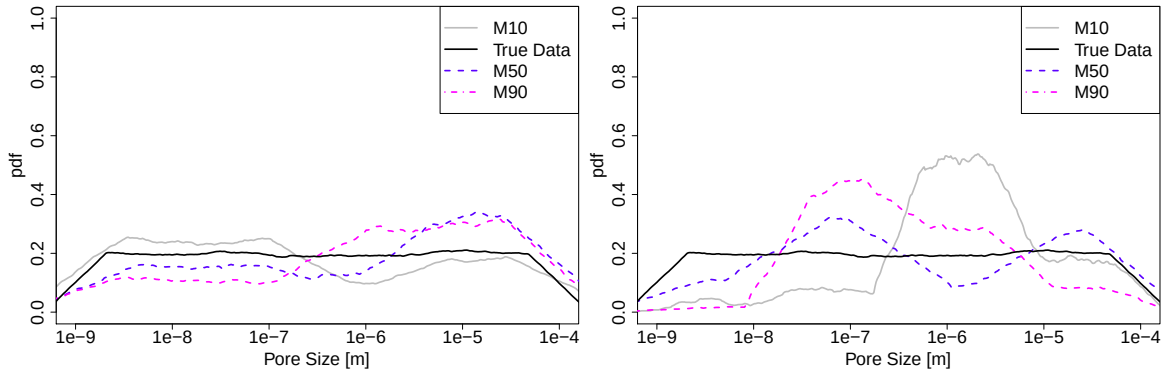

Fig. 6.14 HMC inversion results: M10 is the pore-size distribution corresponding to the P10 quantile model (grey), M10 is the pore-size distribution corresponding to the P50 percentile model (blue) and M90 is the pore-size distribution corresponding to the P90 percentile model (magenta).a) Irregular binning, proposed parameterisation based on equal information per bin ; b) Logarithmically equidistant binning.

Table 6.3 Volume exponent from P10,P50 and P90 models for the two parameterisations.

Percentile	Irregular binning	Logarithmically equidistant binning	True Value
P10	0.485	0.162	0.5
P50	0.427	0.53	0.5
P90	0.432	0.309	0.5

Figures 6.15, 6.16 and 6.17 show parallel coordinate plots for P10, P50 and P90 respectively. Parallel coordinate plot are useful to investigate the clustering and correlations of model parameters around the P10, P50 and P90. The plots are constructed by laying out the axes in parallel, each HMC sample (vector of model parameters) is represented by a line connecting the misfit quantile (Q axis) with the coordination number and the volume exponent .

Using P10, P50 and P90 model may not be representative of the models around this quantiles as shown by the parallel plots in Figs. 6.15, 6.16 and 6.17. The parallel plots show that the models in the neighbourhood of each quantile can be very different though they have a very similar misfit value.

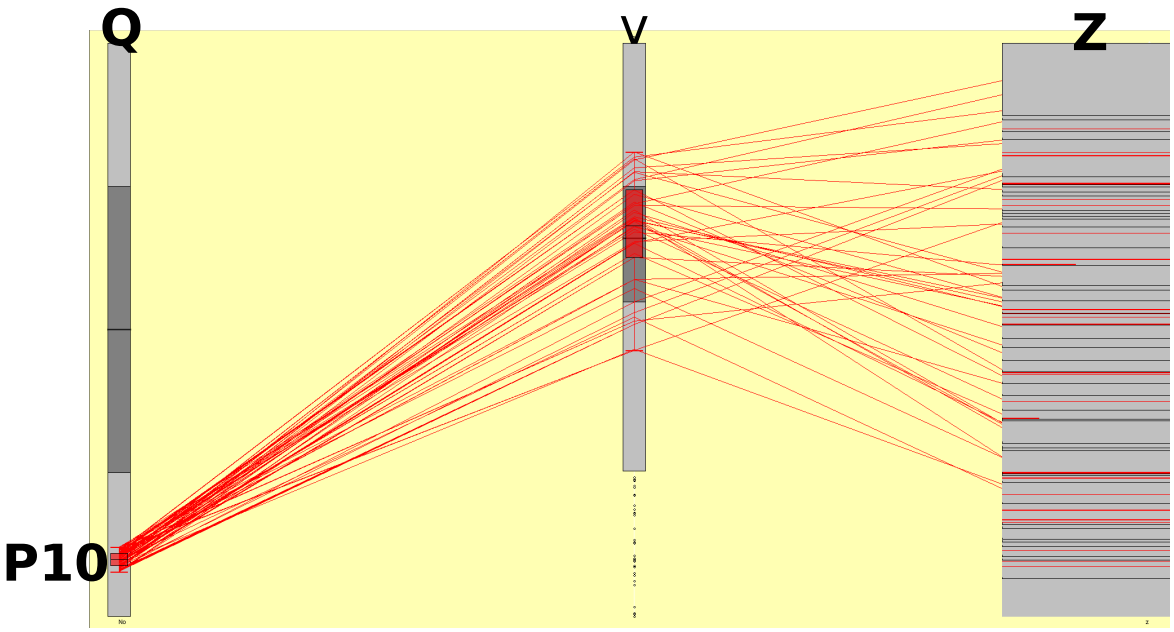

Fig. 6.15 A parallel coordinate plot for quantiles, volume exponent and coordination number. The model parameters, volume exponent and coordination number, for the models in the neighbourhood of the P10 model are connected by a line between all the axes.

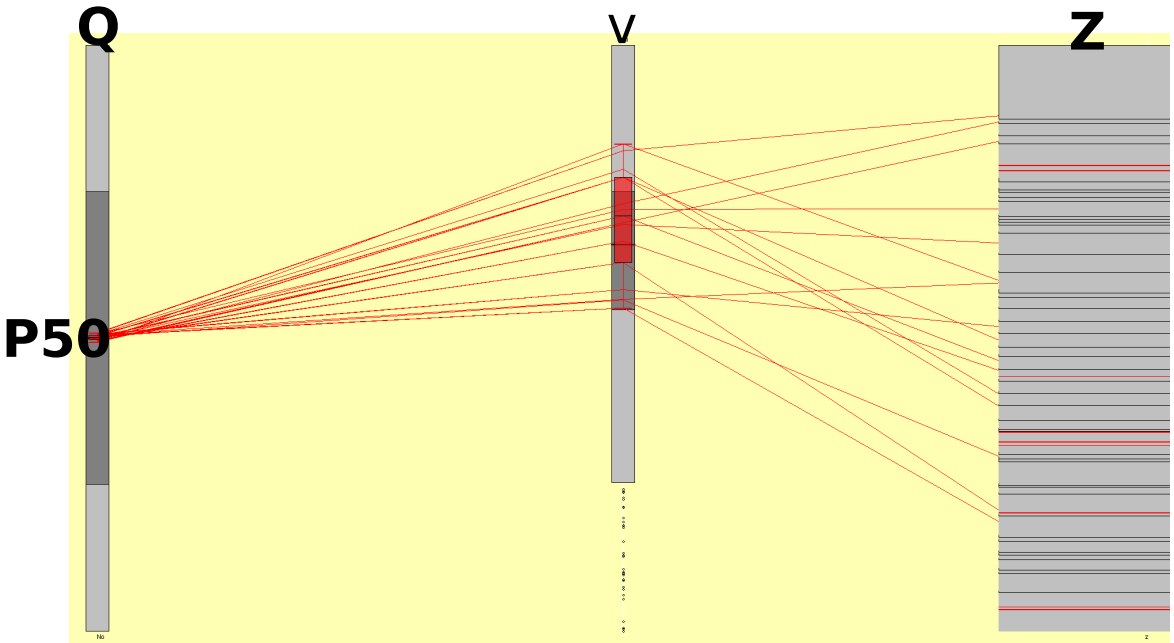

Fig. 6.16 A parallel coordinate plot for quantiles, volume exponent and coordination number. The model parameters, volume exponent and coordination number, for the models in the neighbourhood of the P50 model are connected by a line between all the axes.

Table 6.4 Average coordination number from P10,P50 and P90 models for the two parameterisations.

Quantile	Irregular binning	Logarithmically equidistant binning	True Value
P10	5.51	4.687	4.1
P50	3.229	3.69	4.1
P90	3.672	5.94	4.1

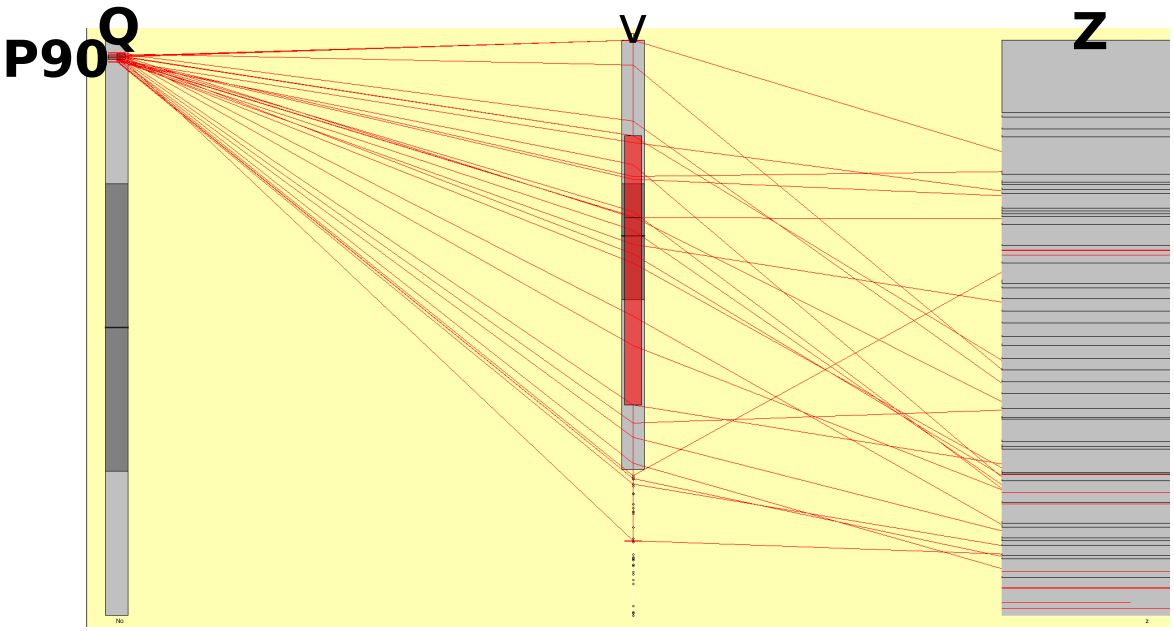

Fig. 6.17 A parallel coordinate plot for quantiles, volume exponent and coordination number. The model parameters, volume exponent and coordination number, for the models in the neighbourhood of the P90 model are connected by a line between all the axes.

6.3 Effect of Network Size

This section investigates the effect of network size on the network parameter inference. The objective is to use smaller networks in the calculation of the statistical solution to the inverse problem and then perform forward prediction of the relative permeability in larger networks. For all of the cases with different network sizes, the stochastic inversions were performed at the same temperature and with the same number of molecular dynamics steps and step size.

v, $\overline{Z}$, and pore-size distribution are shown for a lattice with almost seven times more pores (lattice constant $L = 15$) in Figs. 6.18–6.20. The posterior histograms are only slightly affected by the variation in the lattice size. The bivariate plots show the same features, but the local minima are different. However, the inversion for lattice with $L = 8$ and 15 compare

favourably with the true parameters, and show no sign of systematic deviations.

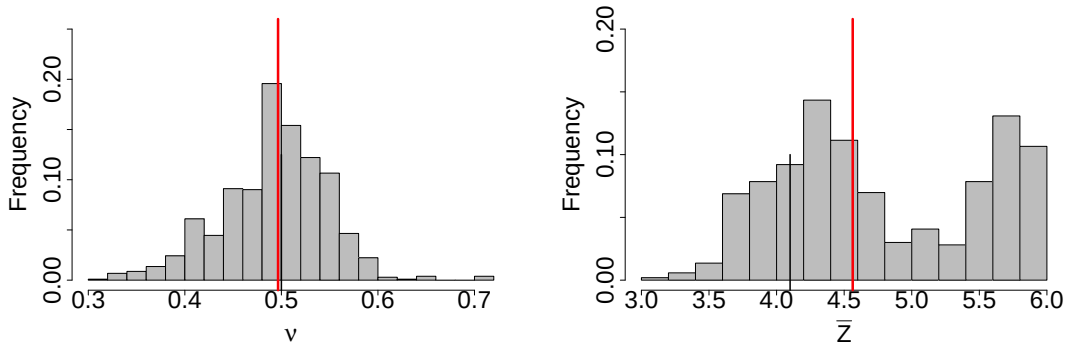

Fig. 6.18 Marginal histogram of the volume exponent ν using the parameterisation proposed in this work for a network size of lattice constant $L = 15$. The vertical red line indicates the median of the samples and the black line indicates the true value of the parameter.

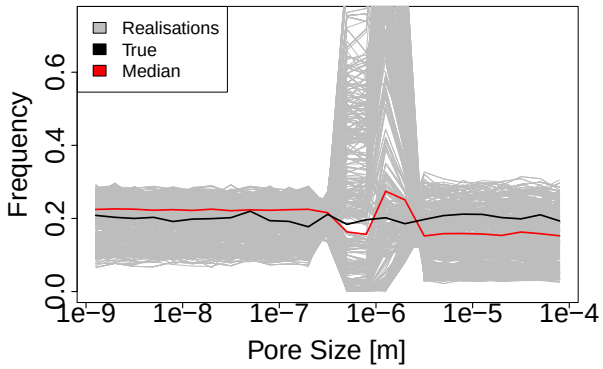

Fig. 6.19 Marginal pore-size distributions using the proposed parameterisation for a network size of lattice constant $L = 15$.

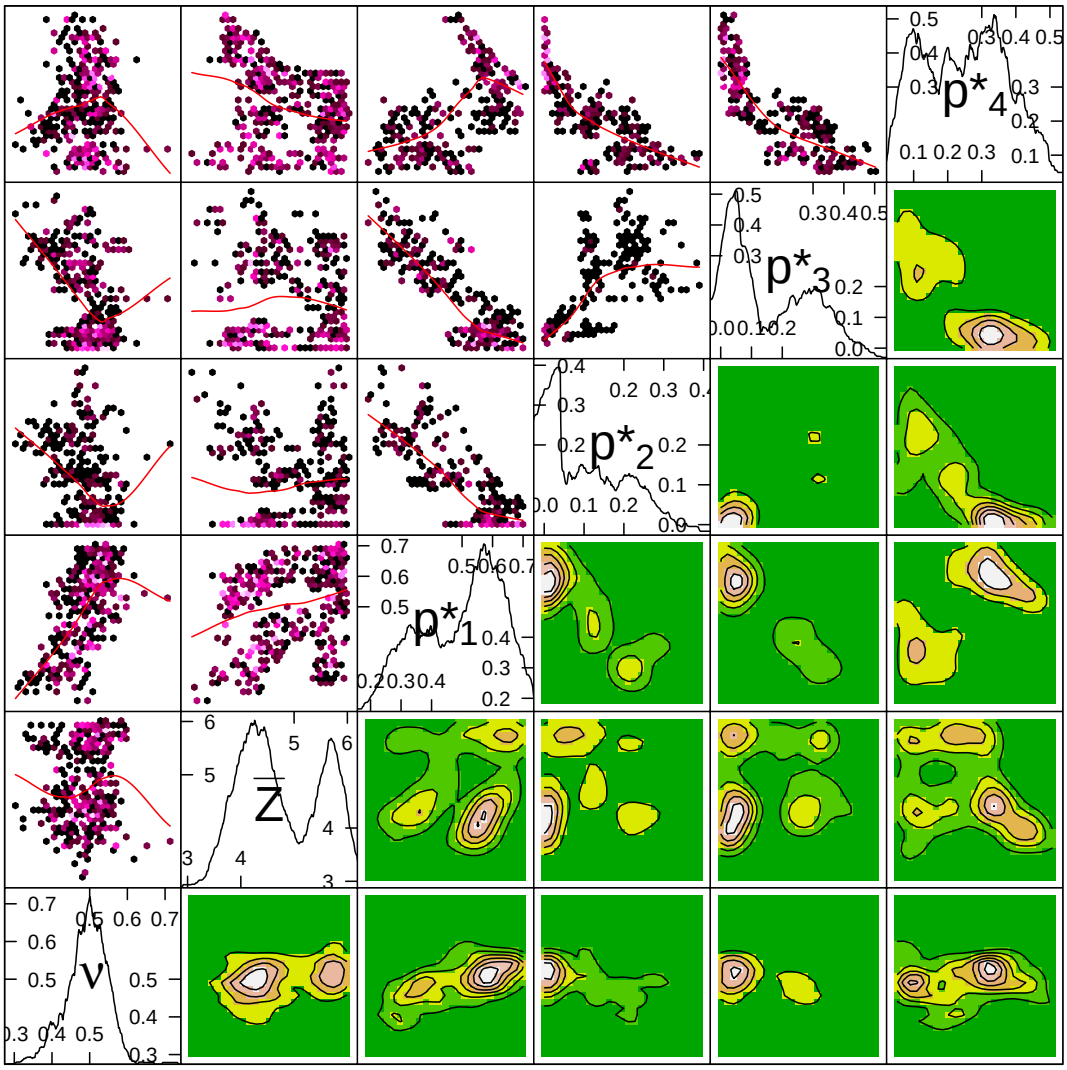

Fig. 6.20 Matrix of all pairs of parameters using the logarithmically equidistant bin parameterisation. The magnified cells show the strong correlations between small contributions from the small pores and the pore-size distribution (bins probabilities p_1^*, p_2^*). The magnified cells on the edge of the matrix show that ν is strongly correlated with p_1^* and p_2^*. The logarithmically equidistant parameterisation creates a more complex topography of the solution space than the parameterisation proposed in this work. Graph equivalent to Fig. 6.6 but for a network size of $15 \times 15 \times 15$.

6.4 Effect of Statistical Temperature

This section includes studies of the effect of temperature on the network parameter inference. As was mentioned in Chapter 4, the temperature (β in Eq. 4.25) behaves as a variance or a scaling parameter.

The posterior histograms show a less defined shape (Fig. 6.21–6.22) with respect to the previous section. However, the differences are almost the same for all of the network sizes ($L = 7, 9, 11,$ and 15). The qualitative difference in these histograms with respect to the previous section is because β in Eq. (4.25) behaves as a variance that controls the variability in the exploration of the total Hamiltonian levels. As expected, the variance in the posterior histograms increased, although the true parameters can be inferred from the median statistics for all network sizes (Fig. 6.21–6.23).

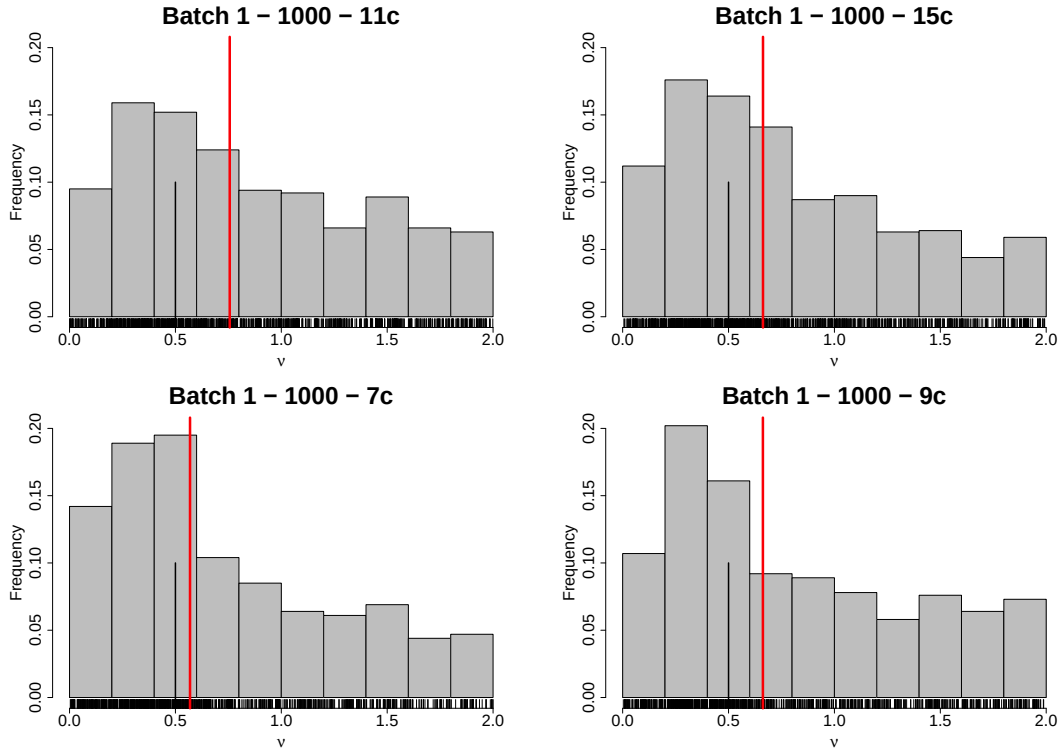

Fig. 6.21 Marginal distributions of the volume exponent for different network sizes: $L = 7$ (bottom left), $L = 9$ (bottom right), $L = 11$ (top left), and $L = 15$ (top right). The vertical red line indicates the median of the samples and the black line indicates the true value of the parameter.

Chapter (4) introduced the concept of bias (bias = $\widehat{m} - m$), which describes the deviation of an estimator from the true value. The median of each distribution shown in Figs. 6.21–

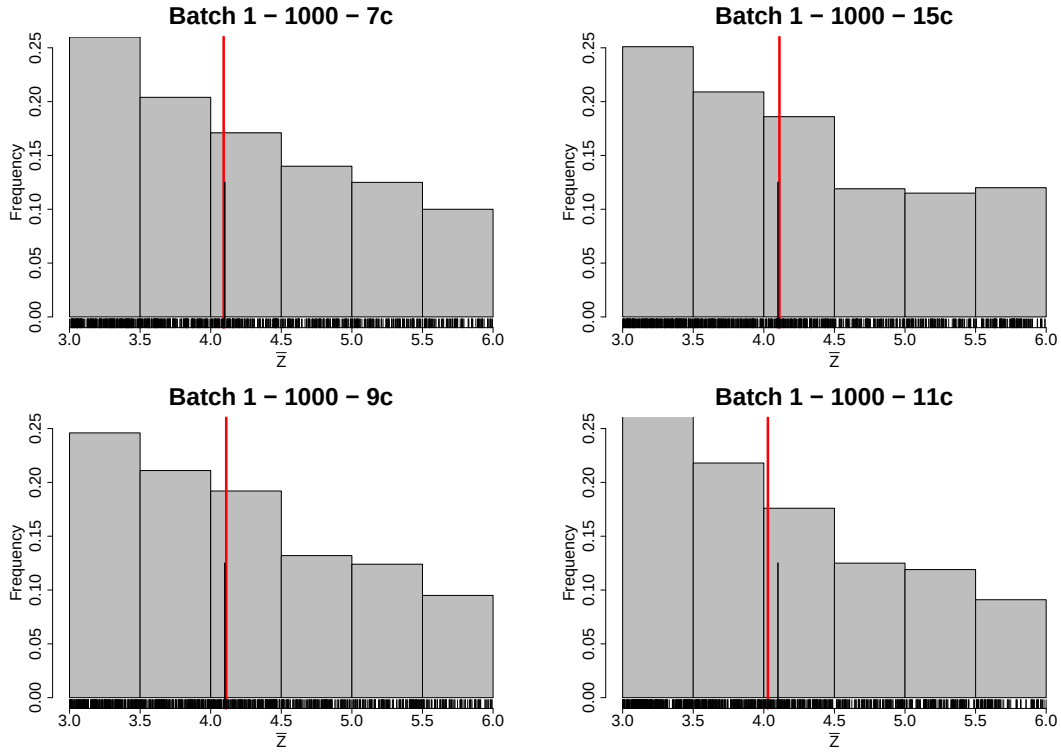

Fig. 6.22 Marginal distributions of the coordination number for different network sizes: $L = 7$ (top left), $L = 9$ (bottom left), $L = 11$ (bottom right), and $L = 15$ (top right). The vertical red line indicates the median of the samples and the black line indicates the true value of the parameter.

6.23) is represented by $\widehat{m}$, and m is the true value of each parameter. In the case of a distribution, the discrepancy between the known and the estimated pore-size distribution is calculated with the KLD. Figure 6.24 shows a statistical summary of the parameters as a function of network size. In the plots of ν and $\overline{Z}$, the medians are free from any systematic bias toward network size, otherwise a systematic deviation would have been observed in the plots. The pore-size distribution shows a weak dependence on the network size because the KLD in the pore-size distribution plot decreases from 7 to 8.

The samples in the chain were grouped in continuous p sub-blocks, and a median and variance was calculated for each sub-block. Following this methodology, with increasing number of blocks, the correlation of the samples decreases and the sample variance estimator better approximates the true variance of the parameter [41]. The correlation time can be calculated by

$$\kappa = \frac{\sigma^2_{block}/N_{block}}{\sigma^2/N} \tag{6.3}$$

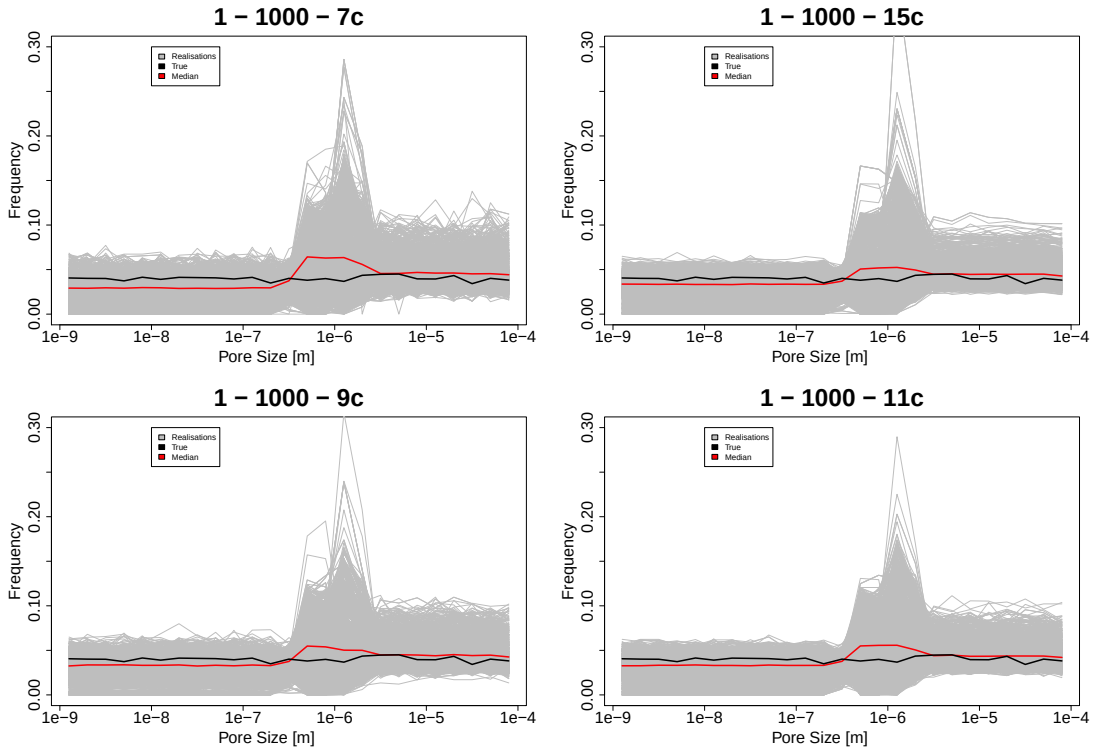

Fig. 6.23 Marginal distributions of pore-size distributions for different network sizes: $L = 7$ (top left), $L = 9$ (bottom left), $L = 11$ (bottom right), and $L = 15$ (top right).

Calculating κ for various blocks shows that the behaviour follows a positive slope and levels off. This is seen in Fig. 6.25 in the intersections TauCnu–Size and TauZ–Size. The network size seems to affect the correlation time (bottom two cells in the first column of Fig. 6.25, which is expected to be because a larger network is less affected by seed noise and slightly larger time steps can be taken, reducing the correlation. The behaviour seems to fluctuate and there is no clear pattern to indicate that using a large network model with $L = 15$ will considerably improve the solution to the inverse problem. The effect of lattice size on estimation of the structural network parameters by the statistical solution to the inverse problem is practically negligible in the range of lattice sizes considered.

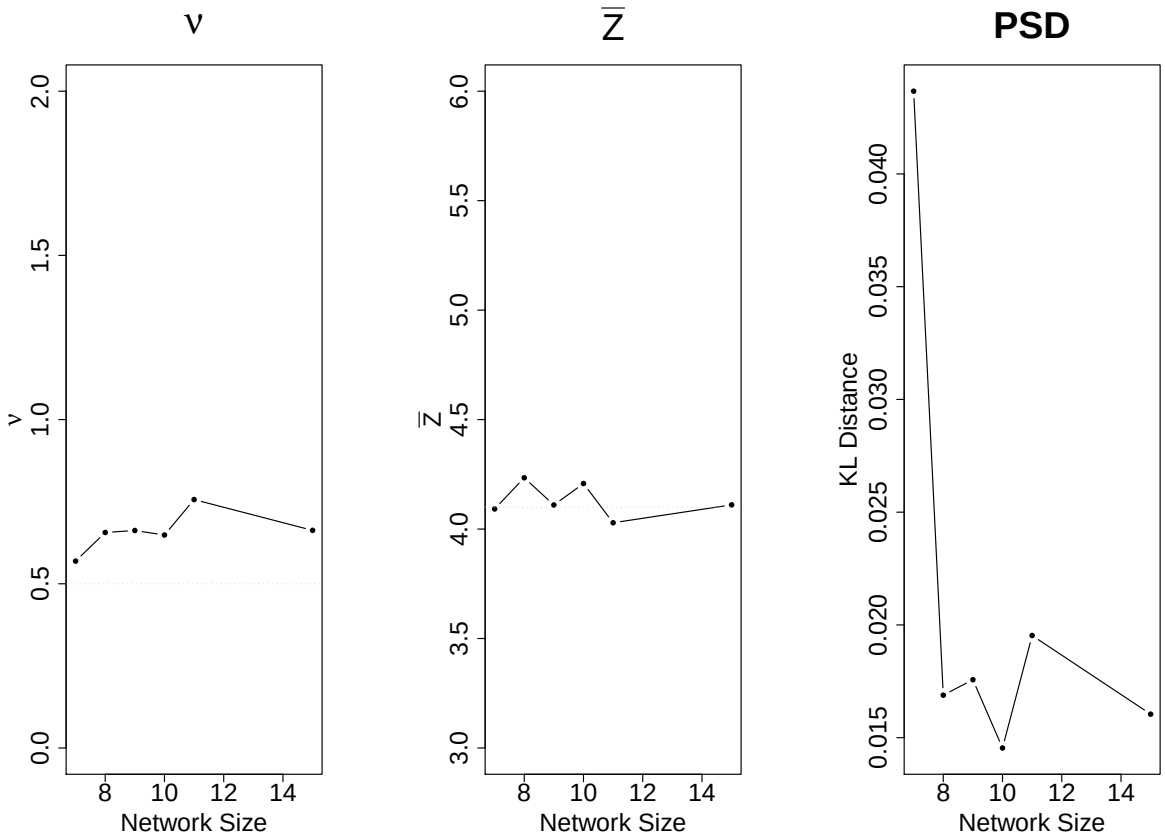

Fig. 6.24 Median statistics as a function of network size. From left to right, volume exponent, coordination number, and pore-size distribution.

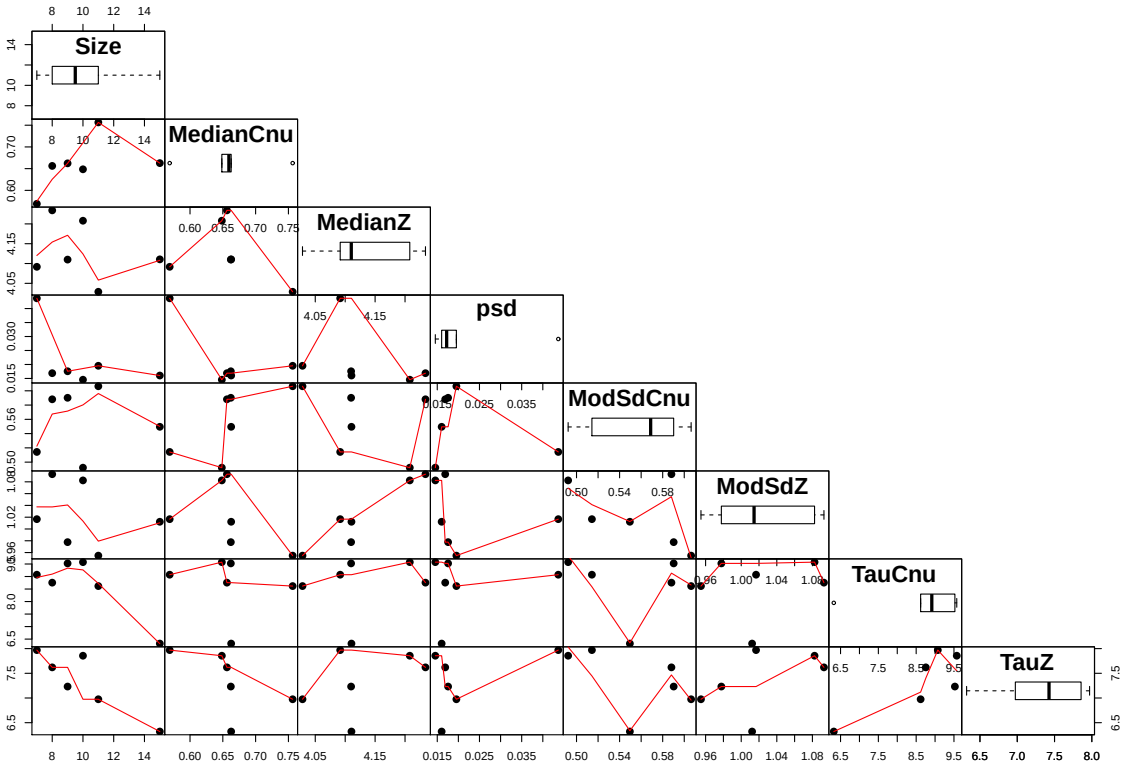

Fig. 6.25 The diagonal panels show box-and-whisker plots, where the thick black bar within the box is the median. The left and right edges of the box are the first and third quantiles. The cross-plots below the diagonal compare all pairs of parameters, namely, network size, volume exponent batch median, coordination number batch median, KLD, pore-size distribution (psd), volume exponent median deviation (indicator of spread instead of the standard deviation when the median is used), coordination number median deviation, volume exponent correlation time, and coordination number correlation time. In each bivariate plot there is an overlay with a smoother to help visually identify any trend in the data.

6.5 Summary of the Chapter

In this chapter, we applied the method developed in Chapters (4) to a synthetic case and the output of HMC reflects the true parameters. The first section investigated the effect of different parameterisations of the pore-size distribution on the estimation of the median network parameters and the results suggested that the proposed parameterisation performed better. In the second part the effect of network size and the temperature was investigated. The results suggested that the network size has a minor influence on the statistical solution to the inverse problem. Thus, it is viable to obtain the statistical solution to the inverse problem with relatively small networks and perform the relative permeability calculations with relatively large networks.

This simulation not only shows that the method can obtain the true values, but also provides a check of the correctness of the program.

The statistical solution to the inverse problem is a hyperspace with dimensions $N+1$. The energy (misfit) is the landscape, or the equivalent probability. The low-energy regions are equivalent to high-probability regions. The last section investigated two-dimensional projections of the solution space. It appears that the regions of high probability are concentrated. The relation between the energy and the parameters is nonlinear. There are multiple maxima, and in some projections the regions of high probability are separated by valleys.

Chapter 7

Carbonate Rock Samples

7.1 Pore-Network Model Structure

This chapter discusses the application of the theory developed in Chapter 4 to three carbonate reservoir samples from the Middle East introduced in Chapter 3. The samples were classified into rock types I (RT-I), II (RT-II), and III (RT-III) in order of decreasing reservoir quality. The three rock type samples are a subset of the extensive data set that was studied by Masalmeh [241] [244]. The reservoir quality refers to two basic geologic properties of the rocks: porosity and permeability [358]. The reservoir quality is determined by the depositional and postdepositional characteristics of the rock.

RT-I, RT-II, and RT-III follow a petrophysical classification that describes the pore space in terms of its fabric, namely, the organisation of the pore space (Lucia classification [224]) and Dunham's classification [98], which takes into account the paleoenvironment where the sediments that made the rock were deposited).

RT-I is a fine to coarse grainstone associated with a high energy shoal and beach paleoenvironment. Therefore, it is an intergrain dominated porosity rock with grain texture [224]. The range of absolute permeabilities is 40–800 mD with very low capillary entry pressure. RT-II is a fine to coarse grain-dominated packstone. The paleoenvironment ranges from high-energy shoal to lagoonal. This sample shows intergrain porosity, but there is also intergrain space filled with mud [224]. The range of absolute permeabilities is 2–5 mD. RT-III is a medium to poorly sorted wackestone to packstone rock, and the paleoenvironment is lagoonal.

Figure 7.1 summarizes the workflow on which the pore-network model parameters are based on. In this section we focus in the HMC inversion of pore-network model structure in (1).

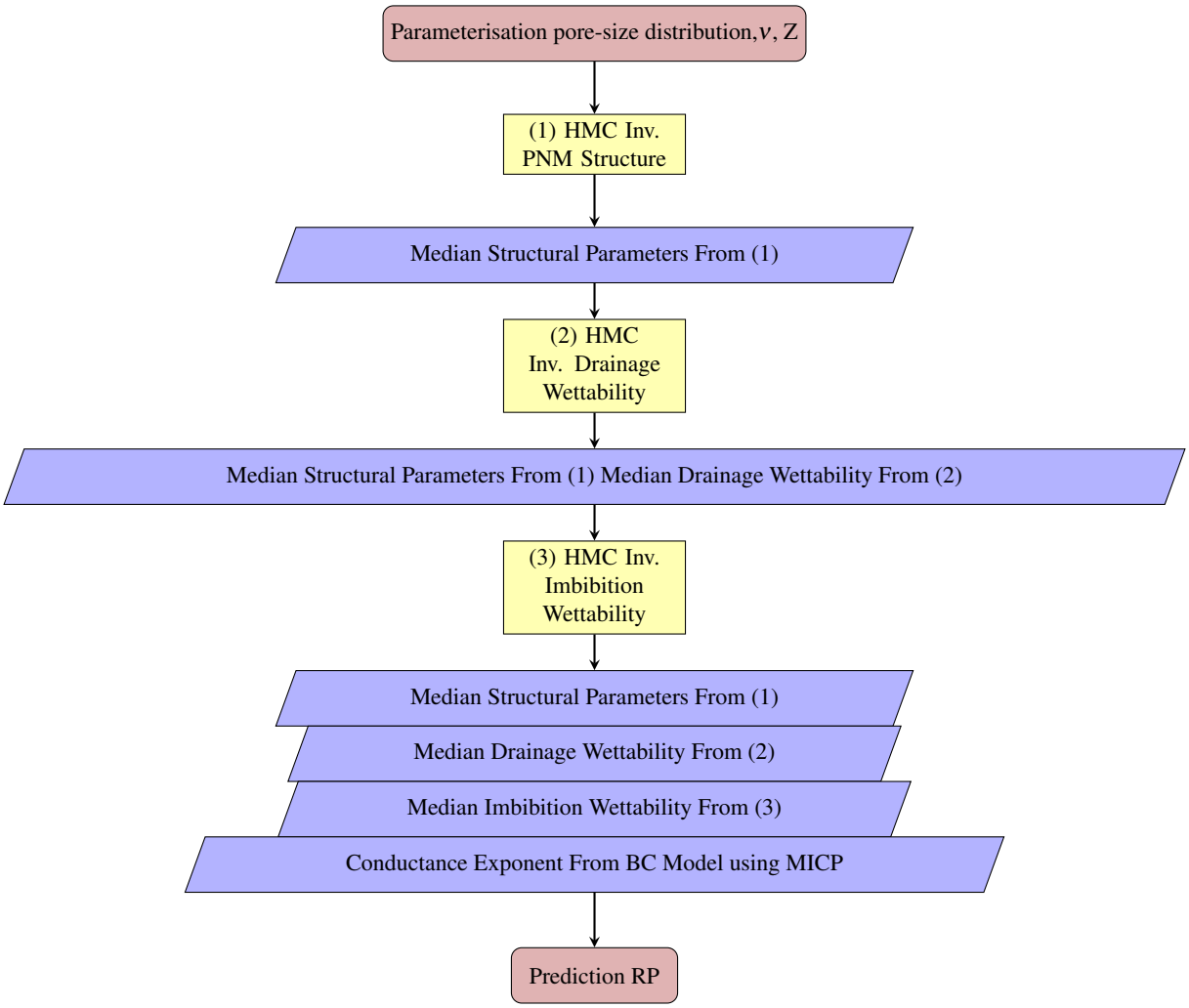

Fig. 7.1 Hamiltonian Monte Carlo Inversion Workflow

7.1.1 Pore-Network Model Structure of RT-I S 28

RT-I fits into the group of grainstones in Dunham's classification system. As shown in Fig. 7.2a, the Ritter and Drake estimator of the pore-size distribution (Eq. (4.3)) overestimates the number of small pores, masking the bimodal shape of the pore-size distribution. The logarithmic derivative (LogDerivative) estimator (Eq. (4.4)) is better than Eq. (4.3) at showing bimodal behaviour, although it overestimates mid- to large-sized pores. Our proposed estimator (Eqs. (4.5) and (4.6), Fig. 7.2a) provides a better balance of all pore sizes. Parameterisation of the pore-size distribution was performed by applying Eq. (4.6) to the mercury intrusion capillary pressure (MICP) data. Equation (4.6) produced the raw histogram shown in Fig. 7.2a (this work). Then, we joined the bins in the raw histogram while ensuring that they all had the same entropy to produce the parameterisation of the

pore-size distribution shown in Fig. 7.2b.

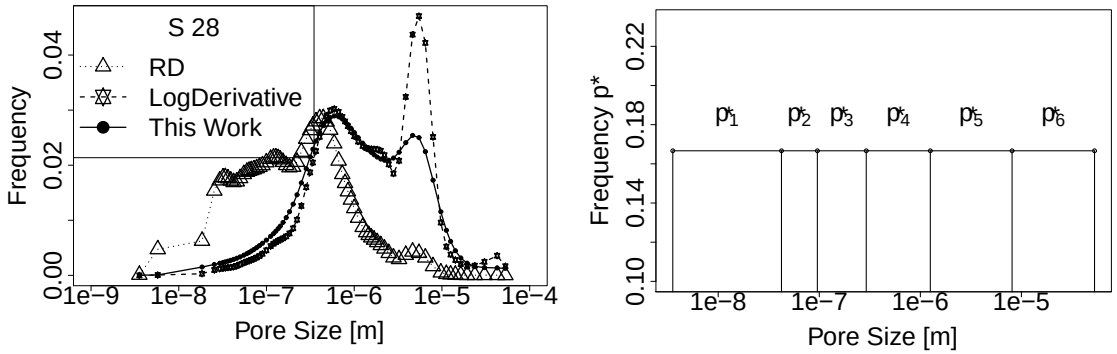

a b

Fig. 7.2 (a) Pore-size distribution estimators applied to S 28 MICP data: Eqs. (4.3) (RD), (4.4) (LogDerivative), and (4.6) (this work). (b) Parameterisation of the pore-size distribution with equal entropy in each bin.

The bimodality was sufficiently captured using six bins. The parameterisation used these six bins (based on Eq. (4.6)) to model the pore-size distribution (Fig. 7.2b), volume exponent ν, and coordination number $\overline{Z}$ (Chapter 4.4). The process described in Chapter 4.2.3 split the distribution into a set of bins with equal entropy while maximizing the total entropy. This produced a coarser pore-size distribution than the other methods, as shown in Fig. 7.2a. The total entropy was maximised with respect to the initial entropy of the pore-size distribution estimator (Fig. 7.2a (this work) and Eq. (4.5)).

Figure 7.3 shows the marginal histograms (ν and $\bar{Z}$) and Fig. 7.4 the bivariate scatterplot for all pairs of parameters for S 28. Both marginal histograms are positively skewed. From Fig. 7.3a, the median estimator obtained by Hamiltonian Monte Carlo (HMC) inversion is greater than the usual assumption that the volume exponent is zero.

The medians of the bin probabilities in the parameterisation of the pore-size distribution (Fig. 7.5a, red solid line) have two well-defined populations: large pores (≥ 2 μm) and small pores (< 2 μm). Because of the known limitation in SEM images to capture the real size of 3D pores, large pores of the sizes seen in Fig Fig. 7.5a cannot be seen. However, it is clear from the SEM images that there is a bimodal distribution. Consistent with Fig. 7.5a.

Figure 7.5b shows a comparison between the MICP measurements (black solid line) and the MICP simulated using the median parameters estimators obtained by HMC inversion (red line). The predicted MICPs based on the median parameters agree well with the data.

Figure 7.5c shows the kernel estimator of the pore-size distribution. Using the sampling

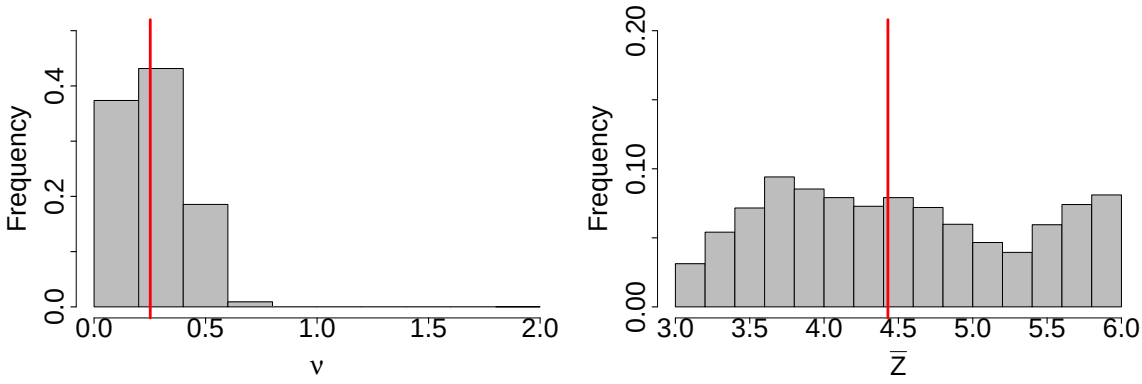

a b

Fig. 7.3 Sample S 28: (a) Marginal posterior histogram of the volume exponent (ν), (b) Marginal posterior histogram of the average coordination number ($\bar{Z}$) (red lines indicates the median values).

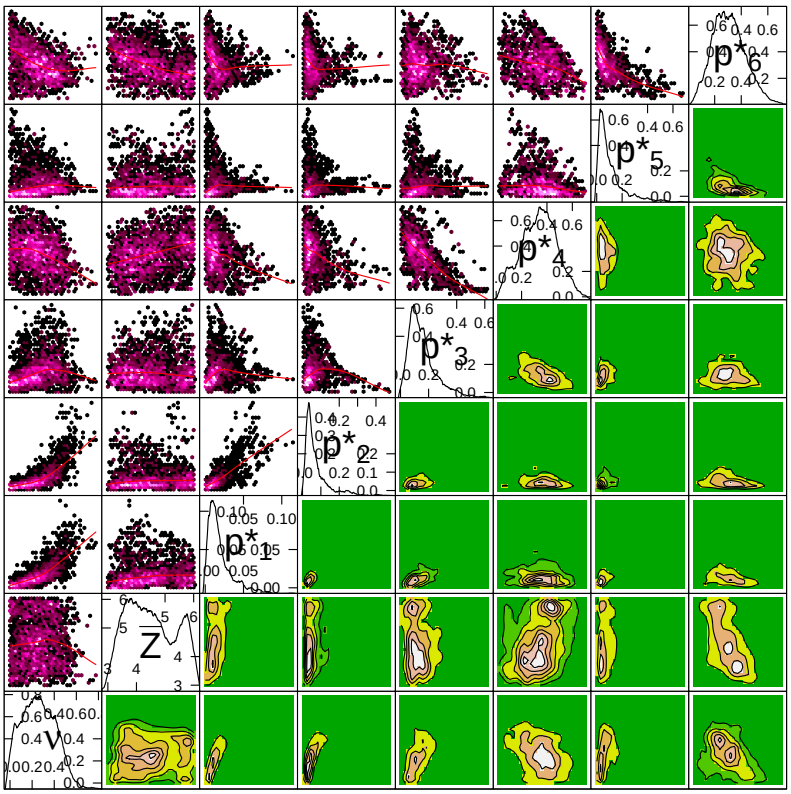

Fig. 7.4 Sample S 28: Bivariate scatter plots of all pairs of parameters. The bivariate scatterplots show the complexity and local minima of the solution space.

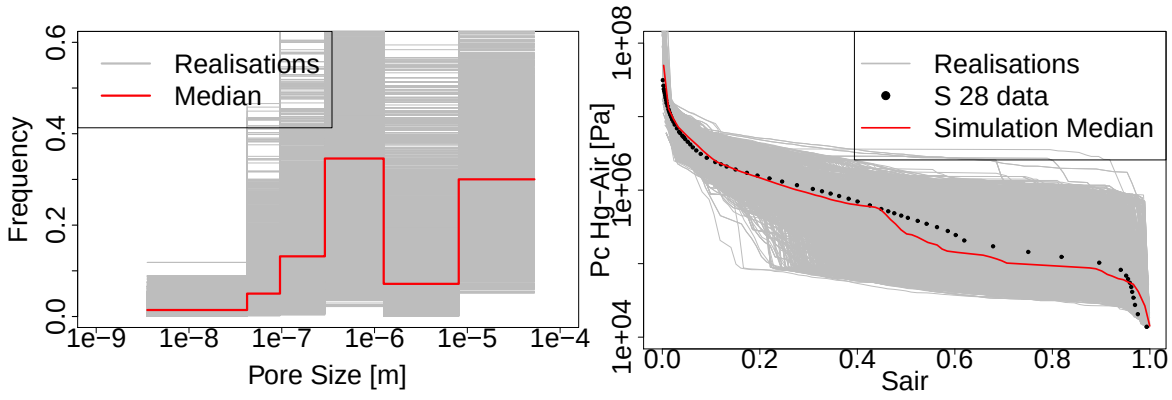

a

b

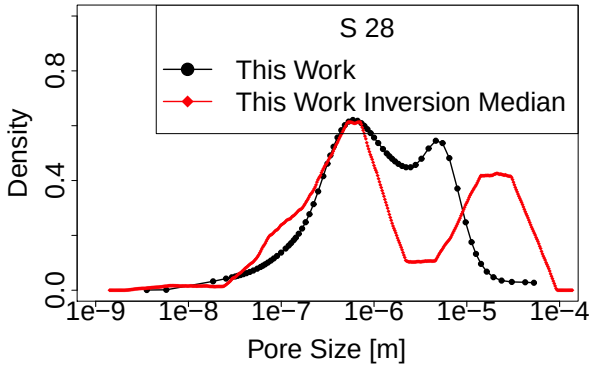

c

Fig. 7.5 (a) Posterior distribution of the probability associated with each bin in the parameterisation shown in Fig. 7.2b (red line indicates the median probabilities for each bin). (b) MICP simulations associated with the HMC realisations corresponding to the parameters in the graph in (a) (grey) and to the graphs in Fig. 7.3. (c) Comparison of the pore-size distribution after HMC inversion with the estimator derived using the MICP (Eq. (4.6)).

method discussed in Chapter 4.2.2, the median bin probabilities and the pore-size distribution parameterisation generated a set of pore-size observations. Then, we applied the kernel density estimator to produce the density function shown in Fig. 7.5c (this work, inversion median). We can use this procedure to easily compare the initial estimators (Eq. (4.6)), which are used to define the parameterisation. The curves were normalised so that the integral in the logarithmic transformation of pore sizes was equal to one. It should be noted that the median pore-size distribution obtained from the HMC inversion had more large pores than the initial estimation with Eq. (4.6). The overlay of the estimator of the pore-size distribution (Eq. 4.3) indicates that a large number of large pores above the small size mode have appeared. This is consistent with the shielding effect caused by the percolation process. The pore-size distribution is bimodal (Fig. 7.5c). It is also interesting to note that the estimator proposed in this work (Eq. (4.6)) almost overlays the results of the inversion in the range of pore sizes below 1 μm. It is important to note that both the Ritter and Drake and LogDerivative methods do not predict the data well.

We assume that the narrower the pore-size distribution, the stronger the correlation between the pore radius and the pore volume. S 28 has a wide bimodal pore-size distribution, because there might be a strong contribution from two families of pores (bimodal behaviour) with different characteristics. Thus, ν is low, indicating that there is a weak correlation with both families of pores as a whole.

7.1.2 Pore-Network Model Structure of RT-II S 2 4

The Dunham classification of RT-II is pack–grainstone (mixture of packstone and grainstone dominated by grainstone). RT-II is poorer in quality than RT-I. The pore-size distribution estimator has similarities to that of the synthetic case (Chapter 6). This suggests that the distribution could be either uniform or unimodal (Fig. 7.6a). Similar to RT-I S 28, the classical Ritter and Drake method positively skews the pore-size distribution estimator.

The resulting parameterisation using the method described in Chapter 4.2.3 has a similar shape to the synthetic case. However, p_1^*, p_2^*, and p_3^* are higher than their equivalents in the synthetic case. Although the shape of the pore-size distribution estimator (Fig. 7.6a) is similar to the one in Fig. 6.2b, the parameterisations are different because the bins were joined based on the calculations of the entropy for the real data (discrete points that represent the data).

Figure 7.7 shows the posterior histograms of volume exponent and average coordination number. In contrast to Fig. 7.3, the median of the volume exponent is two times greater

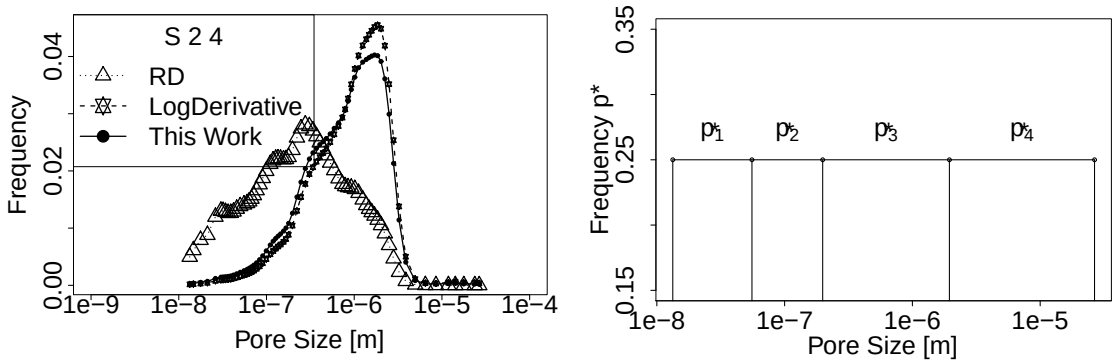

a b

Fig. 7.6 (a) Pore-size distribution estimators applied to S 2 4 MICP data: Eqs. 4.3 Ritter and Drake (RD), 4.4 (LogDerivative), and 4.6 (this work). (b) Parameterisation of the pore-size distribution with equal entropy in each bin.

than for the RT-I case. Although ($\bar{Z}$) median values are similar, the distribution for RT-II is positively skewed with a cluster of data around four.

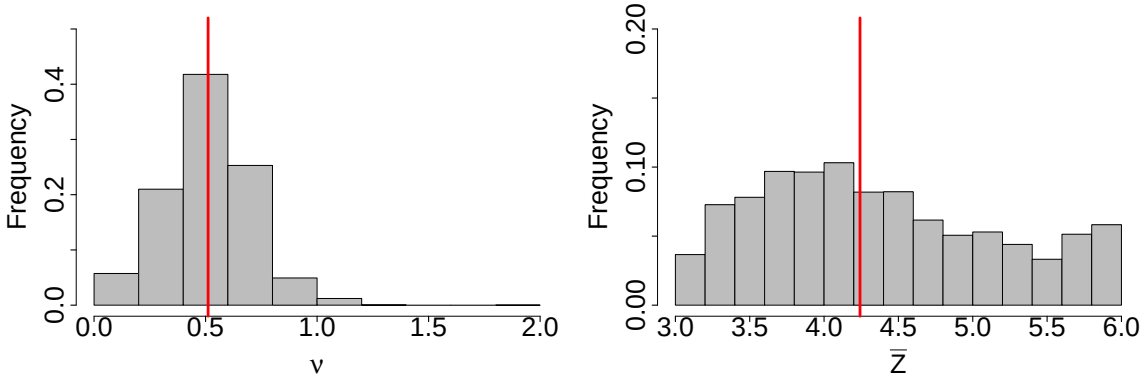

a b

Fig. 7.7 Sample S 2 4: (a) Marginal posterior histogram of volume exponent (ν). (b) Marginal posterior histogram of average coordination number ($\bar{Z}$) (red lines indicate the median values).

Fig. 7.8 shows the general structure of the sample space of RT-II S 2 4. Microporosity (p_1^* and p_2^*) correlates with the volume exponent.

The HMC inversion indicates that the pore-size distribution is uniform, although there are slightly more pores in the small pore-size range (Fig. 7.9a and c). It is also interesting to note that, for this case (the explanation extends to the RT-III sample), the initial estimator

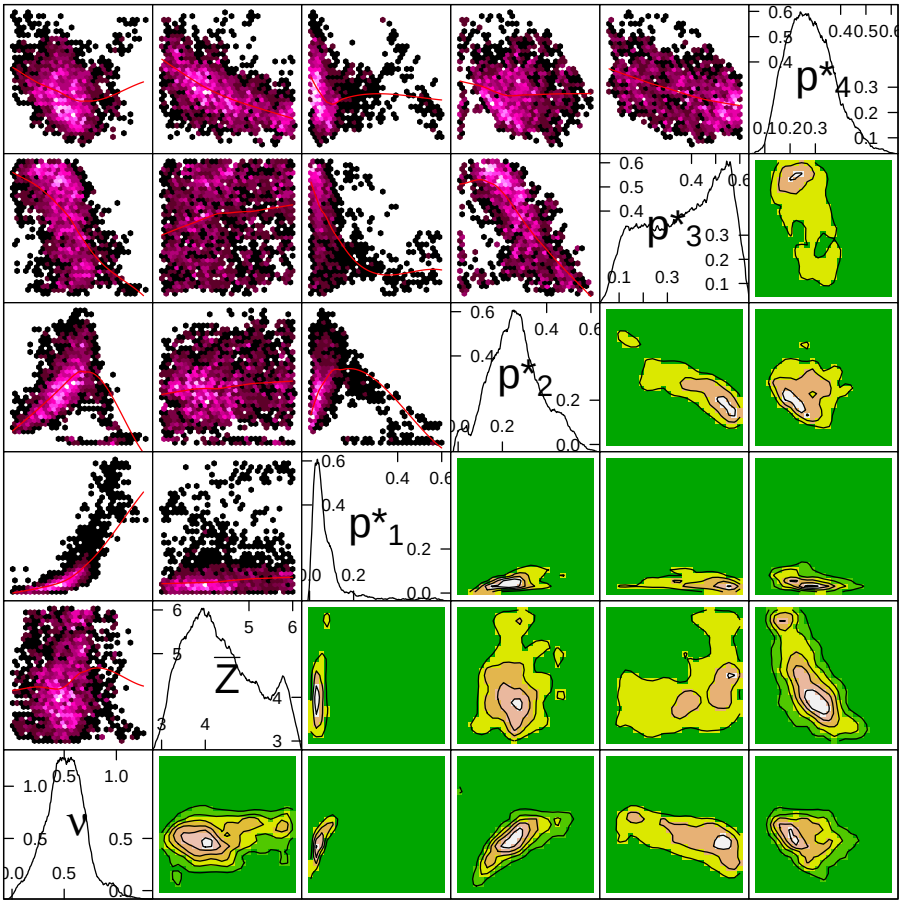

Fig. 7.8 Sample S 2 4: Bivariate scatterplots of all pairs of parameters. The bivariate scatterplots show the complexity and local minima of the solution space.

proposed in this work (Eq. (4.6)) underestimated the pore-size distribution in the range of pore sizes below 0.5 μm. However, the Ritter and Drake still overestimates that region of the pore-size distribution. This is expected because the error in Eq. (4.6) increases as the pore-size distribution becomes more uniform. The closer the pore sizes are to the percolation threshold, the greater the expected error in Eq. (4.6). However, the Ritter and Drake method is unaffected by the percolation threshold. It always produces similar pore-size distribution estimators and only varies in the range of pore sizes (Figs. 7.2a Ritter and Drake, 7.6a Ritter and Drake, and 7.10a Ritter and Drake). However, the estimator proposed in this work gives consistent information about the invasion sequence and is independent of the range of pore sizes. For the sake of argument, if one could tend to the limit of a bundle of tubes in which the pore-volume versus pore-size relationship is unknown, the Ritter and Drake would still depend on the range of pore sizes, while Eq. (4.6) would give a very good estimate of the pore-size distribution.

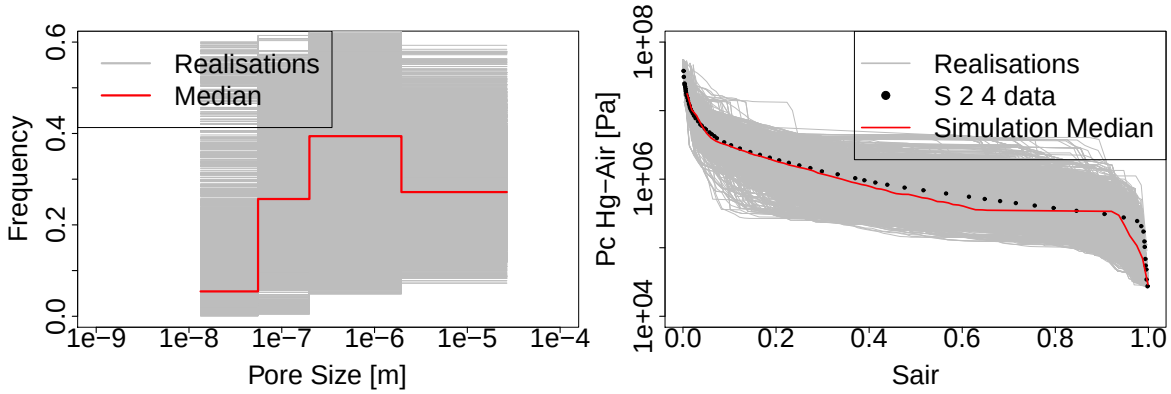

a

b

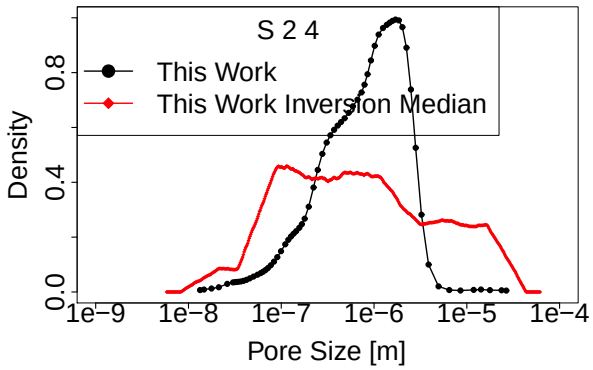

c

Fig. 7.9 Sample S 2 4: (a) Posterior distribution of the bin probabilities in the parameterisation shown in Fig. 7.6b (red lines indicate the median probabilities for each bin). (b) Simulated MICP using the median parameters. (c) Comparison of the pore-size distribution after HMC inversion with the estimator derived using the MICP (Eq. (4.6)).

7.1.3 Pore-Network Model Structure of RT-III S 2 20

RT-III has poorer reservoir quality than RT-II. RT-III is a wackestone–packstone (mixture of wackestone and packstone, where packstone dominates) in the Dunham classification. The pore-size distribution estimator is similar to the synthetic case, although the distribution is more symmetrical and the tails are different. For small pore sizes, there is a gradual decrease in the frequency with decreasing pore size, while there is a sharp decrease for pore sizes greater than the maximum value. In the case of the Ritter and Drake estimator, the peak is flatter compared with the other two samples, making the distribution more positively skewed (Fig. 7.10a).

As explained in the previous examples, the entropy (Eq. (4.8)) was calculated for each

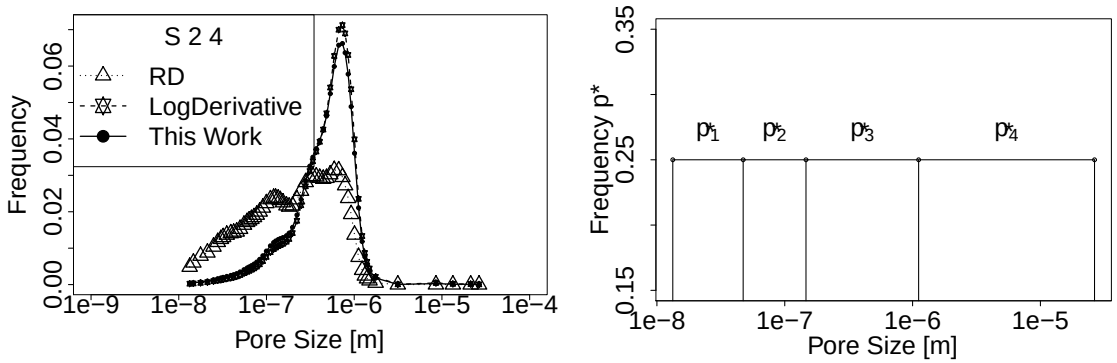

a b

Fig. 7.10 (a) Pore-size distribution estimators applied to S 2 20 MICP data: Eqs. 4.3 Ritter and Drake (RD), 4.4 (LogDerivative), and 4.6 (this work). (b) Parameterisation of the pore-size distribution with equal entropy in each bin.

of the values of the curve (Fig. 7.10a). The parameterisation of the pore-size distribution for sample RT-III 2 20 (Fig. 7.10b) was then calculated by joining the pore-size coordinates of the points to obtain four intervals with the same total entropy.

HMC inversion produced the posterior histograms in Fig. 7.11. The ν histogram is slightly more positively skewed than the corresponding histogram for RT-II S 2 4, and the median is twice the median of RT-I S 28. The average coordination number shows a similar shape to the one for RT-II S 2 4, but it is slightly more positively skewed. It is expected that the right-skewness is related to the rock type.

The medians of each of the posterior histograms of the bin probabilities are shown in Fig. 7.12 (red line). As with the previous cases, we used the sampling method discussed in Chapter 4.2.2 with the median bin probabilities to produce a set of pore-size observations. We then applied the kernel density estimator to produce the density function shown in Fig. 7.12c ('this work inversion median'). The pore-size distribution appears to be similar to RT-II S 2 4, although the contribution of the small pores is greater in RT-III S 2 20 than in RT-II S 2 4.

The general structure of the sample space of RT-III S 2 20 (Fig. 7.13) is similar to that of RT-II S 2 4 . Microporosity (p_1^* and p_2^*) also correlates with the volume exponent.

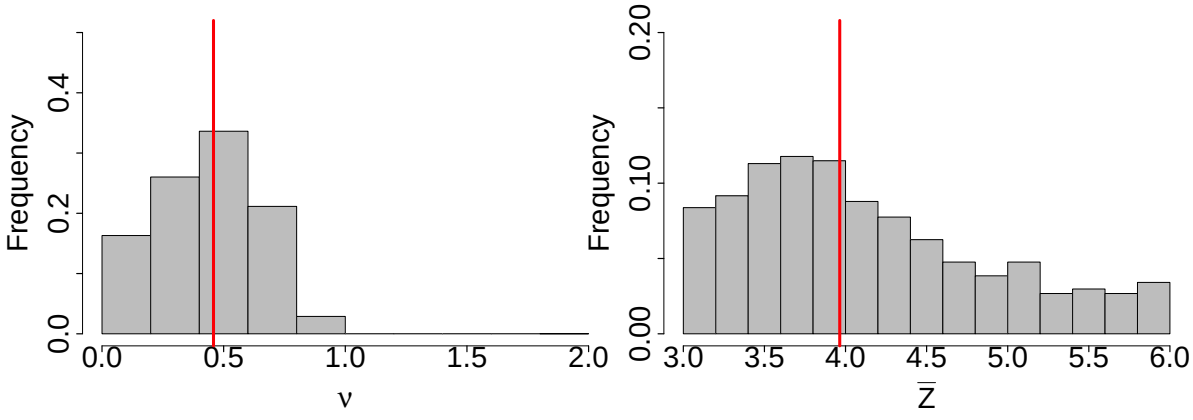

a b

Fig. 7.11 Sample S 2 20: (a) Marginal posterior histogram of the volume exponent (ν). (b) Marginal posterior histogram of the average coordination number ($\bar{Z}$) (red lines indicate the median values).

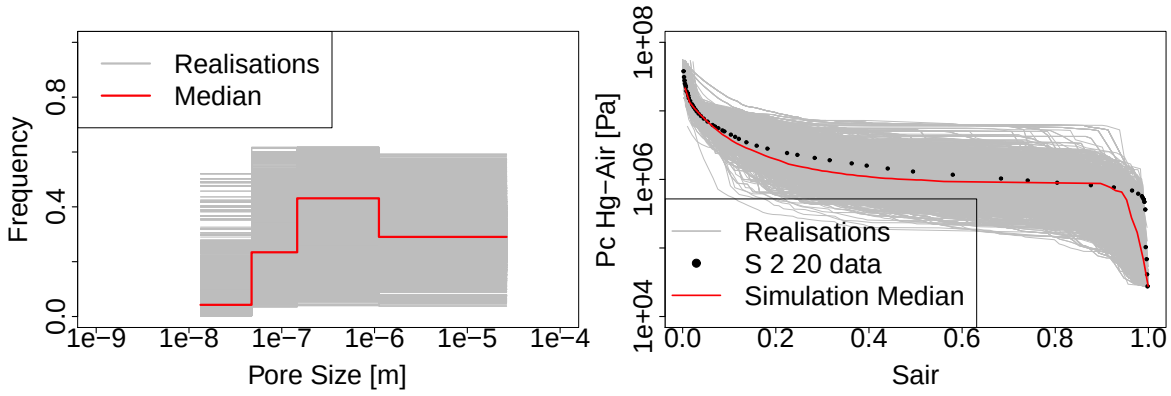

a b

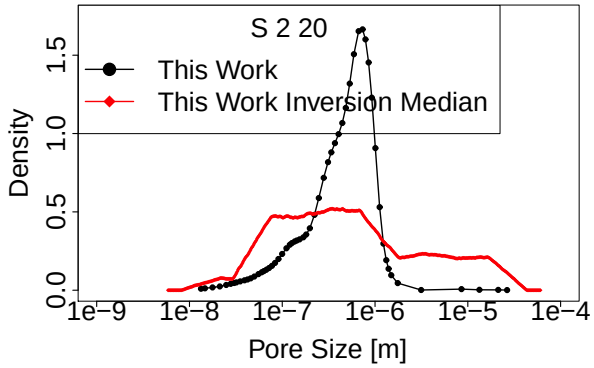

c

Fig. 7.12 Sample S 2 20: (a) HMC realisation data for the bin probabilities in the parameterisation of the pore-size distribution (red line indicates the median probabilities for each bin). (b) MICP simulations associated with the HMC realisation data that correspond to the parameters in the graph in (a) and Fig. 7.11. (c) Comparison of the pore-size distribution after HMC inversion with the estimator derived using MICP data (Eq. (4.6)).

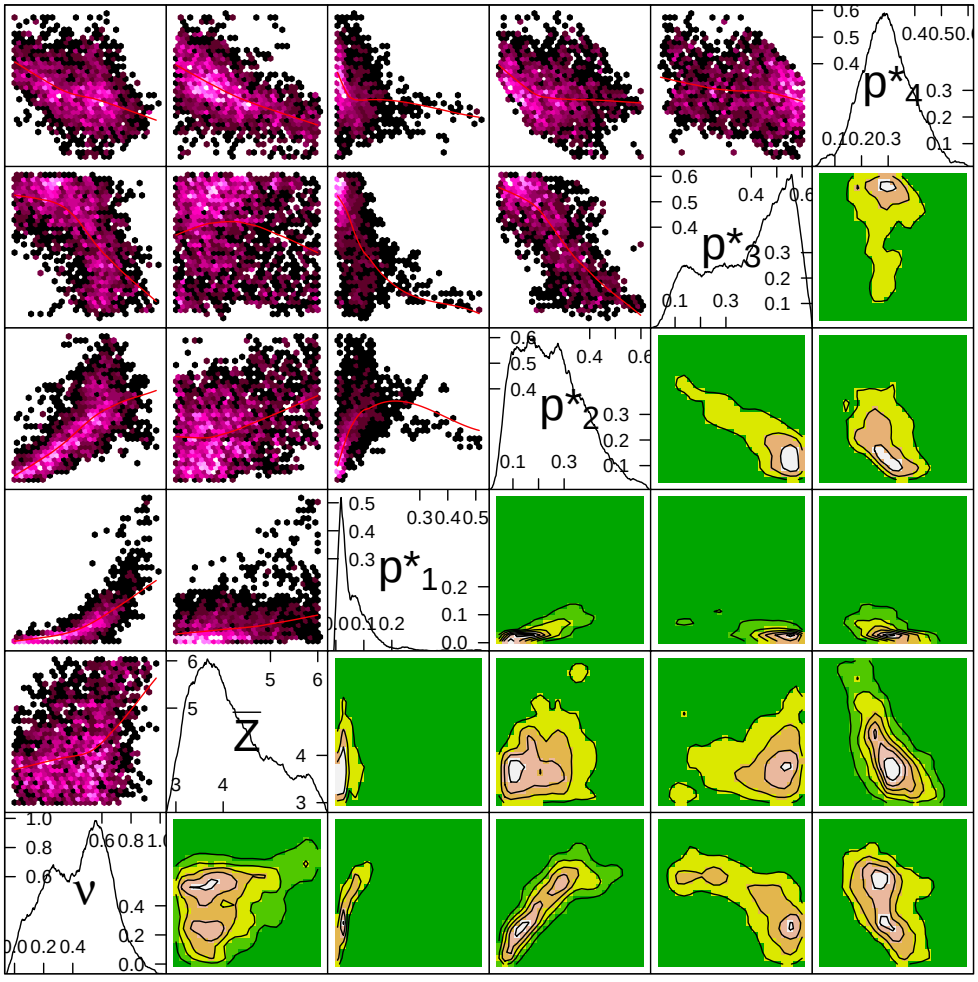

Fig. 7.13 Sample S 2 20: Bivariate scatterplots of all pairs of parameters. The bivariate scatterplots show the complexity and local minima of the solution space.

7.2 Qualitative Comparison of Structural Inversion Patterns with Scanning Electron Microscope Images

Based on the visual patterns on scanning electron microscope images in Chapter 3, we will attempt to make qualitative links with the trends seen in the results presented above about the pore-network model structure parameters. Figures 7.14a1,b1,c1 shows with red outline the porosity and pore shapes identified in the SEM images.

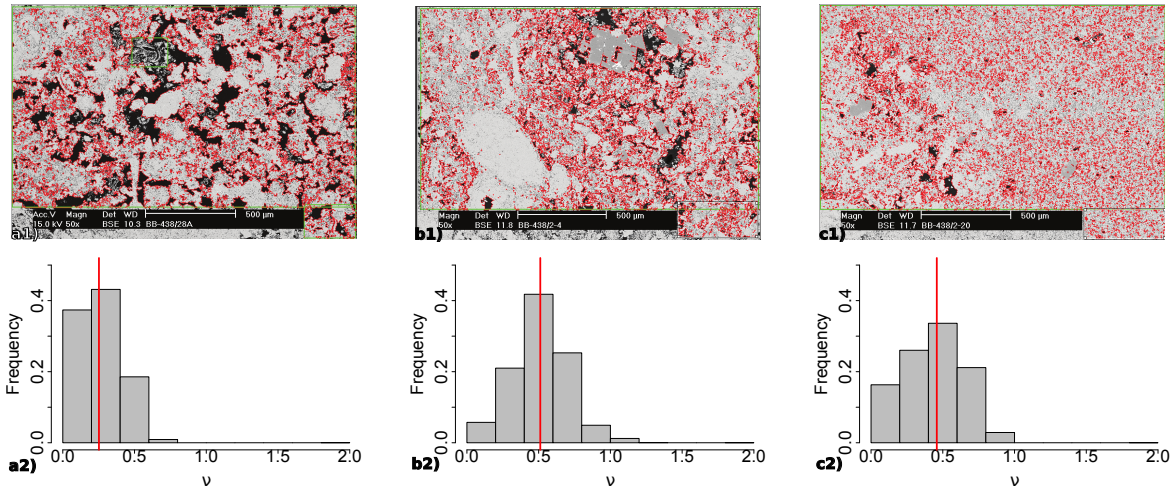

Fig. 7.14 (a1) Scanning electron microscope image of S 28 showing the structure of grains at the largest scale. (a2) Sample S 28 marginal posterior histogram of the volume exponent (red lines indicate the median values). (b1) Scanning electron microscope image of S 2 4 showing the structure of grains at the largest scale. (b2) Sample S 2 4 marginal posterior histogram of the volume exponent (red lines show the median values). (c1) Scanning electron microscope image of S 2 20 showing the structure of grains at the largest scale.(c2) Sample S 2 20 marginal posterior histogram of the volume exponent (red lines show the median values).

Figures 7.14a1,b1 and c1 show 50x magnified SEM images for rock types I, II, and III and Fig. 7.14a2,b2 and c2 show the posterior histogram of volume exponent for rock type I, II and III respectively. It can be seen that there is correlation between the skewness of the posterior histogram and the patterns in images. Consistent with the complex pore shapes seen in the images, we find that volume exponents for the three rock types are smaller than one. Figure 7.14a2 shows that the volume exponent for rock type I is lower than for the other two rock types. In rock type I, the two sets of pores and the dissolution process create a pore structure more irregular reducing the correlation between pore volume and pore radius than the other two samples.

The posterior histograms of the average coordination number, presented in Figs. 7.15a2,

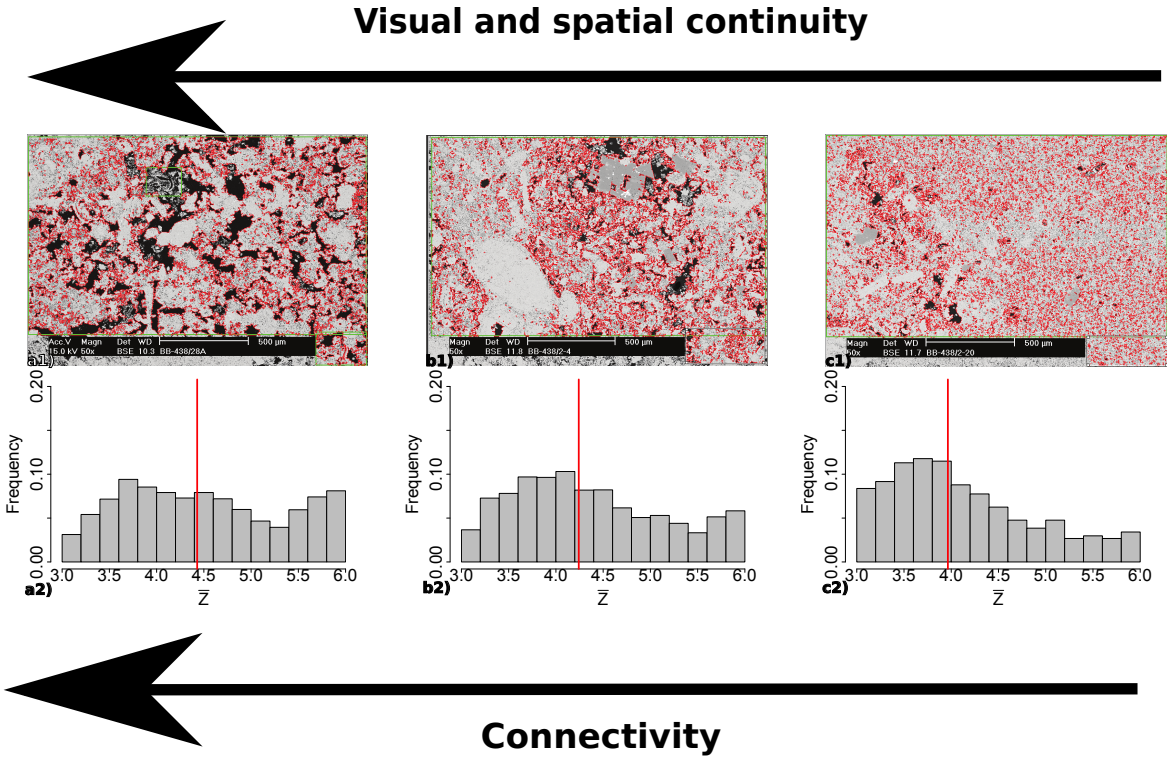

Fig. 7.15 (a1) Scanning electron microscope image of S 28 showing the structure of grains at the largest scale. (a2) Sample S 28 marginal posterior histogram of the average coordination number ($\bar{Z}$) (red lines indicate the median values). (b1) Scanning electron microscope image of S 2 4 showing the structure of grains at the largest scale. (b2) Sample S 2 4 marginal posterior histogram of the average coordination number ($\bar{Z}$) (red lines show the median values). (c1) Scanning electron microscope image of S 2 20 showing the structure of grains at the largest scale. (c2) Sample S 2 20 marginal posterior histogram of the average coordination number ($\bar{Z}$) (red lines show the median values).

b2, c2, show a strong correlation with the visual pattern of connectivity in the porosity of Figs 7.15a1, b1, c1.

Comparison of Figs 7.16a, c, d with the pore-size distribution obtained from the HMC inversion (Figs 7.16b) shows that the bimodalilty is consistent with the images.

As observed in the median pore-size distribution obtained from HMC for sample S 2 4 and S 2 20 Fig. 7.17e and Fig. 7.18g respectively, there is more microporosity than in. The images in Figs 7.17a,b,c,d,e and Figs7.18a, b, c, d, e, f seem to confirm that there is more microporosity in relation to macroporosity. But still a few large pores greater than 100 μm can be seen in Figs. 7.16a, 7.17a and 7.18a.

In general, very good agreement is found between visual features in scanning electron microscope images and the structural pore-network model parameters for the three samples.

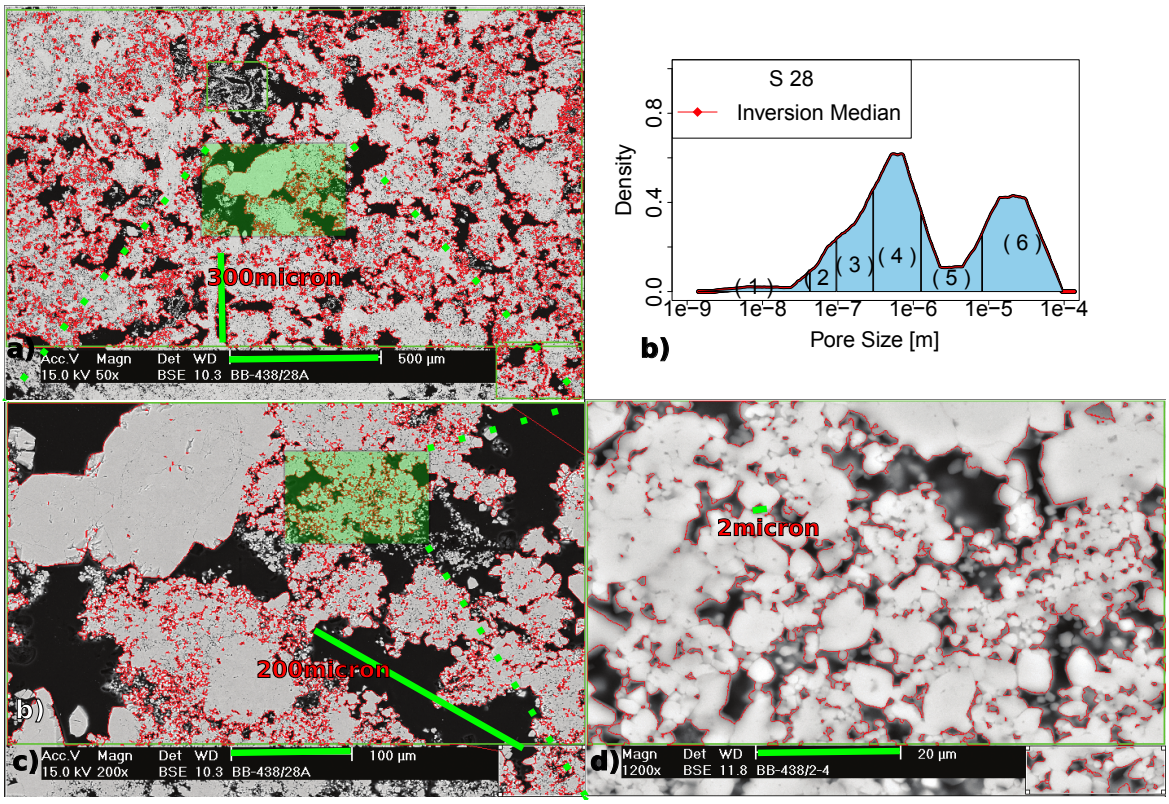

Fig. 7.16 Images of Sample S 28 across multiple scales. (a) 50x. (b) Pore-size distribution from inversion. (c) 200x . (d) 1200x.

However, the images are statistically unrepresentative because there is a lot of heterogeneity in a very small scale (area of the images) and also images are not entirely 2D as there is a third dimension manifested in the grey scale that allows identification of features within the pores.

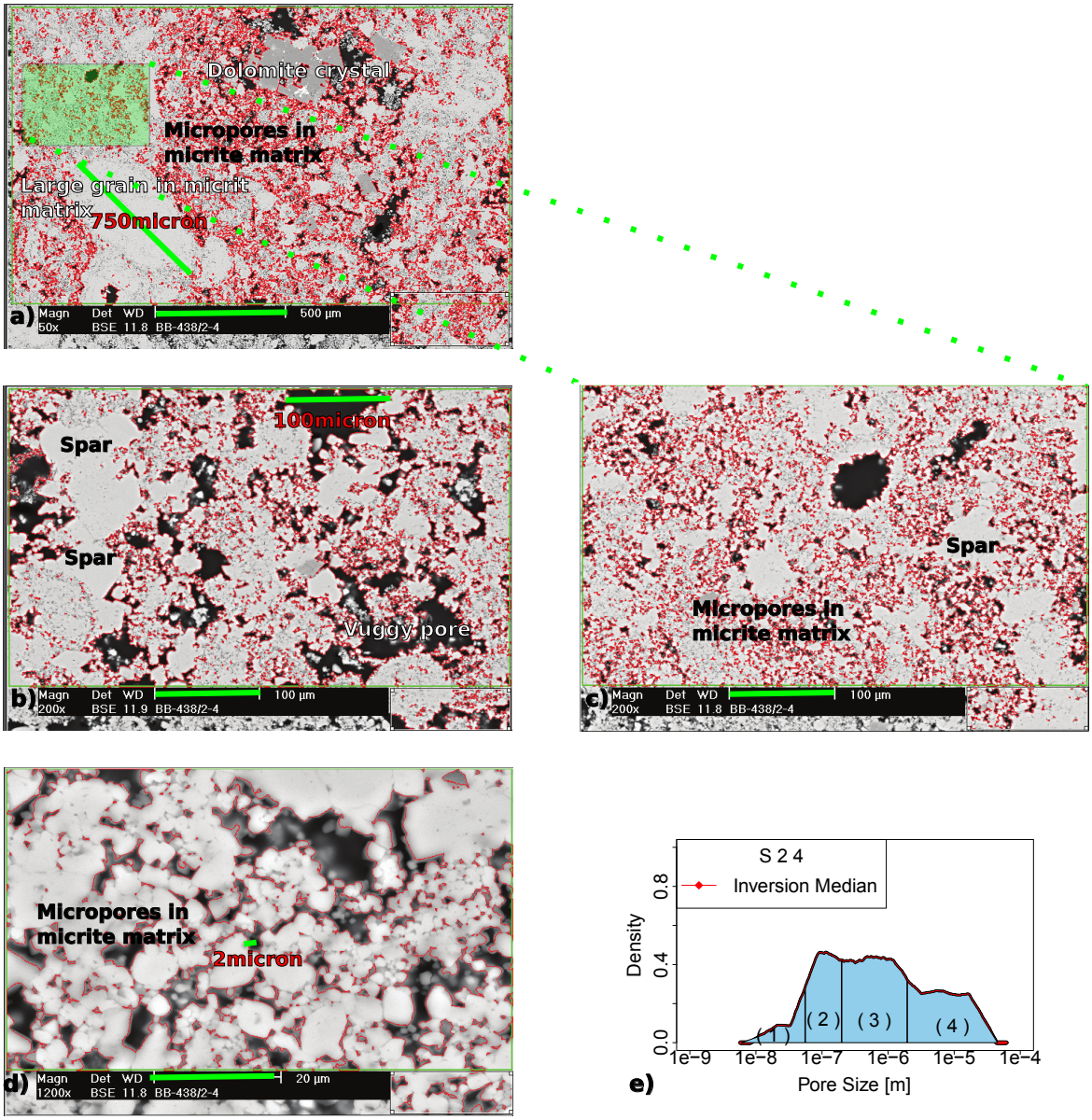

Fig. 7.17 Images of Sample S 2 4 across multiple scales. (a) 50x. (b) 200x. (c) 200x. (d) 1200x. (e) Pore-size distribution from inversion.

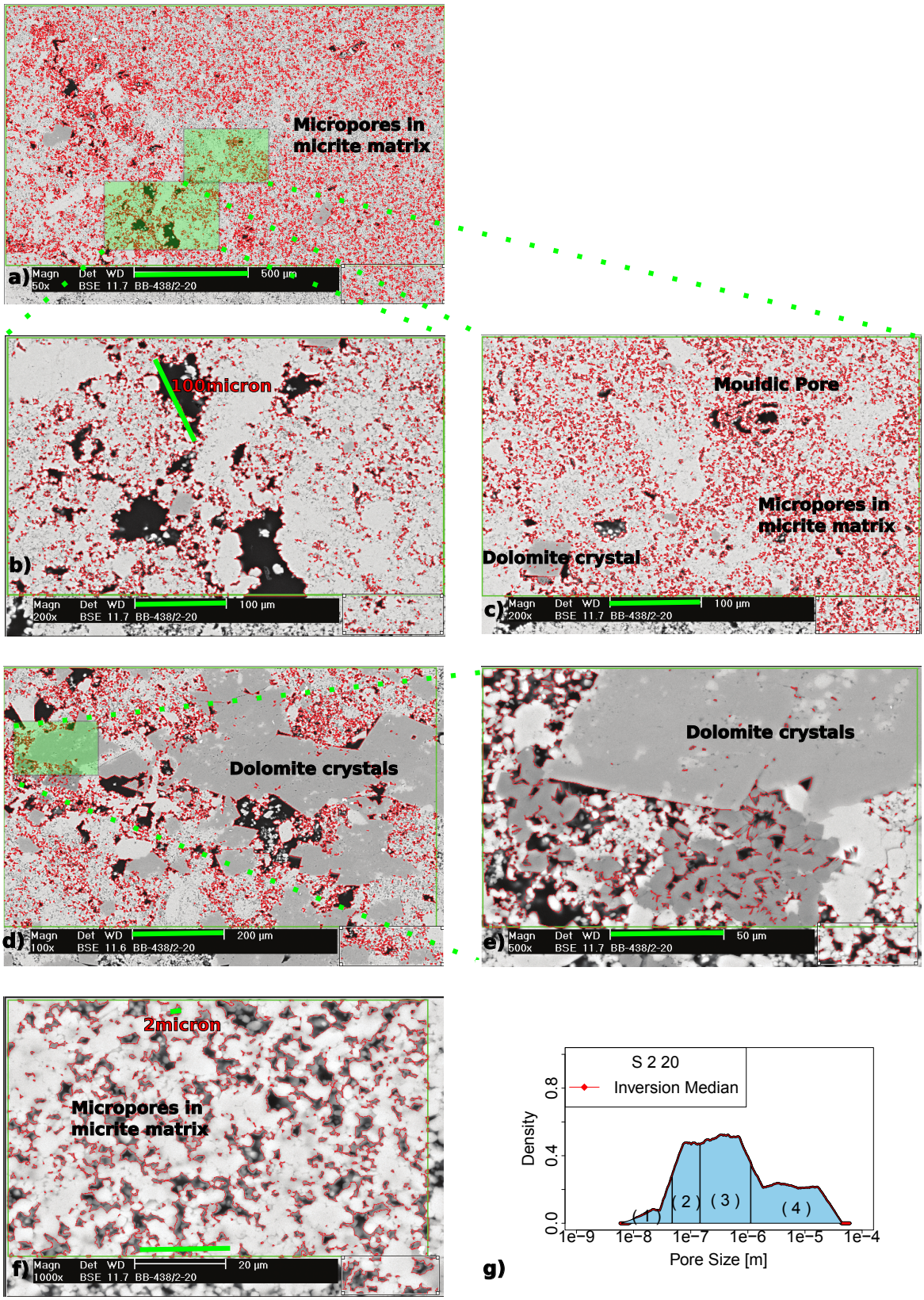

Fig. 7.18 Images of Sample S 2 20 across multiple scales. (a) 50x. (b) 200x. (c) 200x. (d) 100x. (e) 500x. (f) 1000x. (g) Pore-size distribution from inversion.

7.3 Inversion of Pore-Network Model Wettability

The pore-network model structural parameters for the three carbonate samples (i.e., pore-size distribution, volume exponent, and average coordination number) were taken from the inversion given in the previous section [185], and the HMC algorithm was used to invert the wettability parameters. The relative permeabilities were then predicted using the full set of pore-network model parameters.

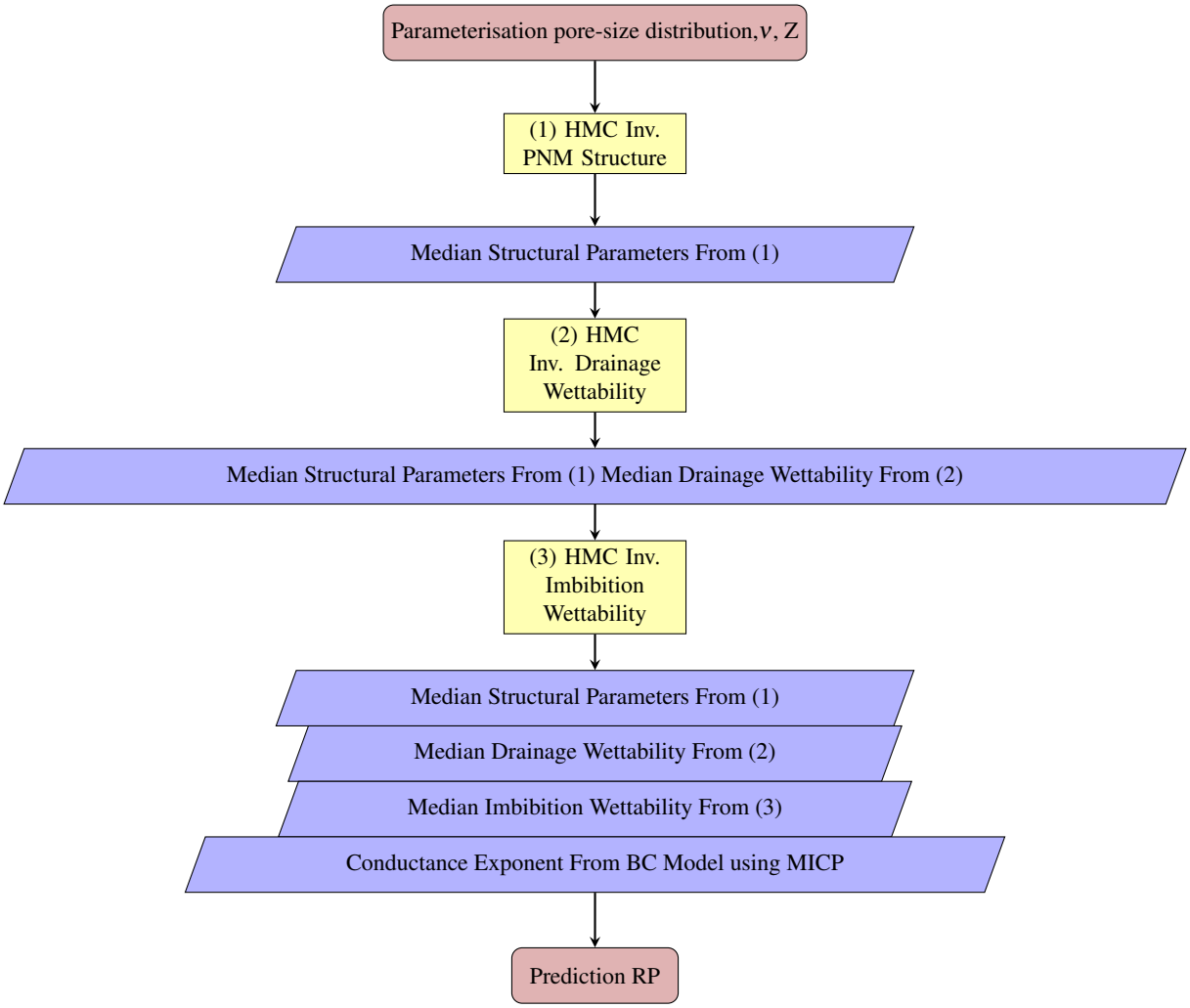

Fig. 7.19 Hamiltonian Monte Carlo Inversion Workflow

Figure 7.19 summarizes the workflow on which the pore-network model parameters are based on. This section focuses in the HMC inversions (2) and (3). The pore radius is assigned to each capillary element in the network according to the nonparametric PDF with the bins probabilities inferred in Section 7.1, which are also reported in Table 7.1. The

volume of each pore is taken according to the proportionalities introduced in Section 4.4.1 Eq. (4.36) and the average coordination number according to Section 4.4.2 (Fig. 4.1).

As numerical estimator of the volume exponent and the coordination number it seems reasonable from the synthetic case to use the estimated posterior median which were inferred in Section 7.1, also they are reported in Table 7.1, 7.4 and 7.6 for each rock type. These pore-network structure parameters were used throughout the inversion of wettability.

The results are organised as follows. For each rock type (RT-I S 28, RT-II S 2 4, and RT-III S 2 20), we applied the HMC algorithm to invert the drainage and imbibition wettability models (Eqs. 4.42 and 4.43, respectively). The results for each of the samples will be presented in separate sections.

To investigate the advancing contact angle owing to ageing, we first performed stochastic inversion of the receding contact angles because this established the oil occupancies and therefore the pores in which wettability alteration could occur. The laboratory procedure for a flooding cycle involved rendering the rock sample under the strongly water-wet conditions predominant in the reservoir during oil migration (a more detailed description of the laboratory procedure is given in [247]).

The second inversion started at the maximum drainage capillary pressure, which was a boundary condition taken from the experimental data. The rock samples were aged at 100 bar and 70 °C for 4 weeks. The HMC algorithm was then used to invert the imbibition wettability model (Eq. (4.43)).

We performed the inversion considering two wetting film threshold cases to investigate the effect of the wetting film criteria on wettability. The two cases are as follow: $\vartheta^{ww}_{ow_{Th}} = 5°$ and $\vartheta^{ww}_{ow_{Th}} = 30°$ for water-wet pores (contact angles below 90°) and $\vartheta^{ww}_{ow_{Th}} = 175°$ with $\vartheta^{ow}_{ow_{Th}} = 150°$ for oil-wet pores (contact angles above 90°). For example, a given pore was assumed to contain water-wetting films whenever the pore had a contact angle $\leq 5°$ and $\geq 175°$ to contain oil–wetting films. The approach was the same for $\vartheta^{ww}_{ow_{Th}} = 30°$ and $\vartheta^{ow}_{ow_{Th}} = 150°$. The oil–water interfacial tension was $\sigma_{ow} = 27$ mN/m.

The ranges of variation of the pore-network model parameters were $\vartheta^{A-rec}_{ow_{MIN}} \in [0,90]$, $\vartheta^{A-rec}_{ow_{MAX}} \in [0,90]$, $f_w \in [0,1]$, $\vartheta^{B-rec}_{ow_{MIN}} \in [0,180]$, and $\vartheta^{B-rec}_{ow_{MAX}} \in [0,180]$ for drainage wettability inversion (Eq. (4.42)), $\vartheta^{A-adv}_{ow_{MIN}} \in [0,180]$, $\vartheta^{A-adv}_{ow_{MAX}} \in [0,180]$, and $R_{Wet} \in [r_{MIN}, r_{MAX}]$ in the pore-size distribution of each sample, and $\vartheta^{B-adv}_{ow_{MIN}} \in [80,180]$ and $\vartheta^{B-adv}_{ow_{MAX}} \in [80,180]$ for imbibition wettability inversion (Eq. (4.43)).

The aim was to use small networks in the calculation of the SSIP, and then perform the forward predictions of the relative permeabilities in large networks. Small network models estimated the network parameters well Chapter 6 [185]. We stopped sampling when the

medians of all the parameters were unchanged ('equilibrium') after twice as many samples were generated. We also made multiple HMC runs to check the reliability of the estimates.

Each sample is a network model. The network model had a lattice defined by $N_x = 8$, $N_y = 8$, and $N_z = 8$ (short form lattice constant $L = 8$), which contained 2268 pores ($3 \times N_x \times N_y \times N_z + N_y \times N_z$). There are problems in plotting bivariate scatterplots of the contact angles versus pore size (posterior joint distribution of contact angles in the pore-size distribution). The regions of high density appear as black spots with a huge numbers of points plotted on top of one another. We resorted to an image plot (referred to as a heat map), which is useful when many points overlap. The blue region is the background where the density is calculated, and in the white region outside the background there are no density calculations. The red regions represent high density and the blue regions represent zero density.

The predicted relative permeabilities for water flooding based on the inversion results are presented at the end of each rock sample section, and they were calculated for $N_x = 20$, $N_y = 20$, and $N_z = 20$ ($L = 20$) lattices, which contained 24,400 pores.

The usual approach in pore-network modelling is to stop invasion–percolation at the observed connate water saturation (S_{wc}^{obs}) value. The experimental data in this study is pressure-controlled capillary pressure data. The residual, namely connate water saturation and residual oil saturation (S_{wc}^{obs} and S_{or}^{obs}) and maximum and minimum capillary pressure ($P_{c,ow_{MAX}}^{obs}$ and $Pc_{c,ow_{MIN}}^{obs}$) are the capillary pressure end points. The usual approach in pore-network modelling is to stop invasion–percolation at the observed critical connate water saturation (S_{wc}^{obs}) value. Therefore, we set $P_{c,ow_{MAX}}^{obs}$ as the main boundary condition and evaluated the merits of the simulations in predicting S_{wc}^{obs}, S_{or}^{obs}, and $P_{c,ow_{MIN}}^{obs}$.

As described previously in Section 7.1, the use of random numbers in the HMC introduces noise in the simulations. Because of the change in random numbers when constructing the pore-network model structure and populating the contact angles, any two simulations with the same pore-network model parameters could have different values of residuals (S_{wc}^{obs} and S_{or}^{obs}) and maximum and minimum capillary pressure ($P_{c,ow_{MAX}}^{obs}$ and $P_{c,ow_{MIN}}^{obs}$). Therefore, throughout the following sections, we will use the term 'match' in the sense of being within a prespecified tolerance ($\pm$ 20% tolerance in the degree of match) in matching the residuals (S_{wc}^{obs} and S_{or}^{obs}) and the maximum and minimum capillary pressure ($P_{c,ow_{MAX}}^{obs}$ and $P_{c,ow_{MIN}}^{obs}$).

7.3.1 Pore-Network Model Wettability of RT-I S 28

RT-I is a rock with a bimodal pore-size distribution, as shown in Fig. 7.20a. Table 7.20 lists the inverted structural parameters taken from the inversion of the structural parameters, which were fixed for inverting the pore-network model wettability parameters.

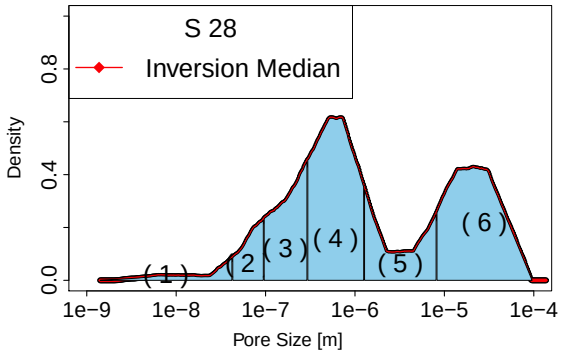

a

Table 7.1 RT-I : Structural Parameters

Parameter	Value
ν	0.22
$\bar{Z}$	4.43
p_1^*	0.01
p_2^*	0.04
p_3^*	0.13
p_4^*	0.34
p_5^*	0.07
p_6^*	0.29

Fig. 7.20 (a) Pore-size distribution of S 28. The numbers identify the ranges of pore sizes that are associated with the pore-size distribution parameters (p^*) in Table 7.1. (b) pore-network model structural parameters of S 28 Section 7.1 [185] . ν is the volume exponent in Eq. (4.36), $\bar{Z}$ is the average coordination number in Chapter 4.4.2, and p_i^* are the pore-size distribution parameters Section 7.1 [185] .

RT–I S 28: Determining Drainage Wettability Parameters for Water-wetting Films with a 5° Threshold

Figure 7.21a shows that few realisations matched S_{wc}^{obs} at the maximum capillary pressure ($P_{c,ow_{MAX}}^{obs}$) (referred to as drainage capillary pressure end-point), whereas others overestimated S_{wc}^{obs} at $P_{c,ow_{MAX}}^{obs}$.

For strongly water-wet conditions, we expected a combination of any fraction (f_w) with similar values for the minimum and maximum bounds $\vartheta_{ow_{MIN}}^{A-rec}$ (Fig. 7.22a) $\approx \vartheta_{ow_{MIN}}^{B-rec}$ (Fig. 7.22c) and $\vartheta_{ow_{MAX}}^{A-rec}$ (Fig. 7.22b) $\approx \vartheta_{ow_{MAX}}^{B-rec}$ (Fig. 7.22d)). As can be seen in the graphs, Fig. 7.21b shows a posterior uniform histogram and the two sets of histograms have comparable bounds (Fig. 7.22a with Fig. 7.22c, and Fig. 7.22b with Fig. 7.22d).

Figure 7.23 shows a scatterplot of the receding contact angle versus the pore radius for all of the pores and all of the realisations. Red represents regions of high density. As expected, small receding contact angles have high density (warmer colours). Notice the

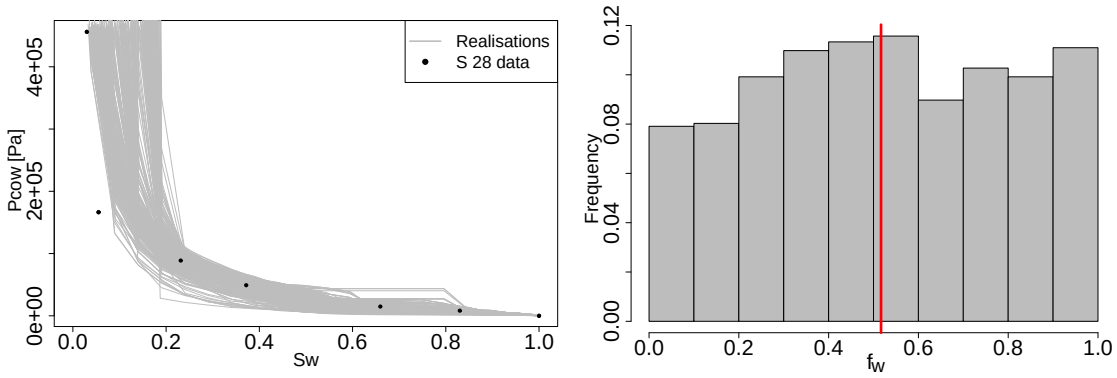

a b

Fig. 7.21 Sample S 28 drainage HMC inversion results for drainage with $\vartheta^{ww}_{ow_{Th}} = 5°$. (a) Posterior HMC realisations (grey lines). The measurements are shown as black filled circles. (b) Posterior marginal histogram of the fraction of pores whose contact angles were assigned to each population in Eq. (4.42). The line in (b) indicates the median.

nonuniform distribution of colours. This spatial information (or size-correlation) within the pore-size distribution concerning the receding contact angle has not been accounted for in previous works. This may have an important effect on the phase occupancies and therefore on the capillary pressure and relative permeabilities.

RT-I S 28: Determining Drainage Wettability Parameters for Water-wetting Films with a 30° Threshold

To investigate the potential effects that the existence criteria for wetting films (represented here by thresholds in the contact angles) may have on the determination of wettability, the same procedure was followed for a wider range of receding contact angles for the existence of water-wetting films ($\leq 30°$). We obtained qualitatively similar results (Figs. 7.24 and 7.25) to those of the previous section, although the case $\vartheta^{ww}_{ow_{Th}} = 30°$ led to better matching of the drainage capillary pressure end-point.

Because the receding contact angle range for water-wetting films is wider than with $\vartheta^{ww}_{ow_{Th}} = 5°$, there is slightly less dispersion of the outlier points (Fig. 7.26).

RT-I S 28: Determining Imbibition Wettability Parameters for 5° and 175° Thresholds for Water- and Oil-Wetting Films

In the following two sections, we use the posterior distribution of receding contact angles obtained in the previous sections (Figs. 7.23 and 7.26). The pore-network model was pop-

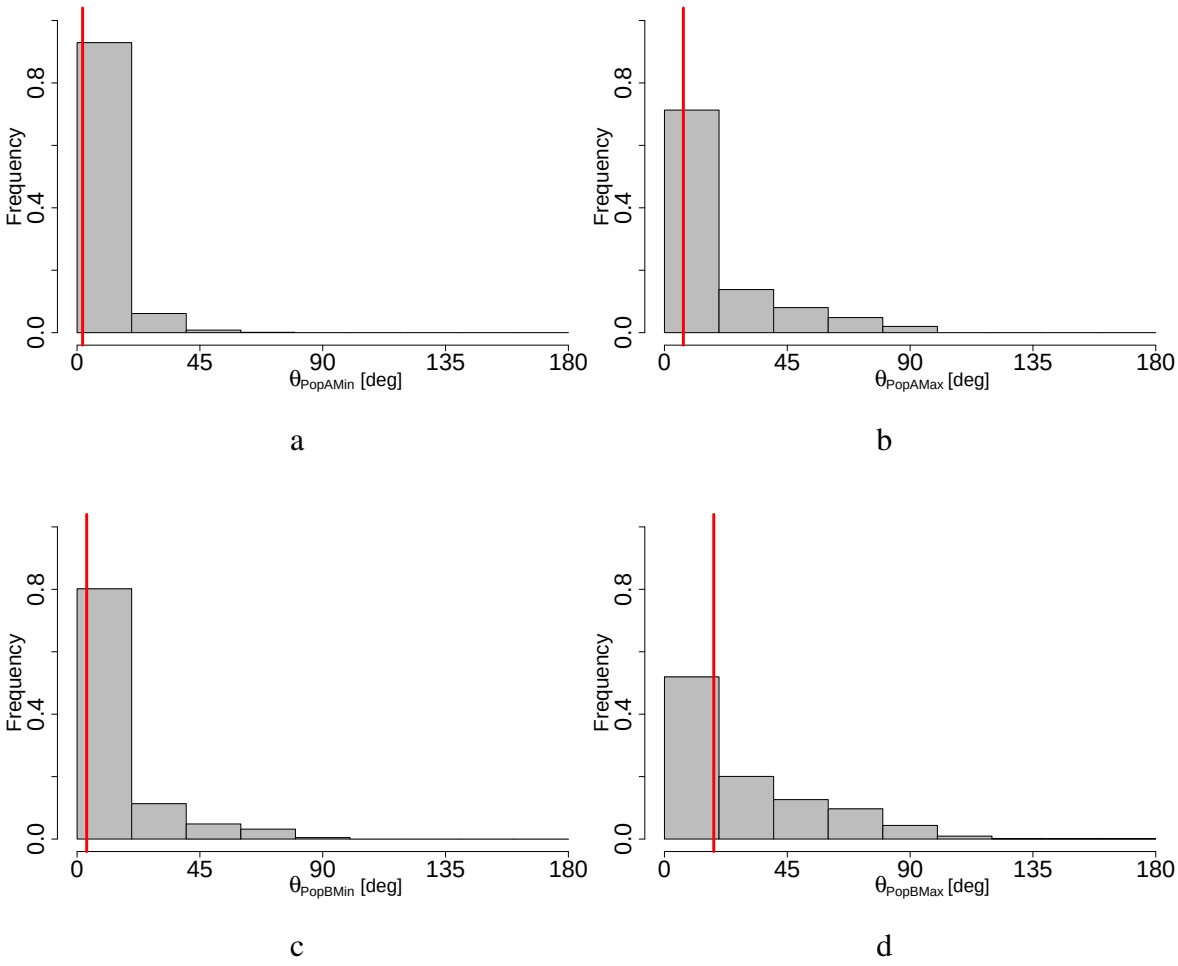

Fig. 7.22 Sample S 28 drainage HMC inversion results for drainage with $\vartheta_{ow_{Th}}^{ww} = 5°$. Posterior histograms of the wettability parameters (Eq. (4.42)): (a) lower bound ($\vartheta_{ow_{MIN}}^{A-rec}$) and (b) upper bound ($\vartheta_{ow_{MAX}}^{A-rec}$) for population A, and (c) lower bound ($\vartheta_{ow_{MIN}}^{B-rec}$) and (d) upper bound ($\vartheta_{ow_{MAX}}^{B-rec}$) for population B. The red line in each histogram indicates the median.

ulated with receding contact angle p-quantiles for each region in the pore-size distribution (i.e., regions (1)–(6) in Fig. 7.20) calculated from each posterior drainage heat map shown in Figs. 7.23 and 7.26.

Oil-flooding was stopped at the $P_{c,ow_{MAX}}^{obs}$ value obtained from the experimental data. Oil-filled pores can then change their contact angle according to the wettability model in Eq. (4.43). Water-flooding started from the final configuration of oil and water in the pore-network model at the end of oil flooding. The HMC algorithm was used to invert the wettability model (Eq. (4.43)).

Figures 7.27–7.29 show the results from the HMC inversion of the wettability param-

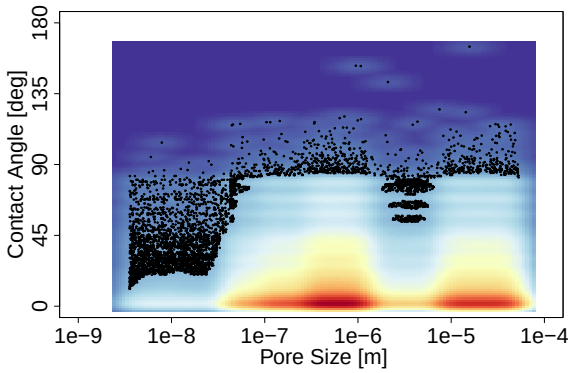

Fig. 7.23 Sample S 28 drainage heat map for drainage with $\vartheta^{ww}_{ow_{Th}} = 5°$. This is a bivariate density representation of the posterior distribution of contact angles in the pore-size distribution. The red regions represent high density and the blue areas represent zero density. The colour intensities indicate a nonuniform distribution.

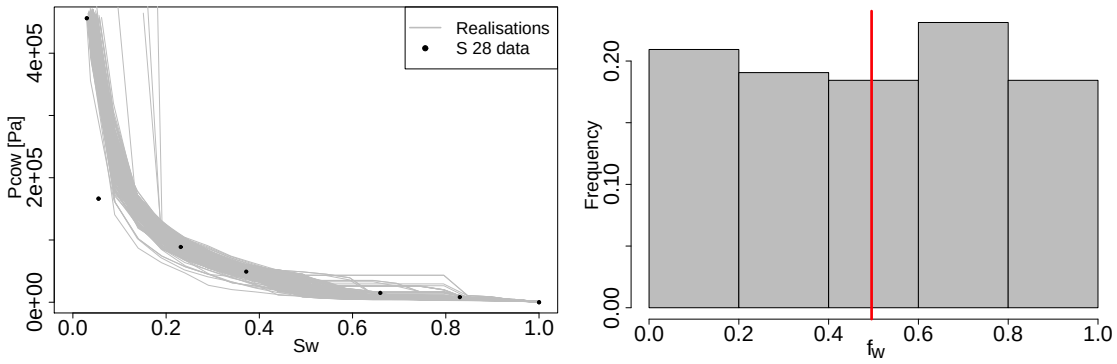

a b

Fig. 7.24 Sample S 28 drainage HMC inversion results for drainage with $\vartheta^{ww}_{ow_{Th}} = 30°$. (a) Posterior HMC realisations (grey lines). The measurements are shown as black filled circles. (b) Posterior marginal histogram of the fraction of pores whose contact angles were assigned to each population in Eq. (4.42).The line in (b) indicates the median.

eters (Eq. (4.43)). There were a few realisations that reached S^{obs}_{or} at ($P^{obs}_{c,ow_{MIN}}$) (referred to as the imbibition capillary pressure end-point), which indicates that the range of contact angles for the existence of wetting films may need to be widened, oil-layer are needed or a more complexity in the implemented physics is required.

Figure 7.29 shows the posterior heat maps for imbibition and drainage. The advancing contact shows a high concentration of points in the range 90°–135°. A less concentrated region is located in the range 0°–90°below 1×10^{-6} m. In addition, there are few pores with advancing contact angles in the range 90°–150°below 1×10^{-7} m (white spotty areas).

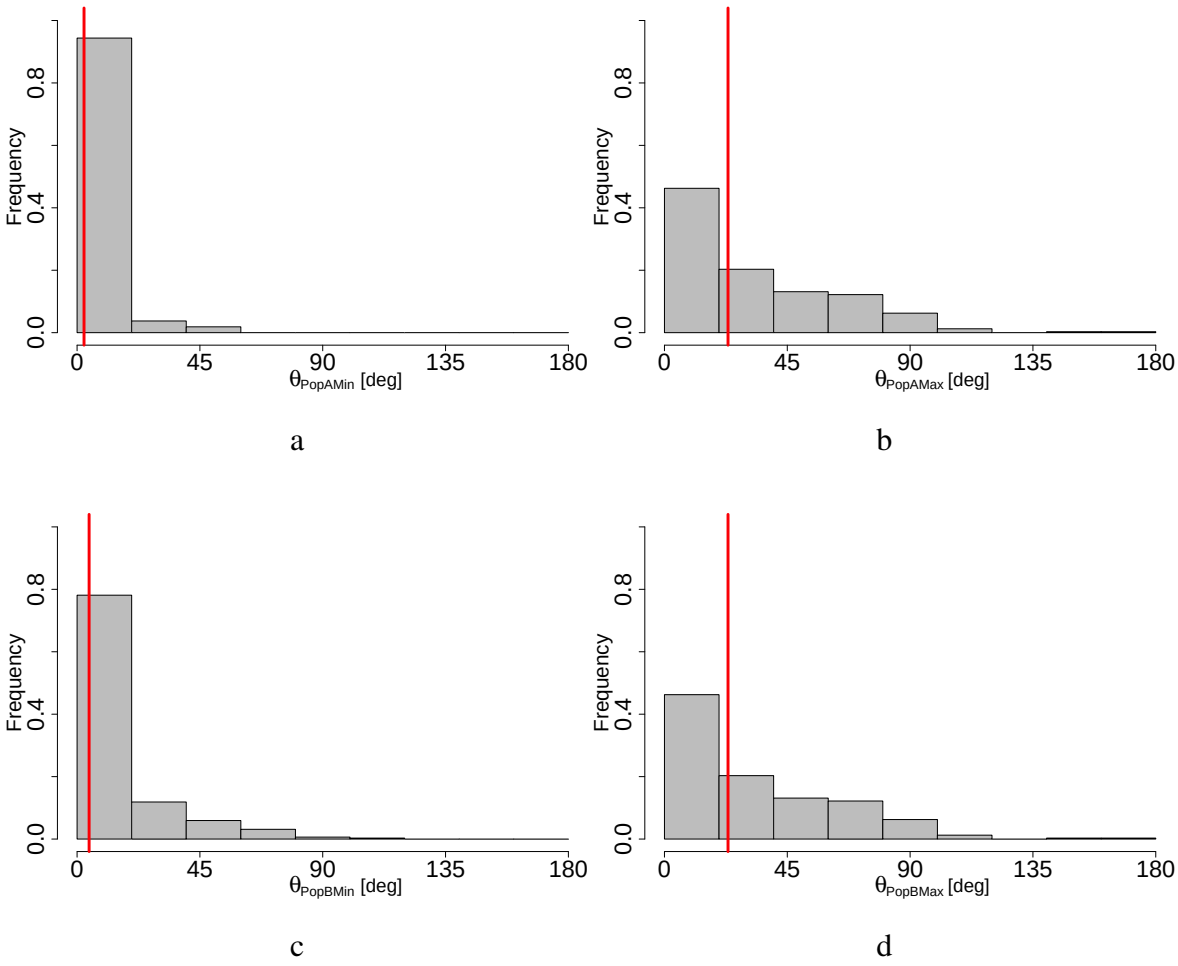

Fig. 7.25 S 28 drainage HMC inversion for drainage with $\vartheta^{ww}_{ow_{Th}} = 30°$. Posterior histograms of the wettability parameters (Eq. (4.42)): (a) lower bound ($\vartheta^{A-rec}_{ow_{MIN}}$) and (b) upper bound ($\vartheta^{A-rec}_{ow_{MAX}}$) for population A, and (c) lower bound ($\vartheta^{B-rec}_{ow_{MIN}}$) and (d) upper bound ($\vartheta^{B-rec}_{ow_{MAX}}$) for population B. The red line in each histogram indicates the median.

RT–I S 28: Determining Imbibition Wettability Parameters for 30° and 150° Thresholds for Water- and Oil-Wetting Films

The HMC inversion of the imbibition pore-network model parameters for S 28 wetting films with $\vartheta^{ww}_{ow_{Th}} = 30°$ and $\vartheta^{ow}_{ow_{Th}} = 150°$ gave similar estimates to those with $\vartheta^{ww}_{ow_{Th}} = 5°$ and $\vartheta^{ow}_{ow_{Th}} = 175°$.

The posterior histograms of the wettability parameters are only slightly affected by the wider range of conditions for the existence of water- and oil-wetting films (Figs. 7.30b, 7.31a, 7.31b, 7.31c, and 7.31d). Figures 7.30b, 7.31a, 7.31b, 7.31c, and 7.31d are qualita-

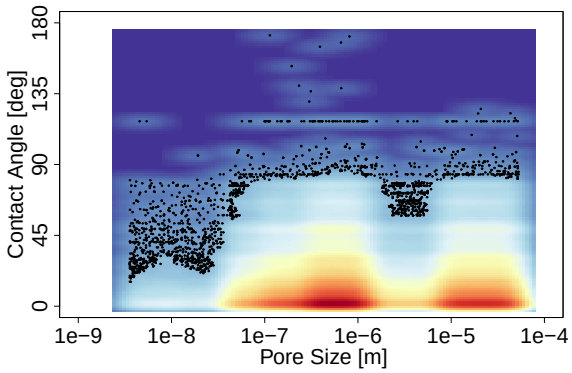

Fig. 7.26 Sample S 28 drainage heat map for drainage with $\vartheta^{ww}_{ow_{Th}} = 30°$. This is a bivariate density representation of the posterior distribution of contact angles in the pore-size distribution. The red regions represent high density and the blue regions represent zero density. The colour intensities indicate a nonuniform distribution.

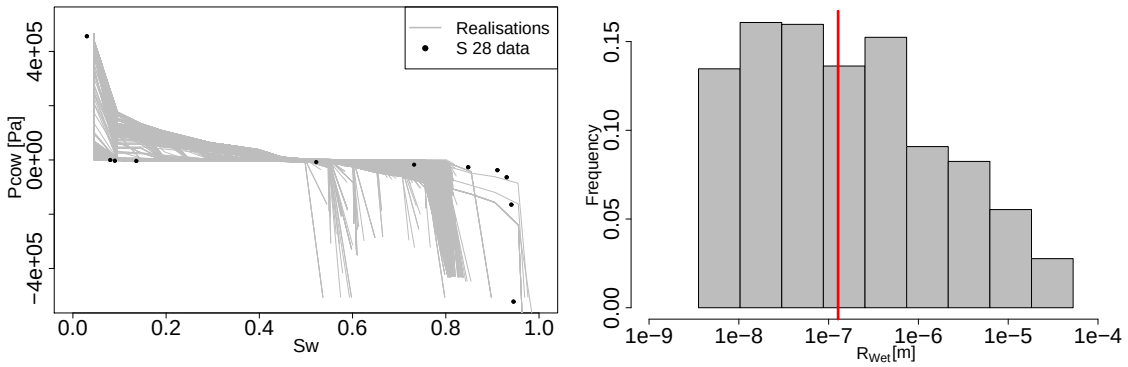

a b

Fig. 7.27 S 28 imbibition HMC inversion results for imbibition with $\vartheta^{ww}_{ow_{Th}} = 5°$ and $\vartheta^{ow}_{ow_{Th}} = 175°$. (a) Posterior HMC realisations (grey lines). The measurements are shown as black filled circles. (b) Posterior marginal histogram of the radius that separates the two pore populations. The contact angles were assigned to each population in Eq. (4.43). The line in (b) indicates the median.

tively similar to Figs. 7.27b, 7.28a, 7.28b, 7.28c, and 7.28d, respectively. However, more realisations reached S^{obs}_{or} at $P^{obs}_{c,ow_{MIN}}$ (Fig. 7.31a), and many more reached S^{obs}_{or} at a much lower capillary pressure than $P^{obs}_{c,ow_{MIN}}$.

Figure 7.32a and 7.32b show the imbibition and drainage heat maps for all realisations, respectively. The following figures will compare imbibition heat maps conditional on those realisations matching (1) the imbibition capillary pressure end-point, (2) only S^{obs}_{or}, and (3) only $P^{obs}_{c,ow_{MIN}}$.

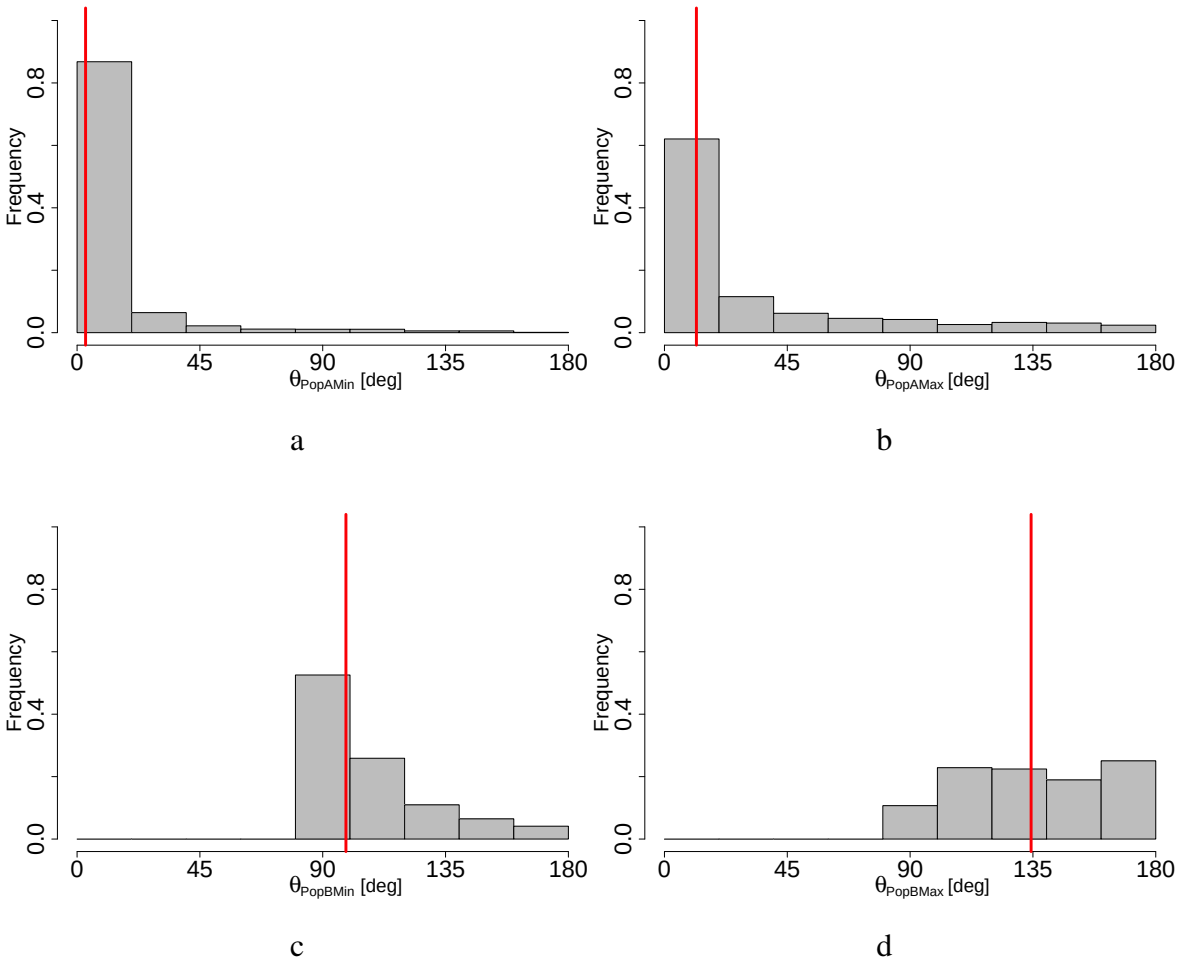

Fig. 7.28 S 28 imbibition HMC inversion results for imbibition with $\vartheta_{ow_{Th}}^{ww} = 5°$ and $\vartheta_{ow_{Th}}^{ow} = 175°$. Posterior histograms of the wettability parameters (Eq. (4.43)): (a) lower bound ($\vartheta_{ow_{MIN}}^{A-adv}$) and (b) upper bound ($\vartheta_{ow_{MAX}}^{A-adv}$) for population A, and (c) lower bound ($\vartheta_{ow_{MIN}}^{B-adv}$) and (d) upper bound ($\vartheta_{ow_{MAX}}^{B-adv}$) for population B. The red line in each histogram indicates the median.

The drainage heat maps for the two cases are similar (Figs. 7.23 and 7.26). However, there are significant differences in the conditional imbibition heat maps given those realisations matching the imbibition capillary pressure end-point (S_{or}^{obs} and $P_{c,ow_{MIN}}^{obs}$) (Fig. 7.33).

There are still significant differences in the conditional heat maps for the two wetting film cases given those realisations matching only S_{or}^{obs} regardless of the $P_{c,ow_{MIN}}^{obs}$ value (Fig. 7.34). This indicates that inferring the wettability at the pore level may be strongly affected by the criteria for the existence of wetting films.

In contrast, the conditional posterior heat maps show similar features for the two wetting

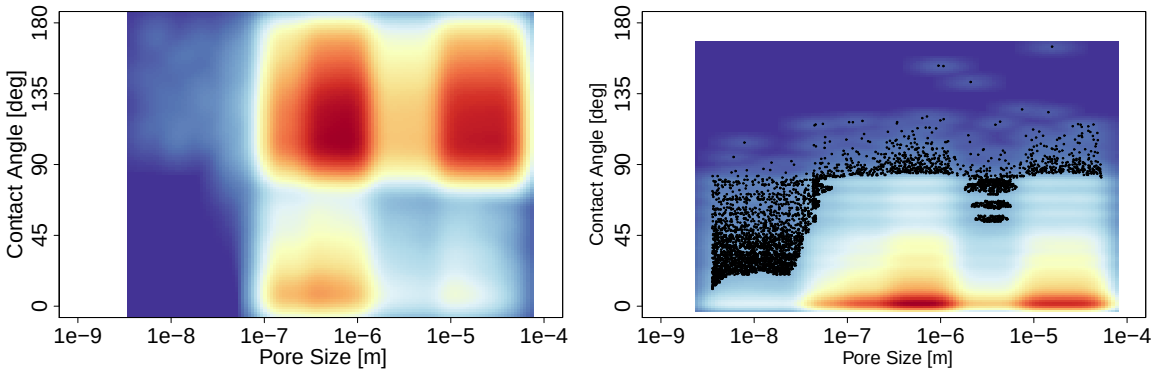

a b

Fig. 7.29 Sample S 28 heat maps for $\vartheta^{ww}_{ow_{Th}} = 5°$ and $\vartheta^{ow}_{ow_{Th}} = 175°$. (a) Imbibition and (b) drainage heat maps. This is a bivariate density representation of the posterior distribution of contact angles in the pore-size distribution. The red regions represent high density and the blue regions represent zero density. The colour intensities indicate a nonuniform distribution.

films cases given those realisations matching only $P^{obs}_{c,ow_{MIN}}$ regardless of the S^{obs}_{or} value (Fig. 7.35). However, there are still significant differences between the two heat maps.

7.3.2 RT-I S 28: Prediction of Relative Permeabilities for Water-Flooding and Comparison with Experiments

Using our network model, described in Chapter 4, we predict the imbibition relative permeabilites with the network parameters obtained from the HMC inversion. The structural network parameters of Table 7.2 were obtained from HMC inversion using the mercury intrusion capillary pressure.

The inversion of wettability using the HMC was derived in the previous sections. Heat maps for wettability inference showed complex patterns. Therefore, in order to reproduce the resulting variability we have calculated the experimental cumulative distribution function (ECDF) for each of the regions in the pore-size distribution (Fig. 7.33b). The ECDFs of receding and advancing contact angles for each region in the pore-size distribution derived are shown in Figs 7.37 (1), (2), (3), (4), (5), (6) were obtained from the conditional posterior heat maps of receding and advancing contact angles given matching of S^{obs}_{or} and $P^{obs}_{c,ow_{MIN}}$ for the case with $\vartheta^{ww}_{ow_{Th}} = 30°$ and $\vartheta^{ow}_{ow_{Th}} = 150°$ for wetting films.

The last parameter required to predict the relative permeabilities is the conductance exponent (Chapter 4). We derived the conductance exponent from the Brooks–Corey (BC)

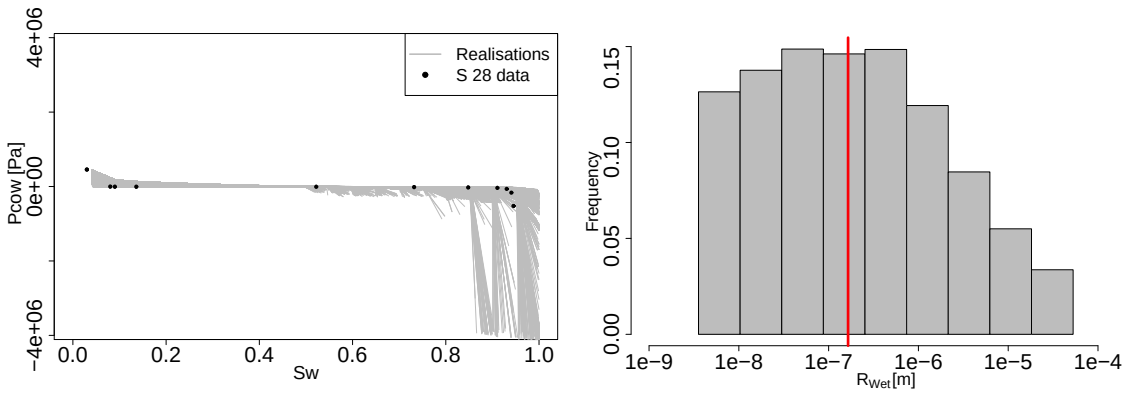

a b

Fig. 7.30 S 28 imbibition HMC inversion results for imbibition with $\vartheta^{ww}_{ow_{Th}} = 30°$ and $\vartheta^{ow}_{ow_{Th}} = 150°$. (a) Posterior HMC realisations (grey lines). The measurements are denoted by black filled circles. (b) Posterior marginal histogram of the radius that separates the two pore populations. Their contact angles were assigned to each population in Eq. (4.43). The line in (b) indicates the median.

relationship using the MICP. The volume exponent was multiplied by the pore-size distribution index from the BC model to determine the conductance exponent.

S 28 is a bimodal sample. Various BC models could be fitted to the different segments of the MICP curve. However, they are similar. Thus, we used a single pore-size distribution index derived by matching the MICP to the BC model ($\Lambda = 0.53330$) and the volume exponent (ν from Table 7.1) to estimate the pore-network model conductance exponent $\lambda = 1.14533$ (Eq. (4.41)).

Note that none of the parameters in our pore-network model could be adjusted or tuned in relation to the relative permeabilities. We used a $20 \times 20 \times 20$ lattice network to predict the relative permeabilities. The predictions agree well with the steady-state experimental data (Fig. 7.36a).

Figure 7.37 summarises the predictions and wettability alteration. The cumulative probability (distribution) functions (ECDFs, labels (1)–(6) in Fig. 7.37) show the hysteresis in the contact angle from receding to advancing (black, grey lines in Fig. 7.37(1)–(6)). The small pores that remained water-wet caused overlapping of the black and grey lines in Fig. 7.37(1)–(2). The large pores have large advancing contact angles. However, the mid-sized pores (microporosity) (Fig. 7.37(3)–(4)) are more oil-wet than the larger pores (Fig. 7.37(5) and (6)) and the ECDF in Fig. 7.37(4) shows an abrupt increase from zero to one. The cumulative probability at 0.5 (i.e., the median) is just above 135°in Fig. 7.37(3)–(4).

The medians in Fig. 7.37(5)–(6) are extremely close to the average value determined by

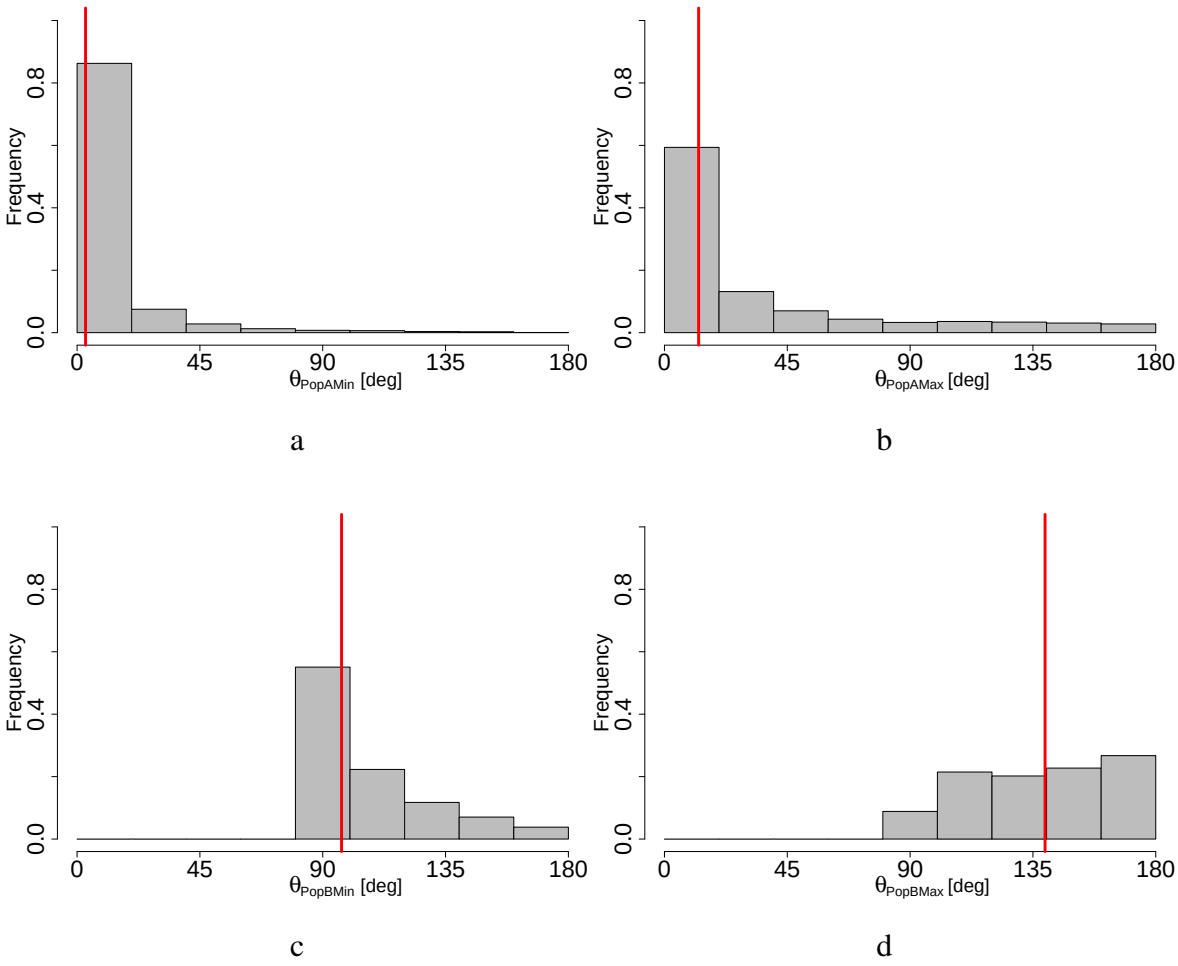

Fig. 7.31 Sample S 28 imbibition HMC inversion results for imbibition with $\vartheta^{ww}_{ow_{Th}} = 30°$ and $\vartheta^{ow}_{ow_{Th}} = 150°$. Posterior histograms of the wettability parameters (Eq. (4.43)): (a) lower bound ($\vartheta^{A-adv}_{ow_{MIN}}$) and (b) upper bound ($\vartheta^{A-adv}_{ow_{MAX}}$) for population A, and (c) lower bound ($\vartheta^{B-adv}_{ow_{MIN}}$) and (d) upper bound ($\vartheta^{B-adv}_{ow_{MAX}}$) for population B. The red line in each histogram indicates the median.

the analytical method in previous work [241]. Contrary to our results, the mid-sized pores (Fig. 7.37(3)–(4)) in [241] were estimated to be in the range 96°–108°, and were less oil-wet than large pores.

It is apparent from the relative permeability data shown in Fig. 7.37 that the behaviour of water relative permeability is not qualitatively consistent with the behaviour of mixed-wet large pore-network model simulations in bimodal systems, such as the one in [30, 33] in which there is an abrupt increase in the water relative permeability.

A full exploration of prediction of relative permeabilities under uncertainty in the pore-

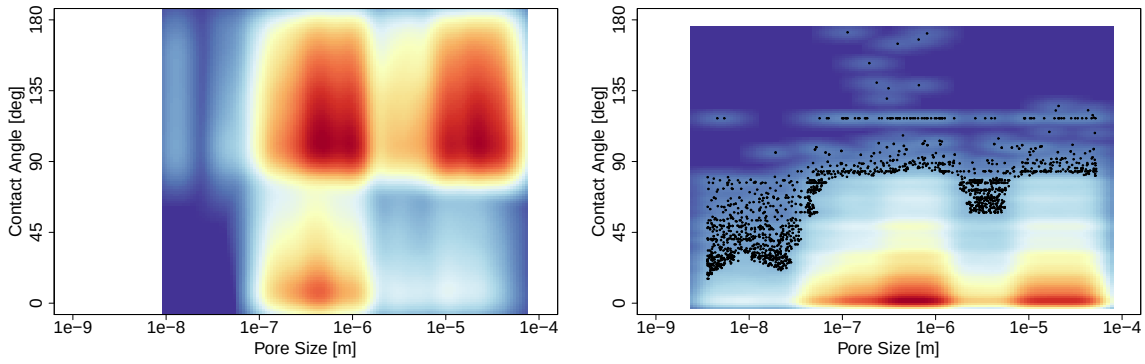

a b

Fig. 7.32 Sample S 28 heat maps for $\vartheta^{ww}_{ow_{Th}} = 30°$ and $\vartheta^{ow}_{ow_{Th}} = 150°$. (a) Imbibition and (b) drainage posterior heat maps. These are bivariate density representations of the posterior distribution of contact angles in the pore-size distribution. The red regions represent high density and the blue regions represent zero density. The colour intensities indicate a nonuniform distribution.

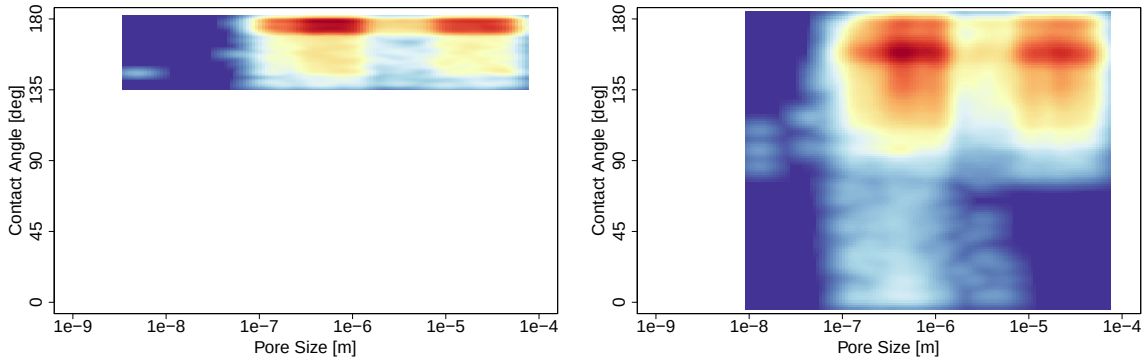

a b

Fig. 7.33 Conditional imbibition posterior heat maps given matching the imbibition endpoint S^{obs}_{or} and $P^{obs}_{c,ow_{MIN}}$. (a) $\vartheta^{ww}_{ow_{Th}} = 5°$ and $\vartheta^{ow}_{ow_{Th}} = 175°$, and (b) $\vartheta^{ww}_{ow_{Th}} = 30°$ and $\vartheta^{ow}_{ow_{Th}} = 150°$.

network model parameters would imply taking each of the samples generated by HMC in the inversion step to prediction mode. This would be computationally much more expensive than the HMC inversion, as large pore-network models are needed to carry out reliable calculations of relative permeabilities. CPU challenges are common in earth sciences in which after stochastic history matching it is impossible in most practical cases to perform many tens of costly production forecasts. Therefore, three models, namely P10, P50 and P90

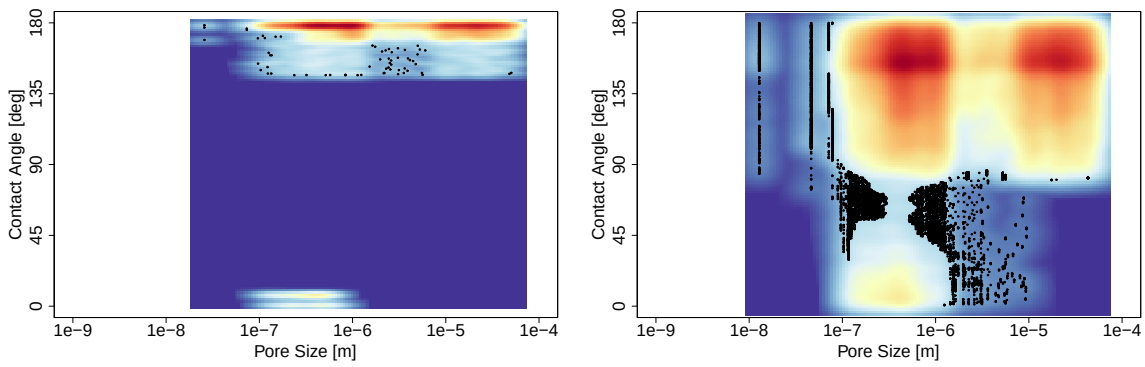

a b

Fig. 7.34 Conditional imbibition posterior heat maps given matching only S_{or}^{obs}: (a) $\vartheta_{ow_{Th}}^{ww} = 5°$ and $\vartheta_{ow_{Th}}^{ow} = 175°$, and (b) $\vartheta_{ow_{Th}}^{ww} = 30°$ and $\vartheta_{ow_{Th}}^{ow} = 150°$.

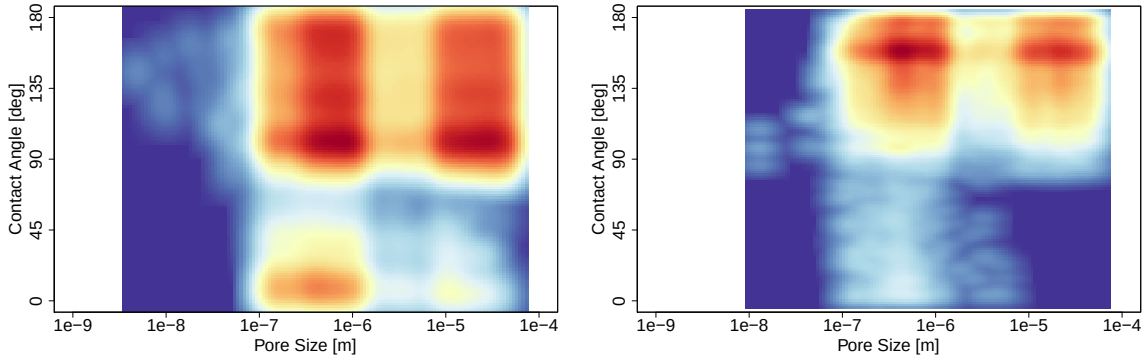

a b

Fig. 7.35 Sample S 28 conditional imbibition posterior heat map given matching $P_{c,ow_{MIN}}^{obs}$: (a) $\vartheta_{ow_{Th}}^{ww} = 5°$ and $\vartheta_{ow_{Th}}^{ow} = 175°$, and (b) $\vartheta_{ow_{Th}}^{ww} = 30°$ and $\vartheta_{ow_{Th}}^{ow} = 150°$.

are often used to assess the uncertainty in the prediction response. Previously, in Section 6.2.1 we discussed P10, P50 and P90 model parameters in the context of the synthetic case. And we show that there is no guarantee that the 'true' predictions will fall in between P10 and P90 models.

For completeness we show the P10, P50 and P90 relative permeability predictions in which we focus on a few statistics of the distribution of misfit values, namely, a low value (P10, tenth lowest), P50 (a middle value), and P90 (representing a high misfit). We run the pore-network model with the model parameters corresponding to the quantiles P10, P50, and P90 in the cumulative distribution function of the misfit. In Fig. 7.38 we plot the

Table 7.2 RT-I : Structural Parameters

Parameter	Value
ν	0.22
$\bar{Z}$	4.43
p_1^*	0.01
p_2^*	0.04
p_3^*	0.13
p_4^*	0.34
p_5^*	0.07
p_6^*	0.29
λ	1.14533

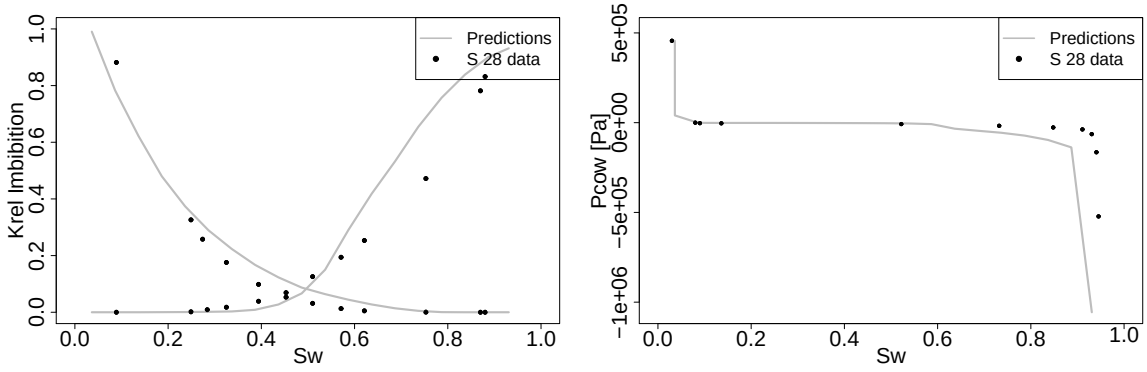

a b

Fig. 7.36 Predicted S 28 imbibition relative permeabilities and capillary pressure. (a) Predicted imbibition relative permeabilities using HMC posterior statistics given matching S_{or}^{obs} and $P_{c,ow_{MIN}}^{obs}$ for a network size of $20 \times 20 \times 20$, and (b) imbibition capillary pressure corresponding to the relative permeabilities in (a).

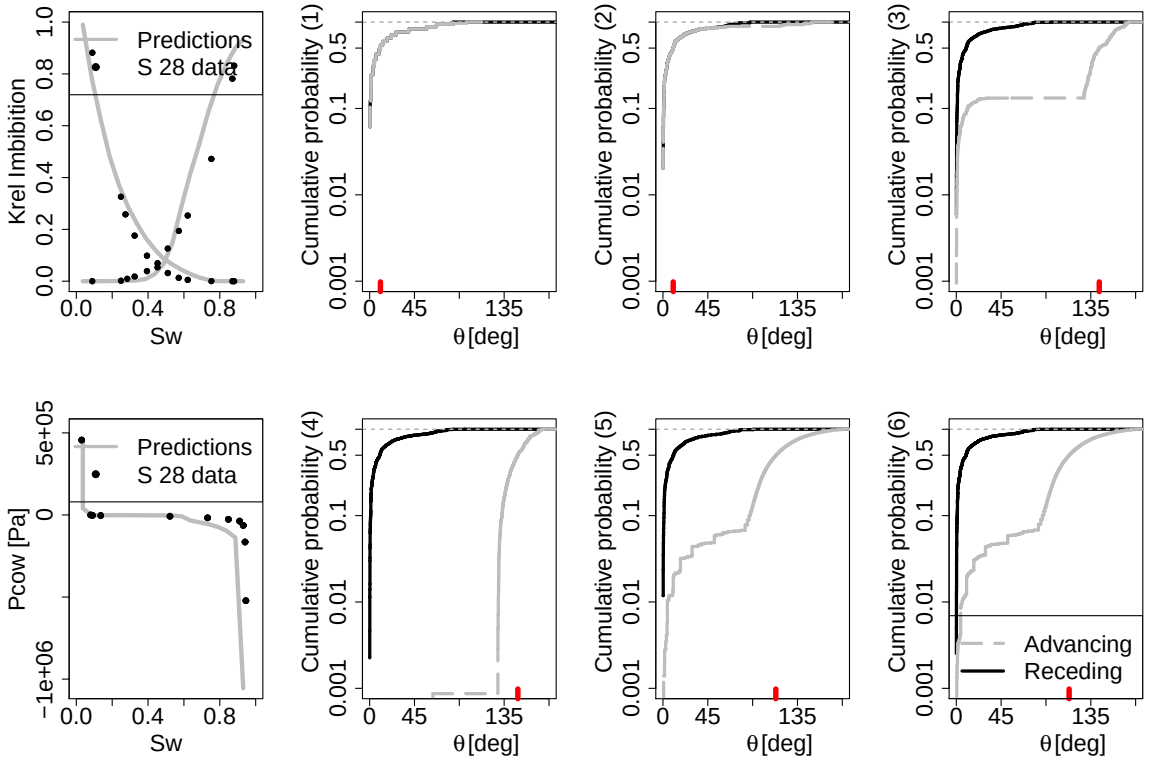

Fig. 7.37 Predicted S 28 imbibition relative permeabilities, capillary pressure, and hysteresis for advancing and receding contact angles. Top row, from left to right, predicted relative permeabilities for imbibition using HMC posterior statistics given matching S_{or}^{obs} and $P_{c,ow_{MIN}}^{obs}$ for a network size of $20 \times 20 \times 20$, and ECDF of contact angles in pore-size regions (1)–(3). Bottom row, from left to right, predicted imbibition capillary pressure using conditional HMC posterior statistics given matching S_{or}^{obs} and $P_{c,ow_{MIN}}^{obs}$ for a network size of $20 \times 20 \times 20$, and ECDF of contact angles in pore-size regions (4)–(6). The marks just above the x axis for (1)–(6) show the median. In (1)–(6), the black line is the water-receding contact angle, and the grey dashed line is the water-advancing contact angle after ageing.

quantiles predictions. Notice that the model parameters P10 and model parameters P90 envelopes do not enclose the measurement data and also the P10, P50 and P90 are not ordered. As we discussed in Section 6.2.1 there is no guarantee that one of these models will be the true model or that the three models will envelope the true predictions or they will be ordered [130].

7.3.3 Pore-Network Model Wettability of RT-II S 2 4

In the following sections, the same procedure was applied to two additional carbonate rock type samples (RT-II S 2 4 and RT-III S 2 20). They both have relatively uniform pore-size

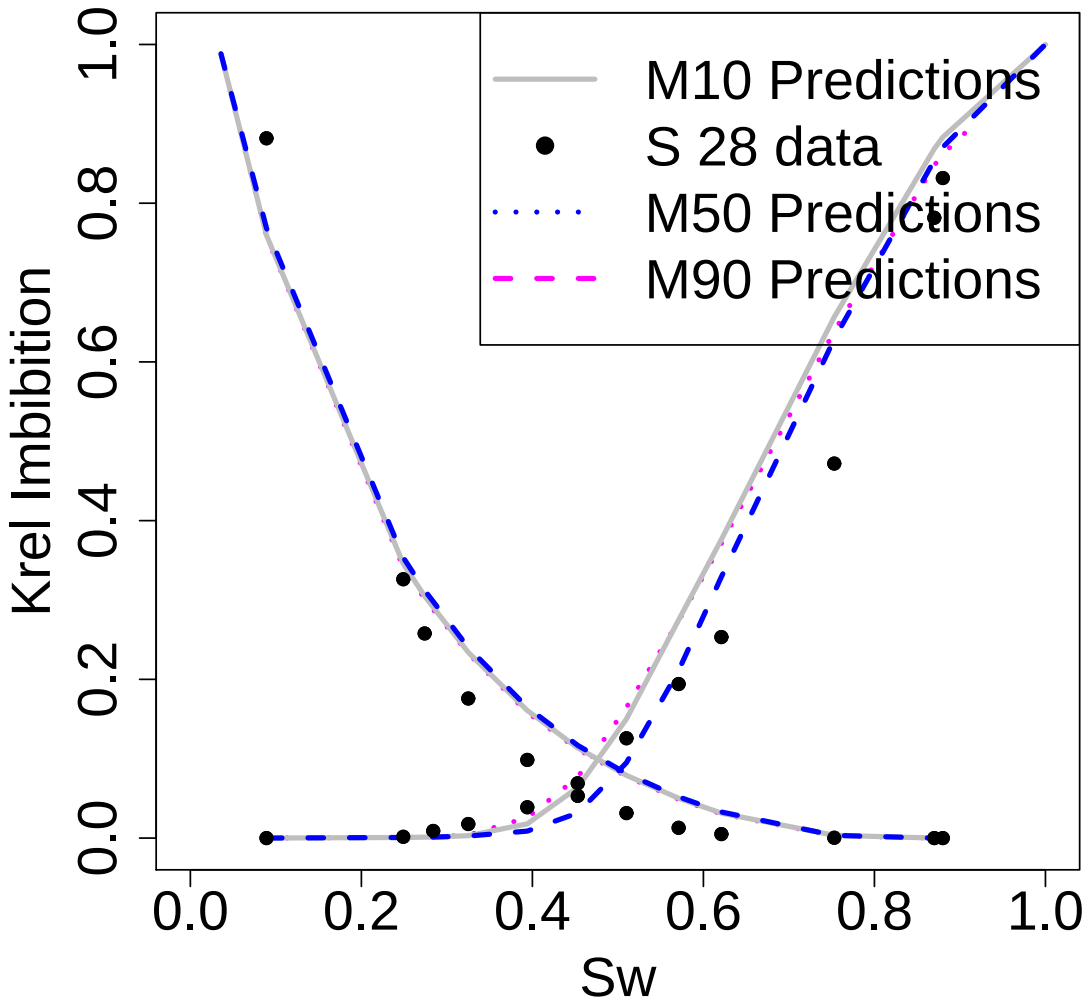

Fig. 7.38 Predicted S 28 imbibition relative permeabilities for inputs taken from the P10 (M10), P50(M50) and P90(M90) model parameters.

distributions (Fig. 7.41a).

Similar to the previous sample, the structural parameters were fixed taken from the Hamiltonian Monte Carlo inversion of structural parameters (Table 7.2).

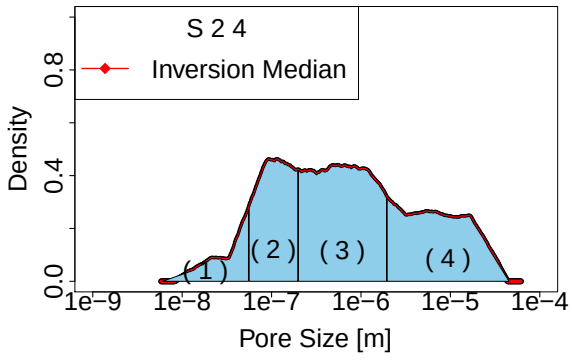

a

Table 7.3 Structural Parameters of RT-II S 2 4.

Parameter	Value
ν	0.51
$\bar{Z}$	4.24
p_1^*	0.001
p_2^*	0.001
p_3^*	0.001
p_4^*	0.001

Fig. 7.39 Sample S 2 4: (a) Pore-size distribution of RT-II S 2 4 Section 7.1 [185]. The numbers identify the ranges of pore sizes, which are associated with the pore-size distribution parameters (p^*) in Table 7.2. (b) pore-network model structural parameters of RT-II S 2 4 Section 7.1 [185]. ν is the volume exponent (Eq. (4.36)), $\bar{Z}$ is the average coordination number (Chapter 4.4.2), and p_i^* are the pore-size distribution parameters .

RT-II S 2 4: Determining Drainage Wettability Parameters for Water-Wetting Films with a 5° Threshold

In this section, we performed the same calculations as for S 28. As shown in Fig. 7.41a, the simulation was evenly distributed around the experimental connate water saturation. The posterior histogram of the fraction of pores in each population is slightly skewed to the left (Fig.7.41b).

Figure 7.41 shows that the maximum bounds (Fig. 7.41b and d) spread over larger receding contact angles than RT-I S 28.

The drainage heat map (Fig. 7.42) shows that the receding contact angles are concentrated in a wider range (0°–22°) than the corresponding case for RT-I S 28.

RT-II S 2 4: Determining Drainage Wettability Parameters for Water-Wetting Films with a 30° Threshold

In contrast, the posterior histogram of the fraction of pores in each population for $\vartheta_{ow_{Th}}^{ww} = 30°$ shows a distinct right-skewed trend (Fig. 7.43b) even for similar matching in the connate water saturation (Fig. 7.43a).

The posterior drainage heat map (Fig. 7.45) strongly depends on the water-wetting film criteria, as shown by the different concentration regions in Fig. 7.45 compared with Fig. 7.42. In Fig. 7.45, the receding contact angles show a wider distribution.

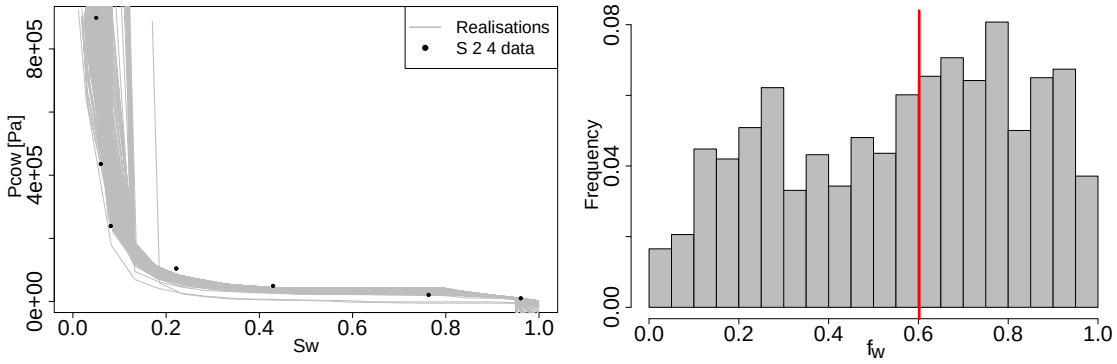

a b

Fig. 7.40 Sample S 2 4 drainage HMC inversion results for drainage with $\vartheta^{ww}_{ow_{Th}} = 5°$. (a) Posterior HMC realisations (grey lines). The measurements are shown as black filled circles. (b) Posterior marginal histogram of the fraction of pores whose contact angles were assigned to each population in Eq. (4.42). The line in (b) indicates the median.

RT-II S 2 4: Determining Imbibition Wettability Parameters for 5° and 175° Thresholds for Water- and Oil- Wetting Films

The realisations of imbibition inversion for $\vartheta^{ww}_{ow_{Th}} = 5°$ and $\vartheta^{ww}_{ow_{Th}} = 175°$ are shown in Fig. 7.46a. The minimum capillary pressure values of all of the realisations are more than two times greater than $P^{obs}_{c,ow_{MIN}}$ (Fig. 7.46a), which is expected from the posterior drainage heat map (Fig. 7.42). The receding contact angles are concentrated in the range 1°–5°(Fig. 7.42). Thus, the absolute value of the minimum possible imbibition capillary pressure will most likely be close to the maximum drainage capillary pressure. The posterior histogram of R_{wet} moved to the left (smaller radius) compared with the RT-I S 28 sample (Fig. 7.46b). It is clear that the evaluation of wettability is dependent on the drainage conditions.

Figure 7.48a shows the posterior imbibition heat map. The values are concentrated in the range 150°–180°.

RT-II S 2 4: Determining Imbibition Wettability Parameters for 30° and 150° Thresholds for Water- and Oil- Wetting Films

The realisations for S 2 4 with $\vartheta^{ww}_{ow_{Th}} = 30°$ and $\vartheta^{ow}_{ow_{Th}} = 150°$ show that the minimum imbibition capillary pressure reached close to $P^{obs}_{c,ow_{MIN}}$ (Fig. 7.49). The posterior histogram of R_{wet} is wider than the case with $\vartheta^{ww}_{ow_{Th}} = 30°$ and $\vartheta^{ow}_{ow_{Th}} = 150°$ (Fig. 7.49b). However, it is similar to the case with $\vartheta^{ww}_{ow_{Th}} = 30°$ and $\vartheta^{ow}_{ow_{Th}} = 150°$ and the medians are similar.

Figure 7.50 shows the posterior histograms of the wettability model parameters in Eq.

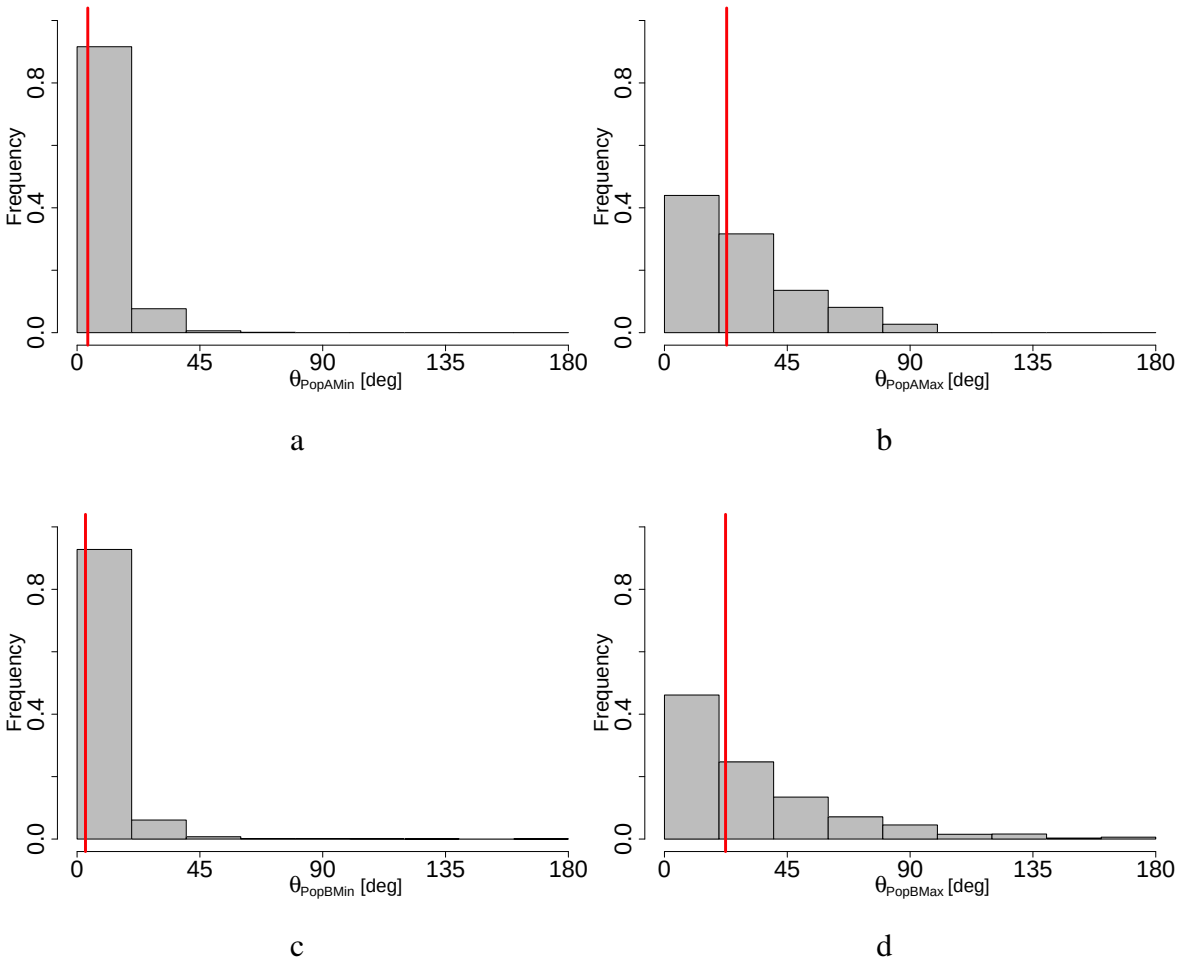

Fig. 7.41 Sample S 2 4 drainage with $\vartheta_{ow_{Th}}^{ww} = 5°$. Posterior histograms of the wettability parameters (Eq. (4.42)): (a) lower bound ($\vartheta_{ow_{MIN}}^{A-rec}$) and (b) upper bound ($\vartheta_{ow_{MAX}}^{A-rec}$) for population A, and (c) lower bound ($\vartheta_{ow_{MIN}}^{B-rec}$) and (d) upper bound ($\vartheta_{ow_{MAX}}^{B-rec}$) for population B. The red line in each histogram indicates the median.

4.43 for each pair of bounds that defined populations A and B. The graphs are different from their $\vartheta_{ow_{Th}}^{ww} = 5°$ and $\vartheta_{ow_{Th}}^{ow} = 175°$ counterparts. The posterior histograms of the bounds of population B spread towards lower contact angles (Fig. 7.50c and d) than the $\vartheta_{ow_{Th}}^{ww} = 5°$ and $\vartheta_{ow_{Th}}^{ow} = 175°$ case.

The minimum imbibition capillary pressure is closer to $P_{c,ow_{MIN}}^{obs}$ (Fig. 7.49b) than the case with $\vartheta_{ow_{Th}}^{ww} = 5°$ and $\vartheta_{ow_{Th}}^{ow} = 175°$. The residual oil saturation is slightly lower than S_{or}^{obs} (Fig. 7.49a). The entry pressure in capillary dominated flow follows the Young–Laplace equation. Therefore, for a given maximum entry pressure, the greater the receding contact angle, the smaller the pores that could be invaded by oil during drainage. Thus, wettability

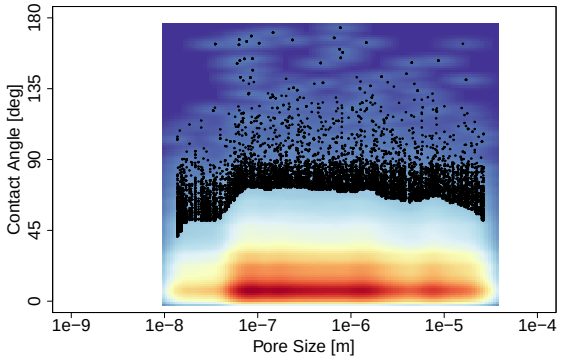

Fig. 7.42 Sample S 2 4 drainage heat map for drainage with $\vartheta^{ww}_{ow_{Th}} = 5°$. This is a bivariate density representation of the posterior distribution of contact angles in the pore-size distribution. The red regions represent high density and the blue regions represent zero density. The colour intensities indicate a nonuniform distribution.

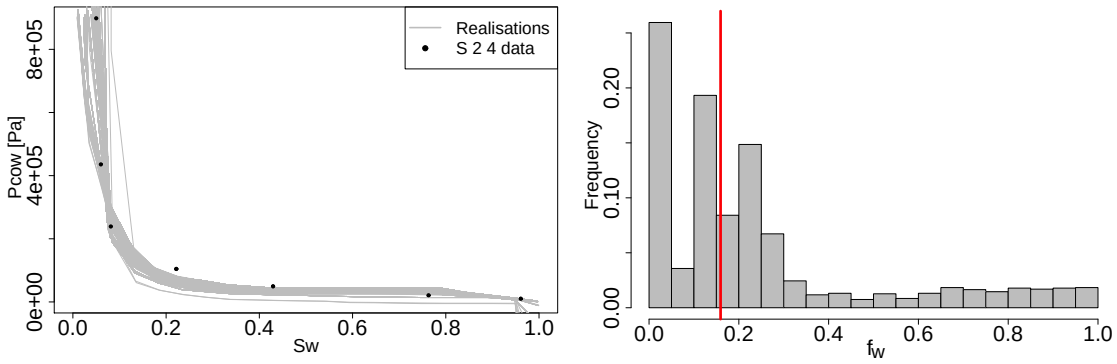

a b

Fig. 7.43 Sample S 2 4 drainage HMC inversion results for drainage with $\vartheta^{ww}_{ow_{Th}} = 30°$. (a) Posterior HMC realisations (grey lines). The measurements are shown as solid black circles. (b) Posterior marginal histogram of the fraction of pores whose contact angles were assigned to each population in Eq. (4.42). The line in (b) indicates the median.

alteration (Fig. 7.51b) could eventually lead to the magnitude of the minimum imbibition capillary pressure being higher than that of the drainage capillary pressure (Fig. 7.49a).

The conditional posterior imbibition heat map given those realisations matching the imbibition capillary pressure end-point (S^{obs}_{or} and $P^{obs}_{c,ow_{MIN}}$) is shown in Fig. 7.52a along with the drainage heat map (Fig. 7.52b). There is slightly higher density for pores in the size range 6×10^{-8} to 1×10^{-7} m (Fig. 7.52a), which were invaded by oil during drainage (Fig. 7.52b). Note the similarities between Fig. 7.48a ($\vartheta^{ww}_{ow_{Th}} = 5°$ and $\vartheta^{ow}_{ow_{Th}} = 175°$) and Fig. 7.52a ($\vartheta^{ww}_{ow_{Th}} = 30°$ and $\vartheta^{ow}_{ow_{Th}} = 150°$) (conditional heat map given matching imbibition

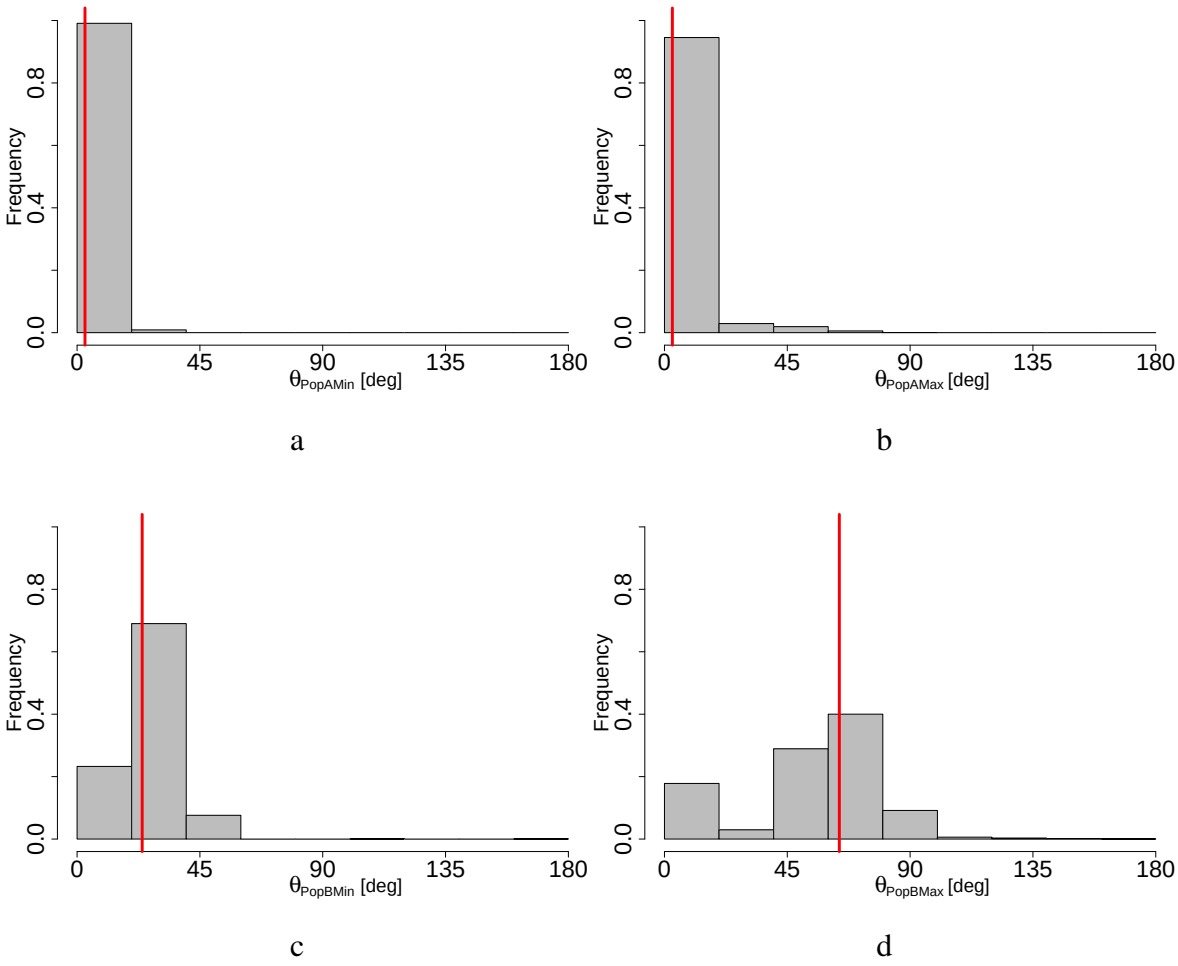

Fig. 7.44 Sample S 2 4 drainage with $\vartheta_{ow_{Th}}^{ww} = 30°$. Posterior histograms of the wettability parameters (Eq. (4.42)): (a) lower bound ($\vartheta_{ow_{MIN}}^{A-rec}$) for and (b) upper bound ($\vartheta_{ow_{MAX}}^{A-rec}$) for population A, and (c) lower bound ($\vartheta_{ow_{MIN}}^{B-rec}$) and (d) upper bound ($\vartheta_{ow_{MAX}}^{B-rec}$) for population B. The red line in each histogram indicates the median.

capillary pressure end-point).

7.3.4 RT-II S 2 4: Prediction of Relative Permeabilities for Water-Flooding and Comparison with Experiments

We repeat the same methodology as before for RT-I. Using the BC pore-size distribution index ($\Lambda = 1.17$) from fitting the MICP and the volume exponent (Table 7.2), we estimated the pore-network model conductance exponent $\lambda = 2.437$ (Eq. (4.41)). And similar to RT-I, the structural network parameters of Table 7.4 along with the ECDF of receding and ad-

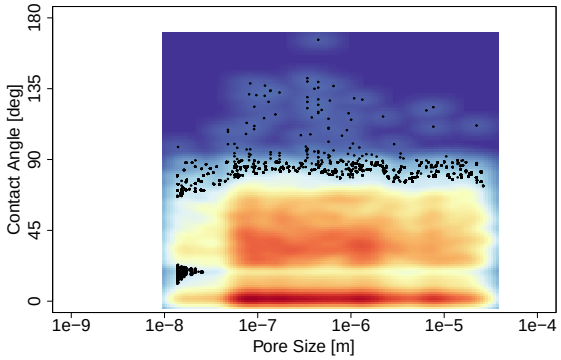

Fig. 7.45 Sample S 2 4 drainage heat map for drainage with $\vartheta^{ww}_{ow_{Th}} = 30°$. This is a bivariate density representation of the posterior distribution of contact angles in the pore-size distribution. The red regions represent high density and the blue regions represent zero density. The colour intensities indicate a nonuniform distribution.

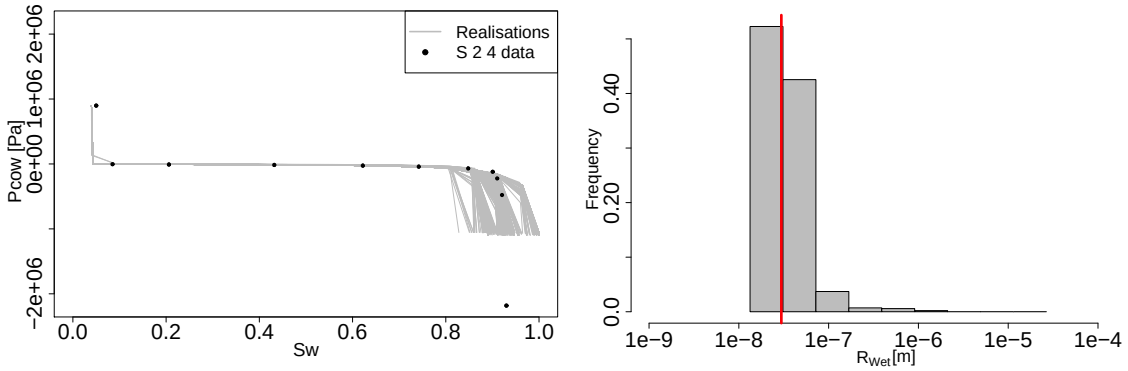

a b

Fig. 7.46 S 2 4 imbibition HMC inversion results for imbibition with $\vartheta^{ww}_{ow_{Th}} = 5°$ and $\vartheta^{ow}_{ow_{Th}} = 175°$. (a) Posterior HMC realisations (grey lines). The measurements are shown as solid black circles. (b) Posterior marginal histogram of the radius that separates the two pore populations. The contact angles were assigned to each population in Eq. (4.43). The line in (b) indicates the median.

vancing contact angles for each region in the pore-size distribution which are shown in Figs 7.541,2,3,4 were used to predict the relative permeabilities shown in Fig. 7.53a. The ECDFs of receding and advancing contact angles were obtained from the conditional posterior heat maps of receding and advancing contact angles given matching of S^{obs}_{or} and $P^{obs}_{c,ow_{MIN}}$ for the case with $\vartheta^{ww}_{ow_{Th}} = 30°$ and $\vartheta^{ow}_{ow_{Th}} = 150°$ for wetting films.

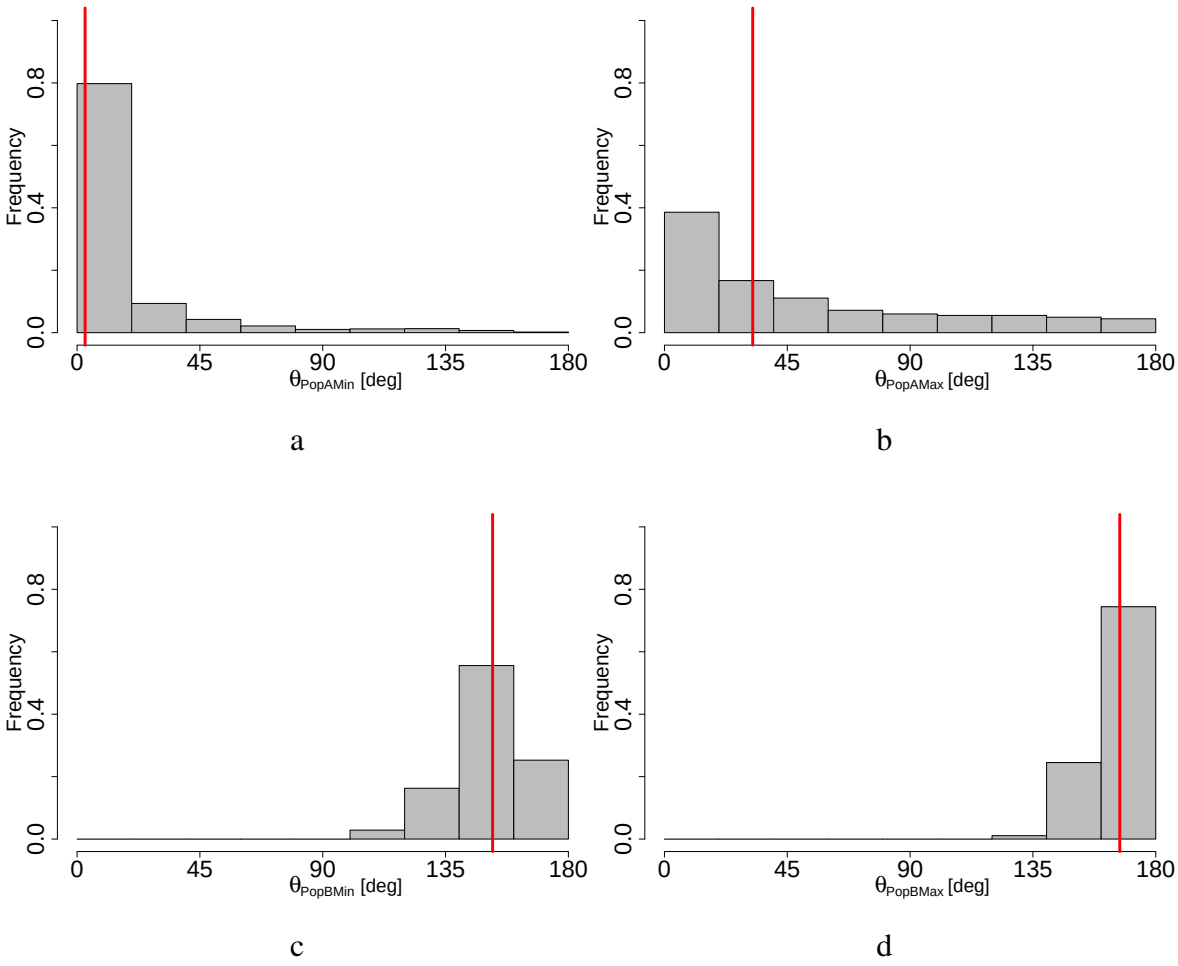

Fig. 7.47 S 2 4 imbibition HMC inversion results $\vartheta_{ow_{Th}}^{ww} = 5°$ and $\vartheta_{ow_{Th}}^{ow} = 175°$. Posterior histograms of the wettability parameters (Eq. (4.43)): (a) lower bound ($\vartheta_{ow_{MIN}}^{A-adv}$) and (b) upper bound ($\vartheta_{ow_{MAX}}^{A-adv}$) for population A, and (c) lower bound ($\vartheta_{ow_{MIN}}^{B-adv}$) and (d) upper bound ($\vartheta_{ow_{MAX}}^{B-adv}$) for population B. The red line in each histogram indicates the median.

Table 7.4 Structural Parameters of RT-II S 2 4.

Parameter	Value
ν	0.51
$\bar{Z}$	4.24
p_1^*	0.001
p_2^*	0.001
p_3^*	0.001
p_4^*	0.001
λ	2.437

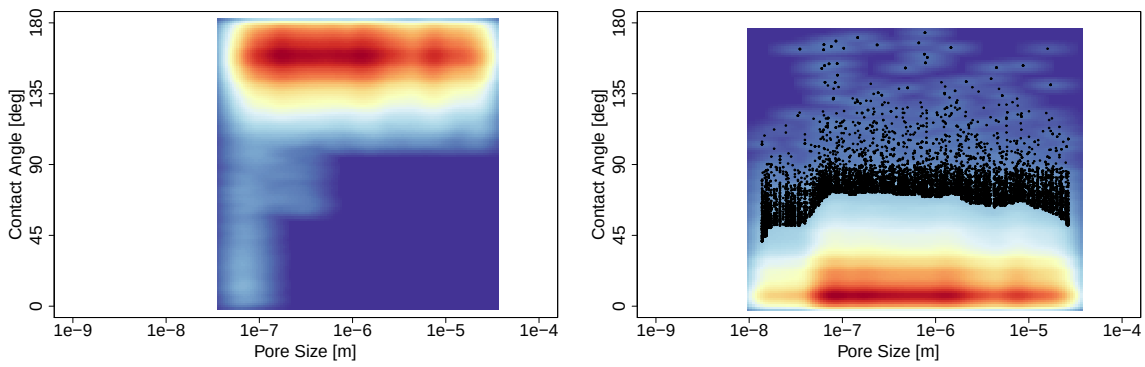

a b

Fig. 7.48 Sample S 2 4 heat maps with $\vartheta^{ww}_{ow_{Th}} = 5°$ and $\vartheta^{ow}_{ow_{Th}} = 175°$. (a) Imbibition and (b) drainage heat maps. These are bivariate density representations of the posterior distribution of contact angles in the pore-size distribution. The red regions represent high density and the blue regions represent zero density. The colour intensities indicate a nonuniform distribution.

Figure 7.54 summarises the predictions and wettability alteration. The ECDFs (Fig. 7.54 (1)–(4)) show the hysteresis in the contact angle from receding to advancing (black and grey lines in Fig. 7.54(1)–(4), respectively). The small pores that remained water-wet caused the overlapping of the black and grey lines in Fig. 7.54(1). The large pores had larger contact angles. However, the mid-sized pores (Fig. 7.54(2)) showed a distinct pattern compared with larger pores (Fig. 7.54(3)–(4)). The cumulative probability at 0.5 for (2)–(4) (i.e., the median) is 180°. This shows that the sample was strongly oil-wet.

This is consistent with the relative permeability intersection being shifted to the left towards lower water saturation. This strong wetting characteristic is somewhat contrary to the average value determined by analytical methods in a previous study of this data set [241], presumably because this sample is suspected to have cleaning problems.

Predictions using model parameters for quantiles P10,P50 and P90 shows less variability between the models in Fig. 7.55. This is caused by the strong wetting characteristics inferred by the HMC inversion.

7.3.5 Pore-Network Model Wettability of RT-III S 2 20

The same HMC inversions were repeated for RT-III S 2 20. This rock type shows structural parameters very similar to RT-II with the only difference being that the magnitude of the minimum capillary pressure is similar to the maximum value for drainage. The connate

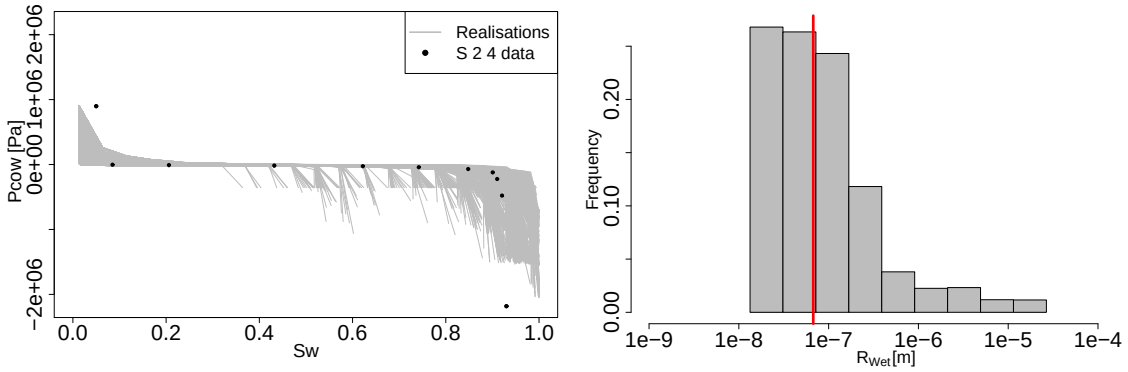

a b

Fig. 7.49 S 2 4 imbibition HMC inversion results for imbibition with $\vartheta^{ww}_{ow_{Th}} = 30°$ and $\vartheta^{ow}_{ow_{Th}} = 150°$. (a) Posterior HMC realisations (grey lines). The measurements are shown as solid black circles. (b) Posterior marginal histogram of the radius that separates the two pore populations. Their contact angles were assigned to each population in Eq. (4.43). The line in (b) indicates the median.

water and residual oil saturation are similar to the values for the other two samples.

RT–III S 2 20: Determining Drainage Wettability Parameters for Water-Wetting Films with a 5° Threshold

The set of graphs is shown in Figs. 7.57–7.59. The results obtained for the case with a $\vartheta^{ww}_{ow_{Th}} = 5°$ for water-wetting films are qualitatively similar to those for the other two samples.

RT–III S 2 20: Determining Drainage Wettability Parameters for Water-Wetting Films with a 30° Threshold

The case with a $\vartheta^{ww}_{ow_{Th}} = 30°$ shows similar behaviour to RT-II S 28. The histogram of the fraction of pores in populations A and B is strongly skewed to the left (Fig. 7.60b). The skewness is opposite to that for RT-II S 28. However, it led to a similar pattern in the drainage heat map to RT-II S 2 24 (Fig.7.45), although with smaller receding contact angles concentrated in two narrow regions close to each other (Fig. 7.62).

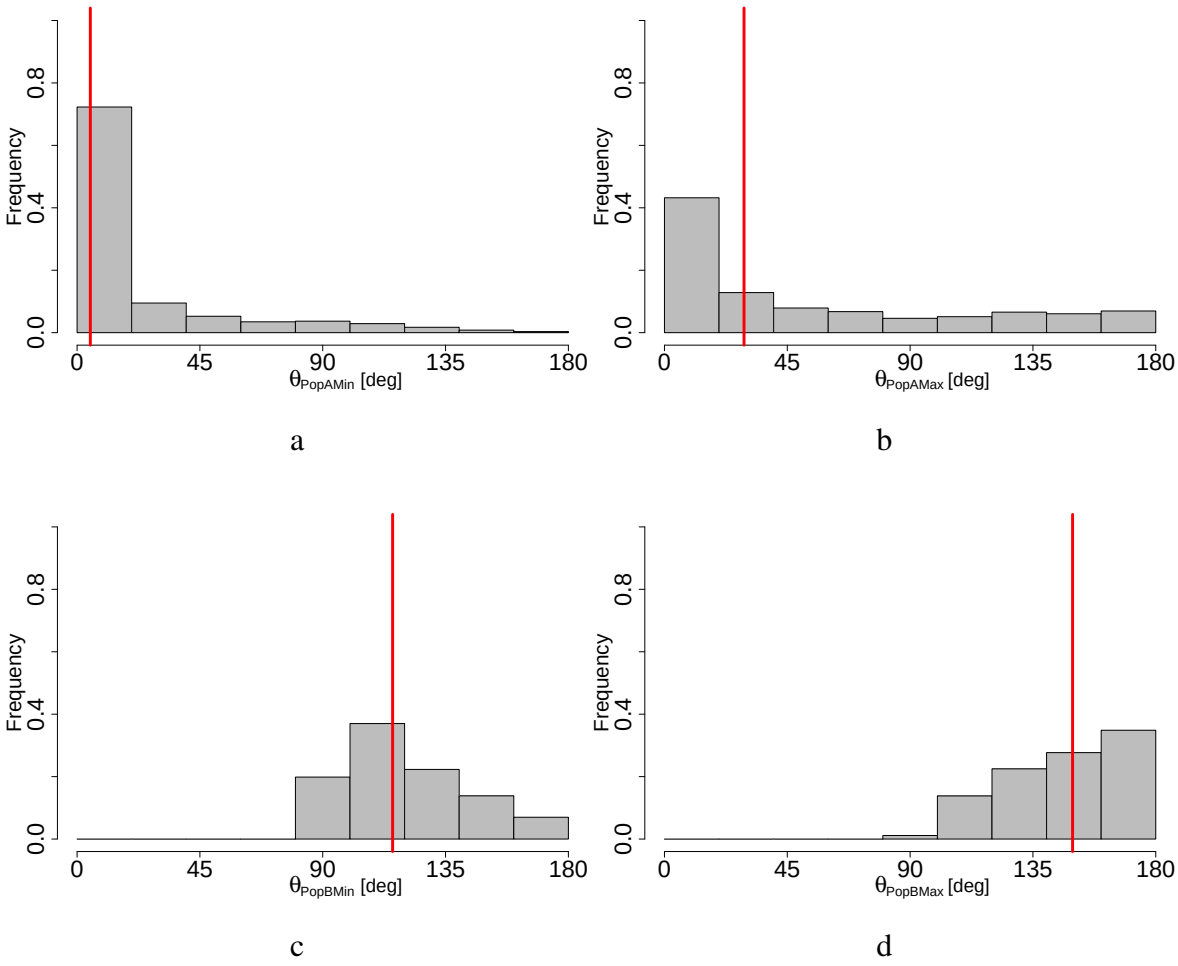

Fig. 7.50 Sample S 2 4 imbibition HMC inversion results for imbibition with $\vartheta^{ww}_{ow_{Th}} = 30°$ and $\vartheta^{ow}_{ow_{Th}} = 150°$. Posterior histograms of the wettability parameters (Eq. (4.43)): (a) lower bound ($\vartheta^{A-adv}_{ow_{MIN}}$) and (b) upper bound ($\vartheta^{A-adv}_{ow_{MAX}}$) for population A, and (c) lower bound ($\vartheta^{B-adv}_{ow_{MIN}}$) and (d) upper bound ($\vartheta^{B-adv}_{ow_{MAX}}$) for population B. The red line in each histogram indicates the median.

RT–III S 2 20: Determining Imbibition Wettability Parameters for 5° and 175° Thresholds for Water- and Oil- Wetting Films

Figure 7.63 shows the imbibition capillary pressure realisations along with the posterior histogram of R_{wet}, which separates populations A and B in Eq. (4.43).

Figure 7.65a shows that above 1×10^{-6} m the advancing contact angles are concentrated in the range 90°–135°, and the concentration slowly decrease towards 180°. Below 1×10^{-6} m, there is an additional region from 0°to 22°with a high concentrate of values.

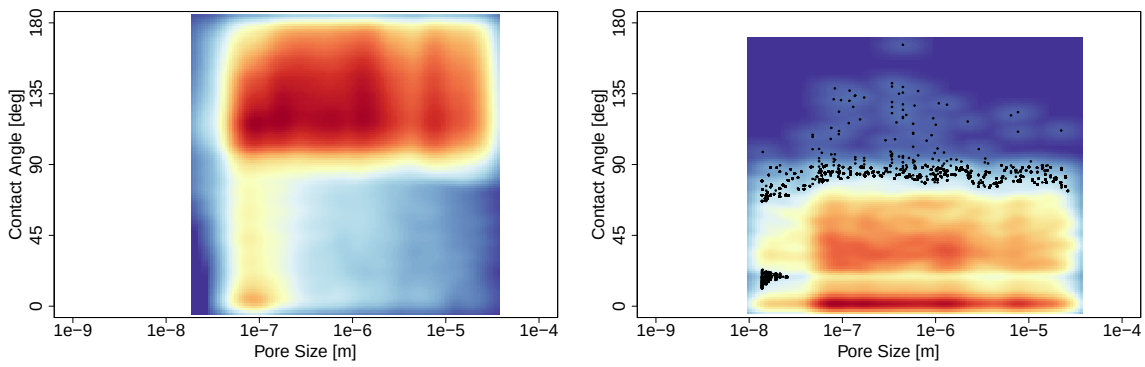

a b

Fig. 7.51 Sample S 2 4 Heat maps with $\vartheta^{ww}_{ow_{Th}} = 30°$ and $\vartheta^{ow}_{ow_{Th}} = 150°$. (a) Imbibition and (b) drainage heat maps. These are bivariate density representations of the posterior distribution of contact angles in the pore-size distribution. The red regions represent high density and the blue regions represent zero density. The colour intensities indicate a nonuniform distribution.

RT–III S 2 20: Determining Imbibition Wettability Parameters for 30° and 150° Thresholds for Water- and Oil-Wetting Films

For the case of S 2 20 with $\vartheta^{ww}_{ow_{Th}} = 30°$ and $\vartheta^{ow}_{ow_{Th}} = 150°$, the data are similar to the data for RT-I S 28, but the R_{wet} posterior histogram is slightly shifted to the left towards smaller pore sizes (Fig. 7.66b).

Figure 7.67 shows the posterior histograms of the model parameters. The general shapes of Fig. 7.67a and b are similar to the equivalent graphs for RT-I S 2 20 and RT-II S 2 24. In contrast to the other two samples, the posterior histograms in Fig. 7.67c and d are concentrated around 90°and 180°, respectively.

The posterior imbibition heat map (Fig. 7.68a) is slightly different from the other two samples. There is a high density in a slightly wider range of pore sizes (6×10^{-8} to 1×10^{-6} m) than for RT-I S 28. The next section will show that the mid-sized pores have a similar median advancing contact angle to the large pores. However, they are moderately less oil-wet in the sense that the ECDF of the advancing contact angles has 10% water-wet pores while the ECDF of the large pores has only 1%.

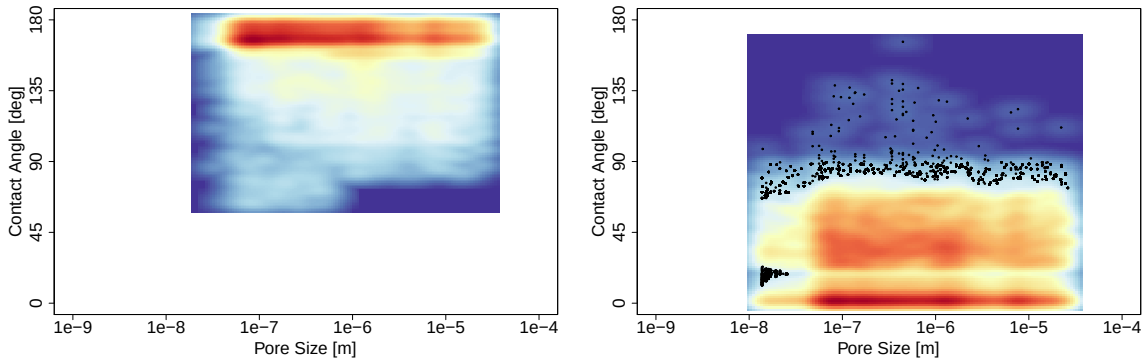

a b

Fig. 7.52 Sample S 2 4 heat maps with $\vartheta^{ww}_{ow_{Th}} = 30°$ and $\vartheta^{ow}_{ow_{Th}} = 150°$. (a) Imbibition heat map conditional to matching of S^{obs}_{or} and $P^{c,obs}_{ow_{MIN}}$, and (b) drainage heat map. These are bivariate density representations of the posterior distribution of contact angles in the pore-size distribution. The red regions represent high density and the blue regions represent zero density. The colour intensities indicate a nonuniform distribution.

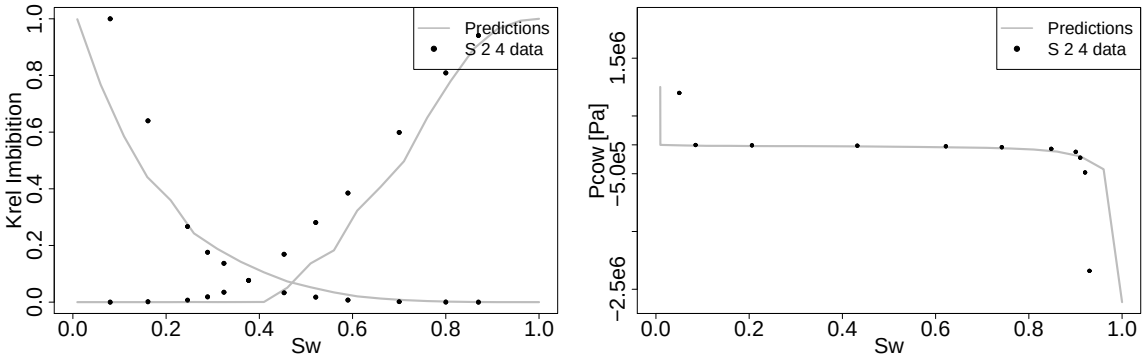

a b

Fig. 7.53 Predicted S 2 4 relative permeabilities and capillary pressure for imbibition. (a) Predicted imbibition relative permeabilities using HMC posterior statistics given matching S^{obs}_{or} and $P^{obs}_{c,ow_{MIN}}$ for a network size of $20 \times 20 \times 20$, and (b) imbibition capillary pressure corresponding to the relative permeabilities in (a).

7.3.6 RT-III S 2 20: Prediction of Relative Permeabilities for Water-Flooding and Comparison with Experiments

As outlined for the two previous samples, we calculated the conductance exponent in the power-law using the BC model and the volume exponent (Table 7.3). The pore-size distribution index derived by matching the MICP to the BC model was $\Lambda = 1.335$ and the volume

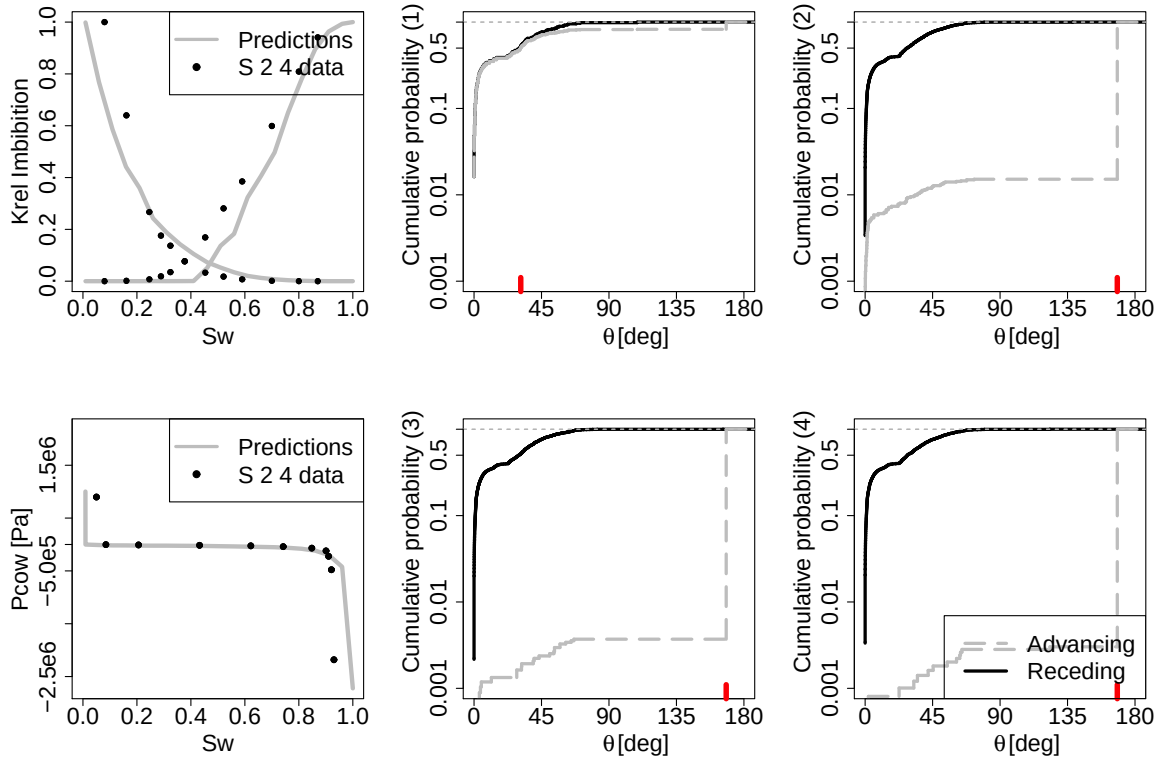

Fig. 7.54 Predicted S 2 4 imbibition relative permeabilities, capillary pressure, and hysteresis for advancing and receding contact angles. Top row, from left to right, predicted imbibition relative permeabilities using HMC posterior statistics given matching S_{or}^{obs} and $P_{c,ow_{MIN}}^{obs}$ for a network size of $20 \times 20 \times 20$, and ECDF of the contact angles in pore-size regions (1) and (2). Bottom row, from left to right, predicted imbibition capillary pressure using conditional HMC posterior statistics given matching S_{or}^{obs} and $P_{c,ow_{MIN}}^{obs}$ for a network size of $20 \times 20 \times 20$, and ECDF of the contact angles in pore-size regions (3) and (4). The black line is the water-receding contact angle, and the grey dashed line is the water-advancing contact angle after ageing. The red lines on the horizontal axes for (1)–(4) show the median values.

exponent (ν from Table 7.3) resulted in the conductance exponent $\lambda = 2.3$ (Eq. (4.41)). We used the conditional posterior distribution of receding and advancing contact angles given matching of S_{or}^{obs} and $P_{c,ow_{MIN}}^{obs}$ for the case with $\vartheta_{ow_{Th}}^{ww} = 30°$ and $\vartheta_{ow_{Th}}^{ow} = 150°$ for wetting films.

The structural network parameters of Table 7.4 along with the ECDF of receding and advancing contact angles for each region in the pore-size distribution which are shown in Figs 7.70 labels (1), (2), (3) and (4) were used to predict the relative permeabilities shown in Fig. 7.69a. The predictions closely agree with the steady-state experimental data, as shown

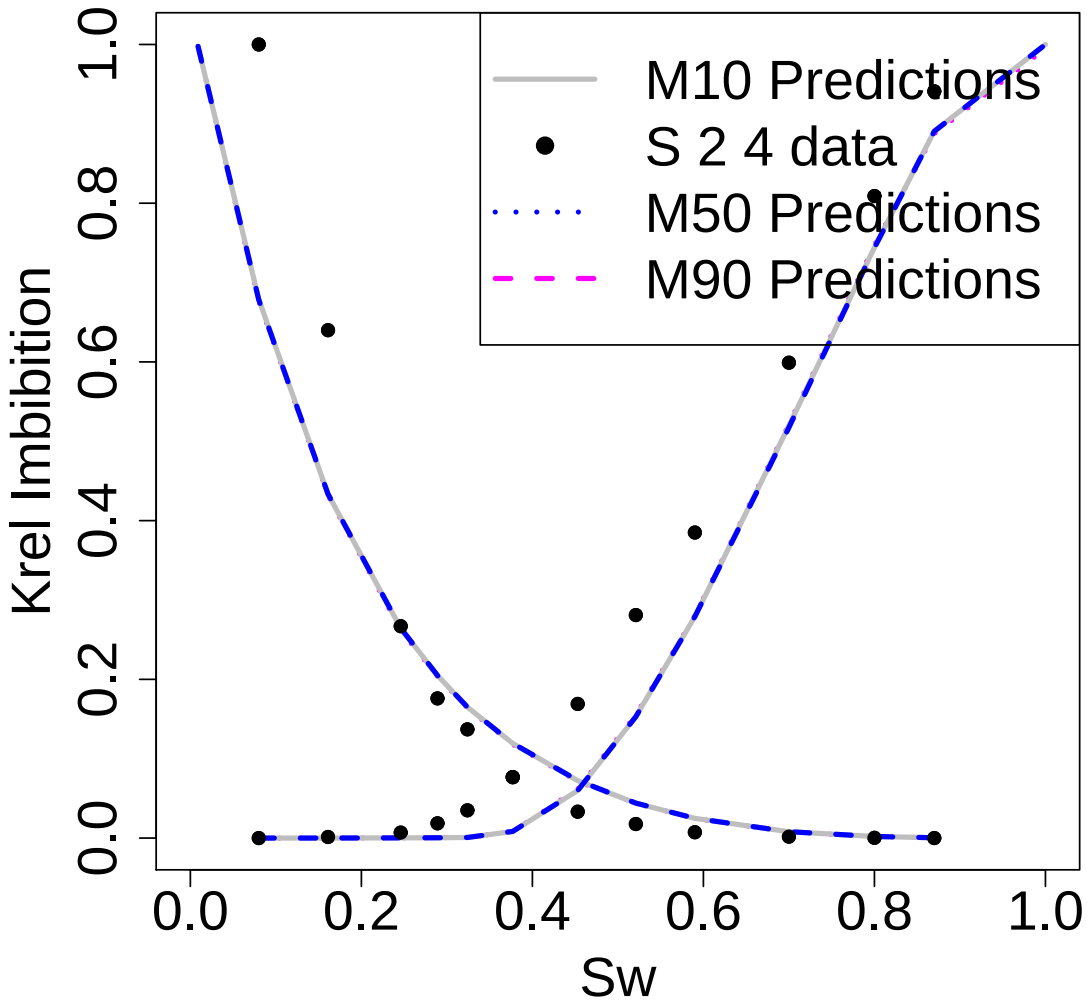

Fig. 7.55 Predicted S 2 4 imbibition relative permeabilities for inputs taken from the P10 (M10), P50(M50) and P90(M90) model parameters.

in Fig. 7.69a.

Similar to the two other rock types, the small pores remained water-wet (overlapping curves in Fig. 7.70(1)). The mid-sized pores (Fig. 7.70(2)) showed a different trend in the advancing contact angle ECDF compared with the larger pores (Fig. 7.70(3)–(4)). Figure 7.70(2) shows around 10% water-wet (less than 90°) pores while Fig. 7.70(3)–(4)) shows only 1%. However, the medians in Fig. 7.70(2)–(4) are around 112°–115°, which agrees very well with the average value determined with the analytical method in [241].

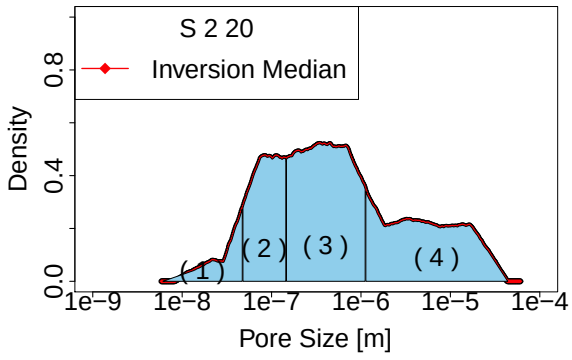

b

Table 7.5 Structural Parameters of RT-III S 2 20.

Parameter	Value
ν	0.45
$\bar{Z}$	3.96
p_1^*	0.041
p_2^*	0.236
p_3^*	0.434
p_4^*	0.290

Fig. 7.56 Sample S 2 20: (a) Pore-size distribution of RT-III S 2 20 Section 7.1 [185]. The numbers identify the ranges of pore sizes, and they are associated with the pore-size distribution parameters (p^*) in Table 7.3. (b) pore-network model structural parameters of RT-III S 2 20 Section 7.1 [185]. ν is the volume exponent (Eq. (4.36)), $\bar{Z}$ is the average coordination number (Chapter 4.4.2), and p_i^* are the pore-size distribution parameters.

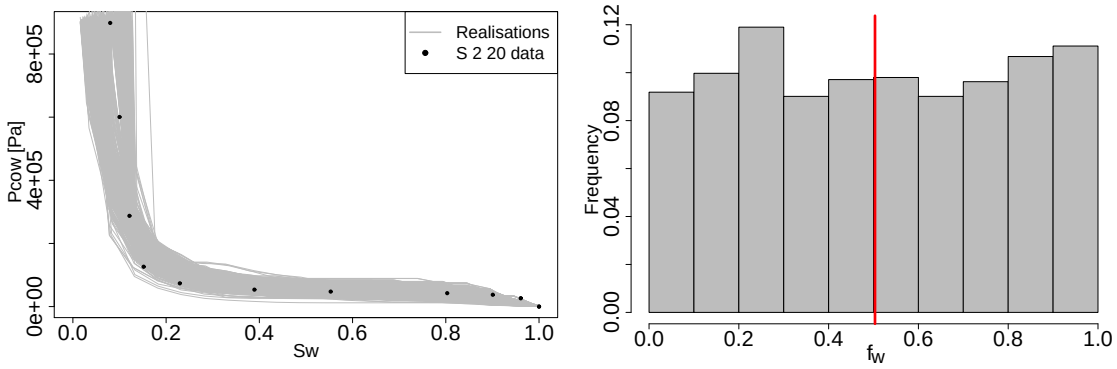

a b

Fig. 7.57 Sample S 2 20 HMC inversion results for drainage with $\vartheta_{ow_{Th}}^{ww} = 5°$. (a) Posterior HMC realisations (grey lines). The measurements are shown as solid black circles. (b) Posterior marginal histogram of the fraction of pores whose contact angles were assigned to each population in Eq. (4.42). The line in (b) indicates the median.

Figure 7.71 shows the quantiles relative permeabilities predictions. Notice that models P10 and P90 envelop all measurements for water relative permeability except for high water saturations.

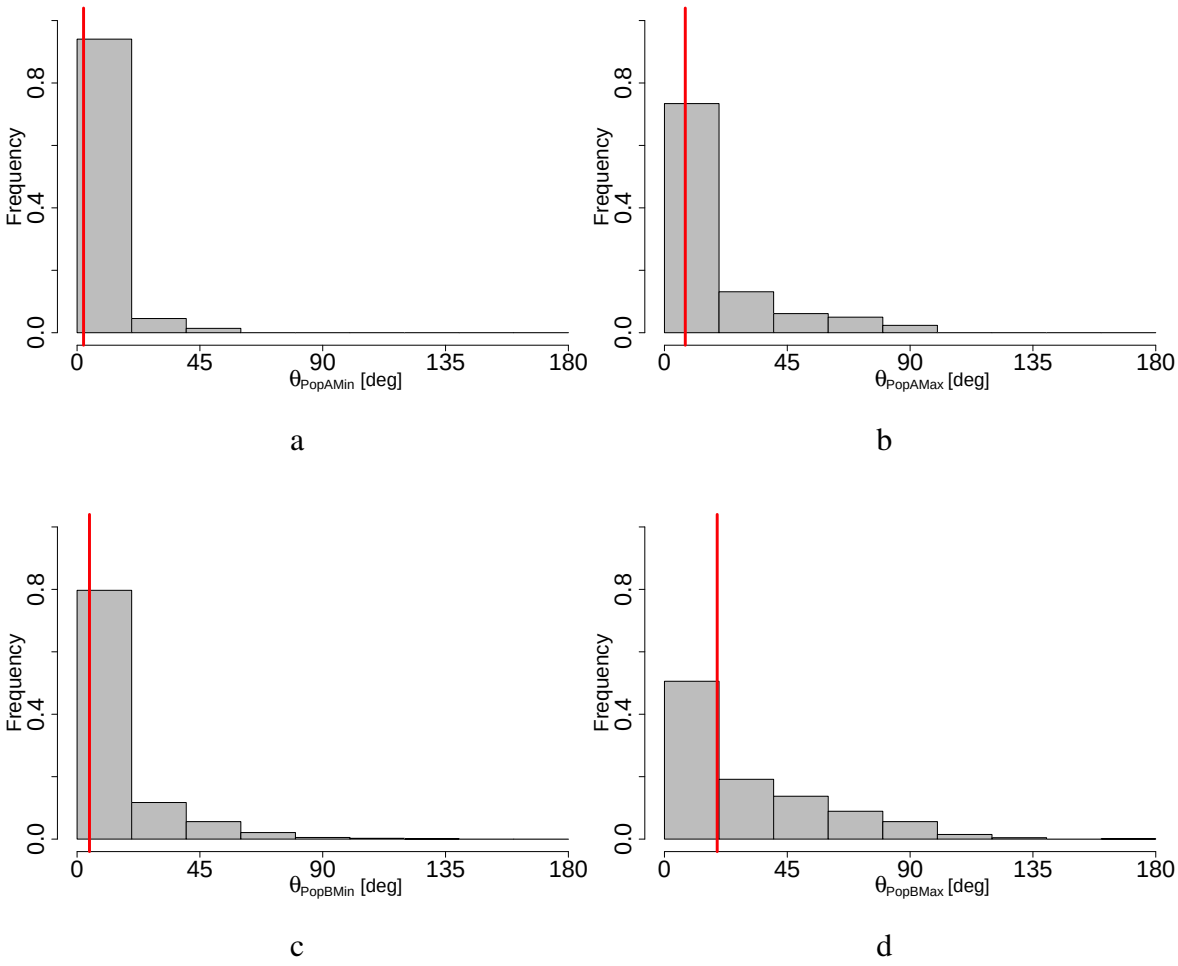

Fig. 7.58 Sample S 2 20 drainage case with $\vartheta_{ow_{Th}}^{ww} = 5°$. Posterior histograms of the wettability parameters (Eq. (4.42)): (a) lower bound ($\vartheta_{ow_{MIN}}^{A-rec}$) and (b) upper bound ($\vartheta_{ow_{MAX}}^{A-rec}$) for population A, and (c) lower bound ($\vartheta_{ow_{MIN}}^{B-rec}$) and (d) upper bound ($\vartheta_{ow_{MAX}}^{B-rec}$) for population B. The red line in each histogram indicates the median.

Table 7.6 Structural Parameters of RT-III S 2 20.

Parameter	Value
ν	0.45
$\bar{Z}$	3.96
p_1^*	0.041
p_2^*	0.236
p_3^*	0.434
p_4^*	0.290
λ	2.3

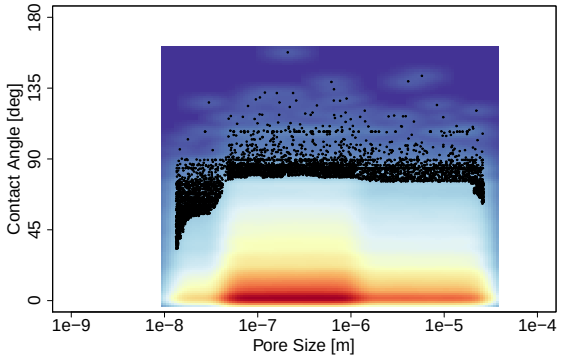

Fig. 7.59 Sample S 2 20 drainage heat map for drainage with $\vartheta^{ww}_{ow_{Th}} = 30°$. This is a bivariate density representation of the posterior distribution of contact angles in the pore-size distribution. The red regions represent high density and the blue regions represent zero density. The colour intensities indicate a nonuniform distribution.

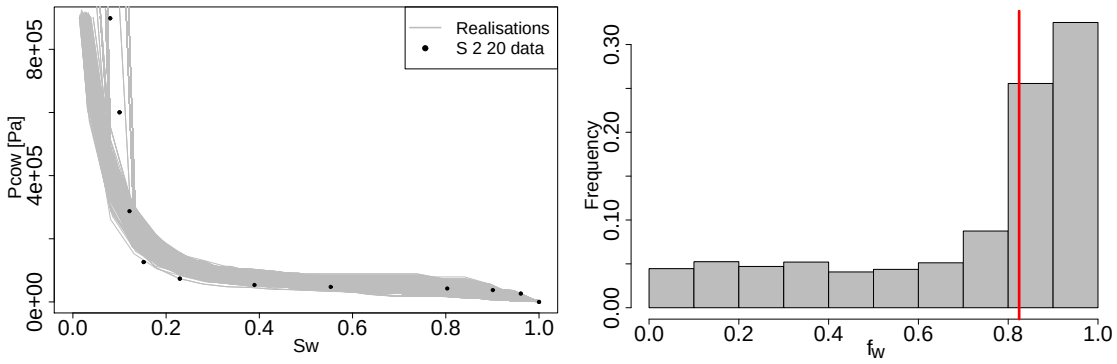

a b

Fig. 7.60 Sample S 2 20 HMC inversion results for drainage with $\vartheta^{ww}_{ow_{Th}} = 30°$. (a) Posterior HMC realisations (grey lines). The measurements are shown as solid black circles. (b) Posterior marginal histogram of the fraction of pores whose contact angles were assigned to each population in Eq. (4.42). The red line in (b) indicates the distribution median.

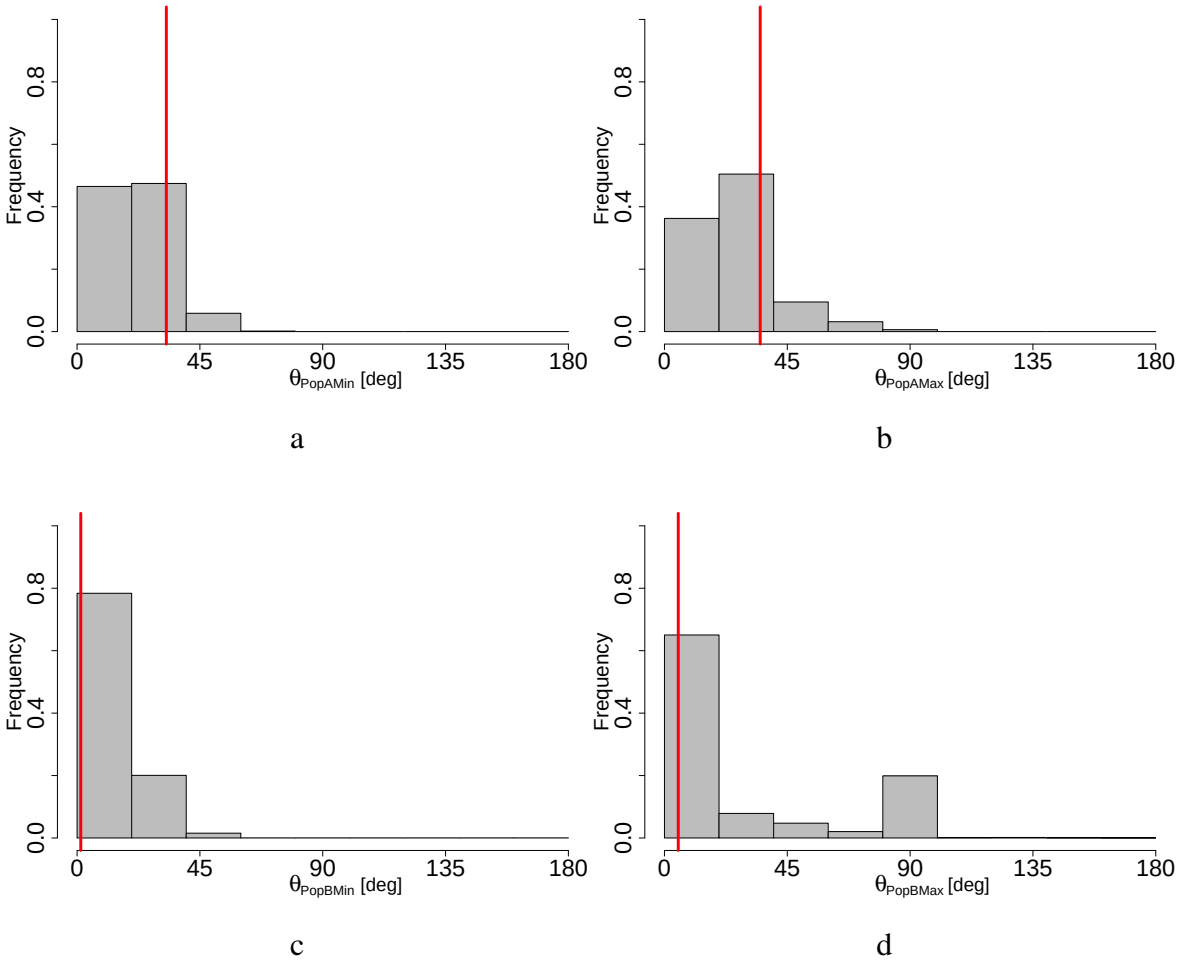

Fig. 7.61 Sample S 2 20 drainage with $\vartheta_{ow_{Th}}^{ww} = 30°$. Posterior histograms of the wettability parameters (Eq. (4.42)): (a) lower bound ($\vartheta_{ow_{MIN}}^{A-rec}$) and (b) upper bound ($\vartheta_{ow_{MAX}}^{A-rec}$) for population A, and (c) lower bound ($\vartheta_{ow_{MIN}}^{B-rec}$) and (d) upper bound ($\vartheta_{ow_{MAX}}^{B-rec}$) for population B. The red line in each histogram indicates the median.

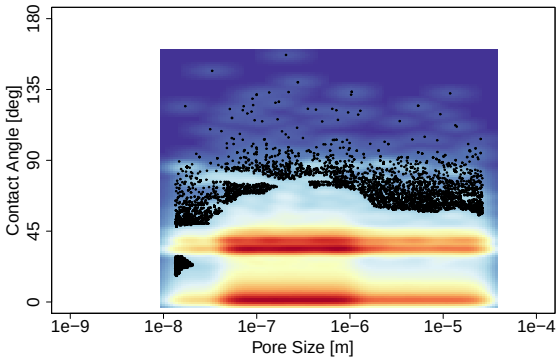

Fig. 7.62 Sample S 2 20 heat map for drainage with $\vartheta^{ww}_{ow_{Th}} = 30°$. This is a bivariate density representation of the posterior distribution of contact angles in the pore-size distribution. The red regions represent high density and the blue regions represent zero density. The colour intensities indicate a nonuniform distribution.

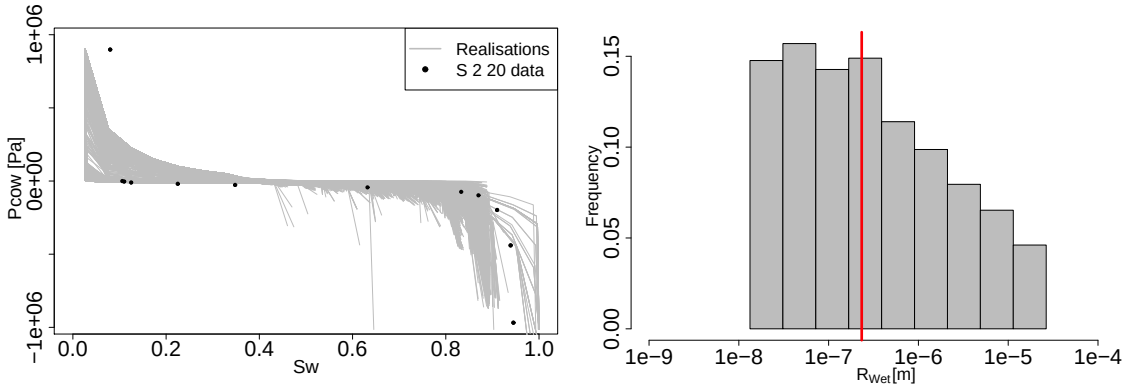

a b

Fig. 7.63 S 2 20 HMC inversion results for imbibition with $\vartheta^{ww}_{ow_{Th}} = 5°$ and $\vartheta^{ow}_{ow_{Th}} = 175°$. (a) Posterior HMC realisations (grey lines). The measurements are shown as solid black circles. (b) Posterior marginal histogram of the radius that separates the two pore populations. The contact angles were assigned to each population in Eq. (4.43). The red line in (b) indicates the median.

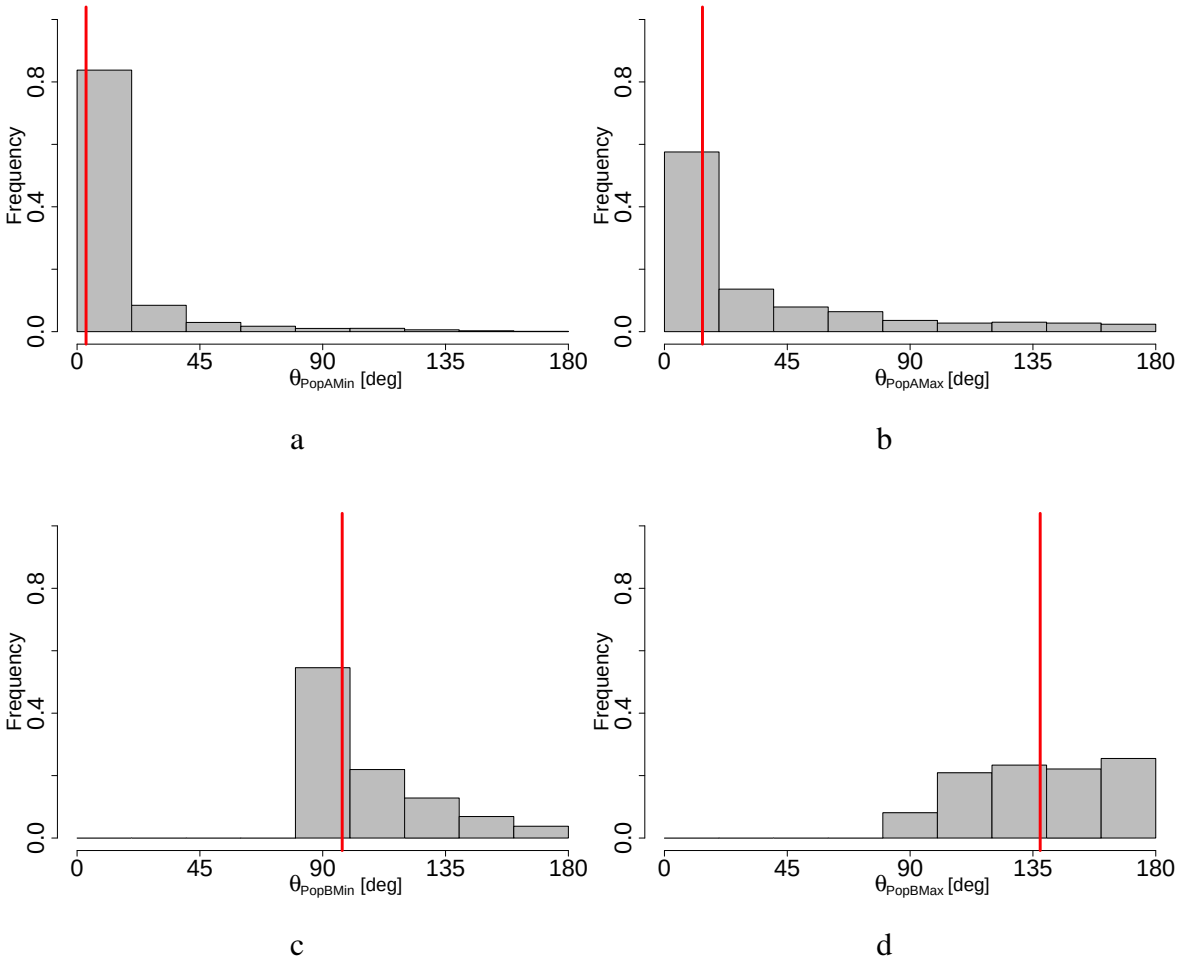

Fig. 7.64 S 2 20 imbibition HMC inversion results for imbibition with $\vartheta_{ow_{Th}}^{ww} = 5°$ and $\vartheta_{ow_{Th}}^{ow} = 175°$. Posterior histograms of the wettability parameters (Eq. (4.43)): (a) lower bound ($\vartheta_{ow_{MIN}}^{A-adv}$) and (b) upper bound ($\vartheta_{ow_{MAX}}^{A-adv}$) for population A, and (c) lower bound ($\vartheta_{ow_{MIN}}^{B-adv}$) and (d) upper bound ($\vartheta_{ow_{MAX}}^{B-adv}$) for population B. The red line in each histogram indicates the median.

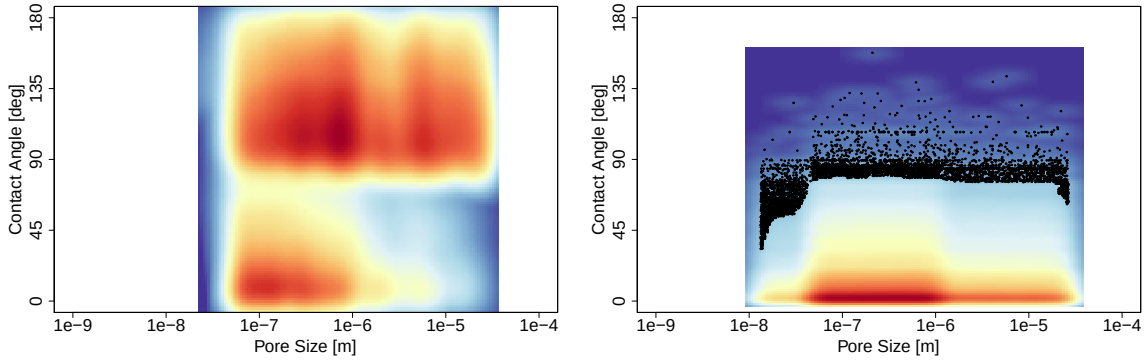

a b

Fig. 7.65 Sample S 2 20 heat maps with $\vartheta^{ww}_{ow_{Th}} = 5°$ and $\vartheta^{ow}_{ow_{Th}} = 175°$. (a) Imbibition and (b) drainage heat maps. These are bivariate density representations of the posterior distribution of contact angles in the pore-size distribution. The red regions represent high density and the blue regions represent zero density. The colour intensities indicate a nonuniform distribution.

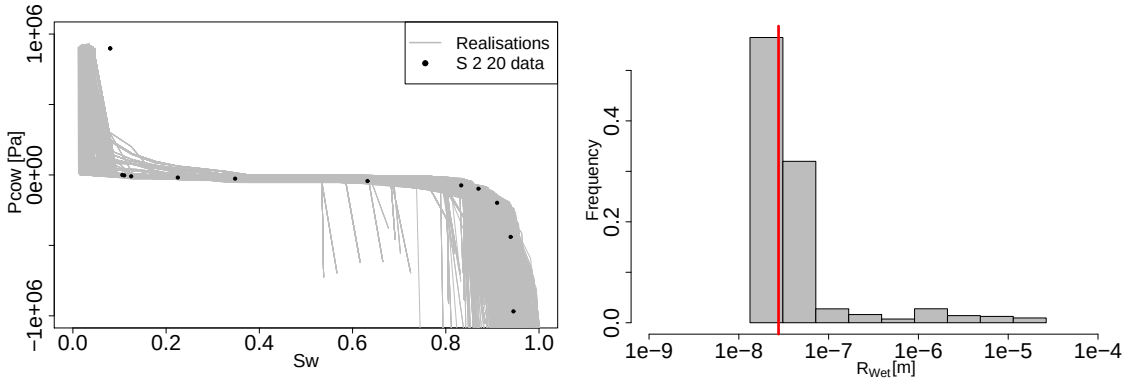

a b

Fig. 7.66 S 2 20 HMC inversion results for imbibition with $\vartheta^{ww}_{ow_{Th}} = 30°$ and $\vartheta^{ow}_{ow_{Th}} = 150°$. (a) Posterior HMC realisations (grey lines). The measurements are shown as solid black circles. (b) Posterior marginal histogram of the radius that separates the two pore populations. Their contact angles were assigned to each population in Eq. (4.43). The red line in (b) indicates the median.

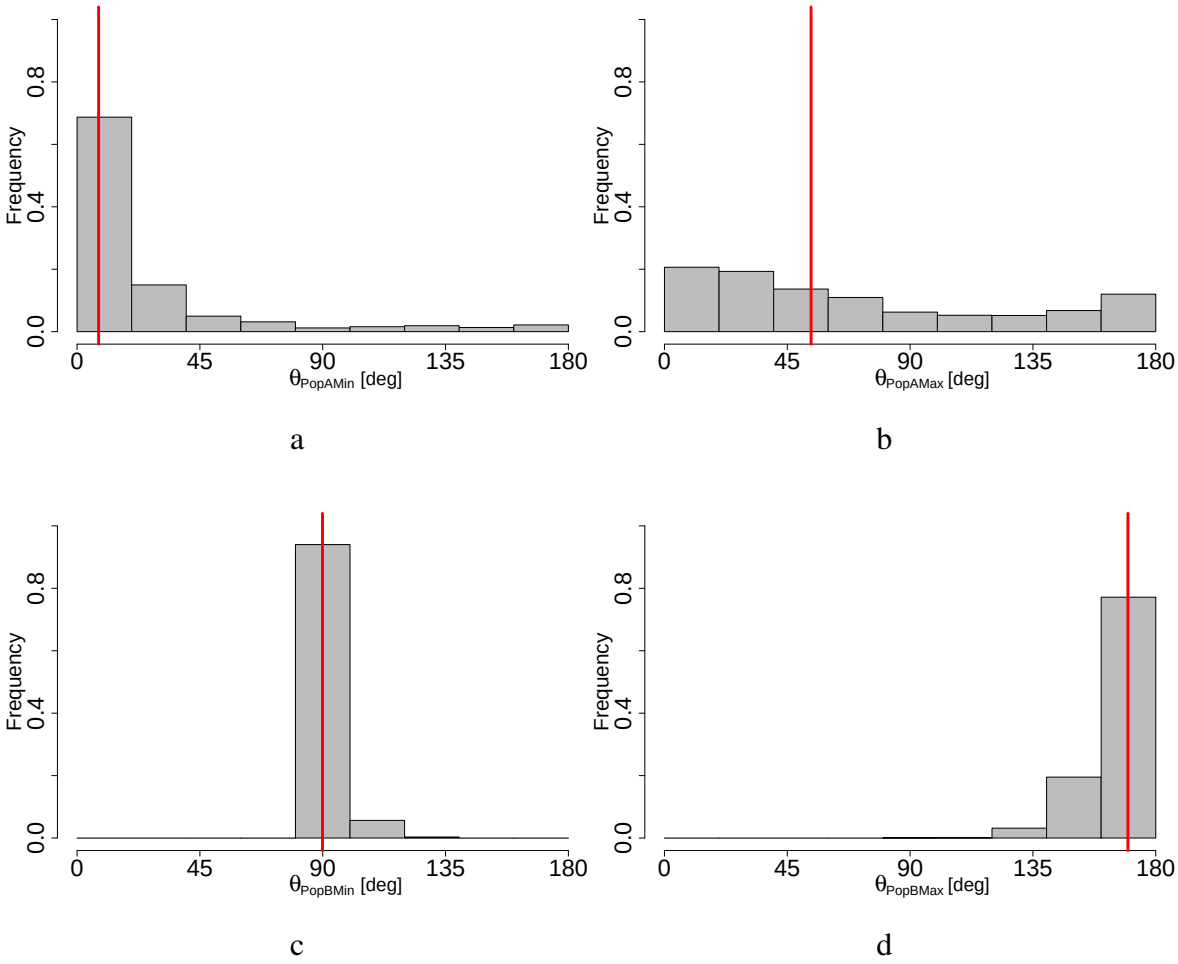

Fig. 7.67 Sample S 2 20 imbibition HMC inversion results for imbibition with $\vartheta_{ow_{Th}}^{ww} = 30°$ and $\vartheta_{ow_{Th}}^{ow} = 150°$. Posterior histograms of the wettability parameters (Eq. (4.43)): (a) lower bound ($\vartheta_{ow_{MIN}}^{A-adv}$) and (b) upper bound ($\vartheta_{ow_{MAX}}^{A-adv}$) for population A, and (c) lower bound ($\vartheta_{ow_{MIN}}^{B-adv}$) and (d) upper bound ($\vartheta_{ow_{MAX}}^{B-adv}$) for population B. The red line in each histogram indicates the median.

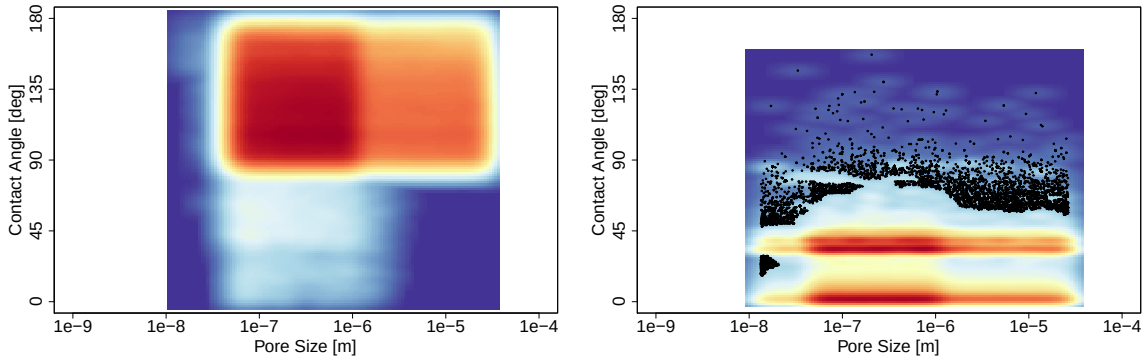

a b

Fig. 7.68 Sample S 2 20 heat maps for $\vartheta^{ww}_{ow_{Th}} = 30°$ and $\vartheta^{ow}_{ow_{Th}} = 150°$. (a) Imbibition and (b) drainage heat maps. These are bivariate density representations of the posterior distribution of contact angles in the pore-size distribution. The red regions represent high density and the blue regions represent zero density. The colour intensities indicate a nonuniform distribution.

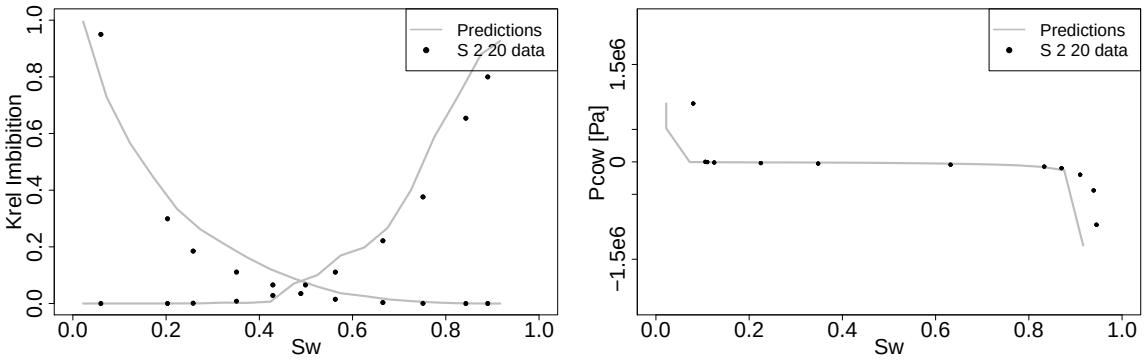

a b

Fig. 7.69 Predicted S 2 20 imbibition relative permeabilities and capillary pressure. (a) Predicted imbibition relative permeabilities using HMC posterior statistics given matching S^{obs}_{or} and $P^{obs}_{c,ow_{MIN}}$ for a network size of $20 \times 20 \times 20$, and (b) imbibition capillary pressure corresponding to the relative permeabilities in (a).

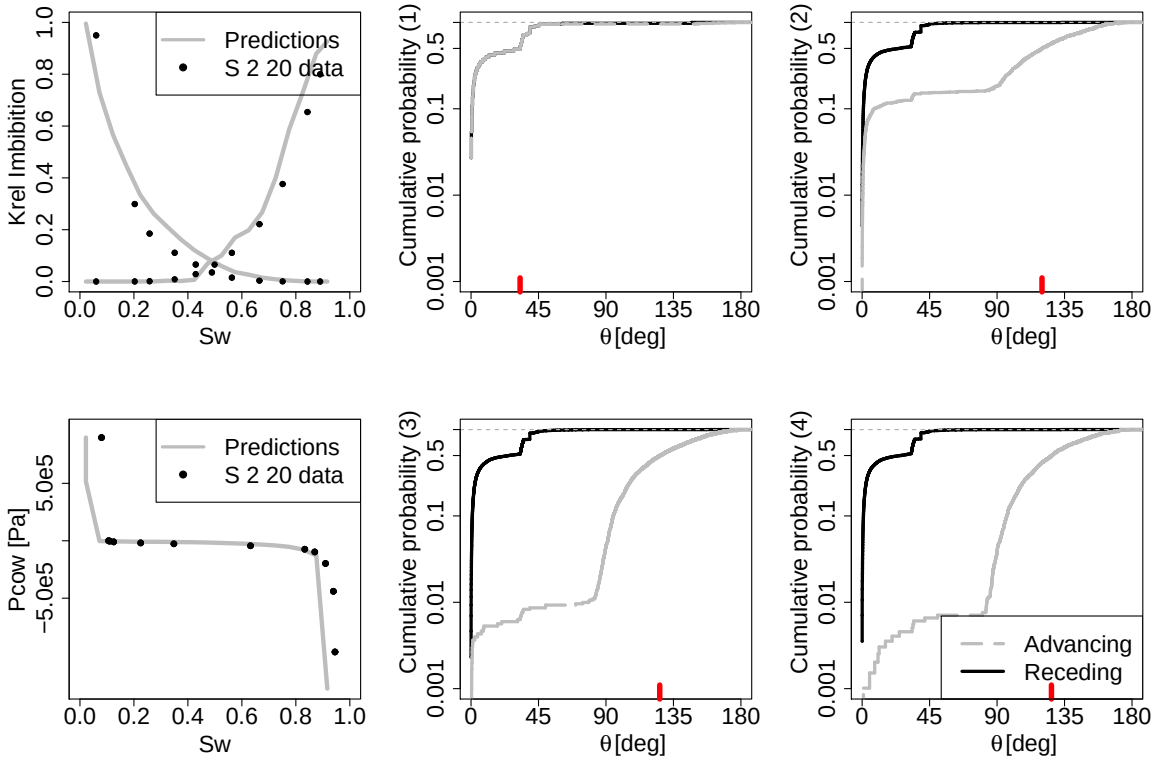

Fig. 7.70 Predicted S 2 20 imbibition relative permeabilities, capillary pressure, and hysteresis for advancing and receding contact angles. Top row, from left to right, predicted imbibition relative permeabilities using HMC posterior statistics given matching S_{or}^{obs} and $P_{c,ow_{MIN}}^{obs}$ for a network size of $20 \times 20 \times 20$, and ECDF of contact angles in pore-size regions (1) and (2). Bottom row, from left to right, predicted imbibition capillary pressure using conditional HMC posterior statistics given matching S_{or}^{obs} and $P_{c,ow_{MIN}}^{obs}$ for a network size of $20 \times 20 \times 20$, and ECDF of contact angles in pore-size regions (3) and (4). The black line is the water-receding contact angle, and the grey dashed line is the water-advancing contact angle after ageing. The red line on the horizontal axes for (1)–(4) show the median values.

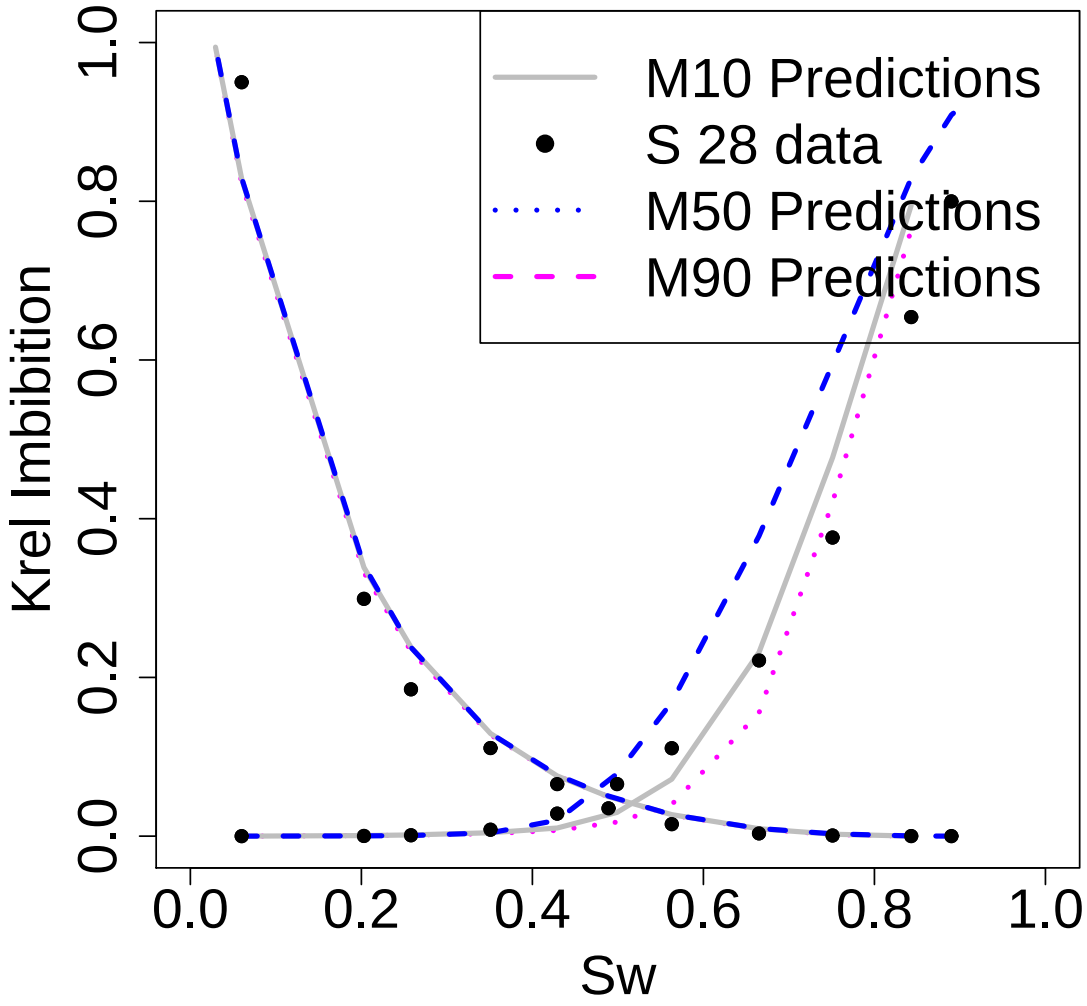

Fig. 7.71 Predicted S 2 20 imbibition relative permeabilities for inputs taken from the P10 (M10), P50(M50) and P90(M90) model parameters.

7.4 Qualitative Comparison of Inversion Wettability Patterns with Scanning Electron Microscope Images

In this section, we attempted to identify patterns in the scanning electron microscope images that can explain the inversion of wettability, described in the light of recent cryogenic high resolution scanning electron microscope images of carbonate wettability [235]. Our observations indicated that the shape of calcite crystals in the microporosity appear to allow for the coexistence of large and small advancing contact angles in small pores. These observations are conjectures, because the scanning electron microscope images shown in Fig. 7.72 are not sufficient to draw strong conclusions.

Figure 7.72 contains very high resolution SEM images of the microporosity of the three rock samples. The microstructure of the calcite has shapes similar to the pattern in Fig. 7.72d4. The calcite crystals intrude on one another so there are no regular shapes as the one shown in Fig. 7.72d1. The intercrystal pore space of the microporosity in contact with the anhedral irregular structure has been associated with large advancing oil/water contact angles [235]. Consistent with Fig. 7.72a2, b2, c2, our inferences using the HMC inversion also show large angles for the advancing oil/water contact angles in the micropores.

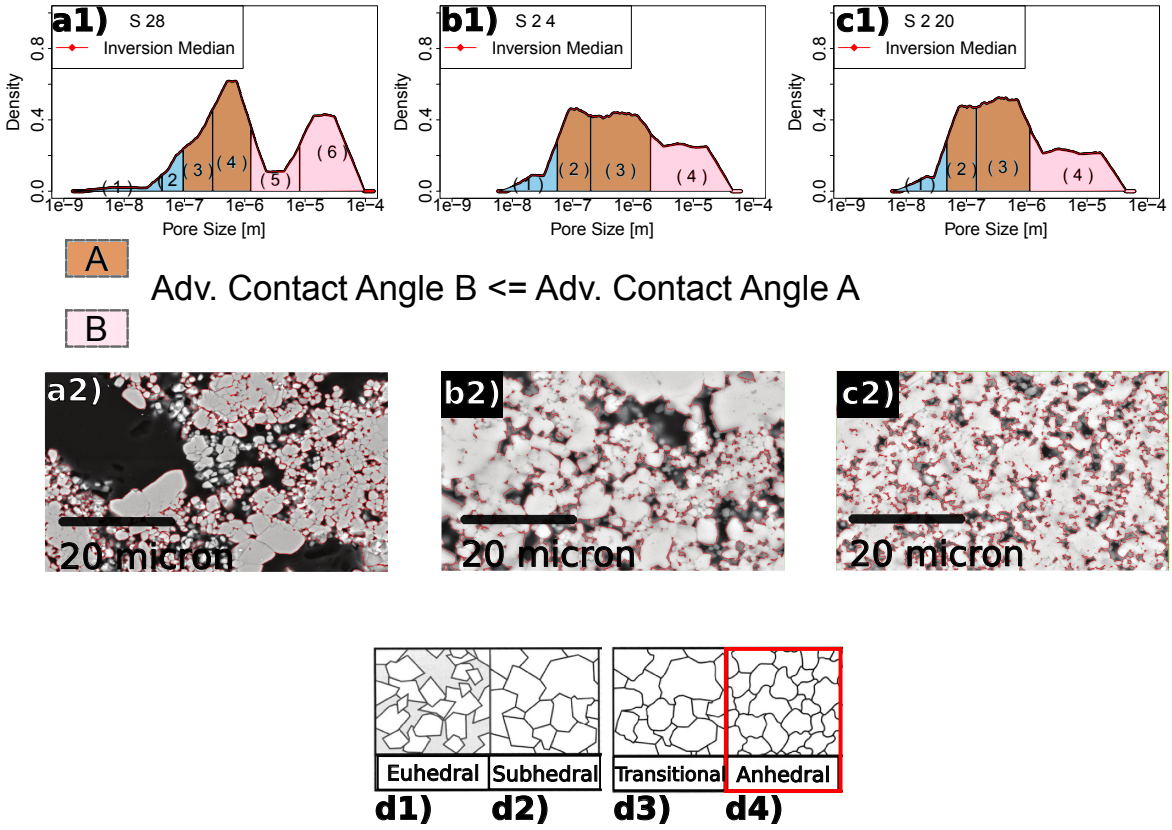

Fig. 7.72 Relationship between microporosity visual structure and wettability. The images show a detailed view of the microporosity in Samples 28, 2 4, and 2 20 shown in Figs. 7.72a2, 7.72b2, and 7.72c2. The structure of the grains suggests anhedral shapes (d4), which appear to be responsible for the large contact angles in the micropores. (a1) Pore-size distribution of RT-I S 28 Section 7.1 [185]. (a2) Microporosity of RT-I S 28 at high resolution in a SEM image. (b1) Pore-size distribution of RT-II S 2 4 Section 7.1 [185]. (b2) Microporosity of RT-II S 2 4 at high resolution in a SEM image. (c1) Pore-size distribution of RT-III S 2 20 Section 7.1 [185]. (c2) Microporosity of of RT-III S 2 20 at high resolution in a SEM image. (d1), (d2), (d3) and (d4) Different possible crystal configurations that form the microporosity; (a2), (b2) and (c2) resemble that of anhedral configuration.

7.5 Discussion

Previous studies have attempted to characterise pore-network model imbibition wettability using Amott/USBM indices or measuring the water-advancing contact angle outside porous media [8, 80, 84, 85, 150]. The common approach to characterise pore-network model imbibition wettability is to tune a fixed-width uniform distribution of water-advancing contact angles to match the imbibition residual oil saturation [8, 29, 33, 113, 256, 258, 320, 367, 396, 399]. Previous studies using lattice pore-network models have used additional data such as relative permeabilities for drainage or resistivity indices to tune the pore-network model parameters [29, 33, 113, 256, 258, 320, 367, 396, 399].

The main problem with using pore-network models is the nonuniqueness of the estimated pore-network model wettability parameters. The distribution of water-receding contact angles and the maximum oil-flooding invasion pressure influence the locations where wettability alteration takes place during ageing. The residual oil saturation depends on the wetting films, which depend on the criteria by which they are assigned based on the pore shape and the contact angles inside the pore. Therefore, uniqueness is not guaranteed (and in fact nonuniqueness is almost always guaranteed).

Recently, research has focused on implementing more complex physics coupled with simplified geometries of pore elements to link wettability with pore shape to define the existence of wetting films. The nonuniqueness of wettability characterisation is more critical when the complexity of the pore-network model increases, because there is complex interplay between different pore-network model parameters. Furthermore, porous media reconstruction methods are not able to capture the full pore-size distribution, and some authors have chosen to ignore microporosity under the assumption that it may not play a large role in the relative permeabilities for water-flooding.

We used the HMC algorithm for inversion of the full set of pore-network model parameters using only capillary pressure to condition the solution based on the misfit function. HMC inversion is a probabilistic approach to deal with the nonuniqueness problem. This method avoids the linearity assumption between the misfit and pore-network model parameters implemented in other studies. The procedure has two parts. The first part involves drainage wettability inversion. The resulting posterior distribution of receding contact angles (drainage heat map) is used to derive p-quantiles for each region in the pore-size distribution. The second part involves drainage wettability inversion starting at the fluid configuration in the network after oil injection under the p-quantile posterior distribution of receding contact angles for each region in the pore-size distribution. This step generates a

second p-quantile posterior distribution of advancing contact angles for each region in the pore-size distribution (imbibition heat map). The calculated heat maps are then used to derive posterior statistics from the posterior models given matching of the observed drainage and imbibition capillary pressure end-point. To predict the relative permeabilities for imbibition, the pore conductance is determined by fitting a BC model to the MICP. The product of the pore-size index from the BC model and the volume exponent is used to define the conductance exponent in the power-law model.

Although our results are more complete in terms of providing a distribution of receding and advancing contact angles to populate the pore-network model and predict relative permeabilities, it is worthwhile to compare our results with those obtained by other methods. Previous work on these carbonate samples has estimated single values for the advancing contact angles based on analytical methods [241]. For RT-I, the single value of the advancing contact angle from the analytical method is consistent with the population median for the larger pores (regions (5) and (6) in the pore-size distribution). In contrast, the analytical method estimated smaller advancing contact angles in mid-sized pores (regions (3) and (4)), while our results showed larger advancing contact angles than the ones in the larger pores (regions (5) and (6)).

RT-II and RT-III have similar structural parameters. However, their respective wettability parameters and relative permeabilities are different. RT-II is oil-wet, while RT-III tends to be weakly oil-wet with a median receding contact angle close to the value estimated by analytical methods. We cannot exclude the possibility that the cleaning problems of RT-II could lead to more oil-wet conditions. However, in the literature, some studies have indicated that cleaning problems before ageing do not change the final wettability alteration. Indeed, cleaning problems could modify the occupancies during drainage, and therefore the location of wettability alteration.

These findings demonstrate that the relative permeabilities for imbibition in carbonates can be predicted using robust stochastic inversion constrained only to capillary pressure data. Our results also confirm that the implementation of progressively more complex pore-scale phenomena demands robust pore-network model parameter estimation methods.

The findings indicate the importance of accounting for the whole pore-size distribution, because mid-sized pores (microporosity) may have higher contact angles than larger pores, which could strongly influence the invasion sequence, and therefore the relative permeabilities. This could indicate that for deriving the wettability from the capillary pressure and predicting relative permeabilities, it is more important to match the maximum oil- and water-flooding pressures than to force the wettability to match the residuals (connate water

and residual oil saturations).

Our estimates of the water relative permeability are more accurate than those in [8]. Our results provide evidence of the importance of accounting for the whole pore-size distribution in carbonates because mid-sized pores play an important role in the connectivity.

It is customary to assume that carbonates follow a mixed-wet large model of wettability. As shown in the imbibition heat maps, the overall behaviour is that of a mixed-wet large (considering the whole range in the pore-size distribution) model. However, there is high degree of variability and mid-sized (micropores invaded by oil) pores seem to show higher contact angles than the larger pores. This local mixed-wet small behaviour provides additional shielding of the larger pores. We suggest that previous approaches underestimated the water relative permeability for water-flooding because the pore-network model wettability was derived by matching the residual oil saturation and that might have led to larger advancing contact angles and less variability.

To the best of our knowledge, this is the first study to estimate relative permeabilities for imbibition in carbonates based on stochastic inversion of the complete set of lattice pore network parameters constrained only to the capillary pressure.

In addition, HMC could be applied to pore-network models that capture more of the physics of pore-scale displacement mechanisms to obtain more robust estimates of the link between the residual oil saturation and contact angles.

These results may indicate that measurements outside porous media, such as the average apparent contact angle and analytical models of contact angle hysteresis, are very limited in their ability to characterise the variability in wettability at the pore scale to supply distributions to pore-network models. Note that explicit treatment of wetting films conductance may improve the relative permeability predictions.

Chapter 8

Conclusions

This chapter summarizes the findings of the thesis. In this thesis, we have explored the prediction of imbibition relative permeabilities for carbonates using stochastic inversion of lattice pore-network model parameters using Hamiltonian dynamics.

The thesis involved three subjects: (a) Hamiltonian inversion of pore-network model structure parameters, (b) Hamiltonian inversion of pore-network model wettability parameters, and (c) comparison of relative permeabilities predictions using the full set of inverted pore-network model parameters with steady-state experimental imbibition relative permeabilities data for carbonates.

8.1 Summary

This thesis took a top-down approach to characterise lattice pore-network model parameters using routinely acquired capillary pressure data. This was accomplished using Hamiltonian Monte Carlo stochastic inversion, which can give valuable insight into pore-network model parameters and may be a useful approach for future modelling. This will also improve our ability to analyse and interpret experimental data.

Pore-network models cover a wide range of pore structures and physical phenomena. This study focussed on lattice pore-network models under capillary-dominated flow. Pore-network models easily match the data and multiple solutions are found. The data used to characterise pore-network model parameters is often static while the data to be predicted is dynamic. This type of problem is difficult to solve.

Various methods for probing porous media directly generate unstructured pore-network models, which facilitate the process only for narrow pore-size distributions. Moreover, the various methods for producing unstructured pore-network models, such as microcomputed

tomography and different algorithms, find it difficult to generate pore-size distributions containing all length scales. This means that it is difficult to generate amenable pore-network models with all length scales (representative elementary volumes) for carbonate reservoirs.

Lattice pore-network models were chosen because they allow the flexibility to integrate the multiple length scales that occur in carbonate rocks. The inverse problem of pore-network model parameter characterisation was solved using a stochastic inversion strategy, which tackled the systematic problem of multiple minima when characterising the pore-network model parameters. The stochastic inversion used routinely acquired laboratory data.

- The main finding of this thesis is that stochastic inversion of lattice pore-network model parameters combined with Hamiltonian dynamics is capable of predicting imbibition relative permeabilities with good accuracy using only routinely obtained data, such as mercury intrusion capillary pressure and oil/water capillary pressure.
- Micropores play an important role in wettability because they are more or equally as oil-wetting as large pores, leading to a gentle water relative permeability curvature.
- The method proposed in this thesis is important because a large percentage of the porosity in carbonates is microporosity.

8.2 Conclusions

1. Pore-size distribution parameterisation
    - We have proposed an estimator for the pore-size distribution using mercury intrusion capillary pressure data that is independent of the range of pore sizes. A wide range of pore sizes introduces scale dependency in the usual Ritter and Drake pore-size distribution estimator, because small pores produce a strongly right-skewed distribution. Carbonate rocks often show three to five orders of magnitude variation in pore sizes. Thus, when the Ritter and Drake method is applied to mercury intrusion capillary pressure data, the pore-size distribution is dominated by small pores.
    - Our intention was to develop an estimator that overcomes the usual problem of right-skewed pore-size distributions while being weakly constrained. In this study, we used information entropy concepts to parameterise the pore-size distribution. The method is based on partitioning the pore sizes into bins of equal

information content. This partitioning increases the entropy with respect to the initial pore-size distribution estimator derived from mercury intrusion capillary pressure data. However, we do not suggest that the underlying true pore-size distribution in the porous media has this form. The parameterisation only makes weak assumptions of the functional form of the pore-size distribution from the prior information at hand, unlike other approaches.

- The proposed parameterisation was compared with a natural choice of a non-parametric parameterisation for this problem using logarithm uniform bin widths for a synthetic case. Bias was observed in the posterior distribution of the volume exponent and the pore-size distribution, whereas our proposed parameterisation is unbiased. This is important because we found that there is a strong correlation between the pore size in the range of microporosity and the volume exponent. This correlation shifts the posterior distribution towards low values of the volume exponent and there is a smaller contribution from microporosity.

2. Hamiltonian stochastic inversion: Synthetic case

    - We used a synthetic case to test the method on a system with multiple minima. Despite the difficulty of the problem, the Hamiltonian Monte Carlo posterior statistics agreed well with the true parameters. Analysing the multivariate relationships of the parameters in the synthetic case, we found that low values of the volume exponent (close to zero) decreased the fraction of small pores. This sheds light on why low volume exponents were used in previous lattice-type pore-network models applied to carbonates, which may lead to erroneous pore-size distributions. Our findings suggest that the volume exponent parameter is correlated with the amount of small pore sizes. This is important because other studies of carbonate rocks have assumed that the volume exponent is zero or close to zero, which produces a very good match with the mercury intrusion capillary pressure but may not correctly predict flow properties. Unlike other pore-network model parameter estimation approaches, we successfully applied the Hamiltonian Monte Carlo algorithm to a difficult synthetic case with pore sizes that varied by up to five orders of magnitude.

3. Hamiltonian stochastic inversion: Carbonate samples

    - We implemented a stochastic inversion algorithm that uses deterministic molecular dynamics combined with stochastic steps by Hamiltonian dynamics to esti-

mate pore-network model parameters. The Hamiltonian Monte Carlo algorithm allows large moves in the phase space, making use of the periodicity caused by the Hamiltonian formulation. Thus, large changes in the model parameters are possible. This improves the effectiveness in capturing the variability in the posterior distribution of pore-network model parameters compared with classical Metropolis algorithms.

- The method was applied to three carbonate samples of different complexity. In the case of pore-network model structure Hamiltonian Monte Carlo inversion, the volume exponent estimates were greater than zero. This has important implications in the prediction of relative permeabilities.
- The results for the three carbonate samples suggest that as the rock quality decreases from rock type I to rock type III, the coordination number skews to the right. The more right-skewed the pore-size distribution of the porous media, the greater the difference between the pore-size distribution of the porous media and the estimator calculated from mercury intrusion capillary pressure data.
- More than 50 % of the pore-size distribution from the pore-network model parameter inversion is in the microporous range. This indicates that it is important to account for the complete range of pore sizes in the parameterisation. The strong correlation between the amount of microporosity and volume exponent suggests that when microporosity is ignored the volume exponent will systematically tend to be strongly underestimated (values close to zero). This may produce a very poor prediction of the relative permeabilities.
- The output of the Hamiltonian Monte Carlo parameter estimation is the structure of the pore-network model. Using this pore-network model structure, the second step involved estimating the posterior distribution of receding and advancing contact angles subject to oil/water capillary pressure.

4. Hamiltonian stochastic inversion: pore-network model wettability

    - We found that intermediate wettability causes mid-sized pores (microporosity) range to be invaded at the same level of pressure as larger pores. The coexistence of these events reduces the tendency for preferential flow through large pores, resulting in more uniform flow at the pore scale compared with the case in which flow is restricted to only large pores. This could explain the more concave curvature of the imbibition water relative permeability compared with the

generally assumed mixed-wet large wettability model, in which mid-sized pores are weakly oil-wet and large pores are more oil-wet.

- Microporosity (mid-sized pores) has an important effect on the connectivity because they could have higher contact angles than larger pores. Therefore, they do not spontaneously imbibe and shield larger pores, improving water-flooding displacement.
- The importance of the maximum and minimum observed capillary pressure is directly connected to accounting for the full pore-size distribution. The common assumption that microporosity can be ignored is unsatisfactory. The existence of wetting films depends on the maximum capillary pressure during drainage, and thus affects wettability alteration during ageing.
- Our results suggest that matching both connate water at the maximum drainage capillary pressure before ageing and residual oil at the minimum imbibition capillary pressure leads to better estimation of the advancing and receding contact angles and more reliable predictions of the relative permeabilities. In contrast, the imbibition water relative permeability was not well-predicted using posterior distributions of contact angles based on models not matching the capillary pressure end-points.
- The distribution of advancing contact angles for the three samples are associated with a high degree of variability in wettability, as shown by the heat maps. The existing methodology in pore-network model tunes the wettability to match the observed residual oil saturation. However, wetting films are linked to the capillary pressure and ignoring the maximum drainage capillary pressure before ageing and the minimum imbibition capillary pressure could cause the advancing contact angles to be overestimated.
- Heat maps for rock type I and rock type III suggested a weakly-oil wettability. This is in agreement with observation in which the low values of connate water and residual oil saturations are associated to weakly-oil conditions [203]. In the case of rock type II, the lower imbibition capillary pressure end-point is related to a slightly more oil-wetness and residual oil saturation. These trends has been seen in more complex pore-network models [336].
- The ranges of advancing and receding contact angles obtained from the inversion were wider than the ranges of apparent advancing contact angles obtained with analytical determinations in previous studies of these samples in the literature,

and in one case our results were contradictory to the analytical determination. It follows that the variability in the advancing and receding contact angles is not reflected in the apparent contact angle data outside porous media. Apparent contact angle data outside porous media cannot completely characterise the wettability in pore-network models because the data do not capture the contact angle variability in porous media.

- Core cleaning problems may result in stronger oil-wetting conditions after ageing. Hamiltonian Monte Carlo wettability inversion for rock type II showed larger advancing contact angles and less variability in the heat maps than the other two samples. This was in agreement with the relative permeabilities intersection point being at lower water saturation.

5. Prediction of imbibition relative permeability

   - Hamiltonian Monte Carlo stochastic inversion provided reliable estimates of the lattice pore-network model parameters. This was demonstrated by applying the method to three carbonate samples from the Middle East. Lattice pore-network models supplied with Hamiltonian Monte Carlo estimates for the pore-network model parameters predicted the experimental steady-state imbibition relative permeabilities for the three carbonate samples with good agreement.
   - The relative permeability data in the literature from pore-network models for weakly wetting conditions are for pore sizes assigned to microporosity that are much larger than the pore sizes identified from mercury intrusion capillary pressure, while the relative permeabilities generated here cover the full range from mercury intrusion capillary pressure. Furthermore, the microporosity range of pore sizes is often assumed not to contribute to flow. The water invasion of mid-sized pores could explain the more concave curvature of the water relative permeability. This result suggests that, water-flooding displacement could be better than the usual assumption that the flow only takes place along the interconnected large pores present in carbonates.

8.3 Future Work

- One of our short-term research goals is to investigate whether the wettability may change once oil layers and wetting films are assigned to each pore based not only on the contact angle, but also on the pore shape.

- The wettability at the minimum residual oil saturation and how it relates to the pore sizes are not fully understood. It would be interesting to determine the combined effect of oil layers and pores sizes on the wettability of carbonate rocks and how they affect the relative permeabilities.

- Using volume-controlled mercury intrusion data as an observable for pore-network model structure characterisation might also lead to a deep understanding of the connectivity in tight rocks, such as the rocks in unconventional reservoirs. In these types of rocks, it is not only challenging to characterise the network structure, but also the dominant physics are also not clear.

- The phase space is characterised by flow maps. It may be possible to transform each parameter depending on its position in the phase space and anticipate the flow to provide an adaptive scheme that is consistent with the detailed balance.

Appendix A

Chapter 6: Posterior Density Functions

A.1 Synthetic Case

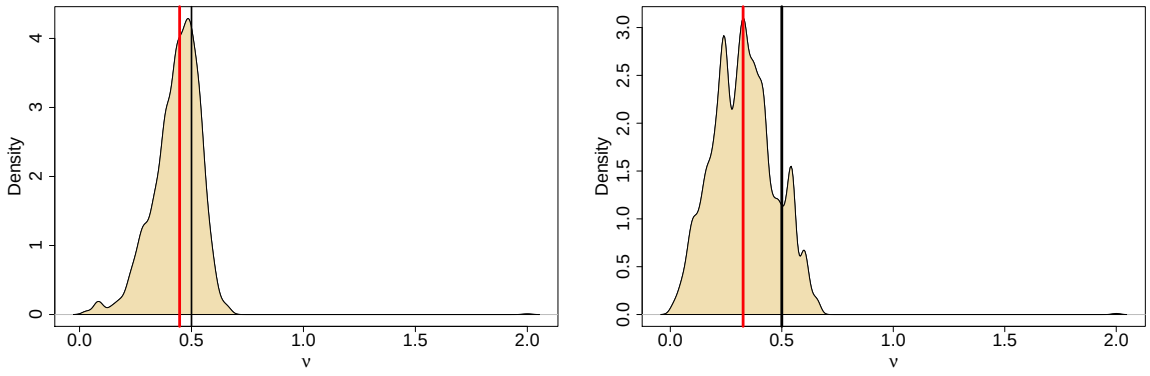

a b

Fig. A.1 (a) Marginal posterior PDF of the volume exponent for the proposed parameterisation. (b) Marginal posterior PDF of the volume exponent for the logarithmically equidistant bin parameterisation.

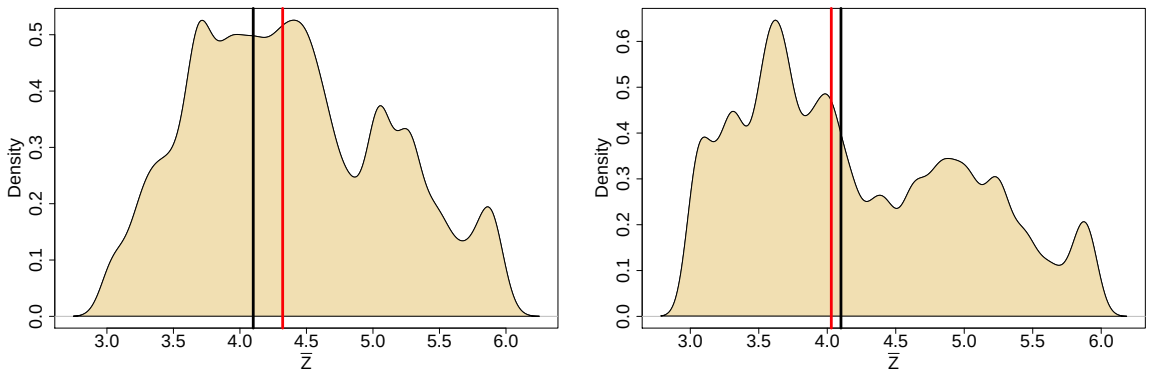

a b

Fig. A.2 (a) Marginal posterior PDF of the average coordination number for the proposed parameterisation. (b) Marginal posterior PDF of the average coordination number for the logarithmically equidistant bin parameterisation.

A.2 Carbonate Rock Samples: Pore-Network Model Structure

A.2.1 RT-I S 28

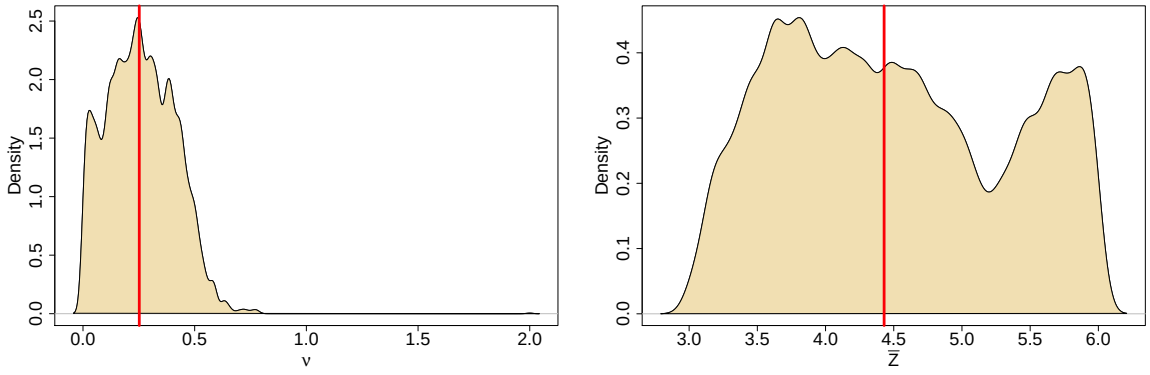

a b

Fig. A.3 Sample S 28: (a) Marginal posterior PDF of the volume exponent (ν), (b) Marginal posterior PDF of the average coordination number ($\bar{Z}$) (red lines indicate the median values).

A.2.2 RT-II S 2 4

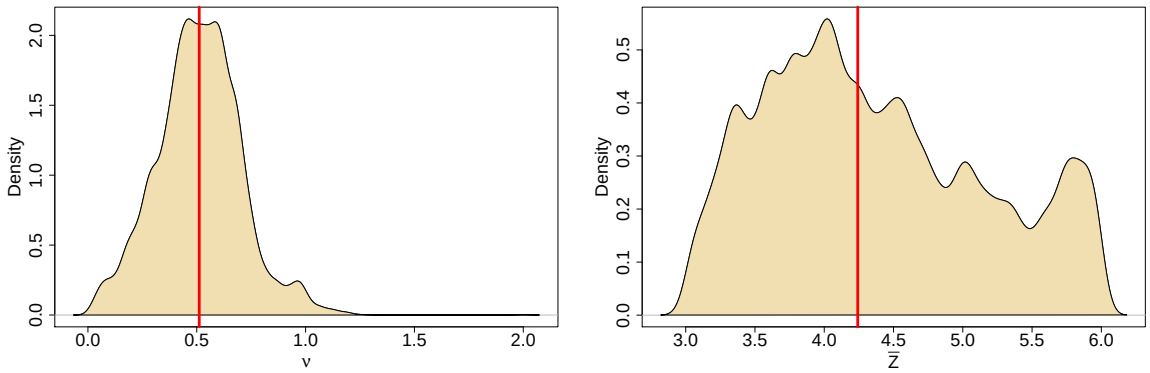

a b

Fig. A.4 Sample S 2 4: (a) Marginal posterior PDF of the volume exponent (ν), (b) Marginal posterior PDF of the average coordination number ($\bar{Z}$) (red lines indicate the median values).

A.2.3 RT-III S 2 20

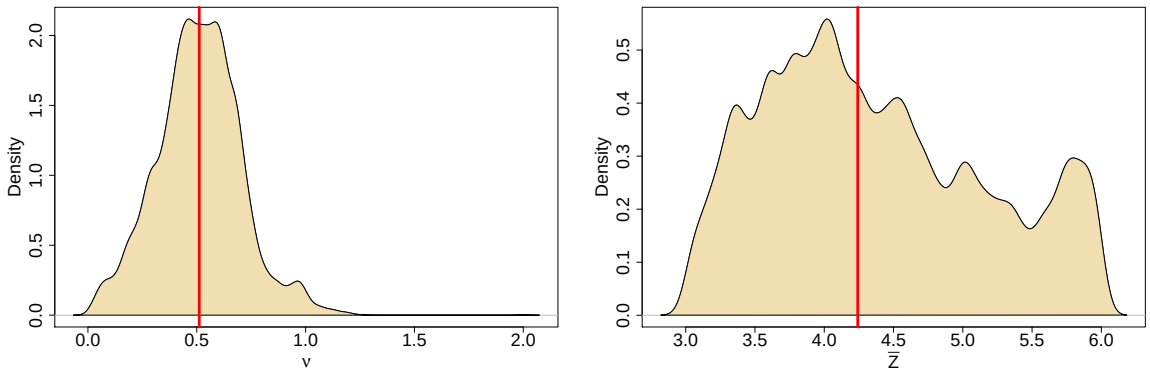

a b

Fig. A.5 Sample S 2 20: (a) Marginal posterior PDF of the volume exponent (ν), (b) Marginal posterior PDF of the average coordination number ($\bar{Z}$) (red lines indicate the median values).

A.3 Carbonate Rock Samples: Pore-Network model Wettability

A.3.1 RT-I S 28

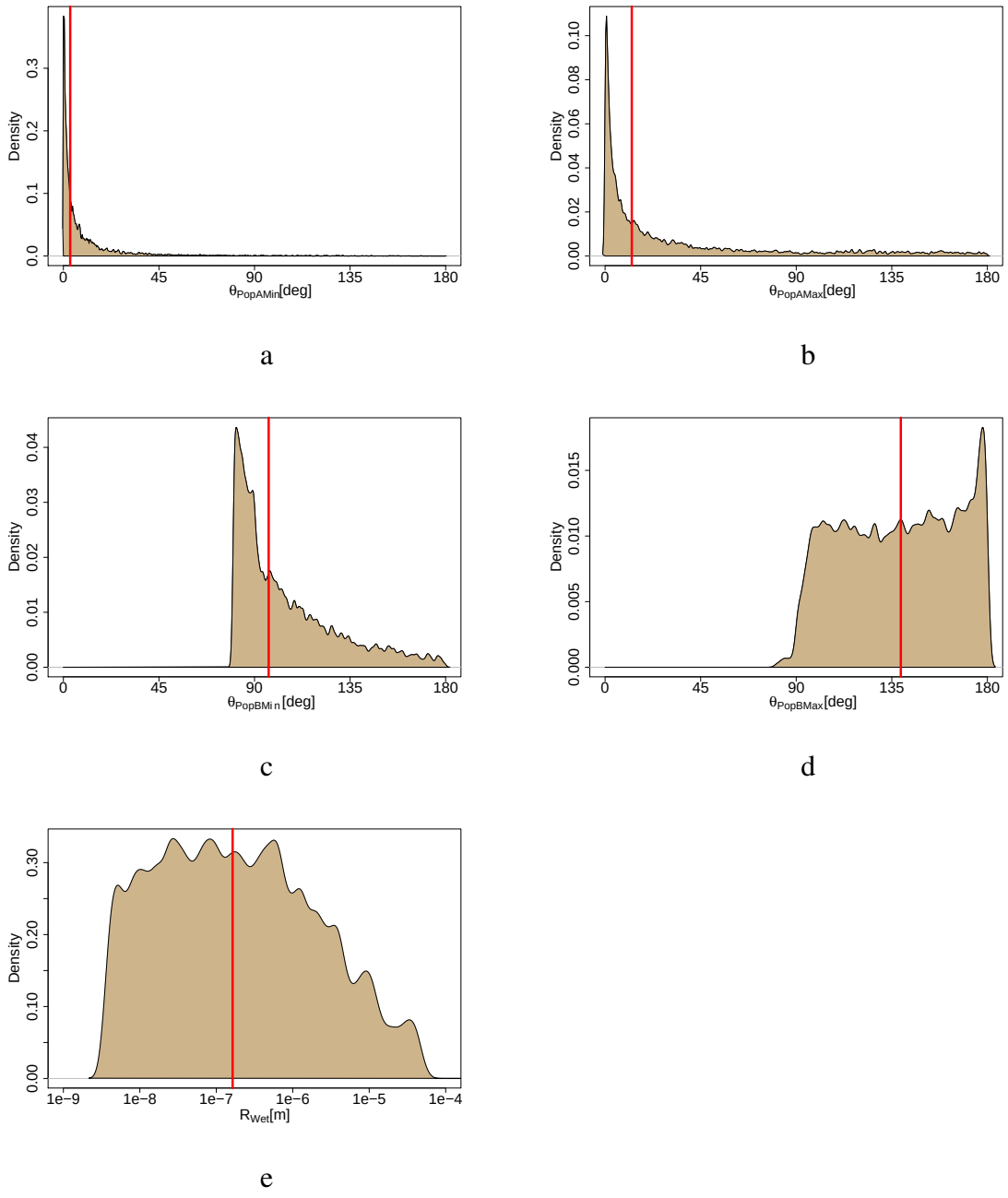

Fig. A.6 S 28 imbibition HMC inversion results for imbibition with $\vartheta^{ww}_{ow_{Th}} = 30°$ and $\vartheta^{ow}_{ow_{Th}} = 150°$. PDF of the wettability parameters (Eq. (4.43)): (a) lower bound ($\vartheta^{A-adv}_{ow_{MIN}}$) and (b) upper bound ($\vartheta^{A-adv}_{ow_{MAX}}$) for population A, and (c) lower bound ($\vartheta^{B-adv}_{ow_{MIN}}$) and (d) upper bound ($\vartheta^{B-adv}_{ow_{MAX}}$) for population B and (e) Posterior density function of the radius that separates the two pore populations. Their contact angles were assigned to each population in Eq. (4.43). The red line indicates the median.

A.3.2 RT-II S 2 4

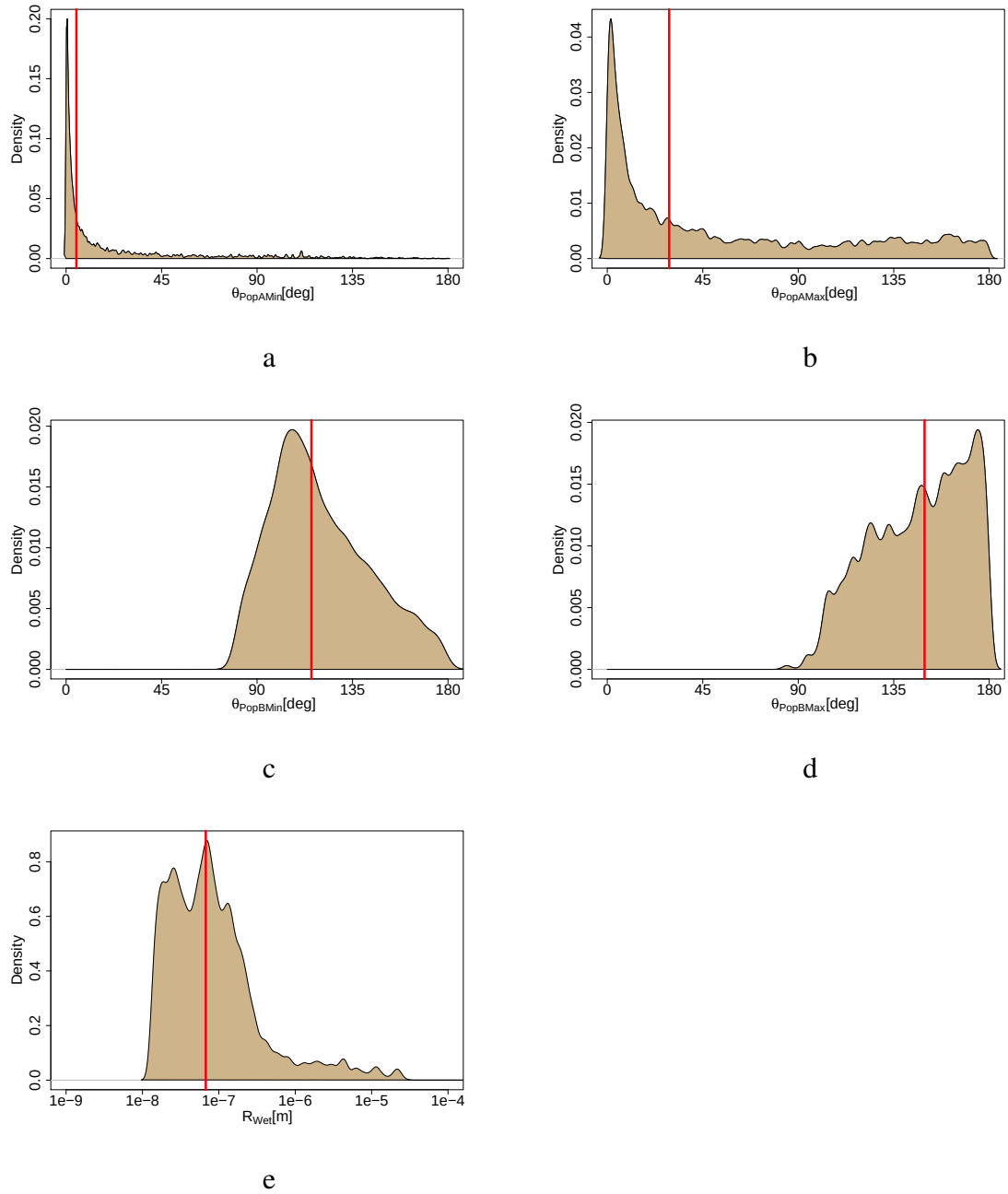

Fig. A.7 S 2 4 imbibition HMC inversion results for imbibition with $\vartheta^{ww}_{ow_{Th}} = 30°$ and $\vartheta^{ow}_{ow_{Th}} = 150°$. PDF of the wettability parameters (Eq. (4.43)): (a) lower bound ($\vartheta^{A-adv}_{ow_{MIN}}$) and (b) upper bound ($\vartheta^{A-adv}_{ow_{MAX}}$) for population A, and (c) lower bound ($\vartheta^{B-adv}_{ow_{MIN}}$) and (d) upper bound ($\vartheta^{B-adv}_{ow_{MAX}}$) for population B and (e) Posterior density function of the radius that separates the two pore populations. Their contact angles were assigned to each population in Eq. (4.43). The red line indicates the median.

A.3.3 RT-III S 2 20

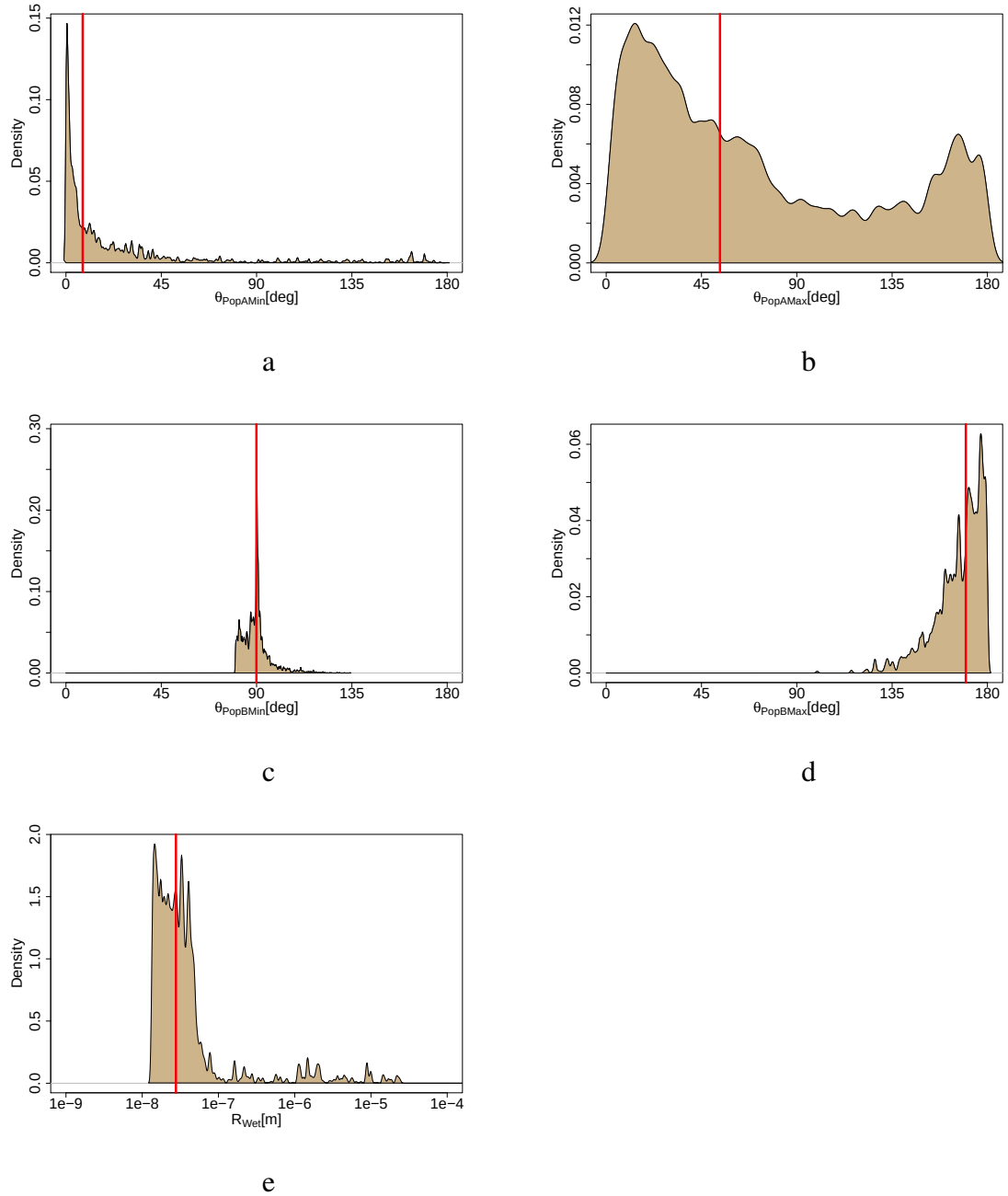

Fig. A.8 S 2 20 imbibition HMC inversion results for imbibition with $\vartheta^{ww}_{ow_{Th}} = 30°$ and $\vartheta^{ow}_{ow_{Th}} = 150°$. PDF of the wettability parameters (Eq. (4.43)): (a) lower bound ($\vartheta^{A-adv}_{ow_{MIN}}$) and (b) upper bound ($\vartheta^{A-adv}_{ow_{MAX}}$) for population A, and (c) lower bound ($\vartheta^{B-adv}_{ow_{MIN}}$) and (d) upper bound ($\vartheta^{B-adv}_{ow_{MAX}}$) for population B and (e) Posterior density function of the radius that separates the two pore populations. Their contact angles were assigned to each population in Eq. (4.43). The red line indicates the median.

Appendix B

RT-I S 28: Prediction of Relative Permeability considering volume exponent equal to zero

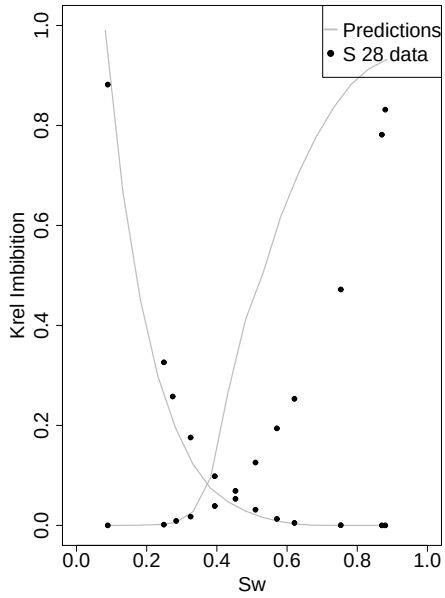

Fig. B.1 Predicted imbibition relative permeabilities using HMC posterior statistics given matching S_{or}^{obs} and $P_{c,ow_{MIN}}^{obs}$ for a network size of $20 \times 20 \times 20$ using volume exponent $\nu = 0$

Appendix C

MCMC versus HMC: RT-I

RT–I S 28: Determination of Imbibition Wettability Parameters for Wetting Films with $\vartheta^{ww}_{ow_{Th}} = 30°$ and $\vartheta^{ow}_{ow_{Th}} = 150°$

Figure C.1 shows the conditional imbibition heat maps given those realisations matching the imbibition capillary pressure end-point (S^{obs}_{or} and $P^{obs}_{c,ow_{MIN}}$) for MCMC and HMC methods. MCMC method while showing similar features to HMC, the variability in the advancing contact angle heat map (Fig. C.1a) is less captured than with HMC (Fig. C.1b) .

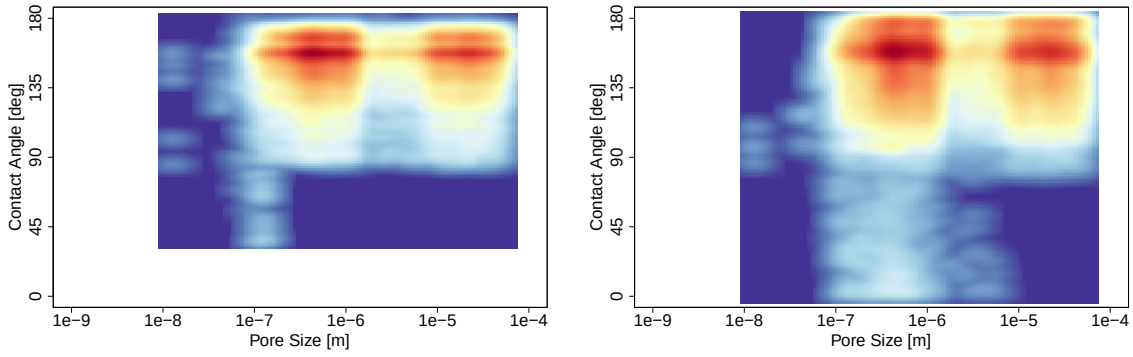

a b

Fig. C.1 These heat maps convey the idea of the variability in the solution to the inverse problem. Conditional imbibition posterior heat maps given matching the imbibition end-point S^{obs}_{or} and $P^{obs}_{c,ow_{MIN}}$. (a) MCMC $\vartheta^{ww}_{ow_{Th}} = 30°$ and $\vartheta^{ow}_{ow_{Th}} = 150°$, and (b) HMC $\vartheta^{ww}_{ow_{Th}} = 30°$ and $\vartheta^{ow}_{ow_{Th}} = 150°$.

References

[1] Adibhatla, B., Mohanty, K., Berger, P., and Lee, C. (2006). Effect of surfactants on wettability of near-wellbore regions of gas reservoirs. *Journal of Petroleum Science and Engineering*, 52(1):227–236.

[2] Adler, P., Jacquin, C., and Quiblier, J. (1990). Flow in simulated porous media. *International Journal of Multiphase Flow*, 16(4):691–712.

[3] Adler, P. M. and Thovert, J.-F. (1999). *Fractures and fracture networks*, volume 15. Springer Science & Business Media.

[4] Agbalaka, C. and Oliver, D. (2008). Application of the EnKF and localization to automatic history matching of facies distribution and production data. *Mathematical Geosciences*, 40(4):353–374.

[5] Akhmatskaya, E., Bou-Rabee, N., and Reich, S. (2009). A comparison of generalized hybrid Monte Carlo methods with and without momentum flip. *Journal of Computational Physics*, 228(6):2256–2265.

[6] Al-Futaisi, A. and Patzek, T. (2003). Impact of wettability alteration on two-phase flow characteristics of sandstones: A quasi-static description. *Water Resour. Res*, 39(2):1042.

[7] Al-Kharusi, A. and Blunt, M. (2007). Network extraction from sandstone and carbonate pore space images. *Journal of Petroleum Science and Engineering*, 56(4):219–231.

[8] Al-Kharusi, A. S. and Blunt, M. J. (2008). Multiphase flow predictions from carbonate pore space images using extracted network models. *Water resources research*, 44(6).

[9] Altmann, Y., Dobigeon, N., and Tourneret, J. Y. (2014). Unsupervised post-nonlinear unmixing of hyperspectral images using a hamiltonian Monte Carlo algorithm. *IEEE Transactions on Image Processing*, 23(6):2663–2675.

[10] Amott, E. (1959). Observations relating to the wettability of porous rock. *Trans*, pages 156–162.

[11] Anderson, W. (1986). Wettability literature survey-part 2: Wettability measurement. *Journal of Petroleum Technology*, 38(11):1246–1262.

[12] Anderson, W. (1987a). Wettability literature survey-part 4: Effects of wettability on capillary pressure. *Journal of Petroleum Technology*, 39(10):1283–1300.

[13] Anderson, W. (1987b). Wettability literature survey-part 6: The effects of wettability on waterflooding. *Journal of petroleum technology*, 39(12):1605–1622.

[14] Andrew, M., Bijeljic, B., and Blunt, M. J. (2014). Pore-scale imaging of trapped supercritical carbon dioxide in sandstones and carbonates. *International Journal of Greenhouse Gas Control*, 22:1–14.

[15] Androutsopoulos, G. and Mann, R. (1979). Evaluation of mercury porosimeter experiments using a network pore structure model. *Chemical Engineering Science*, 34(10):1203–1212.

[16] Ankerst, D. P. (2005). Kendall's advanced theory of statistics, vol. 2b: Bayesian inference. *Journal of the American Statistical Association*, 100(472):1465–1466.

[17] Arnold, D., Demyanov, V., Tatum, D., Christie, M., Rojas, T., Geiger, S., and Corbett, P. (2013). Computers & Geosciences Hierarchical benchmark case study for history matching , uncertainty quantification and reservoir characterisation. *Computers and Geosciences*, 50:4–15.

[18] Badii, R. and Politi, A. (1999). *Complexity: Hierarchical structures and scaling in physics*, volume 6. Cambridge University Press.

[19] Bakke, S. and Øren, P. (1997). 3-D pore-scale modelling of sandstones and flow simulations in the pore networks. *SPE Journal*, 2(2):136–149.

[20] Baldwin, C., Sederman, A., Mantle, M., Alexander, P., and Gladden, L. (1996). Determination and characterization of the structure of a pore space from 3D volume images. *Journal of colloid and interface science*, 181(1):79–92.

[21] Bard, Y. (1974). *Nonlinear parameter estimation*. Academic Press New York.

[22] Barrera, A. (2007). *History matching by simultaneous calibration of flow functions*. PhD thesis, The University of Texas at Austin.

[23] Basan, P., Lowden, B., Whattler, P., and Attard, J. (1997). Pore-size data in petrophysics: a perspective on the measurement of pore geometry. *Geological Society, London, Special Publications*, 122(1):47–67.

[24] Basu, S., Sharma, M. M., et al. (1996). Defining the wettability state of mixed wet reservoirs: Measurement of critical capillary pressure for crude oils. In *SPE Annual Technical Conference and Exhibition*. Society of Petroleum Engineers.

[25] Bauer, D., Youssef, S., Han, M., Bekri, S., Rosenberg, E., Fleury, M., and Vizika, O. (2011). From computed microtomography images to resistivity index calculations of heterogeneous carbonates using a dual-porosity pore-network approach: Influence of percolation on the electrical transport properties. *Physical Review E*, 84(1):011133.

[26] Bazargan, H. (2014). An efficient polynomial chaos-based proxy model for history matching and uncertainty quantification of complex geological structures. pages 1–185.

[27] Bazargan, H., Christie, M., Elsheikh, A. H., and Ahmadi, M. (2015). Surrogate accelerated sampling of reservoir models with complex structures using sparse polynomial chaos expansion. *Advances in Water Resources*.

[28] Behbahani, H. and Blunt, M. (2005). Analysis of Imbibition in Mixed-Wet Rocks Using Pore-Scale Modeling. volume 10, pages 466–474. Society of Petroleum Engineers.

[29] Bekri, S., Howard, J., Muller, J., and Adler, P. (2003). Electrical resistivity index in multiphase flow through porous media. *Transport in Porous Media*, 51(1):41–65.

[30] Bekri, S., Laroche, C., and Vizika, O. (2005). Pore network models to calculate transport and electrical properties of single or dual-porosity rocks. In *SCA*, volume 35, pages 21–25.

[31] Békri, S., Nardi, C., and Vizika, O. (2004a). Effect of Wettability on the Petrophysical Parameters of Vuggy Carbonates: Network Modeling Investigation. In *SCA2004-25, International Symposium of the Society of Core Analysts, Abu Dhabi, UAE.*

[32] Békri, S., Nardi, C., and Vizika, O. (2004b). Effect of Wettability on the Petrophysical Parameters of Vuggy Carbonates: Network Modeling Investigation. In *SCA2004-25, International Symposium of the Society of Core Analysts, Abu Dhabi, UAE.*

[33] Bekri, S. and Vizika, O. (2006). Pore network modeling of rock transport properties: application to a carbonate. In *SCA*, number 2006, pages 12–16.

[34] Bengtsson, T., Bickel, P., and Li, B. (2008). Curse-of-dimensionality revisited: Collapse of the particle filter in very large scale systems. *Probability and Statistics: Essays in Honor of David A. Freedman*, 2:316–334.

[35] Bengtsson, T., Snyder, C., and Nychka, D. (2003). Toward a nonlinear ensemble filter for high-dimensional systems. *J. Geophys. Res*, 108(D24):8775.

[36] Bentz, D. and Martys, N. (1994). Hydraulic radius and transport in reconstructed model three-dimensional porous media. *Transport in porous media*, 17(3):221–238.

[37] Bergeron, V., Hanssen, J. E., and Shoghl, F. (1997). Thin-film forces in hydrocarbon foam films and their application to gas-blocking foams in enhanced oil recovery. *Colloids and Surfaces A: Physicochemical and Engineering Aspects*, 123:609–622.

[38] Bhark, E. W., Jafarpour, B., and Datta-Gupta, A. (2011). A generalized grid connectivity-based parameterization for subsurface flow model calibration. *Water Resources Research*, 47(6):W06517.

[39] Biegler, L., Biros, G., Ghattas, O., Heinkenschloss, M., Keyes, D., Mallick, B., Tenorio, L., van Bloemen Waanders, B., Willcox, K., and Marzouk, Y. (2011). *Large-scale inverse problems and quantification of uncertainty*, volume 712. John Wiley & Sons.

[40] Bijeljic, B., Raeini, A., Mostaghimi, P., and Blunt, M. J. (2013). Predictions of non-fickian solute transport in different classes of porous media using direct simulation on pore-scale images. *Physical Review E*, 87(1):013011.

[41] Bishop, M. and Frinks, S. (1987). Error analysis in computer simulations. *The Journal of chemical physics*, 87(6):3675–3676.

[42] Biswal, B., Held, R., Khanna, V., Wang, J., and Hilfer, R. (2009). Towards precise prediction of transport properties from synthetic computer tomography of reconstructed porous media. *Physical Review E*, 80(4):041301.

[43] Biswal, B., Øren, P., Held, R., Bakke, S., and Hilfer, R. (2007). Stochastic multiscale model for carbonate rocks. *Physical Review E*, 75(6):061303.

[44] Biswal, B., Oren, P., Held, R., Bakke, S., and Hilfer, R. (2008). Modeling of multiscale porous media. *Bulletin of the American Physical Society*, 53.

[45] Blackwell, D. (1973). Discreteness of ferguson selections. *The Annals of Statistics*, 1(2):356–358.

[46] Blunt, M., Jackson, M., Piri, M., and Valvatne, P. (2002a). Detailed physics, predictive capabilities and macroscopic consequences for pore-network models of multiphase flow. *Advances in Water Resources*, 25(8-12):1069–1089.

[47] Blunt, M., Jackson, M., Piri, M., and Valvatne, P. (2002b). Detailed physics, predictive capabilities and macroscopic consequences for pore-network models of multiphase flow. *Advances in Water Resources*, 25(8-12):1069–1089.

[48] Blunt, M. J., Bijeljic, B., Dong, H., Gharbi, O., Iglauer, S., Mostaghimi, P., Paluszny, A., and Pentland, C. (2013a). Pore-scale imaging and modelling. *Advances in Water Resources*, 51:197–216.

[49] Blunt, M. J., Bijeljic, B., Dong, H., Gharbi, O., Iglauer, S., Mostaghimi, P., Paluszny, A., and Pentland, C. (2013b). Pore-scale imaging and modelling. *Advances in Water Resources*, 51:197–216.

[50] Bobek, J., Mattax, C., and Denekas, M. (1991). Reservoir rock wettability-Its significance and evaluation. *Trans*, pages 155–160.

[51] Bondino, I., Hamon, G., Kallel, W., and Kachuma, D. (2012). Relative permeabilities from simulation in 3d rock models and equivalent pore networks: critical review and way forward. In *SCA2012-01, Proceedings of the International Symposium of the Society of Core Analysts, Aberdeen, Scotland, UK*.

[52] Bouch, J. E., Milodowski, A. E., and Ambrose, K. (2004). Contrasting patterns of pore-system modification due to dolomitization and fracturing in dinantian basin-margin carbonates from the uk. *Geological Society, London, Special Publications*, 235(1):325–348.

[53] Brown, H. (1956). Capillary pressure investigations. *Transactions of the American Institute of Mining, Metallurgical and Petroleum Engineers*, page 67.

[54] Brown, R. and Fatt, I. (1956). Measurements of fractional wettability of oil fields' rocks by the nuclear magnetic relaxation method. In *Fall Meeting of the Petroleum Branch of AIME*.

[55] Bryant, S., King, P., and Mellor, D. (1993). Network model evaluation of permeability and spatial correlation in a real random sphere packing. *Transport in Porous Media*, 11(1):53–70.

[56] Buckley, J., Bousseau, C., and Liu, Y. (1996). Wetting alteration by brine and crude oil: from contact angles to cores. *SPE Journal*, 1(3):341–350.

[57] Buckley, J. and Liu, Y. (1998). Some mechanisms of crude oil/brine/solid interactions. *Journal of Petroleum Science and Engineering*, 20(3):155–160.

[58] Buckley, J. S. and Lord, D. L. (2003). Wettability and morphology of mica surfaces after exposure to crude oil. *Journal of Petroleum Science and Engineering*, 39(3):261–273.

[59] Buiting, J. J. M. and Clerke, E. A. (2013). Journal of Petroleum Science and Engineering Permeability from porosimetry measurements : Derivation for a tortuous and fractal tubular bundle. *Journal of Petroleum Science and Engineering*, 108:267–278.

[60] Burkhardt, J., Ward, M., and McLean, R. (1958). Effect of core surfacing and mud filtrate flushing on reliability of core analysis conducted on fresh cores. In *Fall Meeting of the Society of Petroleum Engineers of AIME*.

[61] Busch, R. M. (2011). *Laboratory Manual in Physical Geology*, volume 59.

[62] Byrne, S. and Girolami, M. (2014). Rejoinder : Geodesic Monte Carlo on Embedded Manifolds. 41(2013):19–21.

[63] Caers, J. and Hoffman, T. (2006). The probability perturbation method: A new look at Bayesian inverse modeling. *Mathematical Geology*, 38(1):81–100.

[64] Calvo, M., Lopez-Marcos, M., and Sanz-Serna, J. (1998). Variable step implementation of geometric integrators. *Applied numerical mathematics*, 28(1):1–16.

[65] Cassie, A. and Baxter, S. (1944). Wettability of porous surfaces. *Transactions of the Faraday Society*, 40:546–551.

[66] Chatzis, I. and Dullien, F. (1977). Modelling Pore Structure By 2-D And 3-D Networks With ApplicationTo Sandstones. *Journal of Canadian Petroleum Technology*, 16(1).

[67] Chen, P. and Mohanty, K. K. (2014). SPE-169125-MS Wettability Alteration in High Temperature Carbonate Reservoirs. (April):12–16.

[68] Cheng, Y., Konda, U., Singh, T., and Scott, P. (2011). Bayesian estimation for CBRN sensors with non-gaussian likelihood. *IEEE Transactions on Aerospace and Electronic Systems*, 47(1):684–701.

[69] Christie, M., Glimm, J., Grove, J., Higdon, D., Sharp, D., and Wood-Schultz, M. (2005). Error analysis and simulations of complex phenomena. *Los Alamos Science*, 29(6).

[70] Clarkson, C. R., Solano, N., Bustin, R. M., Bustin, A. M. M., Chalmers, G. R. L., He, L., and Melnichenko, Y. B. (2013). Pore structure characterization of North American shale gas reservoirs using USANS / SANS , gas adsorption , and mercury intrusion. 103:606–616.

[71] Clerke, E. A., Mueller I, H. W., Phillips, E. C., Eyvazzadeh, R. Y., Jones, D. H., Ramamoorthy, R., and Srivastava, A. (2008). Application of thomeer hyperbolas to decode the pore systems, facies and reservoir properties of the upper jurassic arab d limestone, ghawar field, saudi arabia: A rosetta stone approach. *GeoArabia*, 13(4):113–160.

[72] Coles, M., Spanne, P., Muegge, E., and Jones, K. (1994). Computed microtomography of reservoir core samples. In *Proceedings of 1994 International Symposium of SCA*.

[73] Coles, M. E., Hazlett, R. D., Spanne, P., Soll, W. E., Muegge, E. L., and Jones, K. W. (1998). Pore level imaging of fluid transport using synchrotron x-ray microtomography. *Journal of Petroleum Science and Engineering*, 19(1-2):55 – 63.

[74] Constantinides, G. N. and Payatakes, A. C. (1991). A theoretical model of collision and coalescence of ganglia in porous media. *Journal of colloid and interface science*, 141(2):486–504.

[75] Corbett, P. (2009). Petroleum geoengineering: Integration of static and dynamic.

[76] Cuiec, L. (1991). Evaluation of reservoir wettability and its effect on oil recovery. *in Interfacial Phenomena in Petroleum Recovery Ed. by Morrow, N.*, 36:319–375.

[77] Dal Ferro, N., Berti, a., Francioso, O., Ferrari, E., Matthews, G. P., and Morari, F. (2012). Investigating the effects of wettability and pore size distribution on aggregate stability: The role of soil organic matter and the humic fraction. *European Journal of Soil Science*, 63(April):152–164.

[78] Demyanov, V., Subbey, S., and Christie, M. (2004). Uncertainty assessment in punqs3–neighbourhood algorithm framework for geostatistical modelling. In *66th EAGE Conference and Exhibition-Workshops*.

[79] Dicarlo, D. A., Sahni, A., and Blunt, M. J. (2000). The effect of wettability on three-phase relative permeability. *Transport in Porous Media*, 39(3):347–366.

[80] Dixit, A., Buckley, J., McDougall, S., and Sorbie, K. (2000a). Empirical measures of wettability in porous media and the relationship between them derived from pore-scale modelling. *Transport in porous media*, 40(1):27–54.

[81] Dixit, A., Buckley, J., McDougall, S., and Sorbie, K. (2000b). Empirical measures of wettability in porous media and the relationship between them derived from pore-scale modelling. *Transport in porous media*, 40(1):27–54.

[82] Dixit, A., McDougall, S., and Sorbie, K. (1997a). A pore-level investigation of relative permeability hysteresis in water-wet systems. In *SPE international symposium on oilfield chemistry*, pages 229–240.

[83] Dixit, A., McDougall, S., and Sorbie, K. (1998a). A pore-level investigation of relative permeability hysteresis in water-wet systems. *SPE Journal*, 3(2):115–123.

[84] Dixit, A., McDougall, S., and Sorbie, K. (1998b). Analysis of relative permeability hysteresis trends in mixed-wet porous media using network models. In *Symposium on improved oil recovery*, pages 25–38.

[85] Dixit, A., McDougall, S., Sorbie, K., and Buckley, J. (1996a). Pore scale modelling of wettability effects and their influence of oil recovery. In *Symposium on improved oil recovery*, pages 501–515.

[86] Dixit, A., McDougall, S., Sorbie, K., and Buckley, J. (1996b). Pore scale modelling of wettability effects and their influence on oil recovery. In *SPE/DOE Improved Oil Recovery Symposium*.

[87] Dixit, A. B., Mcdougall, S. R., and Sorbie, K. S. (1997b). SPE 39656 Analysis of Relative Permeability Hysteresis Trends in Mixed-wet Porous Media Using Network Models.

[88] Doe, J. (2002). Petrography and sem analysis of carbonate samples. Technical report, Confidential Technical Report, Shell International Exploration and Production.

[89] Domb, C. and Sykes, M. (1961). Cluster size in random mixtures and percolation processes. *Physical Review*, 122(1):77.

[90] Donaldson, E., Thomas, R., and Lorenz, P. (1969). Wettability determination and its effect on recovery efficiency. *Old SPE Journal*, 9(1):13–20.

[91] Dong, H., Fjeldstad, S., Roth, S., Bakke, S., and Øren, P. (2008). Pore Network Modelling on Carbonate: A comparative Study of Different Micro-CT Network Extraction Methods. In *Proc. International Symp. Society of Core Analysts*, pages 2008–31.

[92] Dong, M., Dullien, F., and Chatzis, I. (1995). Imbibition of oil in film form over water present in edges of capillaries with an angular cross section. *Journal of Colloid and Interface Science*, 172(1):21–36.

[93] Drake, L. and Ritter, H. (1945). Macropore-size distributions in some typical porous substances. *Industrial & Engineering Chemistry Analytical Edition*, 17(12):787–791.

[94] Duane, S., Kennedy, A., Pendleton, B., and Roweth, D. (1987). Hybrid monte carlo. *Physics letters B*, 195(2):216–222.

[95] Duane, S. and Kogut, J. (1985). Hybrid stochastic differential equations applied to quantum chromodynamics. *Physical Review Letters*, 55(25):2774–2777.

[96] Duane, S. and Kogut, J. (1986). The theory of hybrid stochastic algorithms* 1. *Nuclear Physics B*, 275(3):398–420.

[97] Dullien, F. and Dhawan, G. (1975). Bivariate pore-size distributions of some sandstones. *Journal of Colloid and Interface Science*, 52(1):129–135.

[98] Dunham, R. (1962). Classification of carbonate rocks according to depositional texture. *Classification of carbonate rocks: American Association of Petroleum Geologists Memoir*, 1:108–121.

[99] Dunsmuir, J., Ferguson, S., D'Amico, K., and Stokes, J. (1991). X-ray microtomography: a new tool for the characterization of porous media. In *SPE Annual Technical Conference and Exhibition*.

[100] Ehrlich, R. and Crane, F. (1969). A model for two-phase flow in consolidated materials. *Old SPE Journal*, 9(2):221–231.

[101] Elsheikh, a. H., Jackson, M. D., and Laforce, T. C. (2012). Bayesian Reservoir History Matching Considering Model and Parameter Uncertainties. *Mathematical Geosciences*, 44:515–543.

[102] Evensen, G. (1994). Sequential data assimilation with a nonlinear quasi-geostrophic model using Monte Carlo methods to forecast error statistics. *JOURNAL OF GEOPHYSICAL RESEARCH-ALL SERIES-*, 99:10–10.

[103] Evensen, G. (2009). *Data assimilation: the ensemble Kalman filter*. Springer Verlag.

[104] Farber, L., Tardos, G., and Michaels, J. (2003). Use of X-ray tomography to study the porosity and morphology of granules. *Powder Technology*, 132(1):57–63.

[105] Fathi, E. and Akkutlu, I. Y. (2013). International Journal of Coal Geology Multi-component gas transport and adsorption effects during CO 2 injection and enhanced shale gas recovery. *International Journal of Coal Geology*, pages 1–10.

[106] Fatt, I. (1956). The network model of porous media: I, II, III. *Trans. Am. Inst. Mem. Metall Pet. Eng*, 207:144–188.

[107] Fatt, I. and Klikoff Jr, W. (1959). Effect of fractional wettability on multiphase flow through porous media. *Journal of Petroleum Technology*, 11(10):71–76.

[108] Fenwick, D. H., Blunt, M. J., et al. (1998). Network modeling of three-phase flow in porous media. *SPE Journal*, 3(01):86–96.

[109] Ferguson, T. S. (1973). A bayesian analysis of some nonparametric problems. *The annals of statistics*, pages 209–230.

[110] Ferreol, B. and Rothman, D. (1995). Lattice-Boltzmann simulations of flow through Fontainebleau sandstone. *Transport in Porous Media*, 20(1):3–20.

[111] Firincioglu, T., Blunt, M., and Zhou, D. (1999a). Three-phase flow and wetability effects in triangular capillaries. *Colloids and Surfaces A: Physicochemical and Engineering Aspects*, 155(2-3):259–276.

[112] Firincioglu, T., Blunt, M. J., and Zhou, D. (1999b). Three-phase flow and wetability effects in triangular capillaries. *Colloids and Surfaces A: Physicochemical and Engineering Aspects*, 155(2):259–276.

[113] Fischer, U. and Celia, M. A. (1999). Prediction of relative and absolute permeabilities for gas and water from soil water retention curves using a pore-scale network model. *Water Resources Research*, 35(4):1089–1100.

[114] Fishman, N. S., Hackley, P. C., Lowers, H. A., Hill, R. J., Egenhoff, S. O., Eberl, D. D., and Blum, A. E. (2012). International Journal of Coal Geology The nature of porosity in organic-rich mudstones of the Upper Jurassic Kimmeridge Clay Formation , North Sea , offshore United Kingdom. *International Journal of Coal Geology*, 103:32–50.

[115] Fleming, P. (1983). An Interpretation of the Petrophysical Properties of Reservoir Rocks Based in Percolation Theory. *paper SPE*, 12515.

[116] Fletcher, R. (1980a). *Practical Methods of Optimization, Vol. 1*. Wiley.

[117] Fletcher, R. (1980b). *Practical Methods of Optimization, Vol. 2*. Wiley.

[118] Fleury, M., Santerre, Y., and Vincent, B. (2007). CARBONATE ROCK TYPING FROM NMR RELAXATION MEASUREMENTS. pages 1–14.

[119] Flugel, E. (2009). *Microfacies of Carbonate Rocks*.

[120] Fox, H. and Zisman, W. (1952). The spreading of liquids on low-energy surfaces. II. Modified tetrafluoroethylene polymers* 1. *Journal of colloid science*, 7(2):109–121.

[121] Freer, E., Svitova, T., and Radke, C. (2003). The role of interfacial rheology in reservoir mixed wettability. *Journal of Petroleum Science and Engineering*, 39(1):137–158.

[122] Friedman, S. P. and Seaton, N. a. (1998). Critical path analysis of the relationship between permeability and electrical conductivity of three-dimensional pore networks. *Water Resources Research*, 34(7):1703–1710.

[123] Fusi, N. and Martinez-martinez, J. (2013). Mercury porosimetry as a tool for improving quality of micro-CT images in low porosity carbonate rocks. *Engineering Geology*, 166:272–282.

[124] Fusseis, F., Xiao, X., Schrank, C., and De Carlo, F. (2014). A brief guide to synchrotron radiation-based microtomography in (structural) geology and rock mechanics. *Journal of Structural Geology*, 65:1–16.

[125] Gaulier, C. (1971). Studying vugular rocks by-constant-rate mercury injection. In *Fall Meeting of the Society of Petroleum Engineers of AIME*.

[126] Geffen, T., Owens, W., Parrish, D., Morse, R., et al. (1951). Experimental investigation of factors affecting laboratory relative permeability measurements. *Trans*, pages 99–110.

[127] Gentle, J. (2002). *Elements of computational statistics*. Springer Verlag.

[128] Goldstein, H. (1980). *Classical mechanics*. Addison-Wesley, Reading, MA, USA, isbn 0-321-18897-7.

[129] Gonzalez, G. and Moreira, M. (1994). The adsorption of asphaltenes and resins on various minerals. *Asphaltenes and asphalts*, 1:207–231.

[130] Good, P. I. and Hardin, J. W. (2012). *Common errors in statistics (and how to avoid them)*. John Wiley & Sons.

[131] Grussaute, T. and Gouel, P. (1998). Computer Aided History Matching of a Real Field Case. In *European Petroleum Conference*. Society of Petroleum Engineers.

[132] Gupta, R., Kilcup, G., and Sharpe, S. (1988). Tuning the hybrid Monte Carlo algorithm. *Physical Review D*, 38(4):1278–1287.

[133] Haines, W. (1927). Studies in the physical properties of soils: IV. A further contribution to the theory of capillary phenomena in soil. *The Journal of Agricultural Science*, 17(02):264–290.

[134] Hairer, E., Lubich, C., and Wanner, G. (2002). *Geometric numerical integration, volume 31 of Springer Series in Computational Mathematics*. Springer-Verlag, Berlin.

[135] Hájek, J. (1999). *Theory of Rank Test*. Academic Press, New York.

[136] Hajian, A. (2007). Efficient cosmological parameter estimation with Hamiltonian Monte Carlo technique. *Physical Review D*, 75(8):83525.

[137] Hammond, P. S. and Unsal, E. (2012). A dynamic pore network model for oil displacement by wettability-altering surfactant solution. *Transport in porous media*, 92(3):789–817.

[138] Hamon, G. (2000). Field-wide variations of wettability. In *SPE Annual Technical Conference and Exhibition*.

[139] Hamon, G. and Pellerin, F. (1997). Evidencing capillary pressure and relative permeability trends for reservoir simulation. In *SPE Annual Technical Conference and Exhibition*.

[140] Hanson, K. (2001). Markov Chain Monte Carlo posterior sampling with the Hamiltonian method. In *Proc. SPIE*, volume 4322, pages 456–467. Citeseer.

[141] Hazlett, R. (1995). Simulation of capillary-dominated displacements in microtomographic images of reservoir rocks. *Transport in porous media*, 20(1):21–35.

[142] Heaviside, J. (1991). Measurement of Relative Permeability. *In Interfacial Phenomena in Petroleum Recovery, NR Morrow ed., Marcel Dekker Inc, New York*, 36:377–411.

[143] Heiba, A., Davis, H., Scriven, L., et al. (1984). Statistical network theory of three-phase relative permeabilities. In *SPE Enhanced Oil Recovery Symposium*. Society of Petroleum Engineers.

[144] Heiba, A., Sahimi, M., Scriven, L., and Davis, H. (1982). Percolation theory of two-phase relative permeability. *SPE Reservoir Engineering*, 7(1):123–132.

[145] Held, R. J. and Celia, M. A. (2001). Pore-scale modeling extension of constitutive relationships in the range of residual saturations. *Water Resources Research*, 37(1):165–170.

[146] Helland, J., van Dijke, M., Sorbie, K., and Skjæveland, S. (2006). Three-phase relative permeability from mixed-wet triangular and star-shaped pores. In *9th International Symposium on Reservoir Wettability, Bergen, Norway*.

[147] Hirasaki, G. J., Miller, C. A., and Puerto, M. (2011). Recent Advances in Surfactant EOR. (December).

[148] Hitchcock, S., Carroll, N., and Nicholas, M. (1981). Some effects of substrate roughness on wettability. *Journal of Materials Science*, 16(3):714–732.

[149] Hoaglin, D., Mosteller, F., and Tukey, J. (1983). *Understanding robust and exploratory data analysis*, volume 3. Wiley New York.

[150] Høiland, L. K., Spildo, K., and Skauge, A. (2007). Fluid flow properties for different classes of intermediate wettability as studied by network modelling. *Transport in Porous Media*, 70(1):127–146.

[151] Holm, R., Kaufmann, R., Dale, E., Aanonsen, S., Fladmark, G., Espedal, M., and Skauge, A. (2009). Constructing Three-Phase Capillary Pressure Functions by Parameter Matching Using a Modified Ensemble Kalman Filter. *Communications in Computational Physics*.

[152] Holmberg, K., Shah, D. O., and Schwuger, M. J. (2002). *Handbook of applied surface and colloid chemistry*, volume 2. Wiley New York.

[153] Hoteit, I., Pham, D., Triantafyllou, G., and Korres, G. (2008). A new approximate solution of the optimal nonlinear filter for data assimilation in meteorology and oceanography. *Monthly Weather Review*, 136(1):317–334.

[154] Huang, W. and Leimkuhler, B. (1997). The adaptive Verlet method. *SIAM Journal on Scientific Computing*, 18(1):239–256.

[155] Huber, P., Huber, P., Huber, P., Statisticien, M., Suisse, E., Huber, P., and Statistician, M. (1996). *Robust statistical procedures*, volume 68. SIAM.

[156] Hui, C., Zhou, Y. X., and Narayana, P. (2010). Fast algorithm for calculation of inhomogeneity gradient in magnetic resonance imaging data. *Journal of magnetic resonance imaging : JMRI*, 32(5):1197–208.

[157] Hui, M.-H. and Blunt, M. J. (2000). Effects of wettability on three-phase flow in porous media. *The Journal of Physical Chemistry B*, 104(16):3833–3845.

[158] Hui, M.-H., Blunt, M. J., et al. (2000). Pore-scale modeling of three-phase flow and the effects of wettability. In *SPE/DOE Improved Oil Recovery Symposium*. Society of Petroleum Engineers.

[159] Hunt, A. G. (2001). Applications of percolation theory to porous media with distributed local conductances. *Advances in Water Resources*, 24(3-4):279–307.

[160] Idowu, N., Nardi, C., Long, H., Øren, P.-E., Bondino, I., and Total, E. (2013). Improving digital rock physics predictive potential for relative permeabilities from equivalent pore networks. In *Paper SCA 2013-17 presented at the International Symposium of the Society of Core Analysts, Napa Valley, California, USA*, pages 16–19.

[161] Ingram, B., Cornford, D., and Csató, L. (2010). Robust Automatic Mapping Algorithms in a Network Monitoring Scenario. *Quantitative Geology and Geostatistics*, 16(November):359–370.

[162] Ingsoy, P., Skjaeveland, S., Hjelmaas, T., and Haga, O. (1998). Introducing Imbibition Capillary Pressure in the Assessment of the Smoerbukk and Smoerbukk South Fields Offshore Norway. In *International Petroleum Conference and Exhibition of Mexico*.

[163] Ioannidis, M. and Chatzis, I. (1993). Network modelling of pore structure and transport properties of porous media. *Chemical Engineering Science*, 48(5):951–972.

[164] Ioannidis, M. and Chatzis, I. (2000). A Dual-Network Model of Pore Structure for Vuggy Carbonates. In *SCA2000-09, International Symposium of the Society of Core Analysts, Abu Dhabi, UAE*.

[165] Ivanov, I. B. and Kralchevsky, P. A. (1997). Stability of emulsions under equilibrium and dynamic conditions. *Colloids and Surfaces A: Physicochemical and engineering aspects*, 128(1):155–175.

[166] Jackson, M., Valvatne, P., and Blunt, M. (2003a). Prediction of wettability variation and its impact on flow using pore-to reservoir-scale simulations. *Journal of Petroleum Science and Engineering*, 39(3-4):231–246.

[167] Jackson, M. D. and Blunt, M. J. (2002). Elliptic regions and stable solutions for three-phase flow in porous media. *Transport in porous media*, 48(3):249–269.

[168] Jackson, M. D., Valvatne, P. H., and Blunt, M. J. (2003b). Prediction of wettability variation and its impact on flow using pore-to reservoir-scale simulations. *Journal of Petroleum Science and Engineering*, 39(3):231–246.

[169] Jamshidi, S., Boozarjomehry, R. B., and Pishvaie, M. R. (2009). Application of ga in optimization of pore network models generated by multi-cellular growth algorithms. *Advances in water resources*, 32(10):1543–1553.

[170] Jasche, J. and Kitaura, F. S. (2009). Fast Hamiltonian sampling for large scale structure inference. *Imprint*.

[171] Jaynes, E. (1967). Foundations of probability theory and statistical mechanics. In *Delaware Seminar in the Foundations of Physics*, volume 1, pages 76–101. Springer-Verlag.

[172] Jaynes, E. (1984). Bayesian Methods: General Background. *Maximum Entropy and Bayesian Methods in Applied Statistics*.

[173] Jaynes, E. and Bretthorst, G. (2003). *Probability theory: the logic of science*. Cambridge Univ Pr.

[174] Jaynes, E. T. (1957). Information theory and statistical mechanics. *Phys. Rev.*, 106(4):620–630.

[175] Jean-françois, C., Sylvain, B., Adalbert, A., Muriel, B.-n., and Mélanie, B. (2015). Global surveys of reservoirs and lakes from satellites and regional application to the Syrdarya river basin. *Environmental Research Letters*, 10(1):15002.

[176] Jerauld, G., Hatfield, J., Scriven, L., and Davis, H. (1984a). Percolation and conduction on Voronoi and triangular networks: a case study in topological disorder. *Journal of Physics C: Solid State Physics*, 17:1519–1529.

[177] Jerauld, G. and Rathmell, J. (1997). Wettability and relative permeability of Prudhoe Bay: A case study in mixed-wet reservoirs. *SPE Reservoir Engineering*, 12(1):58–65.

[178] Jerauld, G. and Salter, S. (1990). The effect of pore-structure on hysteresis in relative permeability and capillary pressure: pore-level modeling. *Transport in Porous Media*, 5(2):103–151.

[179] Jerauld, G., Scriven, L., and Davis, H. (1984b). Percolation and conduction on the 3D Voronoi and regular networks: a second case study in topological disorder. *Journal of Physics C: Solid State Physics*, 17:3429–3439.

[180] Jiang, Z., Dijke, M. I. J., Wu, K., Couples, G. D., Sorbie, K. S., and Ma, J. (2012). Stochastic pore network generation from 3D rock images. *Transport in Porous Media*, 94(2):571–593.

[181] Jiang, Z., Dijke, M. I. J. V., Sorbie, K. S., and Couples, G. D. (2013). Representation of multiscale heterogeneity via multiscale pore networks. 49(January):1–13.

[182] Johnson, R. and Dettre, R. (1969). Wettability and contact angles. *Surface and colloid science*, 2:85–153.

[183] Jonas, M. and Schopper, J. (1994). The radii inversion problem associated with the Hg capillary pressure experiment. *Transport in Porous Media*, 14(1):33–72.

[184] Jordan, M., Sorbie, K., Ping, J., Yuan, M., Todd, A., and Hourston, K. (1994). Phosphonate Scale Inhibitor Adsorption/Desorption and the Potential for Formation Damage in Reconditioned Field Core. In *SPE Formation Damage Control Symposium*.

[185] Juri, J., van Dijke, M. I., and Sorbie, K. S. (2015a). Inversion of lattice network structure subjected to carbonate mercury intrusion capillary pressure: Hamiltonian monte carlo posterior sampling. *Transport in Porous Media*, 106(1):73–106.

[186] Juri, J., van Dijke, M. I., and Sorbie, K. S. (2015b). Inversion of the lattice network wettability subjected to the entire-flooding-cycle capillary pressure: Hamiltonian monte carlo posterior sampling and prediction of the relative permeability. *Submitted to Journal of petroleum science and engineering*.

[187] Kalaei, M. H., Green, D. W., and Willhite, G. P. (2012). A New Dynamic Wettability Alteration Model for Oil-Wet Cores During Surfactant Solution Imbibition. (1998):1–2.

[188] Kallel, W., van Dijke, M., Sorbie, K., Wood, R., Jiang, Z., and Harland, S. (2015). Modelling the effect of wettability distributions on oil recovery from microporous carbonate reservoirs. *Advances in Water Resources*, 000:1–12.

[189] Kalos, M. and Whitlock, P. (2008). *Monte carlo methods*. Wiley-VCH.

[190] Kaminsky, R. and Radke, C. (1998). Water films, asphaltenes, and wettability alteration. Technical report, Lawrence Berkeley Lab., CA (United States).

[191] Kantzas, A. and Chatzis, I. (1988). Network simulation of relative permeability curves using a bond correlated-site percolation model of pore structure. *Chemical engineering communications*, 69(1):191–214.

[192] Kantzas, A., Chatzis, I., Dullien, F., et al. (1988). Mechanisms of capillary displacement of residual oil by gravity-assisted inert gas injection. In *SPE Rocky Mountain Regional Meeting*. Society of Petroleum Engineers.

[193] Keller, A. A., Blunt, M. J., and Roberts, A. P. V. (1997). Micromodel observation of the role of oil layers in three-phase flow. *Transport in Porous Media*, 26(3):277–297.

[194] Kennedy, A. and Pendleton, B. (2001). Cost of the generalised hybrid Monte Carlo algorithm for free field theory. *Nuclear Physics, Section B*, 607(3):456–510.

[195] Kleinberg, R. (1996). Utility of nmr t_2 distributions, connection with capillary pressure, clay effect, and determination of the surface relaxivity parameter p_2. *Magnetic resonance imaging*, 14(7):761–767.

[196] Kleinberg, R., Farooqui, S., and Horsfield, M. (1993a). T1/t2 ratio and frequency dependence of nmr relaxation in porous sedimentary rocks. *Journal of colloid and interface science*, 158(1):195–198.

[197] Kleinberg, R., Kenyon, W., and Mitra, P. (1994). Mechanism of nmr relaxation of fluids in rock. *Journal of magnetic resonance, Series A*, 108(2):206–214.

[198] Kleinberg, R., Straley, C., Kenyon, W., Akkurt, R., and Farooqui, S. (1993b). Nuclear magnetic resonance of rocks: T1 vs. t2. In *SPE Annual Technical Conference and Exhibition*.

[199] Knackstedt, M., Arns, C., Limaye, A., Sakellariou, A., Senden, T., Sheppard, A., Sok, R., Pinczewski, W., and Bunn, G. (2004). Digital core laboratory: Properties of reservoir core derived from 3D images. In *SPE Asia Pacific Conference on Integrated Modelling for Asset Management*.

[200] Konishi, S. and Kitagawa, G. (2007). *Information criteria and statistical modeling*. Springer.

[201] Kovscek, A., Wong, H., and Radke, C. (1993a). A pore-level scenario for the development of mixed wettability in oil reservoirs. *AIChE Journal*, 39(6):1072–1085.

[202] Kovscek, A., Wong, H., and Radke, C. (1993b). A pore-level scenario for the development of mixed wettability in oil reservoirs. *AIChE Journal*, 39(6):1072–1085.

[203] Kowalewski, E., Holt, T., and Torsaeter, O. (2002). Wettability alterations due to an oil soluble additive. *Journal of Petroleum Science and Engineering*, 33(1):19–28.

[204] Kramer, A., Calderhead, B., and Radde, N. (2014). Hamiltonian Monte Carlo methods for efficient parameter estimation in steady state dynamical systems. *BMC bioinformatics*, 15(1):253.

[205] Kwiecien, M., Macdonald, I., and Dullien, F. (1990). Three-dimensional reconstruction of porous media from serial section data. *Journal of microscopy*, 159:343–359.

[206] Langevin, D., Marquez-Beltran, C., and Delacotte, J. (2011). Surface force measurements on freely suspended liquid films. *Advances in colloid and interface science*, 168(1):124–134.

[207] Laroche, C. and Vizika, O. (2005). Two-phase flow properties prediction from small-scale data using pore-network modeling. *Transport in Porous Media*, 61(1):77–91.

[208] Laroche, C., Vizika, O., and Kalaydjian, F. (1999). Network modeling as a tool to predict three-phase gas injection in heterogeneous wettability porous media. *Journal of Petroleum Science and Engineering*, 24(2):155–168.

[209] Larsen, J., Bech, N., Winter, A., et al. (2000). Three-phase immiscible wag injection: micromodel experiments and network models. In *SPE/DOE Improved oil recovery symposium*. Society of Petroleum Engineers.

[210] Latief, F., Biswal, B., Fauzi, U., and Hilfer, R. (2010). Continuum reconstruction of the pore scale microstructure for fontainebleau sandstone. *Physica A: Statistical Mechanics and its Applications*, 389(8):1607–1618.

[211] Lei, J. and Bickel, P. (2009). Ensemble filtering for high dimensional non-linear state space models. *University of California, Berkeley, Rep*, 779:23.

[212] Leimkuhler, B. and Reich, S. (2005). *Simulating hamiltonian dynamics*, volume 14. Cambridge University Press.

[213] Lenormand, R. (1990). Liquids in porous media. *Journal of Physics: Condensed Matter*, 2.

[214] Lenormand, R. (2003). Interpretation of mercury injection curves to derive pore size distribution. In *Proceedings of 2003 International Symposium of SCA*.

[215] Lenormand, R. and Zarcone, C. (1984). Role of roughness and edges during imbibition in square capillaries. SPE 13264. In *Annual Technical Conference and Exhibition, Houston*, pages 16–19.

[216] Lenormand, R., Zarcone, C., et al. (1984). Role of roughness and edges during imbibition in square capillaries. *SPE J*, 13264.

[217] Lenormand, R., Zarcone, C., and Sarr, A. (1983a). Mechanisms of the displacement of one fluid by another in a network of capillary ducts. *J. Fluid Mech*, 135(34):337–353.

[218] Lenormand, R., Zarcone, C., and Sarr, A. (1983b). Mechanisms of the displacement of one fluid by another in a network of capillary ducts. *Journal of Fluid Mechanics*, 135:337–353.

[219] Lerdahl, T. R., Oren, P.-E., Bakke, S., et al. (2000). A predictive network model for three-phase flow in porous media. In *SPE/DOE Improved Oil Recovery Symposium*. Society of Petroleum Engineers.

[220] Li, K. and Horne, R. N. (2008). Estimation of wettability in gas–liquid–rock systems. *Geothermics*, 37(4):429–443.

[221] Liu, H., Zhang, L., and Seaton, N. (1993). Analysis of sorption hysteresis in mesoporous solids using a pore network model. *Journal of Colloid and Interface Science*, 156(2):285–293.

[222] Liu, N. and Oliver, D. S. (2004). Automatic history matching of geologic facies. *Spe Journal*, 9(4):429–436.

[223] Lodoen, O. and Omre, H. (2008). Scale-Corrected Ensemble Kalman Filtering Applied to Production-History Conditioning in Reservoir Evaluation. *SPE Journal*, 13(2):1–34.

[224] Lucia, F. (2007). *Carbonate reservoir characterization*. Springer Verlag.

[225] Luffel, D., Randall, R., et al. (1960). Core Handling and Measurement Techniques for Obtaining Reliable Reservoir Characteristics. In *paper SPE 1642G presented at the 1960 SPE Formation Evaluation Symposium, Houston, Nov*, pages 21–22.

[226] Lugosi, G. and Nobel, A. (1996). Consistency of data-driven histogram methods for density estimation and classification. *The Annals of Statistics*, 24(2):687–706.

[227] Lymberopoulos, D. and Payatakes, A. (1992). Derivation of topological, geometrical, and correlational properties of porous media from pore-chart analysis of serial section data. *Journal of colloid and interface science*, 150(1):61–80.

[228] Ma, X., Al-Harbi, M., Datta-Gupta, A., Efendiev, Y., et al. (2008). An efficient two-stage sampling method for uncertainty quantification in history matching geological models. *SPE Journal*, 13(01):77–87.

[229] MacDonald, I., Kaufmann, P., and Dullien, F. (1986). Quantitative image analysis of finite porous media. I: Development of genus and pore map software= Analyse d'images quantitatives de milieu poreux fini. I. Développement de logiciel de genre et de carte des pores. *Journal of microscopy*, 144(3):277–296.

[230] Machel, H. G. (2004). Concepts and models of dolomitization: a critical reappraisal. *Geological Society, London, Special Publications*, 235(1):7–63.

[231] Mahgoub, L. and Mohamed, Y. (2011). *Novel Sampling Techniques for Reservoir History Matching Optimisation and Uncertainty Quantification in Flow Prediction*. PhD thesis, Heriot-Watt University.

[232] Mandel, J. and Beezley, J. (2009). An ensemble Kalman-particle predictor-corrector filter for non-Gaussian data assimilation. *Computational Science–ICCS 2009*, pages 470–478.

[233] Mani, V. and Mohanty, K. (1997a). Effect of the spreading coefficient on three-phase flow in porous media. *Journal of colloid and interface science*, 187(1):45–56.

[234] Mani, V. and Mohanty, K. (1997b). Pore-level network modeling of three-phase capillary pressure and relative permeability curves. In *SPE annual technical conference*, pages 405–418.

[235] Marathe, R., Turner, M., and Fogden, A. (2012). Pore-scale distribution of crude oil wettability in carbonate rocks. *Energy & Fuels*, 26:6268–6281.

[236] Masalmeh, S. (2001). Experimental Measurements of Capillary Pressure and Relative Permeability Hysteresis. In *Proceedings of the International Symposium of the Society of Core Analysis*, volume 23, pages 17–19.

[237] Masalmeh, S. (2002a). Studying the effect of wettability heterogeneity on the capillary pressure curves using the centrifuge technique. *Journal of Petroleum Science and Engineering*, 33(1-3):29–38.

[238] Masalmeh, S. (2002b). The effect of wettability on saturation functions and impact on carbonate reservoirs in the middle east. In *Abu Dhabi International Petroleum Exhibition and Conference*.

[239] Masalmeh, S. (2003a). The effect of wettability heterogeneity on capillary pressure and relative permeability. *Journal of Petroleum Science and Engineering*, 39(3-4):399–408.

[240] Masalmeh, S., Abu-Shiekah, I., and Jing, X. (2005). Improved Characterization and Modeling of Capillary Transition Zones in Carbonate Reservoirs. In *International Petroleum Technology Conference*.

[241] Masalmeh, S. and Jing, X. (2004). Carbonate SCAL: characterisation of carbonate rock types for determination of saturation functions and residual oil saturations. In *Proceedings of the International Symposium of the Society of Core Analysis held in Abu Dhabi, UAE*, pages 5–9.

[242] Masalmeh, S. and Jing, X. (2006). Capillary Pressure Characteristics of Carbonate Reservoirs: Relationship between Drainage and Imbibition Curves. In *Proceedings of the International Symposium of the Society of Core Analysis*, volume 16, pages 12–16.

[243] Masalmeh, S. and Jing, X. (2007). Improved characterization and modelling of carbonate reservoirs for predicting waterflood performance. In *International Petroleum Technology Conference*.

[244] Masalmeh, S. and Jing, X. (2008). The Importance of speial core analysis in modelling remainig oil saturation in carbonate fields. In *Proceedings of the International Symposium of the Society of Core Analysis*.

[245] Masalmeh, S., Jing, X., Van Vark, W., Christiansen, S., Van der Weerd, H., and Van Dorp, J. (2003a). Impact of SCAL on carbonate reservoirs: how capillary forces can affect field performance predictions. In *Proceedings of the International Symposium of the Society of Core Analysis, Pau, France*.

[246] Masalmeh, S., Jing, X., van Vark, W., and van der Weerd, H. (2003b). S. and van Dorp, J.:Impact of SCAL on Carbonate Reservoirs: How Capillary Forces Can Affect Field Performance Predictions SCA 2003-36 presented at the SCA 2003 conference, Pau, France. In *Proceedings of the International Symposium of the Society of Core Analysis*. October.

[247] Masalmeh, S. K. (2002c). Studying the effect of wettability heterogeneity on the capillary pressure curves using the centrifuge technique. *Journal of Petroleum Science and Engineering*, 33(1):29–38.

[248] Masalmeh, S. K. (2003b). The effect of wettability heterogeneity on capillary pressure and relative permeability. *Journal of Petroleum Science and Engineering*, 39(3):399–408.

[249] Mason, G. and Morrow, N. (1991). Capillary behavior of a perfectly wetting liquid in irregular triangular tubes. *Journal of Colloid and Interface Science*, 141(1):262–274.

[250] Mason, G. and Morrow, N. (2013). Developments in spontaneous imbibition and possibilities for future work. *Journal of Petroleum Science and Engineering*, pages 1–26.

[251] Mathews, T., Matthews, G., and Huggett, S. (1999). Estimating particle size distributions from a network model of porous media. *Powder Technology*, 104(2):169–179.

[252] Matthews, G., Moss, A., and Ridgway, C. (1995). The effects of correlated networks on mercury intrusion simulations and permeabilities of sandstone and other porous media. *Powder Technology*, 83(1):61–77.

[253] Matthews, G., Moss, A., Spearing, M., and Voland, F. (1993). Network calculation of mercury intrusion and absolute permeability in sandstone and other porous media. *Powder Technology*, 76(1):95–107.

[254] McCaffery, F. and Bennion, D. (1974). Effect of wettability on two phase relative permeabilities. *Name: Prepr. Annu. Canadian Inst. of Mining and Metallurgy Petrol. Soc. Tech. Mtg*.

[255] Mcdougall, S., Cruichshank, J., and Sorbie, K. (2002). Anchoring Methodologies For Pore-scale Network Models: Application To Relative Permeability And Capillary Pressure Prediction. *Petrophysics*, 43(4):365–375.

[256] McDougall, S., Cruickshank, J., and Sorbie, K. (2002). Anchoring Methodologies for Pore-Scale Network Models: Application to Relative Permeability and Capillary Pressure Preduction. *Petrophysics*, 43(4):365–375.

[257] McDougall, S. and Sorbie, K. (1995). The impact of wettability on waterflooding: pore-scale simulation. *SPE Reservoir Engineering*, 10(3):208–213.

[258] McDougall, S. and Sorbie, K. (1997). The application of network modelling techniques to multiphase flow in porous media. *Petroleum Geoscience*, 3(2):161.

[259] McDougall, S., Sorbie, K., et al. (1995). The impact of wettability on waterflooding: Pore-scale simulation. *SPE Reservoir Engineering*, 10(03):208–213.

[260] Mcdougall, S. R., Cruickshank, J., and Sorbie, K. S. (2002). Anchoring Methodologies for Pore-Scale Network Models : Application to Relative Permeability and Capillary Pressure Prediction '. 43(4):365–375.

[261] McDougall, S. R., Cruickshank, J., and Sorbie, K. S. (2002). Anchoring methodologies for pore-scale network models: Application to relative permeability and capillary pressure preduction. *PETROPHYSICS-HOUSTON-*, 43(4):365–375.

[262] McDougall, S. R. and Sorbie, K. S. (2002). The missing link between pore-scale anchoring and pore-scale prediction. *Paper SCA*, page A15.

[263] Meakin, P. and Tartakovsky, A. (2009). Modeling and simulation of pore-scale multiphase fluid flow and reactive transport in fractured and porous media. *Reviews of Geophysics*, 47(3).

[264] Melrose, J. (1965). Wettability as related to capillary action in porous media. *Old SPE Journal*, 5(3):259–271.

[265] Melrose, J. (1982). Interpretation of mixed wettability states in reservoir rocks. In *SPE Annual Technical Conference and Exhibition*.

[266] Melrose, J. and Brandner, C. F. (1974). Role of Capillary Forces In Detennining Microscopic Displacement Efficiency For Oil Recovery By Waterflooding. *Journal of Canadian Petroleum Technology*, 13(4).

[267] Metropolis, N., Rosenbluth, A., Rosenbluth, M., Teller, A., and Teller, E. (1953). Equation of state calculations by fast computing machines. *The journal of chemical physics*, 21(6):1087.

[268] Mittal, A., Lyle, N., Harmon, T. S., and Pappu, R. V. (2014). Hamiltonian Switch Metropolis Monte Carlo Simulations for Improved Conformational Sampling of Intrinsically Disordered Regions Tethered to Ordered Domains of Proteins. *Journal of Chemical Theory and Computation*, page 140613083455002.

[269] Moctezuma, A., Bekri, S., Laroche, C., and Vizika, O. (2003). A Dual Network Model For Relative Permeability of Bimodal Rocks: Application in a Vuggy Carbonate. In *SCA2003-12, proceeding of International Symposium of the Society of Core Analysts, Pau, France*.

[270] Mohamed, L., Calderhead, B., Filippone, M., Christie, M., and Girolami, M. (2012a). Population MCMC methods for history matching and uncertainty quantification. *Computational Geosciences*, 16(2):423–436.

[271] Mohamed, L., Calderhead, B., Filippone, M., Christie, M., and Girolami, M. (2012b). Population MCMC methods for history matching and uncertainty quantification. pages 423–436.

[272] Mohanty, K. K. et al. (1983). Multiphase flow in porous media: Iii. oil mobilization transverse dispersion and wettability. In *SPE Annual Technical Conference and Exhibition*. Society of Petroleum Engineers.

[273] Morrow, N. (1970). Physics and thermodynamics of capillary action in porous media. *Industrial & Engineering Chemistry*, 62(6):32–56.

[274] Morrow, N. (1975). The Effects of Surface Roughness On Contact: Angle With Special Reference to Petroleum Recovery. *Journal of Canadian Petroleum Technology*, 14(4).

[275] Morrow, N. (1976). Capillary pressure correlations for uniformly wetted porous media. *Journal of Canadian Petroleum Technology*, 15(4).

[276] Morrow, N. (1990). Wettability and its effect on oil recovery. *Journal of Petroleum Technology*, 42(12):1476–1484.

[277] Morrow, N. (1991). Interfacial Phenomena in Petroleum Recovery. *Interfacial Phenomena in Petroleum Recovery, NR Morrow ed., Marcel Dekker Inc, New York*, pages 1–22.

[278] Morrow, N., Lim, H., and Ward, J. (1986a). Effect of crude-oil-induced wettability changes on oil recovery. *SPE Formation Evaluation*, 1(1):89–103.

[279] Morrow, N. R. et al. (1975). The effects of surface roughness on contact: Angle with special reference to petroleum recovery. *Journal of Canadian Petroleum Technology*, 14(04).

[280] Morrow, N. R., Lim, H. T., Ward, J. S., et al. (1986b). Effect of crude-oil-induced wettability changes on oil recovery. *SPE Formation Evaluation*, 1(01):89–103.

[281] Morton, K. and Mayers, D. (2005). *Numerical solution of partial differential equations: an introduction*. Cambridge university press.

[282] Mosegaard, K. and Tarantola, A. (1995). Monte Carlo sampling of solutions to inverse problems. *J. geophys. Res*, 100(12):431–47.

[283] Mostaghimi, P. and Blunt, M. J. (2012). Computations of Absolute Permeability on Micro-CT Images.

[284] Mostaghimi, P., Blunt, M. J., and Bijeljic, B. (2013). Computations of absolute permeability on micro-ct images. *Mathematical Geosciences*, 45(1):103–125.

[285] Moulu, J.-C., Vizika, O., Egermann, P., and Kalaydjian, F. (1999). A new three-phase relative permeability model for various wettability conditions. In *SPE annual technical conference*.

[286] Moulu, J.-C., Vizika, O., Kalaydjian, F., and Duquerroix, J.-P. (2013). A New Model for Three-Phase Relative Permeabilities Based on a Fractal Representation of the Porous Medium. *SPE Annual Technical Conference and Exhibition*, pages 499–511.

[287] Neal, R. (1992). An improved acceptance procedure for the hybrid Monte Carlo algorithm. *Arxiv preprint hep-lat/9208011*.

[288] Nugroho, D. B. and Morimoto, T. (2015). Estimation of realized stochastic volatility models using Hamiltonian Monte Carlo-Based methods. *Computational Statistics*, 30(2):491–516.

[289] O Carroll, C. and Sorbie, K. (1993). Generalization of the poiseuille law for one-and two-phase flow in a random capillary network. *Physical Review E*, 47(5):3467.

[290] Oblow, E. (1978). Sensitivity theory for reactor thermal-hydraulics problems. *Nuclear Science and Engineering*, 68(3):322–337.

[291] Oh, W. and Lindquist, B. (1999). Image thresholding by indicator kriging. *IEEE Transactions on Pattern Analysis and Machine Intelligence*, 21(7):590–602.

[292] O'Hanlon, M., Black, C., Webb, K., Bin-Daaer, G., and El-Tawil, A. (1996). Identifying the Controls on Waterflood Performance in a Giant Carbonate Reservoir. In *Abu Dhabi International Petroleum Exhibition and Conference*.

[293] Okabe, H. (2004). *Pore-scale modelling of carbonates*. PhD thesis, Imperial College London.

[294] Okasha, T., Funk, J., and Al-Enezi, S. (2003). Wettability and relative permeability of lower cretaceous carbonate rock reservoir, saudi arabia. In *SPE Middle East Oil and Gas Show and Conference*.

[295] Okasha, T. M., Funk, J. J., Rashidi, H. N., et al. (2007). Fifty years of wettability measurements in the arab-d carbonate reservoir. In *SPE Middle East Oil and Gas Show and Conference*. Society of Petroleum Engineers.

[296] Øren, P. and Bakke, S. (2003). Reconstruction of Berea sandstone and pore-scale modelling of wettability effects. *Journal of Petroleum Science and Engineering*, 39(3-4):177–199.

[297] Oren, P., Billiotte, J., Pinczewski, W., et al. (1992). Mobilization of waterflood residual oil by gas injection for water-wet conditions. *SPE Formation Evaluation*, 7(01):70–78.

[298] Oren, P. et al. (1994a). Pore-scale network modelling of waterflood residual oil recovery by immiscible gas flooding. In *SPE/DOE Improved Oil Recovery Symposium*. Society of Petroleum Engineers.

[299] Øren, P.-E. and Bakke, S. (2002). Process based reconstruction of sandstones and prediction of transport properties. *Transport in Porous Media*, 46(2-3):311–343.

[300] Øren, P.-E., Bakke, S., and Arntzen, O. J. (1998). Extending predictive capabilities to network models. *SPE JOURNAL-RICHARDSON-*, 3:324–336.

[301] Oren, P. E., Pinczewski, W. V., et al. (1994b). The effect of wettability and spreading coefficients on the recovery of waterflood residual oil by miscible gasflooding. *SPE Formation Evaluation*, 9(02):149–156.

[302] Osoba, J., Richardson, J., Kerver, J., Hafford, J., Blair, P., et al. (1951). Laboratory measurements of relative permeability. *Trans. AIME*, 192:47–56.

[303] Pakman, A. and Paninski, L. (2013). Auxiliary-variable exact Hamiltonian Monte Carlo samplers for binary distributions. *Journal of Computational and Graphical Statistics*, (February):130610142855008.

[304] Palaz, I. and Marfurt, K. (1997). *Carbonate seismology*. Soc of Exploration Geophysicists.

[305] Patel, P., Christman, P., and Gardner, J. (1987). Investigation of Unexpectedly Low Field-Observed Fluid Mobilities During Some CO2 Tertiary Floods. *SPE Reservoir Engineering*, 2(4):507–513.

[306] Paterson, L., Painter, S., Zhang, X., and Pinczewski, V. (1996). Simulating residual saturation and relative permeability in heterogeneous formations. In *SPE annual technical conference*, pages 321–328.

[307] Pathak, P., Davis, H. T., Scriven, L., et al. (1982). Dependence of residual nonwetting liquid on pore topology. In *SPE Annual Technical Conference and Exhibition*. Society of Petroleum Engineers.

[308] Pereira, G. (1999). Numerical pore-scale modeling of three-phase fluid flow: Comparison between simulation and experiment. *Physical Review E*, 59(4):4229.

[309] Philip, J. (1971). Limitations on Scaling by Contact Angle1. *Soil Science Society of America Journal*, 35(3):507.

[310] Piller, M., Casagrande, D., Schena, G., and Santini, M. (2014). Pore-scale simulation of laminar flow through porous media. In *Journal of Physics: Conference Series*, volume 501, page 012010. IOP Publishing.

[311] Piri, M. and Blunt, M. (2002). Pore-scale modeling of three-phase flow in mixed-wet systems. *paper SPE*, 77726.

[312] Piri, M. and Blunt, M. (2005). Three-dimensional mixed-wet random pore-scale network modeling of two-and three-phase flow in porous media. I. Model description. *Physical Review E*, 71(2):26301.

[313] Piri, M., Blunt, M. J., et al. (2002). Pore-scale modeling of three-phase flow in mixed-wet systems. In *SPE Annual Technical Conference and Exhibition*. Society of Petroleum Engineers.

[314] Portsmouth, R. and Gladden, L. (1991). Determination of pore connectivity by mercury porosimetry. *Chemical Engineering Science*, 46(12):3023–3036.

[315] Prothero, D. and Schwab, F. (2013). *An Introduction to sedimentary Rocks and Stratigraphy*.

[316] Purcell, W. (1949). Capillary pressures–their measurement using mercury and the calculation of permeability therefrom. *Transactions of the American Institute of Mining And Metallurgical Pet. Engineers*, 186:39–48.

[317] Purcell, W. (1950). Interpretation of Capillary Pressure Data. *Transactions*, page 369.

[318] Qajar, J. (2012). *Reactive Flow in Carbonate Cores via Digital Core Analysis*. PhD thesis.

[319] Radlinski, A., Ioannidis, M., Hinde, A., Hainbuchner, M., Baron, M., Rauch, H., and Kline, S. (2004). Angstrom-to-millimeter characterization of sedimentary rock microstructure. *Journal of colloid and interface science*, 274(2):607–612.

[320] Rajaram, H., Ferrand, L. A., and Celia, M. A. (1997). Prediction of relative permeabilities for unconsolidated soils using pore-scale network models. *Water Resources Research*, 33(1):43–52.

[321] Ramakrishnan, T., Ramamoorthy, R., Fordham, E., Schwartz, L., Herron, M., Saito, N., and Rabaute, A. (2001). A model-based interpretation methodology for evaluating carbonate reservoirs. In *SPE Annual Technical Conference and Exhibition*.

[322] Rathmell, J., Braun, P., and Perkins, T. (1973). Reservoir waterflood residual oil saturation from laboratory tests. *Journal of Petroleum Technology*, 25(2):175–185.

[323] Renault, P. (1988). Theoretical studies of mercury intrusion in some networks: testing the applicability of mercury intrusion in the size characterisation of the lacunar pore space of soil samples. *Transport in Porous Media*, 3(6):529–547.

[324] Richardson, J. (1961). Flow through porous media. *Handbook of Fluid Dynamics*, pages 16–1.

[325] Richardson, J., Perkins Jr, F., and Osoba, J. (1954). Differences in Behavior of Fresh and Aged East Texas Woodbine Cores. In *Fall Meeting of the Petroleum Branch of AIME*.

[326] Richardson, L. (1910). The approximate arithmetical solution by finite differences of physical problems involving differential equations. *Philos. Trans. Roy. Soc. London, Set. A*, 210.

[327] Ringrose, P. (2015). *Reservoir Model Design*. Wiley.

[328] Ritter, H. and Drake, L. (1945). Pressure Porosimeter and Determination of Complete Macropore-Size Distributions. Pressure Porosimeter and Determination of Complete Macropore-Size Distributions. *Industrial & Engineering Chemistry Analytical Edition*, 17(12):782–786.

[329] Ritter, H. and Drake, L. (1948). Pore size distribution in porous materials. *Analytical Chemistry*, 20(7):665–670.

[330] Robert, C. (2007). *The Bayesian choice: from decision-theoretic foundations to computational implementation*. Springer Verlag.

[331] Roberts, A. (1997). Statistical reconstruction of three-dimensional porous media from two-dimensional images. *Physical Review E*, 56(3):3203–3212.

[332] Robin, M., Rosenberg, E., and Fassi-Fihri, O. (1995a). Wettability studies at the pore level: a new approach by use of Cryo-SEM. *SPE Formation Evaluation*, 10(1).

[333] Robin, M., Rosenberg, E., and Fassi-Fihri, O. (1995b). Wettability studies at the pore level: A new approach by use of cryo-sem. *SPE Formation Evaluation*, 10(1).

[334] Rubinstein, R. and Kroese, D. (2008). *Simulation and the Monte Carlo method*. Wiley-interscience.

[335] Ruehl, W., Schmid, ., and Wissman, W. (1963). Displacement Tests With Porous Rock Samples Under Reservoir Conditions. *Erdøl und Kohle-Erdgas-Petrochemie*, 16:6–1.

[336] Ryazanov, A. (2011). *Two-phase pore-network modelling: Existence of oil layers during water invasion*. PhD thesis, PhD thesis, Institute of Petroleum Engineering, Heriot Watt University Edinburgh.

[337] Ryazanov, A. V., van Dijke, M. I., Sorbie, K. S., et al. (2010). Pore-network prediction of residual oil saturation based on oil layer drainage in mixed-wet systems. In *SPE Improved Oil Recovery Symposium*. Society of Petroleum Engineers.

[338] Salathiel, R. (1973). Oil recovery by surface film drainage in mixed-wettability rocks. *Journal of Petroleum Technology*, 25(10):1216–1224.

[339] Santos, L., Philippi, P., Damiani, M., and Fernandes, C. (2002). Using three-dimensional reconstructed microstructures for predicting intrinsic permeability of reservoir rocks based on a Boolean lattice gas method. *Journal of Petroleum Science and Engineering*, 35(1-2):109–124.

[340] Sanz-Serna, J. and Calvo, M. (1994). *Numerical hamiltonian problems*. Chapman & Hall London.

[341] Sarker, M. and Siddiqui, S. (2009). Advances in Micro-CT Based Evaluation of Reservoir Rocks. In *SPE Saudi Arabia Section Technical Symposium*.

[342] Sayyad Amin, J., Nikooee, E., Ayatollahi, S., and Alamdari, A. (2010). Investigating wettability alteration due to asphaltene precipitation: Imprints in surface multifractal characteristics. *Applied Surface Science*, 256(21):6466–6472.

[343] Scales, L. (1985). *Introduction to non-linear optimization*. Springer-Verlag New York, Inc.

[344] Schaaf, T., Coureaud, B., Labat, N., and Busby, D. (2009). Using Experimental Designs, Assisted History-Matching Tools, and Bayesian Framework To Get Probabilistic Gas-Storage Pressure Forecasts. *SPE Reservoir Evaluation & Engineering*, 12(5):9–12.

[345] Scher, H. and Zallen, R. (1970). Critical density in percolation processes. *Journal of Chemical Physics*, 53:3759–3761.

[346] Schlueter, E. M., Zimmerman, R. W., Witherspoon, P. A., and Cook, N. G. W. (1997). The fractal dimension of pores in sedimentary rocks and its influence on permeability. *Engineering Geology*, 48(3-4):199–215.

[347] Schmid, C. (1964). The Wettability of Petroleum Rocks and Results of Experiments to Study the Effects of Variations in Wettability of Core Samples. *Erdoel Kohle*, 17(8):605–609.

[348] Scott, D. (1985). Averaged shifted histograms: effective nonparametric density estimators in several dimensions. *The Annals of Statistics*, 13(3):1024–1040.

[349] Seiler, A., Aanonsen, S., and Evensen, G. (2010). Structural Uncertainty Modelling and Updating Using the Ensemble Kalman Filter - Parameters and State Consistency. In *12th European Conference on the Mathematics of Oil Recovery*.

[350] Shannon, C. (1948). The mathematical theory of communication (parts 1 and 2). *Bell Syst. Tech. J*, 27:379–423.

[351] Shante, V. and Kirkpatrick, S. (1971). An introduction to percolation theory. *Advances in Physics*, 20(85):325–357.

[352] Sharma, M. and Wunderlich, R. (1987). The alteration of rock properties due to interactions with drilling-fluid components. *Journal of Petroleum Science and Engineering*, 1(2):127–143.

[353] Sheppard, A., Latham, S., Middleton, J., Kingston, A., Myers, G., Varslot, T., Fogden, A., Sawkins, T., Cruikshank, R., Saadatfar, M., et al. (2014). Techniques in helical scanning, dynamic imaging and image segmentation for improved quantitative analysis with x-ray micro-ct. *Nuclear Instruments and Methods in Physics Research Section B: Beam Interactions with Materials and Atoms*, 324:49–56.

[354] Silverman, B., Silverman, B., Silverman, B., and Silverman, B. (1986). *Density estimation for statistics and data analysis*, volume 3. Chapman and hall London.

[355] Sivia, D. and Skilling, J. (2006). *Data analysis: a Bayesian tutorial*. Oxford University Press, USA.

[356] Sjoblom, J. (2005). *Emulsions and Emulsion Stability: Surfactant Science Series/61*. CRC Press.

[357] Skauge, A., Spildo, K., Hiland, L., Vik, B., and Ottesen, B. (2004). Experimental evidence of different intermediate wetting states. In *Symposium of the Society of Core Analysts (Abu Dhabi, UAE), SCA*.

[358] Slatt, R. M. (2006). *Stratigraphic reservoir characterization for petroleum geologists, geophysicists, and engineers*, volume 61. Elsevier.

[359] Somasundaran, P. and Zhang, L. (2006). Adsorption of surfactants on minerals for wettability control in improved oil recovery processes. *Journal of petroleum science and engineering*, 52(1):198–212.

[360] Sorbie, K. and Skauge, A. (2011). Can network modeling predict two-phase flow functions. In *International Symp. Soc. Core Anal., Austin, TX, USA*, pages 18–21.

[361] Standnes, D. C. and Austad, T. (2000). Wettability alteration in chalk: 1. preparation of core material and oil properties. *Journal of Petroleum Science and Engineering*, 28(3):111–121.

[362] Standnes, D. C. and Austad, T. (2003a). Wettability alteration in carbonates: Interaction between cationic surfactant and carboxylates as a key factor in wettability alteration from oil-wet to water-wet conditions. *Colloids and Surfaces A: Physicochemical and Engineering Aspects*, 216(1):243–259.

[363] Standnes, D. C. and Austad, T. (2003b). Wettability alteration in carbonates: Low-cost ammonium surfactants based on bio-derivatives from the coconut palm as active chemicals to change the wettability form oil-wet to water-wet conditions. *Colloids and Surfaces A: Physicochemical and Engineering Aspects*, 218(1):161–173.

[364] Stewart, W., Caracotsios, M., and Sørensen, J. (1992). Parameter estimation from multiresponse data. *AIChE Journal*, 38(5):641–650.

[365] Stordal, A., Karlsen, H., Nævdal, G., Skaug, H., and Vallès, B. (2010). Bridging the ensemble Kalman filter and particle filters: the adaptive Gaussian mixture filter. *Computational Geosciences*, pages 1–13.

[366] Subbey, S., Christie, M., and Sambridge, M. (2004). Prediction under uncertainty in reservoir modeling. *Journal of Petroleum Science and Engineering*, 44(1-2):143–153.

[367] Svirsky, D., Dijke, M., and Sorbie, K. (2004). Prediction of three-phase relative permeabilities using a pore-scale network model anchored to two-phase data. In *SPE Annual Technical Conference and Exhibition*.

[368] Svirsky, D. S., Dijke, M. I. J. V., and Sorbie, K. S. (2007). Prediction of Three-Phase Relative Permeabilities Using a Pore-Scale Network Model Anchored to Two-Phase Data. (April):26–29.

[369] Talabi, O., Alsayari, S., Blunt, M., Dong, H., and Zhao, X. (2008). Predictive Pore Scale Modeling: From 3D Images to Multiphase Flow Simulations. In *SPE Annual Technical Conference and Exhibition*.

[370] Talash, A. and Crawford, P. (1961). Experimental Flooding Characteristics of Unconsolidated Sands. In *SPE Permian Basin Oil Recovery Conference*.

[371] Tarantola, A. (1987a). *Inverse problem theory*. Elsevier Amsterdam etc.

[372] Tarantola, A. (1987b). *Inverse problem theory: Methods for data fitting and model parameter estimation*. Elsevier Science Pub. Co. Inc., New York, NY.

[373] Taylor, J., Ashdown, M., and Hobson, M. (2008). Fast optimal CMB power spectrum estimation with Hamiltonian sampling. *Monthly Notices of the Royal Astronomical Society*, 389(3):1284–1292.

[374] Tian, H., Pan, L., Xiao, X., Wilkins, R. W. T., and Meng, Z. (2013). A preliminary study on the pore characterization of Lower Silurian black shales in the Chuandong Thrust Fold Belt , southwestern China using low pressure N 2 adsorption and FE-SEM methods as i. *Marine and Petroleum Geology*, 48:8–19.

[375] Tjølsen, C., Scheie, and Damsleth, E. (1991). A Study of the Correlation between Relative Permeability, Air Permeability and Depositional Environment on the Core-Plug Scale. *Advanced in Core Evaluation II, reservoir Appraisal, Gordon and Breach Science Publishers*.

[376] Toledo, P., Scriven, L., and Davis, H. (1994). Pore-space statistics and capillary pressure curves from volume-controlled porosimetry. *SPE Formation Evaluation*, 9(1):46–54.

[377] Treiber, L., Archer, D., and Owens, W. (1972). A laboratory evaluation of the wettability of fifty oil-producing reservoirs. *Old SPE Journal*, 12(6):531–540.

[378] Tsakiroglou, C., Burganos, V., and Jacobsen, J. (2004). Pore-structure analysis by using nitrogen sorption and mercury intrusion data. *AIChE journal*, 50(2):489–510.

[379] Tsakiroglou, C., Ioannidis, M., Amirtharaj, E., and Vizika, O. (2009). A new approach for the characterization of the pore structure of dual porosity rocks. *Chemical Engineering Science*, 64(5):847–859.

[380] Tsakiroglou, C. and Payatakes, A. (1990). A new simulator of mercury porosimetry for the characterization of porous materials. *Journal of colloid and interface science*, 137(2):315–339.

[381] Tsakiroglou, C. and Payatakes, A. (1991). A New Mercury Intrusion-Retraction Simulator Used as a Means for the Characterization of Porous Materials. *Studies in Surface Science and Catalysis*, page 169.

[382] Tsakiroglou, C. and Payatakes, A. (1998). Mercury intrusion and retraction in model porous media. *Advances in Colloid and Interface Science*, 75(3):215–253.

[383] Tsakiroglou, C. and Payatakes, A. (2000). Characterization of the pore structure of reservoir rocks with the aid of serial sectioning analysis, mercury porosimetry and network simulation. *Advances in water resources*, 23(7):773–789.

[384] Tsakiroglou, C. D. (2012). A multi-scale approach to model two-phase flow in heterogeneous porous media. *Transport in Porous Media*, 94(2):525–536.

[385] Tzimas, G., Matsuura, T., Avraam, D., Van der Brugghen, W., Constantinides, G., and Payatakes, A. (1997). The combined effect of the viscosity ratio and the wettability during forced imbibition through nonplanar porous media. *Journal of colloid and interface science*, 189(1):27–36.

[386] Valvatne, P. and Blunt, M. (2003). Predictive pore-scale network modeling. In *SPE Annual Technical Conference and Exhibition*.

[387] Valvatne, P. H. and Blunt, M. J. (2004). Predictive pore-scale modeling of two-phase flow in mixed wet media. *Water Resources Research*, 40(7).

[388] van Dijke, M., Lago, M., Sorbie, K., and Araujo, M. (2004a). Free energy balance for three fluid phases in a capillary of arbitrarily shaped cross-section: capillary entry pressures and layers of the intermediate-wetting phase. *Journal of colloid and interface science*, 277(1):184–201.

[389] van Dijke, M., McDougall, S., and Sorbie, K. (2001a). Three-phase capillary pressure and relative permeability relationships in mixed-wet systems. *Transport in Porous Media*, 44(1):1–32.

[390] van Dijke, M. and Sorbie, K. (2002a). Pore-scale network model for three-phase flow in mixed-wet porous media. *Physical Review E*, 66(4):046302.

[391] van Dijke, M. and Sorbie, K. (2002b). Pore-scale network model for three-phase flow in mixed-wet porous media. *Physical Review E*, 66(4):46302.

[392] van Dijke, M. and Sorbie, K. (2002c). The relation between interfacial tensions and wettability in three-phase systems: consequences for pore occupancy and relative permeability. *Journal of Petroleum Science and Engineering*, 33(1):39–48.

[393] van Dijke, M. and Sorbie, K. (2003). Three-phase capillary entry conditions in pores of noncircular cross-section. *Journal of colloid and interface science*, 260(2):385–397.

[394] van Dijke, M. and Sorbie, K. (2006). Existence of fluid layers in the corners of a capillary with non-uniform wettability. *Journal of colloid and interface science*, 293(2):455–463.

[395] van Dijke, M. and Sorbie, K. (2007). Consistency of three-phase capillary entry pressures and pore phase occupancies. *Advances in water resources*, 30(2):182–198.

[396] van Dijke, M., Sorbie, K., and de Mik, F. (2006). Network model prediction of three-phase relative permeabilities for a mixed-wet reservoir based on anchoring to two-phase data. In *Proceedings of 2006 International Symposium of SCA*. Society of Core Analysts, Society of Core Analysts.

[397] van Dijke, M., Sorbie, K., and McDougall, S. (2001b). Saturation-dependencies of three-phase relative permeabilities in mixed-wet and fractionally wet systems. *Advances in Water Resources*, 24(3):365–384.

[398] van Dijke, M., Sorbie, K., McDougall, S., et al. (2000). A process-based approach for three-phase capillary pressure and relative permeability relationships in mixed-wet systems. In *SPE/DOE Improved Oil Recovery Symposium*. Society of Petroleum Engineers.

[399] van Dijke, M., Sorbie, K., Sohrabi, M., Danesh, A., et al. (2004b). Three-phase flow wag processes in mixed-wet porous media: pore-scale network simulations and comparison with water-wet micromodel experiment. *SPE Journal*, 9(01):57–66.

[400] Vogel, H., Tolke, J., Schulz, V., Krafczyk, M., and Roth, K. (2005). Comparison of a Lattice-Boltzmann model, a full-morphology model, and a pore network model for determining capillary pressure-saturation relationships. *Vadose Zone Journal*, 4(2):380.

[401] Wang, F. (1988). Effect of wettability alteration on water/oil relative permeability, dispersion, and flowable saturation in porous media. *SPE Reservoir Engineering*, 3(2):617–628.

[402] Wang, H., Yang, Y., Wang, Y., Yang, J., Jia, J., and Nie, Y. (2013). Data-constrained modelling of an anthracite coal physical structure with multi-spectrum synchrotron x-ray ct. *Fuel*, 106:219–225.

[403] Washburn, E. (1921). Note on a method of determining the distribution of pore sizes in a porous material. *Proceedings of the National Academy of Sciences of the United States of America*, pages 115–116.

[404] Wellington, S. and Vinegar, H. (1987). X-ray computerized tomography. *Journal of Petroleum Technology*, 39(8):885–898.

[405] Wilkinson, D. and Willemsen, J. (1983). Invasion percolation: a new form of percolation theory. *Journal of Physics A: Mathematical and General*, 16:3365–3376.

[406] Wissmann, R. (1963). Displacement tests with porous rock samples under reservoir conditions. In *6th World Petroleum Congress*.

[407] Wu, K., Nunan, N., Crawford, J., Young, I., and Ritz, K. (2004). An efficient Markov chain model for the simulation of heterogeneous soil structure. *Soil Science Society of America Journal*, 68(2):346.

[408] Wu, S. and Firoozabadi, A. (2010). Permanent alteration of porous media wettability from liquid-wetting to intermediate gas-wetting. *Transport in porous media*, 85(1):189–213.

[409] Wu, Z., Datta-gupta, A., and Texas, A. (2002). Rapid History Matching Using a Generalized Travel-Time Inversion Method. *SPE Journal*, (January):11–14.

[410] Xie, X., Liu, Y., Sharma, M., and Weiss, W. (2009). Wettability alteration to increase deliverability of gas production wells. *Journal of Natural Gas Science and Engineering*, 1(1):39–45.

[411] Xu, B., Kamath, J., and Yortsos, Y. (1999). Use of Pore-Network Models to Simulate Laboratory Corefloods in a Heterogeneous Carbonate Sample. *SPE Journal*, 4(3):179–186.

[412] Yadali Jamaloei, B., Kharrat, R., Asghari, K., and Torabi, F. (2011). The influence of pore wettability on the microstructure of residual oil in surfactant-enhanced water flooding in heavy oil reservoirs: Implications for pore-scale flow characterization. *Journal of Petroleum Science and Engineering*, 77(1):121–134.

[413] Yan, B., Alfi, M., Wang, Y., Killough, J. E., and Texas, A. (2013). SPE 166173 A New Approach for the Simulation of Fluid Flow in Unconventional Reservoirs through Multiple Permeability Modeling.

[414] Yang, F., Ning, Z., and Liu, H. (2014). Fractal characteristics of shales from a shale gas reservoir in the Sichuan. *Fuel*, 115:378–384.

[415] Yang, Y.-W., Zografi, G., and Miller, E. E. (1988). Capillary flow phenomena and wettability in porous media: I. static characteristics. *Journal of colloid and interface science*, 122(1):24–34.

[416] Youssef, S., Han, M., Bauer, D., Rosenberg, E., Bekri, S., Fleury, M., and Vizika, O. (2008). High resolution μ-CT combined to numerical models to assess electrical properties of bimodal carbonates. In *Proceedings of 2008 International Symposium of SCA, Society of Core Analysts*.

[417] Yuan, H. and Swanson, B. (1989). Resolving pore-space characteristics by rate-controlled porosimetry. *SPE Formation Evaluation*, 4(1):17–24.

[418] Zhao, Y., Reynolds, A., and Li, G. (2008). Generating facies maps by assimilating production data and seismic data with the ensemble Kalman filter. In *SPE/DOE Symposium on Improved Oil Recovery*.

[419] Ziman, J. (1968). The localization of electrons in ordered and disordered systems I. Percolation of classical particles. *Journal of Physics C: Solid State Physics*, 1:1532.